



UNIVERSITÀ
DEGLI STUDI
DI PADOVA

UNIVERSITA' DEGLI STUDI DI PADOVA

Dipartimento di Ingegneria Industriale DII

Corso di Laurea Magistrale in Ingegneria Energetica

*Experimental and Theoretical Analysis of Condensation
from Superheated Vapor inside Microfin Tubes*

Relatore: *Ing. Andrea Diani*

Correlatore: *Prof. Luisa Rossetto*

Laureando: *Francesco Benà*

Matricola: *2020217*

Anno Accademico 2022/2023

*Alle mie nonne, Natalina e Gabriella,
nella speranza che vostro nipote
vi abbia rese orgogliose.*

Summary

Today, we are living a time of great changes: new different challenges have presented to the entire humankind. The world in which we are living will not be the same in 20-30 years due to the climate change which we have triggered. In this period of difficulties, the priority of the researchers of all the world is to explore new technologies which will allow us to overcome this huge and dramatic challenge.

The transition to a deep electric system is the key to solve, at least partially, the problem of the climate change. In this perspective, the renewable energy technologies are gaining more and more importance for their capability to generate energy with a very low impact on the environment.

However, the research is not simply limited to the green sources: other technologies require a deep study to allow the humankind to overcome the climate change. One of these technologies regards the heat generation: the heat pumps. The perspective is that these machines will completely overcome the traditional boilers in favour of a more sustainable way to produce heat in domestic and not-domestic applications.

In this field, several investigations have been made to study the impacts of the new refrigerants on the environment. However, not enough studies have been performed to understand the heat transfer mechanisms which appear inside the main components of the machines.

The aim of the present work is to experimentally investigate the mechanism of condensation from superheated vapor inside microfin tubes. A theoretical work of analysis of the existing literature was initially required to fully understand the mechanisms which regulate the condensation from superheated vapor. Several experiments are performed to verify the hypothesis found in literature. The experimental points are then compared with models to verify the predictability of the heat transfer coefficient. Some changes to existing models are proposed to better fit the experimental points and to better predict the heat transfer coefficients of condensation from superheated vapor inside microfin tubes. Finally, an analytical code for the design for a small helicoidal condenser is presented to show the applicability of the tested different models. The code can be used to build an experimental section to test different conditions of application of the proposed condenser, with even the possibility of integration with a hot storage tank.

Within the eventual tank, phase change materials could be disposed to allow to store heat inside the boiler for a larger amount of time. The thesis is subdivided as follow:

- Chapter 1: a presentation of the condensation from superheated vapor;
- Chapter 2: description of the experimental apparatus used for the experiments;
- Chapter 3: description of the adopted experimental method;
- Chapter 4: data reduction;
- Chapter 5: uncertainty analysis;
- Chapter 6: experimental results;
- Chapter 7: comparison of the experimental results with models;
- Chapter 8: design of the condenser;
- Chapter 9: conclusions;
- Appendix A: analysis of the phase change materials properties with T-history method;
- Appendix B: list of the codes used.

The work done for in this master's degree thesis will be useful for further investigations of heat transfer mechanisms inside condensers with microfin tubes.

Riassunto esteso in lingua italiana

Nel presente lavoro, viene presentata un'analisi teorica e sperimentale della condensazione da vapore surriscaldato dentro tubo microaletato.

R.1. Apparato e prove sperimentali

La sezione sperimentale utilizzata per gli esperimenti si trova nel Dipartimento di Ingegneria Industriale nell'Università degli studi di Padova. L'immagine dell'impianto sperimentale è riportata in Figura R.1, mentre in Tabella R.1 si riportano le caratteristiche geometriche del tubo analizzato.



Figura R.1. *Apparato sperimentale.*

OD	ID_{apex}	n	β	h	L
mm	mm	/	°	mm	mm
5	4.28	54	30	0.15	217

Tabella R.1. *Dimensioni principali del tubo micro alettato. Da sinistra, diametro esterno, diametro all'apice dell'aletta, numero alette, angolo d'elica, altezza aletta e lunghezza di scambio termico.*

La sezione sperimentale è stata originariamente sviluppata per testare la condensazione da vapore saturo. Nelle prove sperimentali, il vapore entra surriscaldato all'interno del tubo microaletta. La regolazione di impianto viene eseguita in maniera diversa rispetto al caso della condensazione da vapore saturo. In particolare, si utilizza la resistenza elettrica dell'evaporatore per poter controllare efficacemente il grado di surriscaldamento in ingresso e, quando il grado di surriscaldamento è circa 5 K, si utilizza anche il pre-condensatore per la regolazione.

R.2 Risultati sperimentali

I dati in uscita dalla sezione sperimentale vengono utilizzati per calcolare il coefficiente di scambio termico:

$$HTC = \frac{q_{tot}}{1000(T_{sat} - T_{wall,i})HTA}, \quad (R. 1)$$

dove HTC è il coefficiente di scambio termico [$\text{kW m}^{-2} \text{K}^{-1}$], q_{tot} è il calore scambiato nella sezione [W], T_{sat} è la temperatura di saturazione [$^{\circ}\text{C}$], $T_{wall,i}$ è la temperatura di parete [$^{\circ}\text{C}$] e infine HTA è l'area di scambio termico calcolata con il diametro all'apice dell'aletta come riferimento (ID_{apex}). Un totale di 62 punti sperimentali è stato ottenuto. A titolo di esempio, si riportano in Figura R.2 i risultati sperimentali ottenuti con una portata di massa specifica di $200 \text{ kg s}^{-1} \text{ m}^{-2}$ e con una temperatura di saturazione di $40 \text{ }^{\circ}\text{C}$. Il trend ottenuto è lo stesso anche per gli altri punti sperimentali.

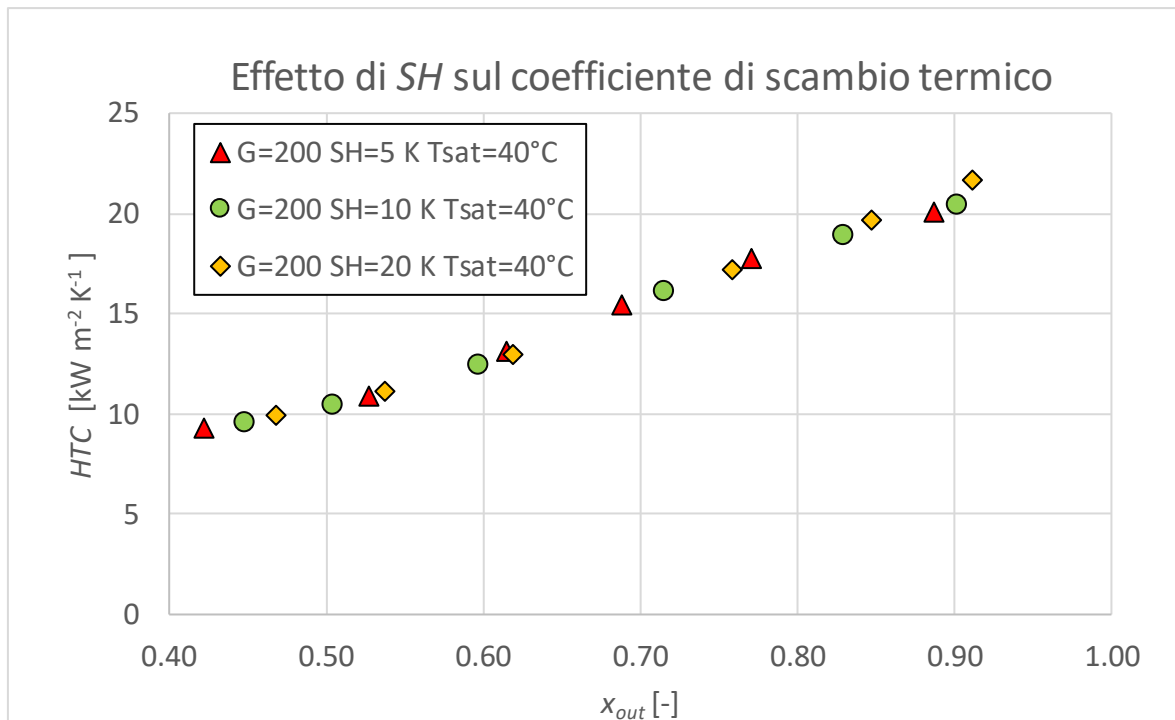


Figura R.2. Risultati sperimentali con $G=200 \text{ kg s}^{-1} \text{ m}^{-2}$ e temperatura di saturazione di 40°C .

I risultati mostrano che l'effetto del grado di surriscaldamento è trascurabile. Non viene infatti osservato alcun incremento rilevante dell' HTC all'aumentare del grado di surriscaldamento. Ciò è in accordo da quanto affermato da Rossetto [1]: se nell'equazione di Newton (R.1) viene utilizzata la differenza di temperatura tra saturazione e parete, il coefficiente di scambio termico della condensazione da vapore surriscaldato si differenzia dal coefficiente di scambio termico in condensazione da vapore saturo di pochi punti percentuali, di solito entro l'errore sperimentale. Ciò dipende dal coefficiente di scambio termico di desurriscaldamento sensibile, presente nella condensazione da vapore surriscaldato ma trascurabile rispetto a quello latente (ovvero il coefficiente che tiene conto del trasporto di massa da vapore a liquido nel processo di condensazione). I risultati sperimentali confermano l'ipotesi e rendono quindi possibile utilizzare modelli sviluppati in origine per il caso di condensazione da vapore saturo anche nel caso di vapore surriscaldato, a patto che la temperatura di parete sia inferiore rispetto alla temperatura di saturazione all'ingresso del tubo.

R.3 Modelli sperimentali

Quattro modelli sono stati testati per il calcolo del coefficiente di scambio termico in condensazione da vapore surriscaldato:

1. Il modello di Cavallini *et al.* [2]. Sviluppato inizialmente per la condensazione da vapore saturo, presenta buoni risultati anche in caso di condensazione da vapore surriscaldato se viene scelto un titolo di ingresso uguale a 0.9999;
2. Il modello di Hirose *et al.* [3]. Questo modello tende a sovrastimare di molto il coefficiente di scambio termico in condensazione se viene scelto un titolo di ingresso uguale a 0.9999;
3. Il modello di Hirose *et al.* modificato. Si tratta dello stesso modello presentato in precedenza ma ricalibrato sui punti sperimentali ottenuti. I risultati sono molto più precisi rispetto al caso precedente;
4. Il modello di Webb [4]. Si tratta dell'unico modello che presenta una simulazione sia del coefficiente di scambio termico bifase o in condensazione saturo (dato da Cavallini *et al.*) sia di quello di desurriscaldamento sensibile del vapore (dato dalla correlazione di Gnielinski e moltiplicato per il parametro R_x [5]). Nonostante la precisione maggiore, i risultati non si distanziano di molto da quelli ottenuti da modello di Cavallini *et al.*, a dimostrazione del fatto che il coefficiente di scambio termico di desurriscaldamento sensibile pesa molto meno di quello latente anche durante condensazione da vapore surriscaldato.

In Tabella R.2, vengono presentati l'errore medio relativo MRPE, l'errore medio assoluto MAPE e la deviazione standar ST delle differenti simulazioni.

Modello	MRPE %	MAPE %	ST %
Cavallini	-17.93	25.91	20.91
Hirose	50.78	50.78	30.37
Hirose modificato	0.91	8.24	10.57
Webb	-6.19	16.95	18.40

Tabella R.2. Errore medio relativo MRPE, errore medio assoluto MAPE e deviazione standar ST dei vari modelli.

A parte il modello originale di Hirose *et al.*, tutti gli altri modelli presentano dei buoni risultati (nel caso di un flusso bifase, un errore del $\pm 30\%$ è da ritenersi accettabile)

R.4 Design del condensatore

I modelli di Hirose *et al.* modificato e di Cavallini *et al.* sono stati utilizzati per il design di un condensatore elicoidale da 1 kW termico integrato con un serbatoio ad acqua fluente. Una volta progettato lo scambiatore, esso può essere utilizzato per costruire una piccola sezione sperimentale nella quale testare anche il regime transitorio dello stesso o per sviluppare un modello di fluidodinamica computazionale per predire le performance di un eventuale accumulatore termico.

Due simulazioni sono state condotte con il tubo cui la geometria è presentata in Tabella R.1., mentre due simulazioni sono state condotte con un altro tubo microaletato, di cui la geometria viene presentata in tabella R.3.

OD	ID_{apex}	ID_{base}	n	β	h	Rx
mm	mm	mm	/	°	mm	/
7	6.14	6.5	50	18	0.18	1.63

Tabella R.3. Dimensioni principali del tubo micro alettato. Da sinistra, diametro esterno, diametro all'apice dell'aletta, numero alette, angolo d'elica, altezza aletta e parametro di incremento dell'area rispetto alla base dell'aletta.

Le condizioni al contorno sono riportate in Tabella R.4.

Tubo	G	T_{sat}	SH	$T_{H2O,IN}$	m_{H2O}
	$kg\ s^{-1}\ m^{-2}$	°C	K	°C	$kg\ h^{-1}$
OD 5 mm	428.65	50	15	10	28.80
OD 7 mm	208.28	50	15	10	28.80

Tabella R.4. Condizioni al contorno per il design dello scambiatore. Da sinistra: Portata di massa specifica (calcolata rispetto a ID_{apex}), temperatura di saturazione del refrigerante, grado di surriscaldamento in ingresso lato refrigerante, temperatura di ingresso dell'acqua, portata di acqua.

I risultati delle 4 simulazioni sono riportati in Tabella R.5.

Modello	N	L_{tot}	H	A_{tot}	Q_{tot}	ΔP_{tot}	$\Delta P_{tot}/L$	$T_{H2O,OUT}$
	/	m	m	m ²	W	bar	bar m ⁻¹	°C
OD 5 Cavallini	33	20.74	0.25	0.33	1007	1.33	0.064	40.20
OD 5 Hirose	40	25.13	0.3	0.39	966	2.22	0.088	38.99
OD 7 Cavallini	23	14.45	0.24	0.32	999	0.15	0.011	39.97
OD 7 Hirose	23	14.45	0.24	0.32	996	0.15	0.010	39.87

Tabella R.5. Risultati delle quattro simulazioni con due tipologie di tubo utilizzando il modello di Cavallini *et al.* e il modello di Hirose *et al.* modificato. Da sinistra: numero spire, lunghezza dello scambiatore, altezza dello scambiatore, area totale dello scambiatore, calore totale scambiato, perdite di carico totali, perdite di carico totali per unità di lunghezza e temperatura di uscita dell'acqua.

I modelli utilizzati su entrambi i tubi per il calcolo del coefficiente di scambio termico lato refrigerante sono Cavallini *et al.* e Hirose *et al.* modificato, per un totale complessivo di 4 simulazioni. Quando viene utilizzato Cavallini *et al.* per il calcolo del coefficiente di scambio termico, le perdite di carico per frizione sono valutate con il modello di Diani *et al.* [6]., mentre nelle le simulazioni con la correlazione di Hirose *et al.* modificata, i gradienti di pressione per frizione sono calcolati direttamente dentro la stessa.

Le simulazioni con tubo da diametro esterno 7 mm riportano buoni risultati e sono raccomandate per la costruzione del condensatore. Le simulazioni con il diametro esterno da 5 mm, invece, presentano diverse criticità. In particolare, le perdite di carico sono troppo alte con entrambi i modelli. Si può notare che, nelle simulazioni con diametro esterno 5 mm, le perdite di carico per unità di lunghezza nel caso di Hirose *et al.* sono molto più importanti rispetto al caso con Cavallini *et al.* (dove la correlazione di Diani *et al.* viene utilizzata per il calcolo dei gradienti di pressione per attrito). Infatti, è molto probabile che i modelli di calcolo delle perdite di carico per attrito divergano nel caso in cui la portata di massa specifica aumenti in maniera considerevole (nel 5 mm, la G è quasi il doppio rispetto al caso con 7 mm). Questo comporta una caduta notevole di pressione, che porta a una drammatica riduzione della temperatura di saturazione e, quindi, del calore scambiato spira per spira. Conseguentemente, lo scambiatore risulta molto più lungo nel caso del tubo di 5 mm rispetto al 7 mm (nel modello di Hirose *et al.* modificato, nemmeno con 40 spire vengono soddisfatte le condizioni di design).

R.5 Conclusioni

Nel presente lavoro, si è dimostrato che:

- Se nell'equazione di Newton (quando la temperatura di parete è minore della temperatura di saturazione all'ingresso del tubo), la differenza di temperatura utilizzata è quella tra la saturazione e la temperatura interna di parete, l'effetto del surriscaldamento in condensazione da vapore surriscaldato è sperimentalmente trascurabile;
- I modelli utilizzati inizialmente per la condensazione da vapore saturo, con le opportune modifiche, possono essere utilizzati anche nel caso di condensazione da vapore surriscaldato ottenendo dei buoni risultati;
- Il condensatore con tubo da diametro esterno 7 mm è migliore rispetto a quello con diametro esterno 5 mm poiché le perdite di carico sono più contenute e, di conseguenza, lo scambiatore risulta essere più compatto e più performante.

INDEX

SUMMARY	I
RIASSUNTO ESTESO IN LINGUA ITALIANA	III
R.1. APPARATO E PROVE SPERIMENTALI	III
R.2. RISULTATI SPERIMENTALI	IV
R.3. MODELLI SPERIMENTALI	VI
R.4. DESIGN DEL CONDENSATORE	VII
R.5. CONCLUSIONI	IX
CHAPTER 1: INTRODUCTION TO SUPERHEATED CONDENSATION	1
1.1 SATURATED FILM CONDENSATION	1
1.2 SUPERHEATED CONDENSATION ACCORDING TO KONDOU AND HRNJACK.....	2
1.2.1 Superheating, subcooling degree and bulk mean enthalpy.....	3
1.2.2 Heat transfer process of condensation from superheated vapor	6
1.2.2.1 Heat balance of condensing superheat zone	6
1.2.2.2 Heat transfer coefficient in the condensing superheat zone.....	8
1.2.2.3 Heat transfer coefficient in the single-phase superheated zone	9
1.2.2.4 Heat transfer coefficient in the two-phase zone	9
1.2.3 Condensation from superheated vapor to saturated liquid	10
1.3 SUPERHEATED CONDENSATION ACCORDING TO WEBB	11
CHAPTER 2: EXPERIMENTAL APPARATUS	13
2.1 GENERAL SCHEME OF THE TEST RIG	13
2.2 COMPONENTS OF THE TEST RIG.....	15
2.2.1 Pump and filter.....	15
2.2.2. Damper	16
2.2.3 Coriolis flowmeter.....	16
2.2.4. Evaporator	17
2.2.5 Pre-condenser	18
2.2.6 Test section.....	19
2.2.6.1 Pressure transducers	19
2.2.6.2 Test section	19
2.2.6.3 Thermocouples	22
2.2.7 Post-condenser and chiller.....	23
2.2.8 Accuracy of the instruments of measurement	24
CHAPTER 3: EXPERIMENTAL METHOD	25
3.1 LOADING OF THE TEST RIG AND DESCRIPTION OF THE REFRIGERANT	25
3.1.1 Refrigerant R1234ze(E).....	26
3.2 POWER ON OF THE TEST RIG	27
3.3 MODULATION AND EXPERIMENTAL PROCEDURE	29
3.3.1 Modulation	29
3.3.1.1 Mass flow rate regulation	29
3.3.1.2 Saturation temperature regulation	30
3.3.1.3 Superheating degree regulation	30
3.3.1.4 Heat flow rate modulation	31
3.3.2 Experimental procedure.....	31
3.4 PLANT SHUT DOWN.....	33

CHAPTER 4: DATA REDUCTION	35
4.1 DATA REDUCTION	35
4.1.1 Reference model.....	35
4.1.2 Data reduction.....	36
CHAPTER 5: UNCERTAINTY ANALYSIS	39
5.1 ISO-GUM.....	39
5.1.1 Uncertainty type A.....	40
5.1.2 Uncertainty type B.....	40
5.1.3 Combined uncertainty.....	40
5.2 UNCERTAINTY ON THE HEAT FLOW RATE	41
5.3 UNCERTAINTY ON THE HEAT TRANSFER COEFFICIENT	42
5.3.1 Uncertainty on the wall temperature.....	42
5.3.2 Uncertainty on the saturation temperature	42
5.3.3 Uncertainty on the heat transfer coefficient	43
5.4 UNCERTAINTY ON THE OUTLET SPECIFIC ENTHALPY	44
5.5 UNCERTAINTY ON THE OUTLET VAPOR QUALITY	44
5.6 RESULTS	45
CHAPTER 6: EXPERIMENTAL RESULTS	47
6.1 EFFECT OF THE SATURATION TEMPERATURE	47
6.2 EFFECT OF SUPERHEATING DEGREE	48
6.3 EFFECT OF THE MASS VELOCITY	52
6.4 CONCLUSIONS	54
CHAPTER 7: MODELS FOR THE EVALUATION OF THE HTC FOR CONDENSATION FROM SUPERHEATED VAPOR	55
7.1 THE CAVALLINI <i>ET AL.</i> 'S MODEL FOR HORIZONTAL SMOOTH TUBES	55
7.1.1 The ΔT dependency flow regime map.....	55
7.1.2 Heat transfer coefficient for condensation in horizontal smooth tubes	57
7.2 THE CAVALLINI <i>ET AL.</i> 'S MODEL FOR HORIZONTAL MICROFIN TUBES	58
7.2.1 Description of the model.....	58
7.2.2 Hypothesis for the application of the model	60
7.2.3 Implementation and results	61
7.3 THE HIROSE <i>ET AL.</i> 'S MODEL FOR MICROFIN TUBES	64
7.3.1 Description of the model.....	64
7.3.2 Hypothesis for the application of the model	66
7.3.3 Implementation and results	66
7.4. THE HIROSE <i>ET AL.</i> 'S MODIFIED MODEL	69
7.4.1 Recalibration of the equations.....	69
7.4.2 Implementation and results	70
7.4.3 Comparison with R450A and R515B experimental data	71
7.4.3.1 Comparison of the models using R450A	72
7.4.3.2 Comparison of the models using R515B	73
7.4.4 Conclusions.....	74
7.5 WEBB'S MODEL	74
7.5.1 Gnielinski's model	75
7.5.1.1 Turbulent flow.....	75
7.5.1.2 Laminar flow	77
7.5.1.3 Transition region	77

7.5.2 Implementation and results	78
7.5.3 Conclusions.....	79
7.6 COMPARISON BETWEEN THE MODELS	80
CHAPTER 8: DESIGN OF THE CONDENSER	83
8.1 SHELL AND HELICAL CONDENSER	83
8.2 THE HEAT TRANSFER COEFFICIENT ON THE WATER SIDE.....	85
8.2.1 Cross flow around a smooth cylinder	85
8.2.2 Other correlations for the evaluation of the heat transfer coefficient on water side	88
8.3 GEOMETRY OF THE CONDENSER	89
8.3.1 Tube selection	89
8.3.2 Geometrical parameters.....	90
8.4 DESIGN PARAMETERS AND PRELIMINARY CALCULATIONS	91
8.4.1 Preliminary calculations on the refrigerant side.....	91
8.4.2 Preliminary calculations on water side.....	92
8.5 PRESSURE DROPS MODELS	92
8.5.1. Total pressure drops	93
8.5.2 Frictional pressure gradients	93
8.5.2.1 The Diani <i>et al.</i> 's model	93
8.5.2.2 The Hirose <i>et al.</i> 's model	95
8.5.3 The momentum pressure gradients	95
8.5.4. Gravity pressure gradients	96
8.6 REFRIGERANT HEAT TRANSFER COEFFICIENT.....	97
8.7 THE PROGRAM	98
8.7.1 Input of the program	100
8.7.2 Structure of the program.....	100
8.7.2.1. Calculation coil per coil	101
8.7.2.2. Heat transferred per coil supposed	101
8.7.2.3. Heat transfer coefficients.....	102
8.7.2.4. Calculation of the real heat transferred.....	103
8.7.2.5 Pressure drops calculation	104
8.7.2.6 Subsequent coil	104
8.8 RESULTS	106
8.8.1 Cavallini <i>et al.</i> 's model with OD 5 mm tube	106
8.8.2 Hirose <i>et al.</i> 's modified model with OD 5 mm tube	108
8.8.3 Cavallini <i>et al.</i> 's model with OD 7 mm tube.....	109
8.8.4 Hirose <i>et al.</i> 's modified model with OD 7 mm tube	111
8.8.5 Heat transfer coefficient.....	112
8.9 CONCLUSIONS	114
CHAPTER 9: CONCLUSIONS	117
9.1 RESULTS	117
9.2 FUTURE DEVELOPMENTS	118
APPENDIX A: T-HISTORY.....	A.1
A.1 INTRODUCTION	A.1
A.2 THERMOCOUPLES CALIBRATION.....	A.2
A.2.1 Types of thermocouples.....	A.2
A.2.2. Experimental setup.....	A.3
A.2.3 Calibration	A.4
A.2.4. Results.....	A.5

A.3 T-HISTORY: MATHEMATICAL MODEL.....	A.6
A.3.1. Principles of the original method	A.6
A.3.2. Hong et al.'s modified method	A.9
A.4: EXPERIMENT.....	A.12
A.4.1 Paraffins data	A.12
A.4.2 Experimental system	A.14
A.4.2.1 Tubes.....	A.14
A.4.2.2. Thermostatic chamber	A.15
A.4.2.3. Thermocouples	A.16
A.4.3 Experimental procedure.....	A.17
A.4.4. Experimental points.....	A.19
A.4.5. Mathematical models.....	A.21
A.4.5.1 Polynomial interpolation	A.22
A.4.5.2 Spline method.....	A.25
A.4.6 Investigation on Biot number	A.28
A.4.6.1 Method 1	A.28
A.4.6.2 Method 2.....	A.28
A.4.6.3 Results	A.30
A.5 RESULTS AND CONCLUSIONS	A.30
A.5.1 Results.....	A.30
A.5.2 Conclusions.....	A.33
APPENDIX B: MATLAB CODES.....	B.1
CODE B.1: MATRIX EXTRACTION	B.1
CODE B.2: CAVALLINI <i>ET AL.</i> 'S MODEL FOR MICROFIN TUBES	B.2
CODE B.3: HIROSE <i>ET AL.</i> 'S MODEL FOR MICROFIN TUBES	B.4
CODE B.4: INTERPOLATION FOR WAVY FLOW POINTS	B.7
CODE B.5: INTERPOLATION FOR ANNULAR FLOW POINTS	B.9
CODE B.6: HIROSE <i>ET AL.</i> 'S MODIFIED MODEL.....	B.11
CODE B.7: WEBB'S MODEL	B.14
CODE B.8: CONDENSER DESIGN WITH CAVALLINI <i>ET AL.</i> 'S MODEL AND OD 7MM	B.17
CODE B.9: CONDENSER DESIGN WITH HIROSE <i>ET AL.</i> 'S MODIFIED MODEL AND OD 7MM.....	B.22
CODE B.10. THERMOCOUPLES CALIBRATION	B.27
CODE B.11. T-HISTORY: POLYNOMIAL INTERPOLATION	B.28
CODE B.12. T-HISTORY: SPLINE INTERPOLATION	B.31

Chapter 1

Introduction to superheated condensation

In this Chapter, the saturated condensation and the superheated condensation phase change processes are presented and briefly described.

1.1 Saturated film condensation

Condensation (Rossetto [1]) is a process that appears when a vapor liquifies. In order to happen, the temperature of the wall must be lower than the saturation temperature of the substance at the given condition. The condensate sub-cools on the surface and consequently more vapor tends to condensate. This process involves a mass transport of the vapor into the liquid film. When the vapor condenses, it releases latent heat which is then transported through the liquid film to the wall.

The most common type of condensation is the liquid film one: vapor condenses in form of a continuous liquid film. The heat transfer resistance could be present in the vapor phase, at the interface or in the liquid film. Considering the case in which the condensation starts from a pure vapor on a vertical wall (Figure 1.1): the temperature change appears in the liquid film and at the interface (in order to have a mass transfer from vapor to liquid, the temperature of the vapor phase must be higher than the liquid one). Instead, in the vapor phase, the temperature drop is negligible: the dominant thermal resistance is concentrated in the liquid film.

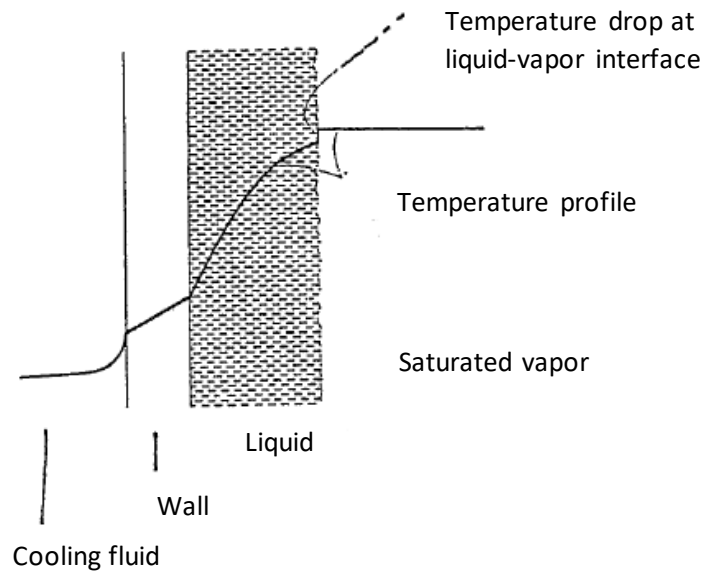


Figure 1.1. *Condensation from saturated vapor of a pure substance [1].*

The type of flow in the liquid film can significantly affect the thermal resistance: whenever the liquid film flow regime is laminar, a higher thermal resistance is expected, compared to the case of turbulent flow. Furthermore, the velocity of the vapor phase plays an important role in the definition of the liquid film thermal resistance: when the mass flow is higher, the shear stress exerted by the vapor phase on the liquid film could generate waves, increase the turbulence of the flow and enhance the heat transfer process. Generally, whenever a mass transport phenomenon (such as in evaporation or condensation) is involved, the heat transfer coefficient is expected to be much higher compared to the case of just sensible heat transfer.

1.2 Superheated condensation according to Kondou and Hrnjack

In an inverse cycle, the vapor exits from the compressor in a superheated state. Indeed, to avoid any possible damage to the compressor, the refrigerant exits from the evaporator already superheated: subsequently, after the compression, the vapor will be far away from the saturated condition. As matter of fact, the condensation could start even before the vapor reaches the saturation temperature: in this case, the process is called superheated condensation¹.

¹ The analysis proposed in this chapter refers to pure substances.

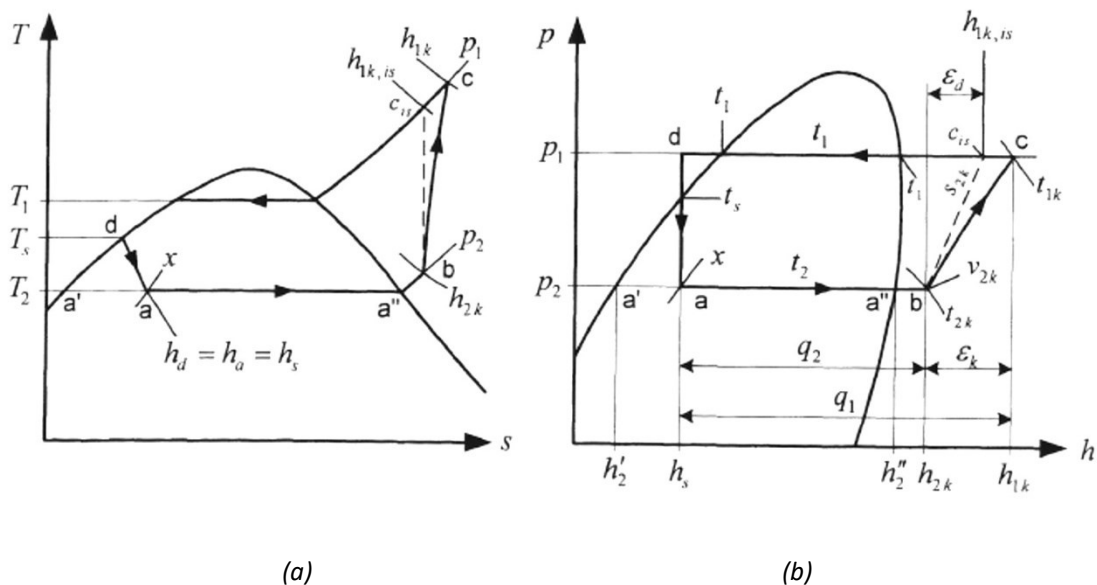


Figure 1.2. Simple vapor compression cycle. The vapor exits from the evaporator in point *b* already superheated and it is compressed up to point *c* [7].

1.2.1 Superheating, subcooling degree and bulk mean enthalpy

Consider a simple case of a tube-in-tube condenser: the refrigerant flows in the inner tube and the cooling fluid (water or air) flows outside. According to Kondou and Hrnjack [8], in the normal application, when the vapor enters inside the condenser, its temperature is above the saturation one and the refrigerant rejects just sensible heat. At a certain point along the tube, the temperature of the wall reaches the saturation condition: condensation from superheated vapor starts. The main difference of this process from the saturated film condensation is the simultaneous presence of latent and sensible desuperheating heat transfer: the vapor starts to condensate because the wall temperature is lower than the saturation one but, at the same time, since the refrigerant temperature is higher than the saturation temperature, the vapor is cooled and its temperature decreases. In Figure 1.3, all the process is represented.

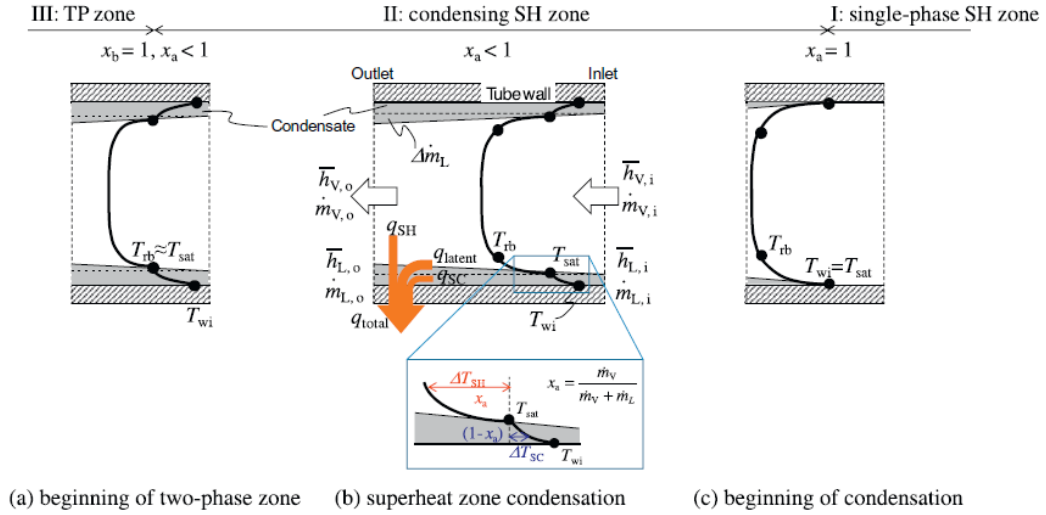


Figure 1.3. Heat transfer process along the cooling segment [8].

Looking at the Figure 1.3, it is possible to notice the presence of a parameter which defines the beginning of the superheated condensation. The parameter is the actual vapor quality x_a , defined as follow:

$$x_a = \frac{\dot{m}_V}{\dot{m}_{tot}}, \quad (1.1)$$

where \dot{m}_V is the vapor flow rate [kg s^{-1}] and \dot{m}_{tot} is the total flow rate [kg s^{-1}] (sum of the vapor flow rate \dot{m}_V and the liquid flow rate \dot{m}_L). When this parameter becomes equals to 1, condensation from superheated vapor starts. Note that the actual quality of vapor is different compared to the thermodynamic quality, which is evaluated at the equilibrium under diabatic condition:

$$x_a \neq x_b \approx f_{equilibrium}(h_b, P), \quad (1.2)$$

where x_b is the thermodynamic quality, P [bar] is the pressure of the system and h_b [J kg^{-1}] is the bulk mean specific enthalpy of the flow passing through the cross section of the tube:

$$h_b = \frac{\int (C_p T_r \rho u) ds}{\int (\rho u) ds}, \quad (1.3)$$

where C_p, ρ, u are respectfully the specific heat [$\text{J kg}^{-1} \text{K}^{-1}$], the density [kg m^{-3}] and the velocity [m s^{-1}] of the refrigerant in a small cross-sectional area ds . T_r [K] is the temperature of the refrigerant.

Similarly, the average vapor and liquid specific enthalpies [J kg^{-1}] can be written as:

$$\bar{h}_V = h_{V,sat} + \frac{\int (C_{p,V} \Delta T_{SH} \rho_V u_V) ds}{\int (\rho_V u_V) ds}, \quad (1.4)$$

$$\bar{h}_L = h_{L,sat} - \frac{\int (C_{p,L} \Delta T_{SC} \rho_L u_L) ds}{\int (\rho_L u_L) ds} = h_{V,sat} - \Delta h_{LV} - \frac{\int (C_{p,L} \Delta T_{SC} \rho_L u_L) ds}{\int (\rho_L u_L) ds}, \quad (1.5)$$

where $h_{V,sat}$ and $h_{L,sat}$ are the specific enthalpies of saturated vapor and liquid [J kg^{-1}], Δh_{LV} is the latent heat ($h_{V,sat} - h_{L,sat}$), ΔT_{SH} and ΔT_{SC} are the superheating and subcooling degree [K] with respect to the saturation temperature of the refrigerant T_{sat} [K]. The average heat carried by the superheated vapor $\Delta \bar{h}_{SH}$ and by subcooled liquid $\Delta \bar{h}_{SC}$ is simplified as follow:

$$\frac{\int (C_{p,V} \Delta T_{SH} \rho_V u_V) ds}{\int (\rho_V u_V) ds} = \Delta \bar{h}_{SH}, \quad (1.6)$$

$$\frac{\int (C_{p,L} \Delta T_{SC} \rho_L u_L) ds}{\int (\rho_L u_L) ds} = \Delta \bar{h}_{SC}, \quad (1.7)$$

Consequently, it is possible to write:

$$\bar{h}_V = h_{V,sat} + \frac{\int (C_{p,V} \Delta T_{SH} \rho_V u_V) ds}{\int (\rho_V u_V) ds} = h_{V,sat} + \Delta \bar{h}_{SH}, \quad (1.8)$$

$$\bar{h}_L = h_{L,sat} - \frac{\int (C_{p,L} \Delta T_{SC} \rho_L u_L) ds}{\int (\rho_L u_L) ds} = h_{V,sat} - \Delta h_{LV} - \Delta \bar{h}_{SC}. \quad (1.9)$$

Substituting in in (1.3) the equations (1.8) and (1.9), the bulk enthalpy can be finally rewritten as follow:

$$h_b = \frac{\bar{h}_L \dot{m}_L + \bar{h}_V \dot{m}_V}{\dot{m}_{tot}} = (h_{V,sat} + \Delta\bar{h}_{SH}) \frac{\dot{m}_V}{\dot{m}_{tot}} + (h_{V,sat} - \Delta h_{LV} - \Delta\bar{h}_{SC}) \frac{\dot{m}_L}{\dot{m}_{tot}}. \quad (1.10)$$

1.2.2 Heat transfer process of condensation from superheated vapor

1.2.2.1 Heat balance of condensing superheat zone

According to the continuity equation, the total mass of refrigerant flowing in the tubes \dot{m}_{tot} is equal to:

$$\dot{m}_{tot} = \dot{m}_{V,IN} + \dot{m}_{L,IN} = \dot{m}_{V,OUT} + \dot{m}_{L,OUT}, \quad (1.11)$$

where \dot{m}_V and \dot{m}_L are the mass flow rates of vapor and liquid at the inlet (subscript *IN*) and at the outlet (subscript *OUT*) of the superheated condensing segment. The amount of condensate generated through the segment is equal to:

$$\Delta\dot{m}_L = \dot{m}_{L,OUT} - \dot{m}_{L,IN} = \dot{m}_{V,IN} - \dot{m}_{V,OUT} = \Delta\dot{m}_V. \quad (1.12)$$

According to (1.10), the total heat flow rate at the inlet of the segment is equal to:

$$h_{b,IN} \dot{m}_{tot} = (h_{V,sat} + \Delta\bar{h}_{SH,IN})(\dot{m}_{V,OUT} - \Delta\dot{m}_L) + (h_{V,sat} - \Delta h_{LV} - \Delta\bar{h}_{SC,IN})\dot{m}_{L,IN}, \quad (1.13)$$

Similarly, the total heat flow rate at the outlet of the segment is equals to:

$$h_{b,OUT} \dot{m}_{tot} = (h_{V,sat} + \Delta\bar{h}_{SH,OUT})\dot{m}_{V,OUT} + (h_{V,sat} - \Delta h_{LV} - \Delta\bar{h}_{SC,OUT})(\dot{m}_{L,IN} + \Delta\dot{m}_L), \quad (1.14)$$

Subtracting the equation (1.14) from (1.13), the enthalpy change through the superheated condensing segment can be written:

$$(h_{b,IN} - h_{b,OUT})\dot{m}_{tot} = (\Delta\bar{h}_{SH,IN}\dot{m}_{V,IN} - \Delta\bar{h}_{SH,OUT}\dot{m}_{V,OUT}) + \Delta h_{LV}\Delta\dot{m}_L + (\Delta\bar{h}_{SC,OUT}\dot{m}_{L,OUT} - \Delta\bar{h}_{SC,IN}\dot{m}_{L,IN}). \quad (1.15)$$

This equation shows the superheated condensation is composed by three different heat transfer processes: the sensible de-superheating of the vapor \dot{Q}_{SH} , the latent heat rejection to the coolant \dot{Q}_{latent} and the subcooling of the liquid phase \dot{Q}_{SC} . The equation can be rewritten in terms of heat \dot{Q}_{tot} [W]:

$$\dot{Q}_{tot} = \dot{Q}_{SH} + \dot{Q}_{latent} + \dot{Q}_{SC}, \quad (1.16)$$

where:

$$\dot{Q}_{tot} = (h_{b,IN} - h_{b,OUT})\dot{m}_{tot}, \quad (1.17)$$

$$\dot{Q}_{SH} = \Delta\bar{h}_{SH,IN}\dot{m}_{V,IN} - \Delta\bar{h}_{SH,OUT}\dot{m}_{V,OUT}, \quad (1.18)$$

$$\dot{Q}_{latent} = \Delta h_{LV}\Delta\dot{m}_L, \quad (1.19)$$

$$\dot{Q}_{SC} = \Delta\bar{h}_{SC,OUT}\dot{m}_{L,OUT} - \Delta\bar{h}_{SC,IN}\dot{m}_{L,IN}. \quad (1.20)$$

Dividing (1.16) by the heat transfer area, the heat fluxes are obtained [W m⁻²]:

$$q_{tot} = q_{SH} + (q_{latent} + q_{SC}). \quad (1.21)$$

1.2.2.2 Heat transfer coefficient in the condensing superheat zone.

Similarly to equation (1.3), a bulk mean temperature of the refrigerant $T_{b,r}$ [K] can be defined through the cross section of the tube:

$$T_{b,r} = \frac{\int (T_r \rho u) ds}{\int (\rho u) ds}. \quad (1.22)$$

This temperature could be evaluated with an equilibrium correlation from the bulk mean enthalpy and the pressure of the refrigerant:

$$T_{b,r} \approx f_{equilibrium}(h_b, P). \quad (1.23)$$

In the superheated zone, $T_{b,r}$ should be greater than T_{sat} since the flow is still far from the saturated condition. In this point, $\Delta \bar{T}_{SH}$ (average superheat in vapor flow or superheating degree [K]) should exceed zero. When the temperature of the wall reaches T_{sat} (Figure 1.3 (c)), superheated vapor starts to condense and x_a begins to decrease from unity: the superheated condensation starts. Compared to the T_{sat} , the liquid presents a degree of subcooling ΔT_{SC} (Figure 1.3 (b)). Instead, the liquid-vapor interface is at the saturated conditions. The process continues until $T_{b,r}$ approaches T_{sat} (Figure 1.3(a)): in this point, the thermodynamic quality is equals to 1 and the saturated condensation starts.

During the condensation from superheated vapor, the driving temperature difference for the de-superheating process (equation (1.18)) is supposed $T_{b,r} - T_{sat}$. The remaining heat transfer processes can be evaluated as a heat flux from saturated condensation. Since the condensation process requires a certain degree of subcooling of the liquid (Paragraph §1.2), the heat transfer coefficient HTC of saturated condensation includes both q_{latent} and q_{SC} . The driving temperature difference in this case is $T_{sat} - T_{wall,i}$ where $T_{wall,i}$ is the inner wall temperature. Finally, equation (1.21) can be rewritten as follow:

$$\alpha(T_{b,r} - T_{wall,i}) = \alpha_{SH}(T_{b,r} - T_{sat}) + \alpha_{TP}(T_{sat} - T_{wall,i}), \quad (1.24)$$

$$\alpha = \frac{q_{tot}}{T_{b,r} - T_{wall,i}} \quad \text{at } T_{wall,i} < T_{sat} \quad \text{and } h_b > h_{v,sat}, \quad (1.25)$$

where α is the overall *HTC* from condensation of superheated vapor [$\text{W kg}^{-1} \text{K}^{-1}$], α_{SH} is the sensible *HTC* in the de-superheating process and α_{TP} (subscript *TP* stands for two-phase) is the *HTC* accounting for the vapor mass transfer into the liquid and the subcooling of the condensate formed.

1.2.2.3 Heat transfer coefficient in the single-phase superheated zone

If the vapor enters superheated inside the condenser but the temperature of the wall $T_{wall,i}$ is higher than T_{sat} , the conditions for the condensation are not satisfied: just sensible heat transfer rejection appears. The following equations can be written:

$$q_{tot} = q_{SH}, \quad (1.26)$$

$$\alpha(T_{b,r} - T_{wall,i}) = \alpha_{SH}(T_{b,r} - T_{wall,i}), \quad (1.27)$$

$$\alpha = \frac{q_{tot}}{T_{b,r} - T_{wall,i}} \quad \text{at } T_{wall,i} > T_{sat} \quad \text{and } h_b > h_{v,sat}. \quad (1.28)$$

1.2.2.4 Heat transfer coefficient in the two-phase zone

When the bulk enthalpy becomes h_b equals to the vapor saturation enthalpy $h_{v,sat}$, the saturated condensation begins (Figure 1.3 (a)). The thermodynamic quality becomes equals to one ($x_b = 1$) and the process described in paragraph §1.1 appears. The *HTC* is equals to:

$$\alpha = \frac{q_{tot}}{T_{b,r} - T_{wall,i}} \quad \text{at } T_{wall,i} < T_{sat} \approx T_{b,r} \quad \text{and } h_{L,sat} \leq h_b \leq h_{v,sat}. \quad (1.29)$$

1.2.3 Condensation from superheated vapor to saturated liquid

Vapor enters superheated inside the condenser. If temperature of the wall is higher than the saturation temperature of the refrigerant at the given pressure ($T_{wall,i} > T_{sat}$) just sensible heat transfer appears. (§1.2.2.3). When the temperature of the wall drops below the saturation temperature ($T_{wall,i} \leq T_{sat}, x_a = 1$), the condensation from superheated vapor starts (§1.2.2.2) with simultaneous sensible and latent heat transfer. Finally, when the bulk enthalpy approaches the saturated vapor enthalpy (the mean bulk temperature becomes equals to the saturation temperature, $T_{wall,i} < T_{sat} \approx T_{b,r}, x_b = 1$) condensation in saturated condition begins (§1.2.2.4). Figure 1.11 shows an example of counter-current heat exchanger, where the wall temperature is above the saturation one at the inlet of the condenser.

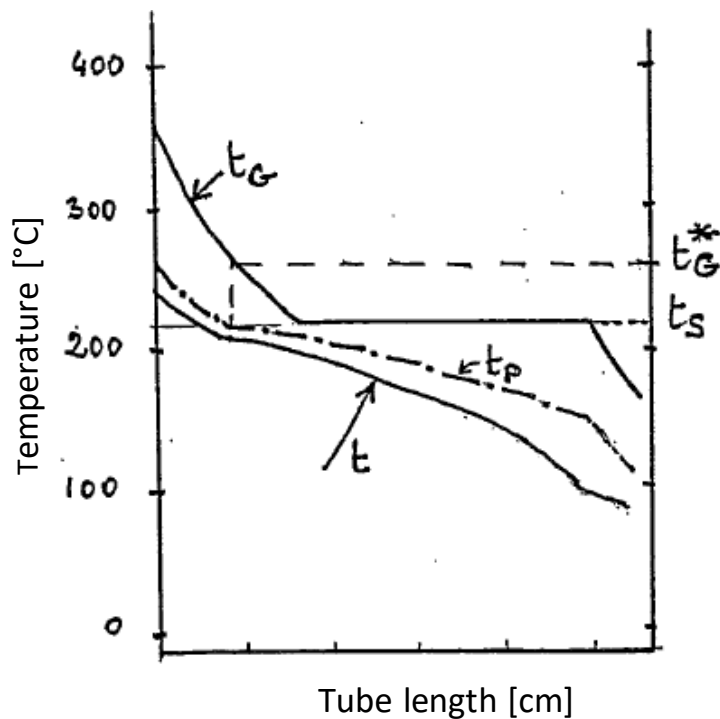


Figure 1.4. Temperature evolution in a counter-current condenser. The temperature of the wall t_p at the inlet is higher than the saturation temperature t_s . The condensation from superheated vapor starts in t_G^* [1].

1.3 Superheated condensation according to Webb

The theory presented by Kondou and Hrnjack [8] is one of the most recent studies on the condensation process from superheated vapor. However, the theory is quite elaborate. Indeed, to be applied in laboratory, the calculations of local heat transfer coefficients must be allowed: the bulk refrigerant temperatures and bulk refrigerant enthalpies in different parts of the tube must be known. As it will be described in Chapter §2, the test apparatus was not originally developed for the study of condensation from superheated vapor. Consequently, it does not allow to reduce data on the local bulk refrigerant temperatures and, consequently, on the local bulk refrigerant enthalpies. Since this master thesis is a first attempt to study the condensation from superheated vapor, a simpler theory is chosen as reference to the experiments. The theory is the one proposed by Webb [4]. According to this paper, the heat transfer coefficient in condensation from superheated vapor can be modelled as:

$$\alpha(T_{sat} - T_{wall,i}) = \alpha_{SH}(T_{b,r} - T_{sat}) + \alpha_{TP}(T_{sat} - T_{wall,i}). \quad (1.30)$$

The main difference between this theory and the one presented by Kondou and Hrnjack is the driving temperature difference on the left side of the equation, which is $T_{sat} - T_{wall,i}$. The bulk refrigerant temperature is not required for the evaluation of the overall heat transfer coefficient.

The demonstration of the hypothesis presented by Rossetto [1] is the aim of the experiments performed and later presented: if the driving temperature difference in both side of the Newton's equation is $T_{sat} - T_{wall,i}$, the condensation heat transfer coefficient from superheated vapor α is within few percent of the one of saturated condensation α_{TP} (two-phase heat transfer coefficient). This implies that models initially studied for saturated condensation can be adopted with good level of precision to calculate the heat transfer coefficient even in the case of condensation from superheated vapor. In the following chapters, this hypothesis will be verified and different models will be proposed to properly predict the overall heat transfer coefficient.

Chapter 2:

Experimental apparatus

In this Chapter, a detailed description of the experimental apparatus used for the tests on the condensation from superheated vapor is presented. The test rig is the same illustrated in Diani *et al.* [9] and in Donno [10]. It is located in the “Heat Transfer in Microgeometries Laboratory” in the Department of Industrial Engineering at the University of Padova.

2.1 General scheme of the test rig

In Figure 2.1, the schematic diagram of the test rig is present. In Figure 2.2, a picture of the experimental apparatus is shown.

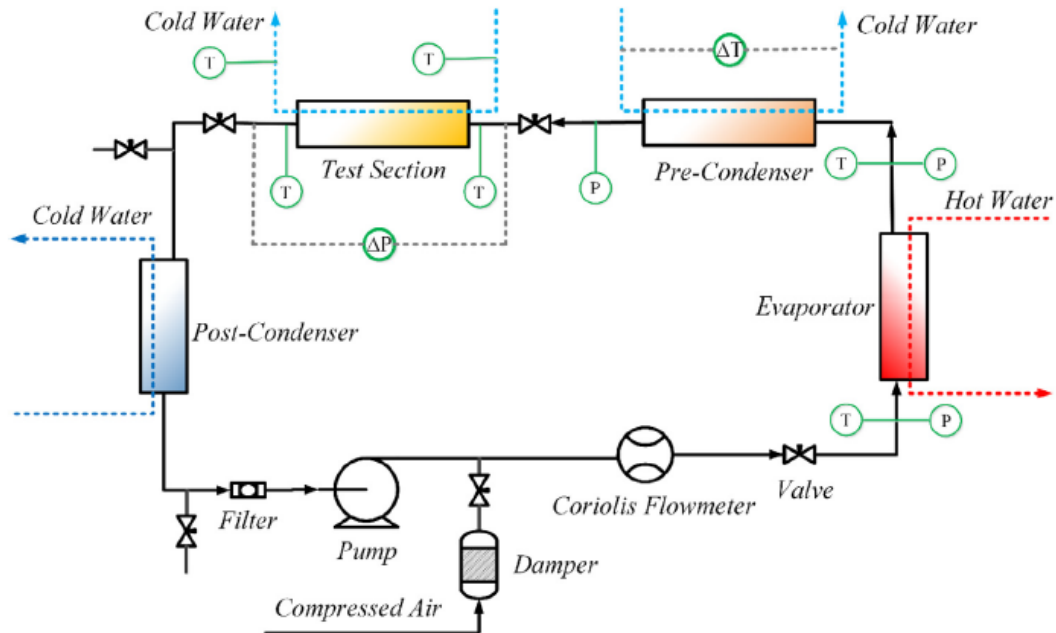


Figure 2.1. Diagram of the test rig. The T and P symbols represent the points where the temperature and the pressures are measured [9].

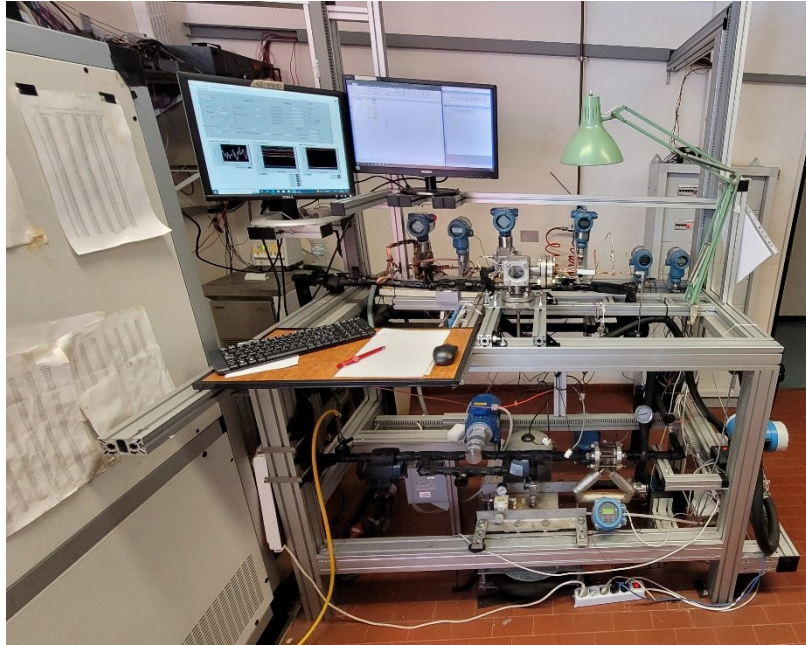


Figure 2.2. *Experimental apparatus.*

The Figure 2.1 shows the test rig which includes four different water loops and one single refrigerant loop. Before entering in the details of each component, a general description of the refrigerant circuit is mandatory:

1. The subcooled refrigerant is pumped by a magnetically coupled gear pump (subparagraph §2.2.1) in the Coriolis flowmeter (subparagraph §2.2.3), for the measurement of the mass flow rate [kg h^{-1}];
2. The fluid enters inside the evaporator (subparagraph §2.2.4), where it exits superheated;
3. The superheated vapor passes then inside a pre-condenser (subparagraph §2.2.5), where is precooled. This component in the experiments is used to keep stable the degree of superheating when the temperature difference is around 5 K (for more details on the experimental procedure, please refer to Chapter §3);
4. The vapor enters inside the test section (subparagraph §2.2.6) and exits with a thermodynamic quality greater than 0;
5. The fluid exits from the test section and enters inside a post-condenser (paragraph §2.2.7), where the condensation process is completed and then it is subcooled;
6. After passing through a cleaning filter, the refrigerant goes back inside the pump and the cycle starts again.

2.2 Components of the test rig

2.2.1 Pump and filter

The pump (Figure 2.3(a)) is a magnetically coupled gear type. This component gives to the refrigerant the proper head necessary for the circulation inside the plant to overcome the pressure drops. It is coupled with an inverter. By means of a control panel located on the general control system (Figure 2.3(b)), the rotational speed can be modified, changing subsequently the refrigerant mass flow rate \dot{m}_R for the different test conditions. Despite not being used during the experiments, a bypass of the pump is also present. Upstream of the pump, a cleaning filter is located to remove the impurities present in the circuit.



(a)



(b)

Figure 2.3. On the left: magnetically coupled gear pump. On the right, general control system. On the panel, all the switchers for the different parts of the plant are located. In yellow, the control device for the pump rotational speed.

2.2.2. Damper

The damper is a system which allows to control the saturation pressure inside the circuit P_{sat} . A valve is used to make compressed air flow inside the damper. This regulation allows a straight control of the saturation temperature T_{sat} (which is a function of the saturation pressure and it is calculated with REFPROP 10 [11]).

2.2.3 Coriolis flowmeter

The Coriolis flowmeter (Figure 2.4) is located downstream the pump. It is able to evaluate the pumped refrigerant mass flow rate \dot{m}_R in the circuit: the refrigerant passes through an Ω section, generating a Coriolis force which is opposite to the one generated by the electronics of the flowmeter. The opposition to the vibrations of the tubes induces a time lag between the inlet and the outlet of the flowmeter which is proportional to the flow rate. For the accuracies of the experimental instruments, please refer to Table 2.2.



Figure 2.4. Coriolis flowmeter.

2.2.4. Evaporator

After passing through a regulation valve, the refrigerant flows inside the evaporator. By means of an electric resistance of nominal power 1.67 kW (modulated by a PID regulator, whose set point temperature can be adjusted) the water is heated. The water enters inside the counter flow plate heat exchanger (Figure 2.5 (a)) and supplies the heat to the refrigerant, which evaporates and exits in superheated state. The control of the power supplied by the water is fundamental to stabilize the superheating degree before entering the test section. Two thermocouples are present at the inlet and at the outlet of the evaporator. A flow meter is located at the inlet of the heat exchanger (water side) to measure the flow rate of the water which is entering in the evaporator (Figure 2.5 (b)).



(a)



(b)

Figure 2.5. On the left: brazed plate heat exchanger (evaporator). On the right, volumetric flow meter for water at the evaporator.

2.2.5 Pre-condenser

Before entering the test section, the refrigerant passes through a pre-condenser. This component was used in the past works [9, 10] to control the quality of vapor at the inlet of the test section, since the previous investigations regarded the condensation from vapor in saturated conditions. However, the aim of the present work is the investigation of the condensation from superheated vapor. Consequently, the stabilization of the superheating degree is necessary. The pre-condenser is turned on to stabilize the superheating degree when the desired inlet temperature is just few degrees above the saturation one (5 K) since the control by means of the evaporator electric resistance could involve several hours before the desired inlet condition is reached.

The pre-condenser is a tube-in-tube heat exchanger. The water which absorbs the heat rejected by the pre-condenser is cooled down by the thermal machine chiller Rock 4 (Figure 2.6), which allows a temperature regulation of the water at the inlet within ± 0.1 K.



Figure 2.6. Chiller Rock 4.

2.2.6 Test section

The test section is the part of the plant where the refrigerant rejects the heat to the water which comes from the LAUDA water thermostatic bath (Figure 2.12 (a)) and condenses. It is the most important part of the circuit, since there the condensation process is analysed.

2.2.6.1 Pressure transducers

Two absolute pressure transducers (Figure 2.7) are located upstream and downstream the evaporator (for the accuracies of the experimental instruments, please refer to Table 2.2). A differential pressure transducer (Figure 2.7) measures the pressure drop inside the test section. An absolute pressure transducer (used to evaluate the $P_{ref,IN}$) is also present at the inlet of the test section (Figure 2.7).

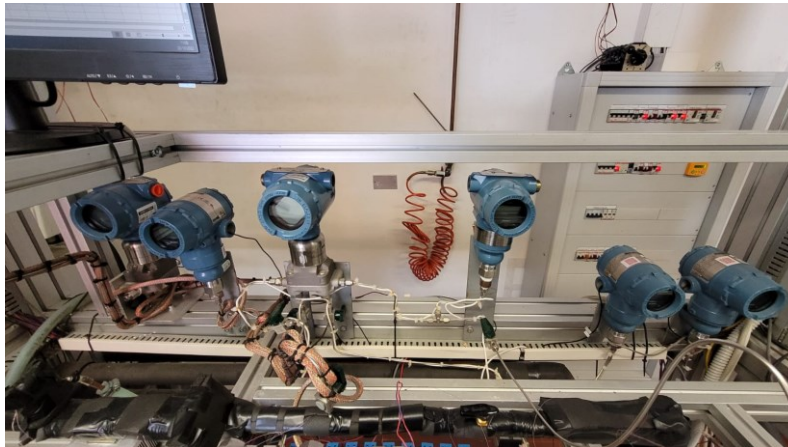


Figure 2.7. On the right, the two absolute pressure transducers at the inlet and at the outlet of the evaporator. On the left, the differential and the absolute pressure transducers for the test section.

2.2.6.2 Test section

The refrigerant passes inside the microfin tube (in brown in Figure 2.8). Compared to the smooth one, the microfin tube presents a larger heat transfer area. Furthermore, the presence of fins improves the turbulence of the liquid film, leading to a lower thermal resistance and an increase of the heat transfer coefficient. On the other hand, the pressure drops are higher than in the smooth tube, due to the higher resistance to

the flow induced by the fins. A lot of research has been conducted on the enhance of the heat transfer process with microfin tubes (for instance, Diani *et al.* [9], Cavallini *et al.* [2]) from saturated vapor, but just few trials have been performed in condition of condensation from superheated vapor.

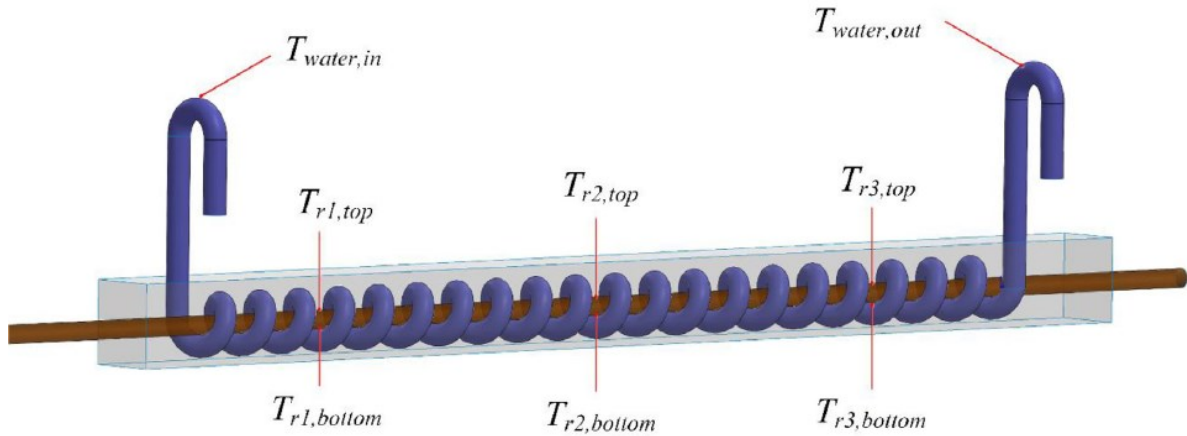


Figure 2.8. Schematic representation of the test section [9].

The geometry of the microfin tube plays a crucial role in the heat transfer process. In Figure 2.9, all the geometrical parameters for a generic microfin tube are reported. In Figure 2.10, a cross section of a real microfin tube can be seen.

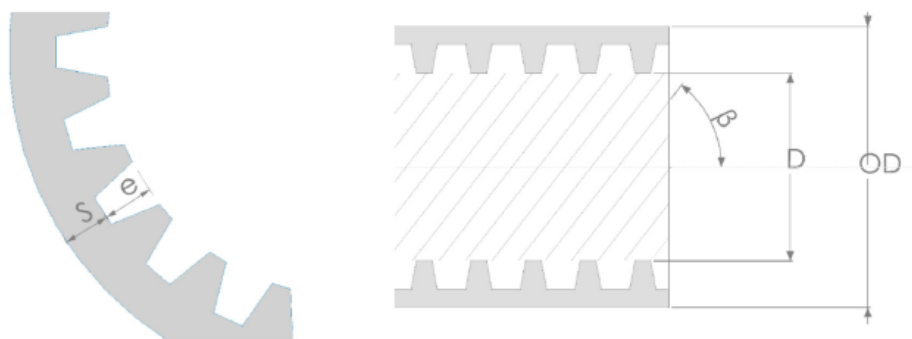


Figure 2.9. Schematic diagrams of the geometrical parameters in a microfin tube.

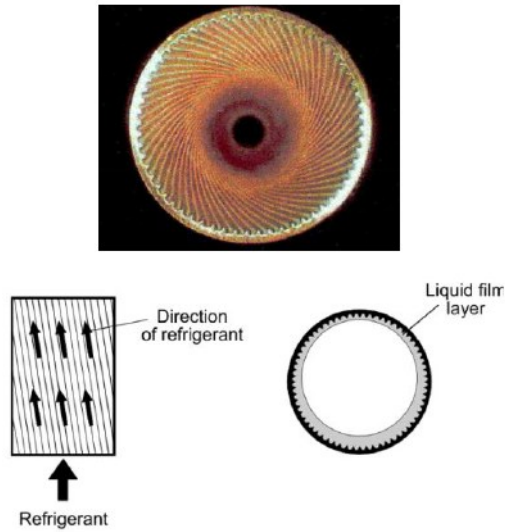


Figure 2.10. Cross section of a real microfin tube [10].

The tube used in the experiment is the same adopted in Donno [10]. The geometrical parameters are listed in Table 2.1.

OD	ID_{apex}	n	β	h	L
mm	mm	/	$^{\circ}$	mm	mm
5	4.28	54	30	0.15	217

Table 2.1. Geometrical parameters of the test tube. From left: Outer diameter, Inner diameter at the apex of the fin (D in Figure 2.9), number of fins, elix angl, height of the fin (e in Figure 2.9) and heat transfer length of the tube in the experimental section.

A smooth helical copper tube surrounds the microfin one (in purple, Figure 2.8). Inside, the water which comes from the thermostatic water bath LAUDA Proline RP1845 flows (Figure 2.11 (a)). This system is used to control the condensing process in the inner tube section, cooling down the refrigerant up to an outlet quality of vapor generally greater than 0.2. The water bath has a minimum operative temperature of 4°C, with an accuracy of the setting temperature within ± 0.01 K. The water flow rate is evaluated with a volumetric flow meter [l/h] (Figure 2.11 (b)).



(a) (b)
Figure 2.11 On the left: water bath LAUDA Proline RP1845. On the right: volumetric flow meter for the cooling water.

The two tubes are hosted by an aluminium alloy box with an alloy of tin-lead occupying the space between them to assure thermal contact. The whole section is covered by foam insulation to guarantee the minimum heat losses possible.

2.2.6.3 Thermocouples

At the inlet and at the outlet of the water tube (Figure 2.8), two thermocouples are located for the evaluation of the water temperature. Furthermore, six other thermocouples are located at 55 mm (T1, B1), 110 mm (T2, B2) and 165 mm (T3, B3) from the inlet of the water. Their task is to measure the temperature of the wall in the refrigerant side. For the accuracies of the thermocouples, please refer to Table 2.2.

2.2.7 Post-condenser and chiller

In the experiments, the refrigerant exits from the test section in saturated conditions (the thermodynamic quality is greater than 0). To complete the condensation, the fluid passes through a post-condenser (which is a plate heat exchanger similar to the evaporator). From there, the fluid exits in the subcooled liquid state. The water used as heat sink is cooled by a chiller LAUDA Variocool VC300 (Figure 2.12). Inside the chiller, a cooling cycle with operative fluid R404A operates to reject heat to the surrounding environment.



Figure 2.1. Chiller LAUDA Variocool VC300.

2.2.8 Accuracy of the instruments of measurement

All the instruments used for the data reduction are subjected to experimental uncertainty. This value is reported in the Table 2.2 for each sensor in the circuit. For more details on the uncertainty analysis, please refers to Chapter §5.

T -type thermocouples	± 0.05 K
Coriolis flowmeter	$\pm 0.10\%$ of reading
Volumetric flowmeter at pre-condenser	$\pm 0.25\%$ of reading
Volumetric flowmeter at evaporator	$\pm 0.25\%$ of reading
Volumetric flowmeter at test section	$\pm 0.50\%$ of reading
Absolute pressure transducers	± 1950 Pa
Differential pressure transducer	± 25 Pa

Table 2.2. Accuracy of the experimental instruments [9].

Chapter 3:

Experimental method

In the present Chapter, a detailed analysis of the experimental procedure is presented. The aim of the experiments is to obtain experimental points of the heat transfer coefficient during condensation from superheated vapor.

3.1 Loading of the test rig and description of the refrigerant

Before starting the operation the experimental apparatus, it is necessary to remove any possible presence of air inside the test rig. Indeed, the presence of air could alter the heat transfer process in the test section. To allow the proper extraction of air, the vacuum is generated with a vacuum pump.

After the removal of the air, the system is loaded with 2.5 kg of refrigerant R1234ze(E). The substance is inside a cylinder (Figure 3.1) which is heated up and put upside down to change the facility with the refrigerant in liquid state.



Figure 3.1. Refrigerant cylinder.

3.1.2 Refrigerant R1234ze(E)

The R1234ze(E) or trans-1,3,3,3-tetrafluoropropene (Lemmon *et al.* [12]) is a refrigerant fluid which belongs to the family of the hydrofluoroolefins (HFO). It is a refrigerant widely used in energy-efficient chillers, commercial air conditioning systems of supermarkets and commercial buildings, as well as in other medium temperature applications like heat pumps, refrigerators, vending machines, beverage dispensers, air dryers, CO₂ cascade systems in commercial refrigeration. Its most interesting feature is its instability in the atmosphere: the carbon-carbon bond makes the refrigerant unstable in a free-air environment, resulting on a global warming potential (GWP) lower than 1 compared to CO₂ over a 100 year-time horizon. As stated in Diani *et al.* [9], lots of research have been conducted in order to explore its feasibility as possible substitute to R134a, which presents a much higher GWP.

Table 3.1 presents the main properties of the R1234ze(E) compared to the ones of the R134a (thermal properties are obtained with REPFROP 10 [11]).

		R134a	R1234ze(E)
ASHRAE safety classification	/	A1	A2L
ODP	/	0	0
100-year GWP	/	1300	<1
Critical temperature	K	374.21	328.51
Critical pressure	kPa	4059.28	3634.9
NBP	K	247.08	253.88
Liquid density (273 K)	kg m ⁻³	1295.27	1240.56
Vapor density (273 K)	kg m ⁻³	14.35	11.65
Liquid c _p (273 K)	kJ kg ⁻¹ K ⁻¹	1.34	1.32
Vapor c _p (273 K)	kJ kg ⁻¹ K ⁻¹	0.9	0.88
Latent heat of vaporization	kJ kg ⁻¹	198.72	184.28
Liquid thermal conductivity (273 K)	W m ⁻¹ K ⁻¹	9.21E-02	8.31E-02
Vapor thermal conductivity (273 K)	W m ⁻¹ K ⁻¹	1.15E-02	1.16E-02
Liquid viscosity (273 K)	Pa s	2.67E-04	2.69E-04
Vapor viscosity (273 K)	Pa s	1.07E-05	1.12E-05

Table 3.1. Main refrigerant properties of R1234ze(E) and R134a [11].

From Table 3.1, it is immediately possible to notice the much lower GWP of R1234ze(E) compared to R134a. Despite this, the study of Mota-Babiloni *et al.* [13] demonstrated

that the cooling capacity and the coefficient of performance of R1234ze(E) are lower than those of R134a in vapor compression systems. The results of Colombo *et al.* [14] indicates that the COP and the heat capacity of the R1234ze(E) are lower to the ones of R134a in heat pump systems. Fukuda *et al.* [15] found that R1234ze(E) is more suitable for high temperature heat pumps rather than traditional air conditioners. Furthermore, Del Col *et al.* [16] experimentally compared the flow condensation performance of R1234ze(E), R32, R134a and R1234yf in a 0.96 mm *ID* smooth tube. They found that R1234ze(E) has a heat transfer coefficient comparable with R134a and the largest pressure gradients. Longo *et al.* [17] experimentally found that R1234ze(E) presents a similar heat transfer coefficients and pressure drops as R134a in a 4 mm *ID* smooth tube during saturated condensation. Diani *et al.* [18] explored the heat transfer coefficients and frictional pressure drop in microfin tube during condensation and found that R1234ze(E) in some specific conditions can present higher heat transfer coefficients compared R134a.

No papers have been found related to the condensation from superheated vapor of R1234ze(E) in microfin tubes. Furthermore, this refrigerant presents saturation pressures at the operative conditions desired in the experiments which are the lowest between the refrigerants available in laboratory. Since a new part of the test rig was built recently and never tested, the desired operative condition were the ones with the lowest pressure. Consequently, the experiments are performed with this refrigerant.

3.2 Power on of the test rig

Once the refrigerant has been changed, the plant operation can start:

1. The general switch is turned on;
2. The KAYE K170 is turned on. This device (Figure 3.2) allows to set the 0°C as reference temperature for the second junction of the thermocouples for the data acquisition. The device requires at least one hour before reaching the stabilization;
3. The valves of the circuit are opened;



Figure 3.2. System KAYE K170.

4. The transducers and acquisition systems are turned on;
5. The software LabVIEW [19] for the acquisition of the experimental points and REFPROP 10 [11] are loaded in the computer;
6. The refrigerant pump is activated and, by means of the control panel, a reference mass flow rate is imposed in the system. It will be corrected later depending on the type of test;
7. The electrical resistance of the evaporator circuit is turned on. In the experiments, just the moduable one of the three resistance installed on the plant is activated;
8. The pre-condenser chiller is turned on, with the water temperatures regulated depending on the test conditions;
9. The post-condenser chiller is set at a refence temperature between 0 °C and -10°C depending on the test conditions;
10. The damper is regulated according to the saturation temperature desired in the system.

3.3 Modulation and experimental procedure

3.3.1 Modulation

To evaluate the heat transfer coefficient, the experiments have been performed setting the following boundary conditions:

- Mass velocity G [$\text{kg s}^{-1} \text{m}^{-2}$], which is calculated with reference to the equivalent cross section area of the smooth tube with an inner diameter equals to ID_{apex} ;
- Saturation temperature T_{sat} [$^{\circ}\text{C}$], which is evaluated using REFPROP 10 knowing the saturation pressure P_{sat} [bar];
- Degree of superheating SH [K], calculated as the difference between the inlet temperature of the refrigerant in the experimental section $T_{ref,in}$ and T_{sat} .

At the beginning of each test section, these three parameters are chosen. Different experimental points are consequently taken varying the heat flow rate exchanged in the experimental section. Note that the time required for the system to reach the desired conditions is much higher than the time required in the previous experiments [9, 10] due to the thermal inertia of the pre-condenser (refer to sub-subparagraph §3.3.1.2 for more details). Consequently, a much lower number of experimental points can be obtained for each test session.

3.3.1.1 Mass flow rate regulation

The refrigerant mass flow rate \dot{m}_{ref} which flows in the microfin tube is regulated by means of the control panel: by changing the rotational speed of the pump, the mass flow rate can be adjusted and settled around the desired value. In terms of G , a maximum variation of $\pm 5 \text{ kg s}^{-1} \text{m}^{-2}$ from the desired value is considered acceptable.

During the tests where the mass velocity is low ($G=100 \text{ kg s}^{-1} \text{m}^{-2}$) the control of the pump is no more sufficient for the regulation. Indeed, when the rotational speed of the pump is contained, the machine is not capable to guarantee a good control of the flow: the regime inside of the facility is very similar to a natural convection. To regulate the flow, it is consequently necessary to adjust the opening/closing of a valve located downstream the Coriolis flowmeter.

3.3.1.2 Saturation temperature regulation

The saturation temperature T_{sat} is controlled with the damper. By means of a valve, compressed air can flow inside the damper, increasing the P_{sat} and consequently the T_{sat} . If the temperature increases too much, the same valve can be used to depressurize the damper until the desired value of T_{sat} is obtained. A maximum variation of ± 0.3 °C from the desired value is considered acceptable for the data acquisition.

3.3.1.3 Superheating degree regulation

The superheating degree is the hardest parameter to control because of the large inertia of the pre-condenser system. The SH is settled imposing a certain temperature to the water heated by the modifiable electrical resistance: the water then enters in the evaporator and heats up the refrigerant. However, after exiting from the evaporator, the refrigerant heats up the stagnant water located in the pre-condenser, increasing the time required to reach the desired superheating degree.

For safety reasons, a maximum temperature of 80 °C is imposed in the evaporator water. When the SH is large (10 to 30 K), the system reacts and stabilizes in about one hour and no problem in the modulation occurs. However, if the degree of superheating is lower, the system becomes very difficult to regulate just with the use of the evaporator. Consequently, when the experiments are performed with $SH=5$ K, the pre-condenser is turned on: in this way, setting the proper value of temperature of the water in the chiller Rock 4, the stabilization is reached more rapidly. This approach is not possible with higher superheating degree since it would require a too high water temperature in the pre-condenser and the chiller is not able to sustain it: the high pressure sensor of the machine detects a too high pressure at the evaporator and shuts down the chiller.

Since the stabilization of the SH requires more time and it is more difficult compared to the saturation temperature modulation, a maximum range of ± 0.5 °C is considered acceptable (in the tests with low mass velocity, the range is increased because the plant is more difficult to control).

3.3.1.4 Heat flow rate modulation

The heat flow rate in the experimental section is controlled with the thermostatic bath LAUDA: the temperature of the water is settled by means of the display of the bath. After 10-20 minutes, the whole bath reaches the new equilibrium temperature, and the temperatures change inside the test section until the desired heat flow rate is obtained. Another strategy to control the heat flow rate is the mass flow rate of water \dot{m}_{H_2O} regulation: the thermostatic bath LAUDA is equipped with a pump whose velocity can be settled. This type of control strategy is faster compared to the temperature regulation. However, the flowmeter which register the volumetric flow rate of water is not able to measure flow rates higher than 20 l h^{-1} . When this limit is reached, the temperature regulation is mandatory.

3.3.2 Experimental procedure

Once the specific mass velocity, the saturation temperature and the superheating degree are stabilized, the acquisition can start. To acquire the data necessary for the calculations presented in Chapter §4 and §5, it is initially necessary to set the heat flow rate to obtain the desired outlet vapor quality. After a certain amount of time, the condition inside the experimental apparatus changes and consequently a new equilibrium point must be reached adjusting the G , T_{sat} and SH (if the parameters exits from the acceptability range) with the methods described in subparagraph §3.3.1. The instruments register the following data list:

- Temperature of the water at the inlet of the pre-condenser $T_{H_2O,precond,IN}$ [°C];
- Temperature of the water at the outlet of the pre-condenser $T_{H_2O,precond,OUT}$ [°C];
- Temperature of the water at the inlet of the evaporator $T_{H_2O,eva,IN}$ [°C];
- Temperature of the water at the outlet of the evaporator $T_{H_2O,eva,OUT}$ [°C];
- Temperature of the water at the outlet of the post-condenser $T_{H_2O,postcond,OUT}$ [°C];
- Temperature of the refrigerant at the inlet of the evaporator $T_{ref,eva,IN}$ [°C];
- Temperature of the refrigerant at the outlet of the evaporator $T_{ref,eva,OUT}$ [°C];

- Temperature of the refrigerant at the outlet of the pre-condenser $T_{ref,precond,OUT}$ [°C];
- Temperature of the refrigerant at the inlet of the test section $T_{ref,IN}$ [°C];
- Temperature of the refrigerant at the outlet of the test section $T_{ref,OUT}$ [°C];
- Temperature of the water at the inlet of the test section $T_{H_2O,IN}$ [°C];
- Temperature of the water at the outlet of the test section $T_{H_2O,OUT}$ [°C];
- Temperature of the wall in position T1 $T_{wall,T1}$ [°C];
- Temperature of the wall in position B1 $T_{wall,B1}$ [°C];
- Temperature of the wall in position T2 $T_{wall,T2}$ [°C];
- Temperature of the wall in position B2 $T_{wall,B2}$ [°C];
- Temperature of the wall in position T3 $T_{wall,T3}$ [°C];
- Temperature of the wall in position B3 $T_{wall,B3}$ [°C];
- Temperature of the thermopile at the pre-condenser $T_{pile,precond}$ [°C];
- Temperature of the thermopile at the evaporator $T_{pile,eva}$ [°C];
- Refrigerant mass flow rate \dot{m}_{ref} [kg h⁻¹];
- Volumetric flow rate of water at the evaporator $\dot{Q}_{V,H_2O,eva}$ [l h⁻¹];
- Volumetric flow rate of water at the pre-condenser $\dot{Q}_{V,H_2O,precond}$ [l h⁻¹];
- Absolute refrigerant pressure at the outlet of the evaporator $P_{ref,eva,OUT}$ [bar];
- Absolute refrigerant pressure at the inlet of the evaporator $P_{ref,eva,IN}$ [bar];
- Differential pressure in the test section ΔP [bar];
- Absolute refrigerant pressure at the inlet of the test section $P_{ref,IN}$ [bar];
- Volumetric flow rate of water in the test section \dot{Q}_{V,H_2O} [l h⁻¹].

All the data are visualized in real time with the LabVIEW interface (Figure 3.3). Once the wall temperatures, the refrigerant and the water temperatures are stabilized, the number of the reading is taken. Starting from this point, 100 following values are extracted. The code B.1 called “matrix extraction” reported in APPENDIX B is used to calculate, for each scanned property, the mean values of the 100 points considered. The values are then printed in Microsoft Excel for the data reduction.

The outlet quality of vapor is estimated for each point using the specific enthalpies of saturated vapor and saturated liquid and the outlet condition. This calculation is used later to verify if the measurements taken are correct.

Once the 100 values are registered by the software, the heat flow rate can be changed again, and other points can be taken for the same condition of mass velocity, superheating degree and saturation temperature. The number of points taken depends on the boundary condition of the experiments: for instance, when the mass velocity is high the number of points taken is at maximum 5 because with the present experimental apparatus it is not possible to achieve lower vapor qualities at the exits of the test section due to the constraints (flow rate and temperature) of the thermostatic bath.

3.4 Plant shut down

At the end of the tests, the plant is shut down turning off each element from the control panel. It is important to notice that the water pump in the hot loop should always be in operation until the evaporator thermal resistance is turned off for safety reasons.

Once the system has been entirely turned off, the valves upstream and downstream the test section are closed: in this way, if there is a loss of refrigerant, it would be seen by the absolute pressure transducer, which will indicate a lower pressure compared to the saturation one in the following experiment day.

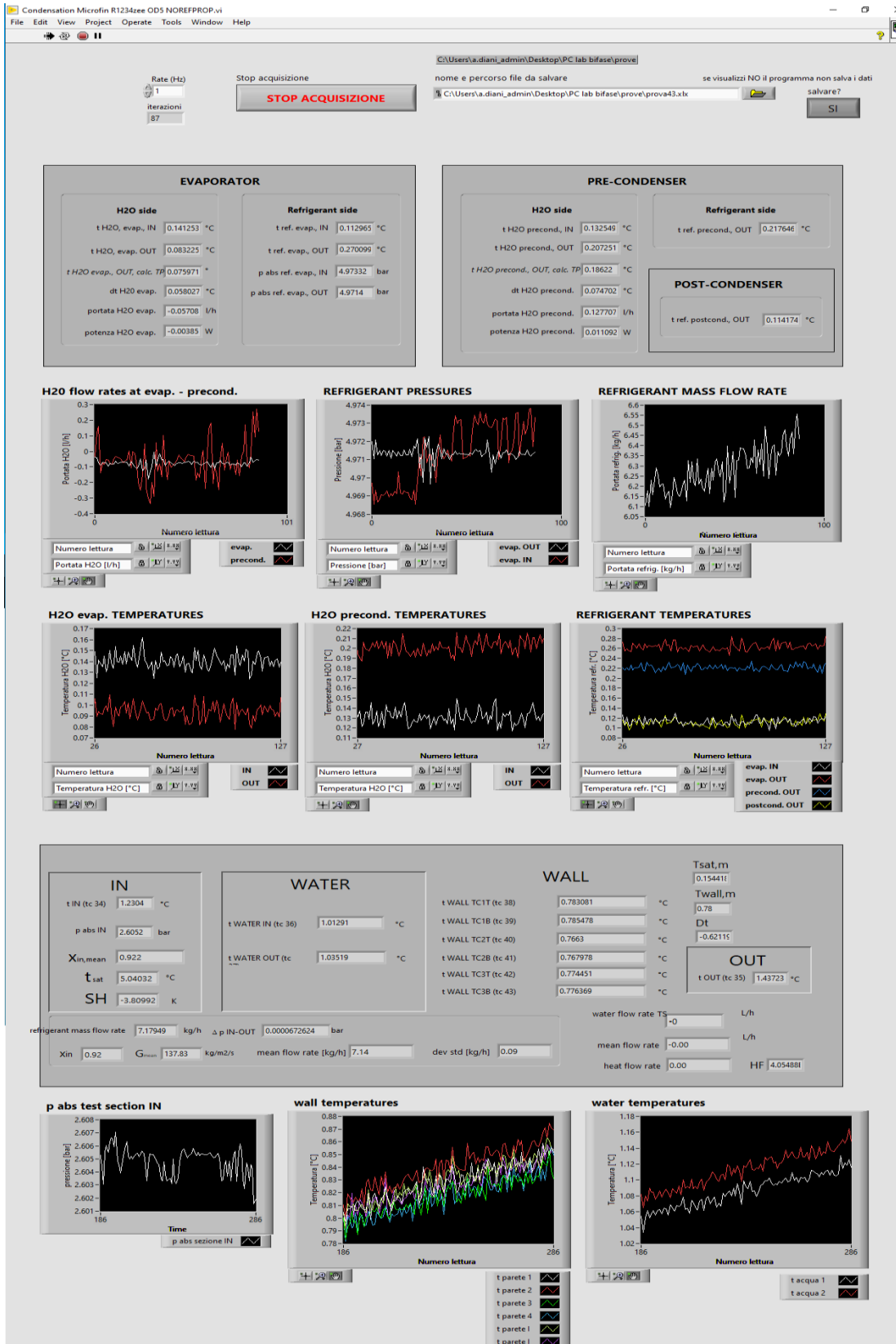


Figure 3.3. Screenshot of the labVIEW interface at the computer for the regulation of the plant and the registration of the data.

Chapter 4:

Data reduction

A total amount of 62 points have been taken during the tests. In this Chapter, a detailed description of the data reduction method is presented.

4.1 Data reduction

4.1.1 Reference model

In Chapter §1, a detailed description of the condensation from superheated vapor is presented. According to Kondou and Hrnjack [8], the heat transfer coefficient in the superheated region can be modelled as follow:

$$\alpha(T_{b,r} - T_{wall,i}) = \alpha_{SH}(T_{b,r} - T_{sat}) + \alpha_{TP}(T_{sat} - T_{wall,i}), \quad (4.1)$$

where α is the total heat transfer coefficient [$\text{W m}^{-2} \text{K}^{-1}$], $T_{b,r}$ is the bulk refrigerant temperature [K], $T_{wall,i}$ is the mean temperature of the wall, α_{SH} is the heat transfer coefficient of the sensible de-superheating process of the vapor [$\text{W m}^{-2} \text{K}^{-1}$], T_{sat} is the refrigerant saturation temperature [K] and α_{TP} is the two phase heat transfer coefficient [$\text{W m}^{-2} \text{K}^{-1}$]. Indeed, according to this model, the condensation from superheated vapor could be visualized as a combination of two different process: the sensible de-superheating of the vapor and the saturated condensation.

This model, to be experimentally validated, requires the subdivision of the test tube into small segments to calculate the bulk refrigerant temperature and consequently evaluate where the condensation from superheated vapor starts and ends. However, in the test section described in Chapter §2, the calculation of the local temperatures results impossible since the tube length is relatively small. As preannounced in paragraph §1.3, the approach followed for the data reduction is the one proposed by Webb [4]. In this paper, the author proposed to model the heat flux as follow:

$$\frac{q_{tot}}{A} = \alpha(T_{sat} - T_{wall,i}), \quad (4.2)$$

where α is the total heat transfer coefficient [$\text{W m}^{-2} \text{K}^{-1}$], q_{tot} is the heat flow rate exchanged [W] divided by the heat transfer area A [m^2]. In this way, the heat transfer coefficient can be calculated considering the temperature difference between the saturation and the wall. This approach simplifies the calculations since it is not required to know the refrigerant local bulk temperature.

4.1.2 Data reduction

All the data available from the tests are listed in §3.3.2. The mean values of 100 scanning are taken as input for the data reduction, as described in §3.3.2. First, the heat flow rate exchanged in the test section is evaluated:

$$q_{tot} = \frac{\dot{m}_{H_2O} c_{P,H_2O} (T_{H_2O,OUT} - T_{H_2O,IN})}{3600}, \quad (4.3)$$

where q_{tot} is the heat exchanged [W], \dot{m}_{H_2O} is the mass flow rate of water [kg h^{-1}] (evaluated with the volumetric flow rate and assuming a water density in liquid state equals to 1000 kg m^{-3}), c_{P,H_2O} is the specific heat capacity of water (assumed equals to $4186 \text{ J kg}^{-1} \text{K}^{-1}$), $T_{H_2O,OUT}$ and $T_{H_2O,IN}$ are respectively the outlet and inlet temperature of water in the test section.

Using REFPROP 10 [11], the inlet specific enthalpy is calculated $h_{ref,IN}$ [kJ kg^{-1}]:

$$h_{ref,IN} = f_{REFPROP}(T_{ref,IN}, P_{ref,IN}), \quad (4.4)$$

where $T_{ref,IN}$ is the refrigerant inlet temperature [$^{\circ}\text{C}$] and $P_{ref,IN}$ is the refrigerant inlet pressure [bar].

The $P_{ref,OUT}$ is calculated:

$$P_{ref,OUT} = P_{ref,IN} - \Delta P, \quad (4.5)$$

where ΔP are the pressure drops in the test section [bar]. The refrigerant outlet specific enthalpy $h_{ref,OUT}$ [kJ kg⁻¹] is evaluated:

$$h_{ref,OUT} = h_{ref,IN} - \frac{q_{tot}}{1000 \dot{m}_{ref}}, \quad (4.6)$$

where \dot{m}_{ref} is the refrigerant mass flow rate [kg s⁻¹]. From the $P_{ref,OUT}$, the vapor and liquid saturation specific enthalpies $h_{V,sat}$ and $h_{L,sat}$ [kJ kg⁻¹] calculated with REFPROP 10. The saturation temperature T_{sat} [°C] is calculated with the mean pressure $P_{ref,MEAN}$ between the inlet and the outlet:

$$h_{V,sat} = f_{sat,REFPROP}(P_{ref,OUT}), \quad (4.7)$$

$$h_{L,sat} = f_{sat,REFPROP}(P_{ref,OUT}), \quad (4.8)$$

$$T_{sat} = f_{sat,REFPROP}(P_{ref,MEAN}). \quad (4.9)$$

The outlet vapor quality x_{OUT} can be evaluated and compared with the estimated one taken during the experiments to verify the correctness of the calculations:

$$x_{OUT} = \frac{h_{ref,OUT} - h_{L,sat}}{h_{V,sat} - h_{L,sat}}. \quad (4.10)$$

Finally, the heat transfer coefficient HTC [kW m⁻² K⁻¹] can be calculated:

$$HTC = \frac{q_{tot}}{1000(T_{sat} - T_{wall,i})HTA'} \quad (4.11)$$

where $T_{wall,i}$ is the average wall temperature [°C] on the six values measured by the thermocouples and HTA [m²] is the heat transfer area, calculated as follow:

$$HTA = \pi ID_{apex} L. \quad (4.12)$$

Chapter 5

Uncertainty analysis

Before the results discussion, the uncertainty analysis must be provided. Every experimental measurement must not be assumed as absolute truth since the measurement itself and the instrumentation used for the measurement suffer of uncertainty. Consequently, a detailed analysis of the uncertainty of the different measurements and of the values calculated is required. The normative taken as reference is the UNI-CEI-ENV-13005 [20], or ISO GUM.

5.1 ISO-GUM

According to the normative, each result of a measurement is an aleatory variable. The guide proposes 5 steps for the calculation of the uncertainty:

1. Analysis of the uncertainty sources and correction of the systematic errors;
2. Calculation of the standard uncertainty for each possible source;
3. Evaluation of the combined uncertainty;
4. Determination of the extended uncertainty;
5. Presentation of the measurement.

The step 4 is not presented since it would require defining a level of confidence. Once the systematic errors have been corrected and the uncertainty sources identified, it is possible to proceed to the second step: evaluation of the standard uncertainties.

Two different types of uncertainties are identified:

1. Uncertainty type A, related to a set of experimental data;
2. Uncertainty type B, related to previous knowledge on the population of the involved quantities.

5.1.1 Uncertainty type A

The easiest way to calculate $u_A(X_i)$ (uncertainty type A of a given quantity X_i) is to evaluate the standard deviation $\sigma_{std}(X_i)$ of the mean value \bar{X}_n on the n measurements:

$$\bar{X}_n = \frac{1}{n} \sum_{i=1}^n X_i; \quad (5.1)$$

$$u_A(X_i) = \sigma_{std}(X_i) = \frac{1}{n-1} \sum_{i=1}^n (X_i - \bar{X}_n)^2. \quad (5.2)$$

In the present work, the code B.1 in APPENDIX B, which is the same used for the extraction of the average values of 100 scanned points, is also used for the calculation of $\sigma_{std}(X_i)$ on the 100 lectures.

5.1.2 Uncertainty type B

Each instrument used for the measurements suffers of uncertainties which are reported in Table 2.2. Since the previous knowledge on the population of the involved quantities is unknown, a uniform probability density function is assumed for each instrument. According to the normative:

$$u_B(X_i) = \sigma_{std,unfirom}(X_i) = \frac{a}{\sqrt{3}}; \quad (5.3)$$

where a represents the accuracy of the instrument reported in Table 2.2.

5.1.3 Combined uncertainty

For each measured quantity, the combined uncertainty $u_c(X_i)$ can be simply evaluated as:

$$u_c(X_i) = \sqrt{u_A(X_i)^2 + u_B(X_i)^2}. \quad (5.4)$$

However, this approach cannot be used in the case the quantity Y is obtained from a calculation and not directly measured (for instance, the heat transfer coefficient is not directly obtained by a measurement, but it is calculated using other measured data, such as the saturation temperature or the wall temperature). In this case, the equations of Kline and McClintock [21] must be adopted. Given:

$$Y = f(X_1, X_2, \dots, X_n), \quad (5.5)$$

the combined uncertainty can be obtained:

$$u_c(Y) = \pm \sqrt{\sum_{i=1}^n [\theta_i u_c(X_i)]^2}, \quad (5.6)$$

where θ_i is called sensitivity index, calculated as:

$$\theta_i = \left. \frac{\partial Y}{\partial x} \right|_{x=X_i}. \quad (5.7)$$

5.2 Uncertainty on the heat flow rate

According to equation (5.3), the heat flow rate depends on $\dot{m}_{H_2O}, c_{P,H_2O}$ and $(T_{H_2O,OUT} - T_{H_2O,IN})$. The combined uncertainty of the water mass flow rate is calculated with (5.6). The specific heat capacity of water is assumed constant. The uncertainty on $T_{H_2O,OUT}$ and on $T_{H_2O,IN}$ are calculated with (5.6). The results obtained are very similar. Consequently, it is possible to write:

$$u_c(\Delta T_{H_2O}) = \sqrt{u_c(T_{H_2O,IN})^2 + u_c(T_{H_2O,OUT})^2} = \sqrt{2}u_c(T_{H_2O,OUT}). \quad (5.8)$$

Applying (5.8), the uncertainty on the heat flow rate $u_c(q_{tot})$ is calculated:

$$u_c(q_{tot}) = \sqrt{(c_{P,H_2O} \Delta T_{H_2O} u_c(\dot{m}_{H_2O}))^2 + (c_{P,H_2O} \dot{m}_{H_2O} \sqrt{2} u_c(T_{H_2O,OUT}))^2} . \quad (5.9)$$

The results are presented in Table 5.1 at the end of the Chapter.

5.3 Uncertainty on the heat transfer coefficient

According to (4.11), the *HTC* depends on the heat flow rate exchanged in the test section q_{tot} and on the temperature difference between the wall and the saturation temperature. It also depends on the heat transfer area, on which the uncertainty is neglected.

5.3.1 Uncertainty on the wall temperature

$T_{wall,i}$ is calculated as average between the six values measured by the thermocouples glued to the surface of the tube. Once the combined uncertainty is evaluated for each thermocouple, the combined uncertainty of the average is calculated:

$$u_c(T_{wall,i}) = \frac{1}{6} \sum_{j=1}^6 (u_c(T_{wall,j}))^2, \quad (5.10)$$

where $u_c(T_{wall,j})$ is the combined uncertainty for each one of the six thermocouples.

5.3.2 Uncertainty on the saturation temperature

T_{sat} is calculated starting from the mean pressure inside the tube P_{sat} . Since the instruments presents an accuracy of 1950 Pa, the maximum and the minimum T_{sat} is evaluated:

$$T_{sat,min} = f_{sat,REFPROP}(P_{sat} - 1950 \times 10^{-5}), \quad (5.11)$$

$$T_{sat,max} = f_{sat,REFPROP}(P_{sat} + 1950 \times 10^{-5}). \quad (5.12)$$

The combined uncertainties are consequently calculated:

$$u_c(T_{sat,min}) = T_{sat} - T_{sat,min}, \quad (5.13)$$

$$u_c(T_{sat,max}) = T_{sat,max} - T_{sat}. \quad (5.14)$$

The maximum between the two is taken as combined uncertainty of the saturation temperature.

5.3.3 Uncertainty on the heat transfer coefficient

According to (5.6), the uncertainty on HTC can be evaluated in two different ways:

$$u_{c,1}(HTC) = \sqrt{\left(\frac{\partial HTC}{\partial q_{tot}} u_c(q_{tot})\right)^2 + \left(\frac{\partial HTC}{\partial T_{sat}} u_c(T_{sat})\right)^2 + \left(\frac{\partial HTC}{\partial T_{wall,i}} u_c(T_{wall,i})\right)^2}, \quad (5.15)$$

$$u_{c,2}(HTC) = \sqrt{\left(\frac{\partial HTC}{\partial q_{tot}} u_c(q_{tot})\right)^2 + \left(\frac{\partial HTC}{\partial \Delta T} u_c(\Delta T)\right)^2}, \quad (5.16)$$

where:

$$\Delta T = T_{sat} - T_{wall,i}, \quad (5.17)$$

$$u_c(\Delta T) = \sqrt{2} u_c(T_{wall,i}). \quad (5.18)$$

The maximum between (5.15) and (5.16) is taken as $u_c(HTC)$. The results are presented at the end of the chapter in Table 5.1.

5.4 Uncertainty on the outlet specific enthalpy

According to (4.6), the $h_{ref,OUT}$ depends on the inlet specific enthalpy $h_{ref,IN}$, on q_{tot} and on \dot{m}_{ref} ($u_c(\dot{m}_{ref})$ is evaluated as described in §5.1.3). The inlet specific enthalpy is calculated with REFPROP 10. To each quantity evaluated with the software, an uncertainty of 1% of the values is associated:

$$u_c(h_{ref,IN}) = 0.01 \cdot h_{ref,IN}. \quad (5.19)$$

The combined uncertainty on the outlet specific enthalpy is calculated:

$$u_c(h_{ref,OUT}) = \sqrt{\left(\frac{\partial h_{ref,OUT}}{\partial q_{tot}} u_c(q_{tot})\right)^2 + \left(\frac{\partial h_{ref,OUT}}{\partial h_{ref,IN}} u_c(h_{ref,IN})\right)^2 + \left(\frac{\partial h_{ref,OUT}}{\partial \dot{m}_{ref}} u_c(\dot{m}_{ref})\right)^2}. \quad (5.20)$$

5.5 Uncertainty on the outlet vapor quality

According to (4.10), the outlet vapor quality x_{OUT} depends on $h_{ref,OUT}$, $h_{L,sat}$ and $h_{V,sat}$. Since the saturation enthalpies are evaluated with REFPROP 10, an uncertainty of 1% on the actual value is considered. Consequently, it is possible to write:

$$u_c(x_{OUT}) = \sqrt{\left(\frac{\partial x_{OUT}}{\partial h_{ref,OUT}} u_c(h_{ref,OUT})\right)^2 + \left(\frac{\partial x_{OUT}}{\partial h_{L,sat}} u_c(h_{L,sat})\right)^2 + \left(\frac{\partial x_{OUT}}{\partial h_{V,sat}} u_c(h_{V,sat})\right)^2}. \quad (5.21)$$

5.6 Results

In Table 5.1, the results of the uncertainty analysis are reported. The values are in acceptable range: the measurements can be considered satisfying. It is possible to proceed with the analysis of the results.

	$u_c(q_{tot})$	$u_c(q_{tot})$	$u_c(HTC)$	$u_c(HTC)$	$u_c(h_{ref,OUT})$	$u_c(h_{ref,OUT})$	$u_c(x_{OUT})$
	W	%	$\text{kW m}^{-2} \text{K}^{-1}$	%	kJ/kg	%	/
Min	± 0.96	0.60	± 0.071	1.18	± 4.11	1.06	± 0.036
Max	± 3.53	5.35	± 3.26	17.44	± 4.62	1.56	± 0.050
Mean	± 1.93	1.32	± 0.82	4.64	± 4.32	1.20	± 0.043

Table 5.1. Results of the uncertainty analysis.

Chapter 6:

Experimental results

A total quantity of 62 experimental points has been taken. The parametric analysis of the mass velocity, saturation temperature and superheating degree has been performed. In particular, the effects of two different T_{sat} (30 and 40 °C), four different specific mass velocities G (100, 200, 300 and 400 kg s⁻¹ m⁻²) and four different superheating degrees SH (5, 10, 20 K and one experiment with 30 K) have been tested. All the $HTCs$ are plotted in the following graphs in the y-axis, whereas the x_{OUT} is plotted in the x-axis.

6.1 Effect of the saturation temperature

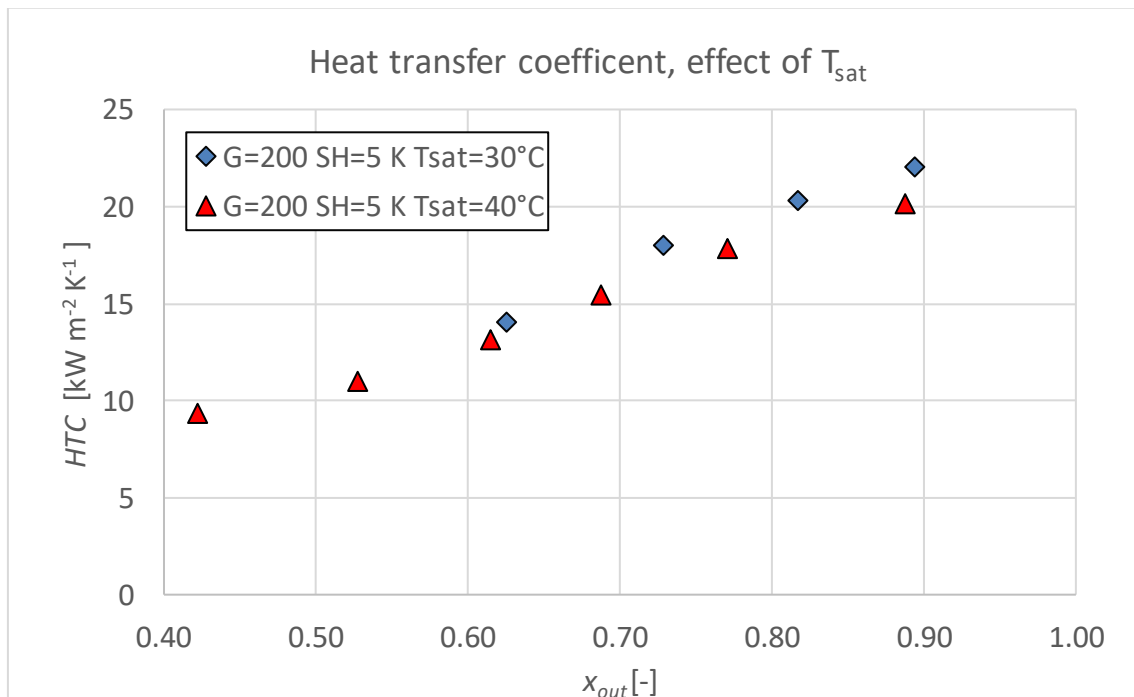
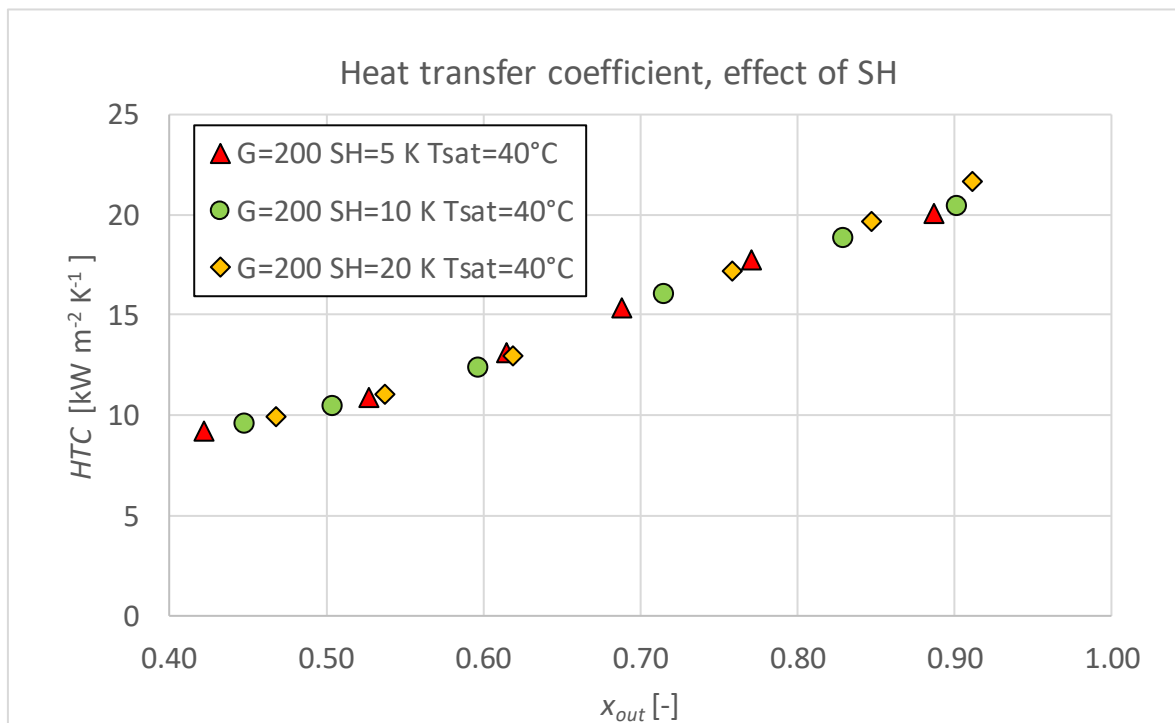


Figure 6.1. Heat transfer coefficient, effect of different saturation temperature.

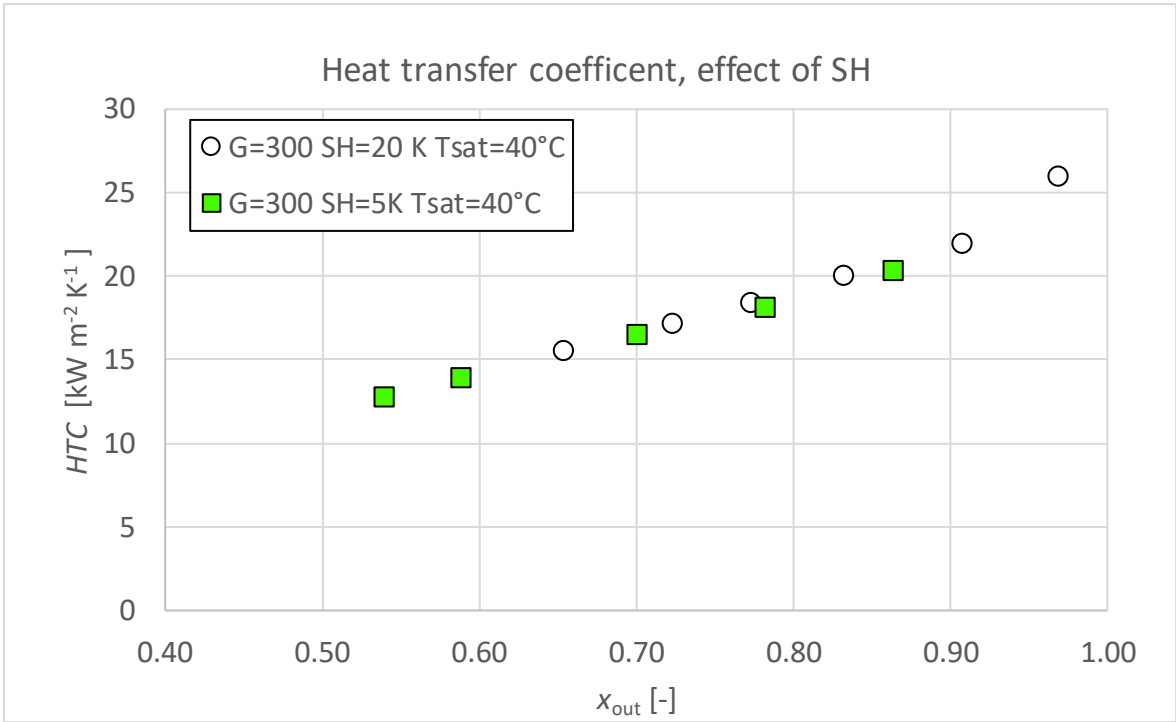
In Figure 6.1., two different series of points are plotted with different saturation temperature T_{sat} . A small enhance of the heat transfer coefficient is noticeable when the output vapor quality is relatively high at lower saturation temperature. This is

probably due to the vapor density: it decreases when the T_{sat} is lower, which means a large vapor velocity with the same mass flux. Consequently, the shear stress exerted by the vapor on the liquid film is improved, leading to a higher turbulence and to an enhanced heat transfer coefficient. The effect decreases when the output vapor quality decreases since a lower content of vapor is present at the outlet of the test section and the liquid film thickness is increased.

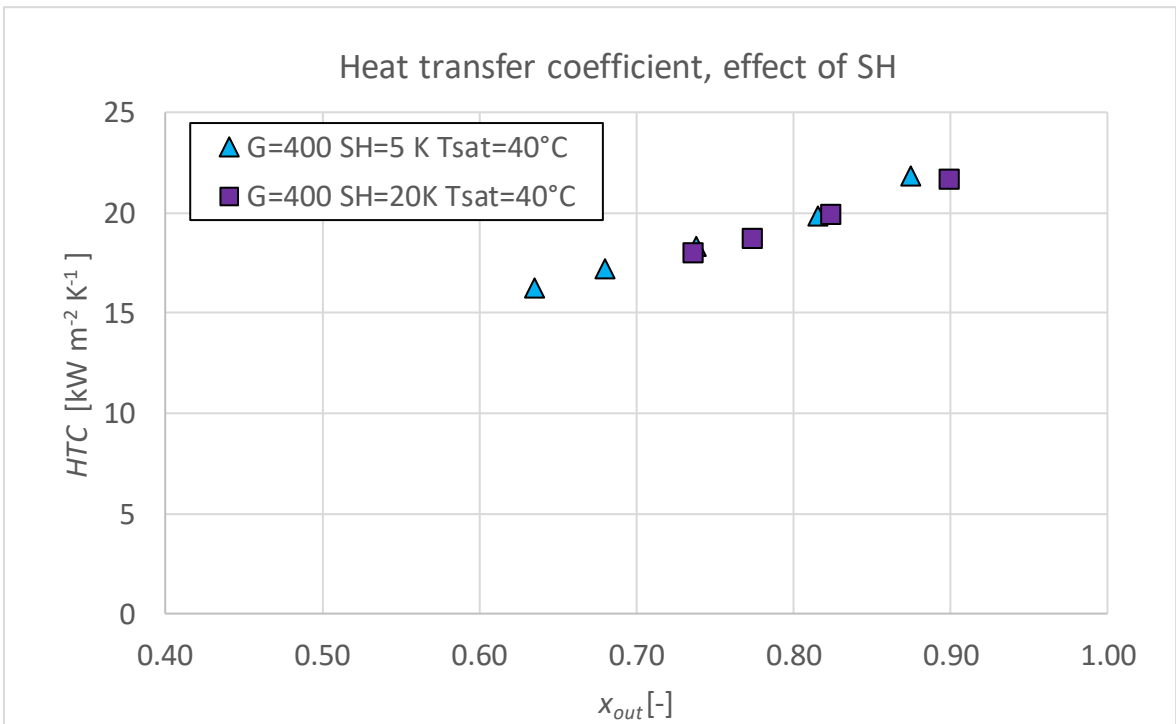
6.2 Effect of superheating degree



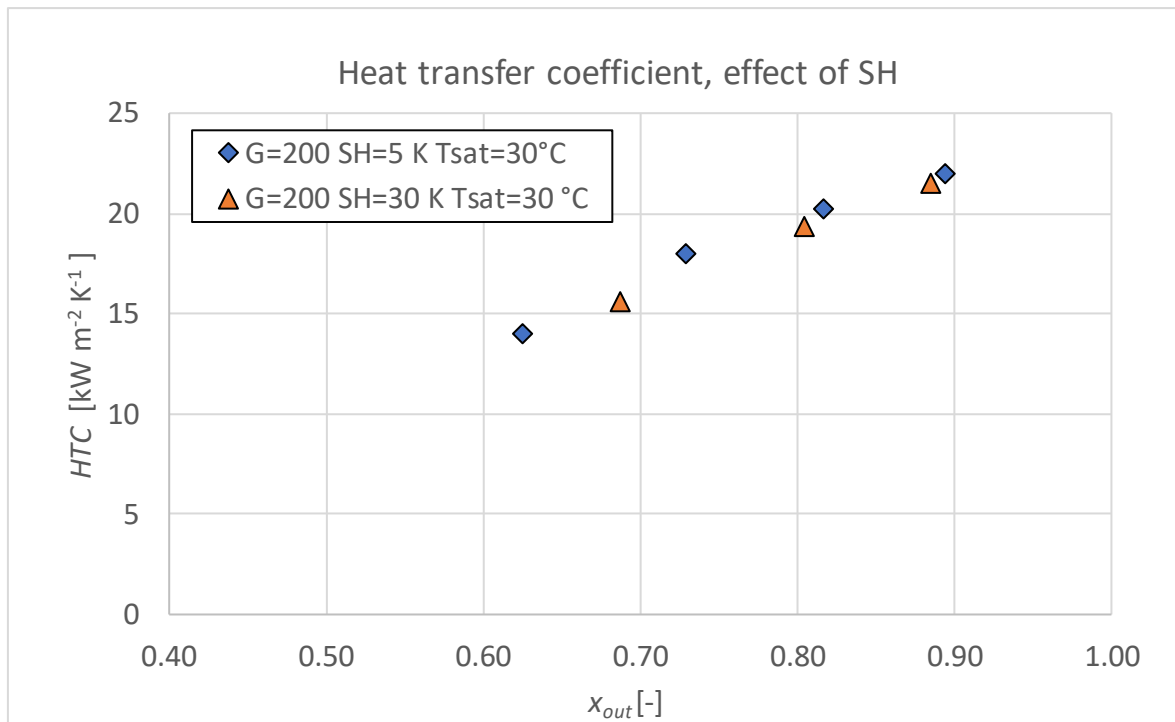
(a)



(b)



(c)



(d)

Figure 6.2. Effect of the superheating degree in the evaluation of the heat transfer coefficient.

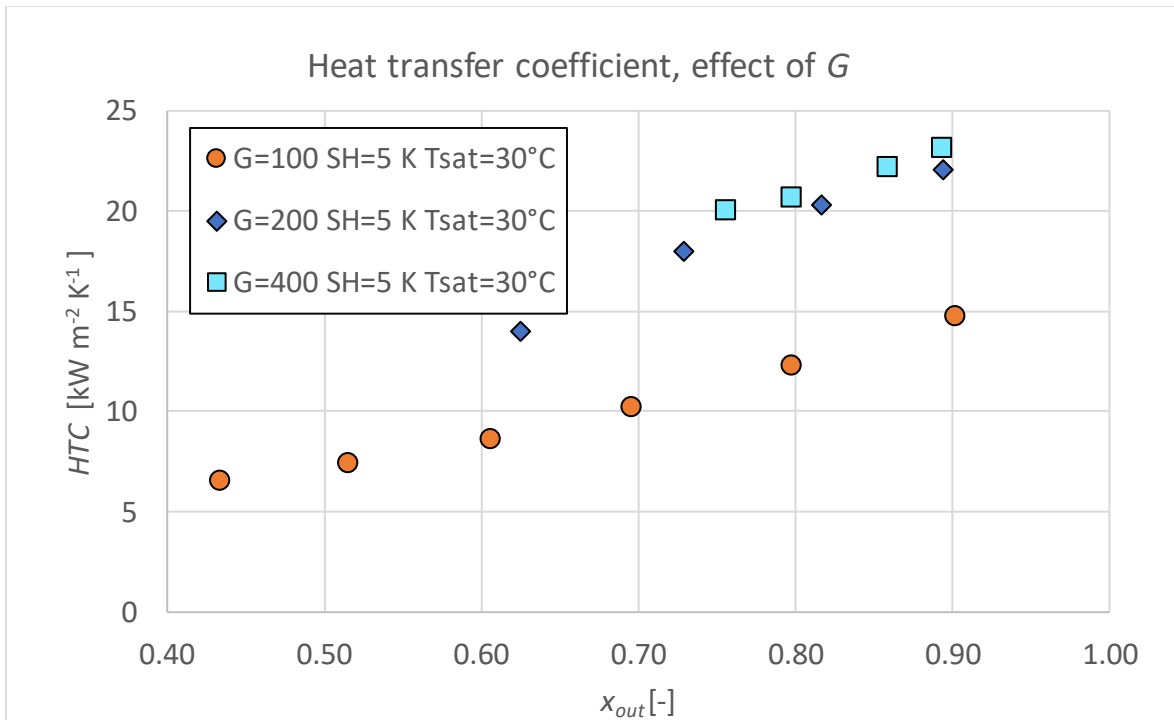
In Figure 6.2, the effect of the SH on the heat transfer coefficient is evaluated. In particular:

- The points of Figure 6.2 (a) have been taken with a $G=200 \text{ kg s}^{-1} \text{ m}^{-2}$ and $T_{sat}=40^\circ\text{C}$;
- The points of Figure 6.2 (b) have been taken with a $G=300 \text{ kg s}^{-1} \text{ m}^{-2}$ and $T_{sat}=40^\circ\text{C}$;
- The points of Figure 6.2 (c) have been taken with a $G=400 \text{ kg s}^{-1} \text{ m}^{-2}$ and $T_{sat}=40^\circ\text{C}$;
- The points of Figure 6.2 (d) have been taken with a $G=200 \text{ kg s}^{-1} \text{ m}^{-2}$ and $T_{sat}=30^\circ\text{C}$.

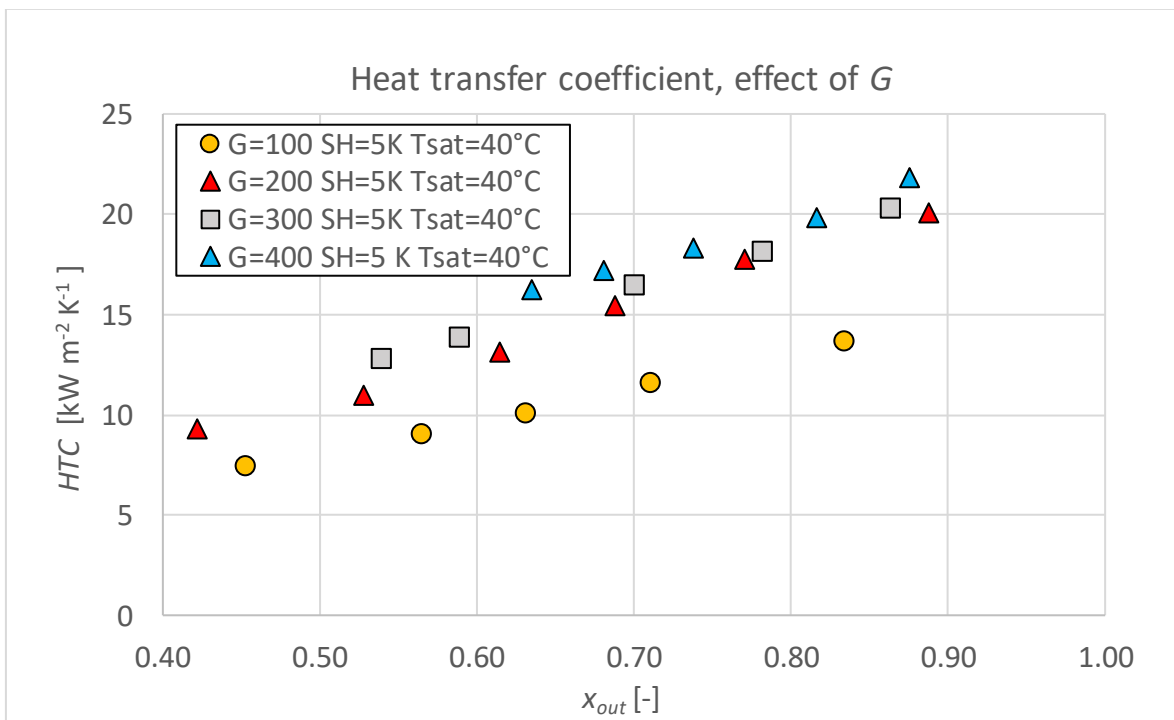
The trend of the experimental points is clear in each graph: the heat transfer coefficient decreases when the outlet vapor quality decreases. This is related to the thermal resistance of the liquid film, which is the dominant thermal resistance in the condensation process: when the outlet vapor quality decreases, a higher quantity of vapor condenses. Consequently, a thicker layer of liquid is formed on the tube wall, leading to a higher thermal resistance and to a lower heat transfer coefficient. This behaviour is noticeable even in Figure 6.1.

For what concerns the superheating degree, no important effect on the heat transfer coefficient is visualized with increasing SH in all the four graphs, a part for a relatively small increase at high vapor quality. This is due to the effect of superheated condensation: as stated by Kondou and Hrnjack [8] (Paragraph §1.2) and by Webb [4] (Paragraph §1.3), condensation from superheated vapor appears to be a simultaneous sensible (de-superheating of vapor) and latent heat transfer process. When the SH is higher, the vapor enters in the test section hotter: a larger portion of sensible heat is expected to be rejected to the cooling water. However, the increase on the heat transfer coefficient (even with $SH=30$ K in Figure 6.2(d)) is not greater than 5%, at high outlet vapor qualities. This could be explained considering the geometry of the tube. Since the number of fins in this geometry is extremely high, the liquid film could be subjected to a centrifugal movement which dramatically reduces the thermal resistance of the liquid. This mechanism would promote the latent heat transfer, which is the dominant process. No papers concerning this phenomenon have been found in literature and further investigations could be necessary (for instance, a comparison of the heat transfer coefficients considering an equivalent tube smooth tube with the same test conditions would be interesting to understand the effect of the fins in superheated condensation). Overall, the hypothesis supposed initially in §1.3 is experimentally verified: since no particular effect of the superheating degree is noticeable and since the driving temperature difference supposed is $T_{sat} - T_{wall,i}$, the heat transfer coefficient is within few percent the one of the condensation from saturated vapor. In fact, the sensible heat transfer mechanism is negligible compared to the latent one. As consequence, models which were originally obtained for condensation in saturated condition can be modified to be adapted even for the case of condensation from superheated vapor (refer to Chapter §7 for more details).

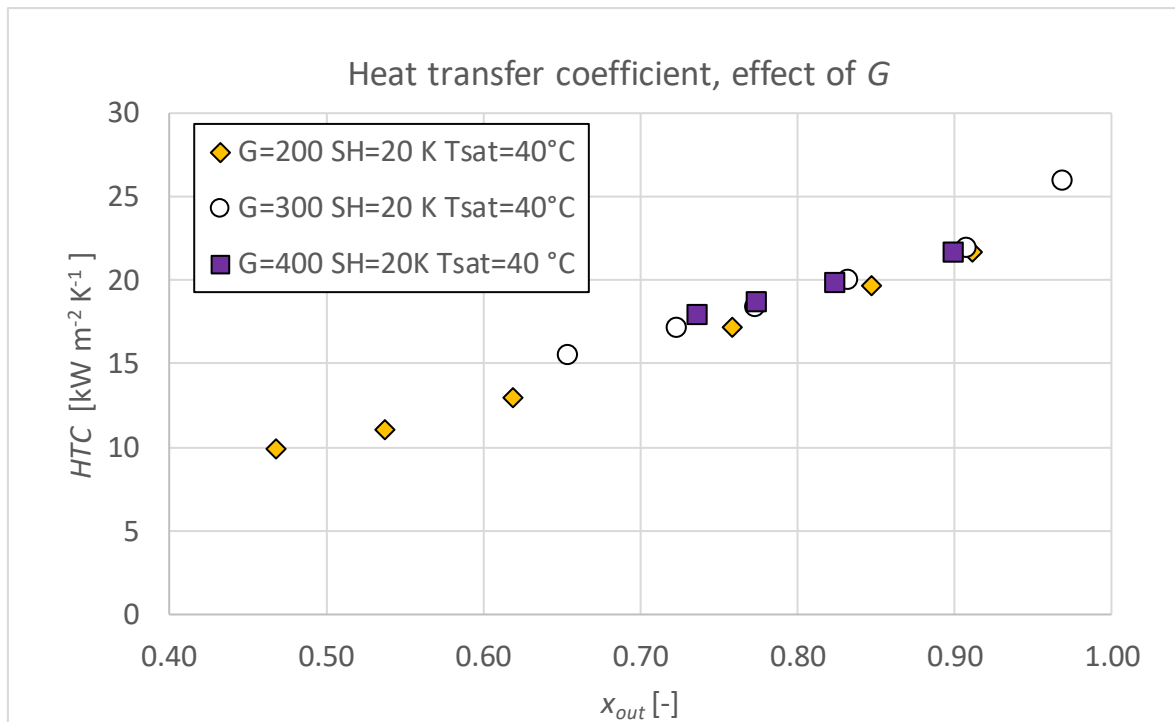
6.3 Effect of the mass velocity



(a)



(b)



(c)

Figure 6.3. Effect of the specific mass flow rate on the heat transfer coefficient.²

In Figure 6.3, the effect of G can be seen. In particular:

- The points of Figure 6.3 (a) have been taken with a $SH=5$ K and $T_{sat}=30^{\circ}\text{C}$;
- The points of Figure 6.3 (b) have been taken with a $SH=5$ K and $T_{sat}=40^{\circ}\text{C}$;
- The points of Figure 6.3 (c) have been taken with a $SH=20$ K and $T_{sat}=40^{\circ}\text{C}$;

In the first two graphs, a similar trend can be identified when G changes from 100 to $200 \text{ kg s}^{-1}\text{m}^{-2}$: the heat transfer coefficient dramatically increases. This is related to the change of flow pattern which evolves from stratified ($100 \text{ kg s}^{-1}\text{m}^{-2}$) to annular flow ($200 \text{ kg s}^{-1}\text{m}^{-2}$). In the stratified regime, the liquid film thickness is higher. This induces to higher thermal resistance on the bottom side and lower heat transfer coefficients (furthermore, the vapor velocity is lower and consequently the turbulence of the liquid is lower compared to higher vapor speed conditions). When the flow reaches the annular flow (above $200 \text{ kg s}^{-1}\text{m}^{-2}$), the HTC is enhanced since the liquid film is thinner and the higher velocity of the vapor induces larger turbulence in the liquid, leading globally to a lower thermal resistance. At high mass velocities, the points diverge when the outlet vapor quality decreases: this is due to the larger turbulence of the liquid

² In figure 6.3 (c), the points with $G=100 \text{ kg s}^{-1}\text{m}^{-2}$ are not plotted since the stabilization of the plant at such low specific flow rates and with such high degree of superheating was difficult to obtain.

formed at the outlet of the test section when the mass flux is larger. This effect is barely noticeable in the experimental points here presented, since the tube is relatively short and consequently, at high mass velocities, it results impossible to exit at vapor qualities lower than 0.6.

6.4 Conclusions

In this chapter, the experimental points of condensation from superheated vapor have been analysed. The following conclusions are summarized:

- When the saturation temperature increases, the *HTC* decreases. This is probably due to the lower vapor density at higher saturation temperature, which induces a larger turbulence of the liquid at the same mass flux;
- No relevant effect of the superheating degree has been reported during the tests. This is probably related to the microfin tube. The large number of fins could induce a centrifugal motion of the liquid film and consequently an enhancement of the latent heat transfer mechanism compared to the sensible one. A small effect is visible when the outlet quality is high because of the large quantity of vapor present in the tube. Overall, the condensation from superheated vapor is dominated by latent heat transfer phenomenon and consequently can be modelled as if it is in saturated condensation conditions;
- When the specific mass velocity increases above $200 \text{ kg s}^{-1} \text{ m}^{-2}$, the flow regime changes from stratified to annular flow, leading to an increase of the *HTC*. At low outlet vapor qualities and at high mass fluxes ($200, 300$ and $400 \text{ kg s}^{-1} \text{ m}^{-2}$) the points sets diverge since the turbulence of the liquid film is greater when the mass flux is larger.

In the next chapter, a detailed analysis of the models used to predict the heat transfer coefficients will be presented.

Chapter 7:

Models for the evaluation of the HTC for condensation from superheated vapor

In this Chapter, different models for the calculation of the heat transfer coefficient for condensation from superheated vapor are proposed, analysed and eventually modified.

7.1 The Cavallini *et al.*'s model for horizontal smooth tubes

Cavallini *et al.* [22] were among the first researchers to present an innovative model for the calculation of the heat transfer coefficient for condensation in horizontal smooth tubes. The principal feature of the model is its simplicity. Compared to other works present at the time, the Cavallini *et al.*'s model implements just the minimum number of necessary equations and is capable, with discrete good precision, to predict the experimental data of several papers. For this reason, the model is still widely used today in lots of works (such as in Kondou and Hrnjack [8])

7.1.1 The ΔT dependency flow regime map

At the time, other researchers tried to model the heat transfer coefficient in condensation. However, these models required a visual examination and classification of the pattern flow in order to understand in which flow regime the condensation appears. Cavallini *et al.* [22] proposed a different way to classify the flow regime, based not on the observation but on the parameters which can affect the heat transfer coefficient during condensation. When the tube is horizontal, the dependence on the ΔT (defined as temperature difference between the saturation T_{sat} and the wall temperature $T_{wall,i}$) occurs only when the gravity is the prevailing force (stratified flow). Thus, the flow regime is distinguished between ΔT -dependent and ΔT -independent. For smooth tubes, the authors found a correlation which defines the transition line between

the two different flow regimes (Figure 7.1), distinguishing between hydrocarbons and other types of refrigerants.

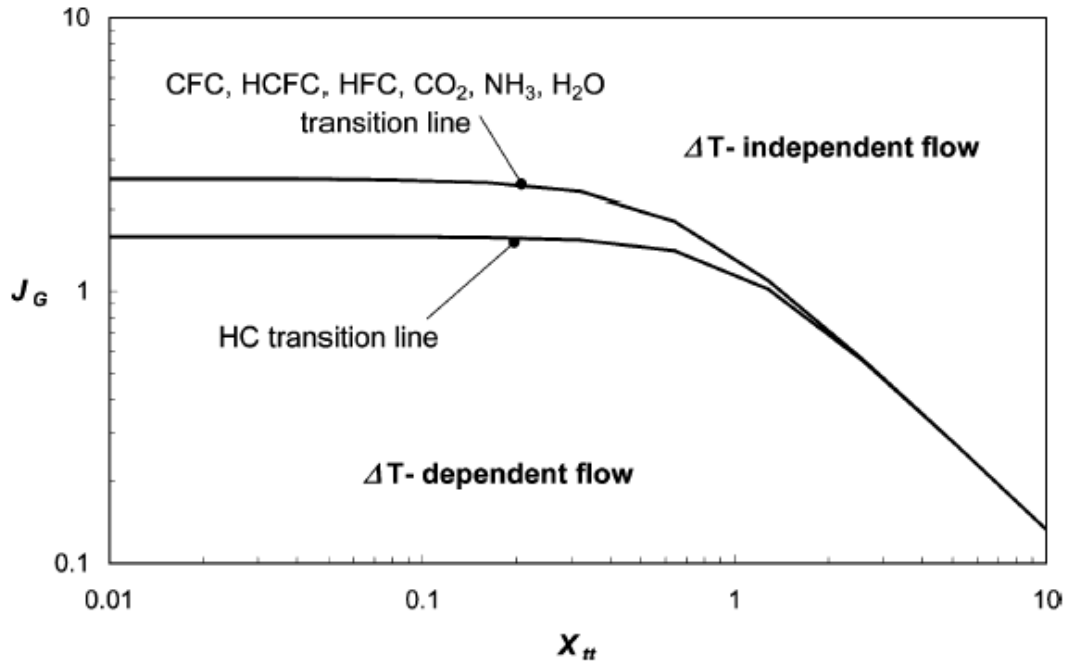


Figure 7.1. Transition line between ΔT -dependent and ΔT -independent flow regime. The lower line represents the transition for the hydrocarbons, the upper one is the transition line for the other refrigerants.

The equation of the transition line is:

$$\begin{cases} J_G^T = \left\{ \left[\frac{7.5}{(4.3X_{tt}^{1.111} + 1)} \right]^{-3} + C_t^{-3} \right\}^{-\frac{1}{3}}, \\ C_t = 1.6, \text{ hydrocarbons} \\ C_t = 2.6, \text{ other refrigerants} \end{cases}, \quad (7.1)$$

where J_G^T is the transition dimensionless gas velocity and X_{tt} is the Martinelli parameter, calculated as:

$$X_{tt} = \left(\frac{1-x}{x} \right)^{0.9} \left(\frac{\rho_V}{\rho_L} \right)^{0.5} \left(\frac{\mu_L}{\mu_V} \right)^{0.1}, \quad (7.2)$$

where x is the vapor quality, ρ_V is the density of the vapor [kg m^{-3}], ρ_L is the density of the liquid [kg m^{-3}], μ_V is the viscosity of the vapor [$\text{kg m}^{-1} \text{s}^{-1}$] and μ_L is the viscosity of the liquid [$\text{kg m}^{-1} \text{s}^{-1}$]. This parameter expresses the liquid fraction of the flowing fluid.

7.1.2 Heat transfer coefficient for condensation in horizontal smooth tubes

The dimensional gas velocity is calculated:

$$J_G = \frac{x \cdot G}{[gID\rho_V(\rho_L - \rho_V)]^{0.5}}, \quad (7.3)$$

where ID is the inner tube diameter [m], g is the gravity acceleration [m s^{-2}], G is the mass velocity [$\text{kg s}^{-1} \text{m}^{-2}$].

Once the type of flow regime has been established, the calculations can proceed. In particular, for the ΔT -independent regime ($J_G > J_G^T$):

$$\alpha_A = \alpha_{LO} \left[1 + 1.128x^{0.8170} \left(\frac{\rho_L}{\rho_V}\right)^{0.3685} \left(\frac{\mu_L}{\mu_V}\right)^{0.2363} \left(1 - \frac{\mu_V}{\mu_L}\right)^{2.144} \text{Pr}_L^{-0.100} \right], \quad (7.4)$$

where Pr_L is the Prandtl number of the liquid phase:

$$\text{Pr}_L = \frac{c_{p,L}\mu_L}{\lambda_L}, \quad (7.5)$$

where λ_L is the thermal conductivity in liquid state [$\text{W m}^{-1} \text{K}^{-1}$]. For ΔT -dependent regime ($J_G < J_G^T$):

$$\alpha_D = \left[\alpha_A \left(\frac{J_G^T}{J_G}\right)^{0.8} - \alpha_{STRAT} \right] \left(\frac{J_G^T}{J_G}\right) + \alpha_{STRAT}, \quad (7.6)$$

$$\alpha_{LO} = \frac{0.023\text{Re}_{LO}^{0.8}\text{Pr}_L^{0.4}\lambda_L}{ID}, \quad (7.7)$$

$$\alpha_{STRAT} = 0.725 \left[1 + 0.741 \left(\frac{1-x}{x} \right)^{0.3321} \right]^{-1} \times \left[\frac{\lambda_L^3 \rho_L (\rho_L - \rho_V) g h_{LV}}{\mu_L ID \Delta T} \right]^{0.25} + (1-x^{0.087}) \alpha_{LO}, \quad (7.8)$$

where h_{LV} is the latent heat [J kg^{-1}], ΔT is the temperature difference between the saturation and the wall and Re_{LO} is the liquid-only Reynolds number:

$$Re_{LO} = G \frac{ID}{\mu_L}. \quad (7.9)$$

It is important to notice that all the calculations are performed using the mean thermodynamic vapor quality between the inlet and the outlet of the condenser. The properties of the liquid phase should be evaluated at the mean temperature between T_{sat} and $T_{wall,i}$, whereas the properties of vapor phase should be evaluated at T_{sat} .

7.2 The Cavallini *et al.*'s model for horizontal microfin tubes

7.2.1 Description of the model

Some years later, the same researchers of [22] proposed a new computational procedure for the calculation of the heat transfer coefficient in horizontal microfin tubes which is also applicable to near azeotropic refrigerants (Cavallini *et al.* [2]). The model is based on the work presented in §7.1.2, with some modifications to consider the enhancement of the heat transfer process due to the presence of the fins inside the tube. The present model is valid when the ratio between h (height of the fins [m]) and ID_{apex} [m] is less than 0.04 (in the present case study, this condition is verified). A new transition dimensionless gas velocity J_G^* is introduced for microfin tubes:

$$J_G^* = 0.6 \left\{ \left[\frac{7.5}{(4.3X_{tt}^{1.111} + 1)} \right]^{-3} + 2.5^{-3} \right\}^{\frac{1}{3}}. \quad (7.10)$$

The heat transfer coefficient is defined with reference to the heat transfer area of the smooth tube with inner diameter ID_{apex} , equals to the fin tip diameter of the microfin tube:

$$\alpha = [\alpha_A^3 + \alpha_D^3]^{0.3333}, \quad (7.11)$$

where α_A is the heat transfer coefficient for the ΔT -independent zone and α_D is the heat transfer coefficient for the ΔT -dependent zone. The forced convective condensation term is obtained by (7.3) (to distinguish the two terms, α_A in (7.4) will be referred from now on as α_{AS}) multiplied by two terms:

$$\alpha_A = \alpha_{AS} \cdot A \cdot C, \quad (7.12)$$

where A is a function of the geometry enhancement factor Rx and of the Froude number Fr . The term C acts to lower the heat transfer coefficient when the number of fins n is greater than the optimal one n_{opt} for the given diameter ID_{apex} (γ is the apex angle [rad] and β is the helix angle [rad]):

$$A = 1 + 1.119Fr^{-0.3821}(Rx - 1)^{0.3586}, \quad (7.13)$$

$$Fr = \frac{G^2}{g ID_{apex} (\rho_L - \rho_V)^2}, \quad (7.14)$$

$$Rx = \left\{ \frac{2h n \left[1 - \sin\left(\frac{\gamma}{2}\right) \right]}{\pi ID_{apex} \cos\left(\frac{\gamma}{2}\right)} + 1 \right\} \left(\frac{1}{\cos\beta} \right) \quad (7.15)$$

$$\begin{cases} C = 1 & \text{if } n_{opt}/n \geq 0.8, \\ C = \left(\frac{n_{opt}}{n}\right)^{1.904} & \text{if } n_{opt}/n < 0.8, \\ n_{opt} = 4064.4 ID_{apex} + 23.257, \end{cases} \quad (7.16)$$

The heat transfer coefficient for the ΔT -dependent zone α_D is expressed as function of C , Rx and the coefficient α_{DS} from Cavallini *et al.* [22]. If the dimensionless gas velocity

is lower than the transition gas velocity ($J_G < J_G^*$), the heat transfer coefficient is reduced through the constant C_1 :

$$\alpha_D = C[2.4x^{0.1206}(Rx - 1)^{1.466}C_1^{0.6875} + 1]\alpha_{DS} + C(1 - x^{0.087})Rx\alpha_{LO}, \quad (7.17)$$

$$\alpha_{DS} = 0.725 \left[1 + 0.741 \left(\frac{1-x}{x} \right)^{0.3321} \right]^{-1} \times \left[\frac{\lambda_L^3 \rho_L (\rho_L - \rho_V) g h_{LV}}{\mu_L ID_{apex} \Delta T} \right]^{0.25}, \quad (7.18)$$

$$\begin{cases} C_1 = 1 & \text{if } J_G \geq J_G^*, \\ C_1 = \left(\frac{J_G}{J_G^*} \right) & \text{if } J_G < J_G^*. \end{cases} \quad (7.19)$$

The presented model is applied to evaluate the heat transfer coefficient previously calculated in the data reduction Chapter §4. However, some crucial hypothesis must be specified before proceeding with the calculations.

7.2.2 Hypothesis for the application of the model

The model presented in §7.2 was originally developed for calculation of the heat transfer coefficient in saturated conditions. However, in the present case study, the refrigerant enters in the test section as superheated vapor. In that specific region, it is impossible to define a thermodynamic quality, since x_t cannot exceed the unity. The optimal approach would be the subdivision of the test tube into smaller sections, to identify the region where the vapor condenses in superheated state and where it reaches the saturation conditions. However, the test section is quite small and the division into different areas results difficult to perform. Consequently, the heat transfer coefficient is modelled considering just the latent heat transfer and neglecting the sensible de-superheating during the superheated condensation. In this way, all the process can be modelled using just the correlation for saturated vapor, without concerning about the sensible heat transfer. As reported in Rossetto [1], experimentally the heat transfer coefficient during condensation from superheated vapor should be within few percent of that during condensation from saturated vapor if in both cases the driving temperature difference is the one between the saturation and the wall temperature (this hypothesis was previously confirmed in Chapter §6 by the experimental results: different degrees of superheating seem to not affect the heat transfer coefficients).

Consequently, Cavallini *et al.*'s model can be adopted for modelling the condensation from superheated vapor. This simplification of the real heat transfer process, which is given as a combination of sensible and latent heat transfer, would for sure lead to an error which however is expected to be not so much relevant, since the sensible heat transfer coefficient is expected to be one order of magnitude lower than the latent one. As previously stated, the Cavallini *et al.*'s model requires the inlet vapor quality as input. Consequently, since x_t cannot exceed the unity, the vapor quality at the inlet of the tube is assumed equal to 0.9999 (simplification proposed by Kondou and Hrnjack [8]). In this way, it is possible to calculate a mean vapor quality between the inlet and the outlet and adopt a correlation originally developed for condensation in saturated condition even in the case the vapor enters in the test section in superheated conditions.

The last hypothesis regards the optimal number of fins: since the model was developed some years ago, the new refrigerants, such as R1234ze(E), were not invented yet. Different experiments (such the one performed by Donno [10]) demonstrated that the correction on the optimal number of fins tends to dramatically underestimate the heat transfer coefficient for certain refrigerants and for certain geometries. Consequently the parameter C (equations (7.16)) is assumed always equals to 1. Further investigations would be necessary to understand the effect of this parameter for different new refrigerants.

7.2.3 Implementation and results

Following the hypothesis of the previous subparagraph, the Cavallini *et al.*'s model is implemented. The code is the B.2 in the APPENDIX B. In the code, the mean percentage error $\bar{\varepsilon}$, the absolute error \bar{E} and the standard deviation σ are calculated:

$$\bar{\varepsilon} = \left(\frac{1}{n} \sum_{i=1}^n \frac{HTC_{calculated} - HTC_{expected}}{HTC_{expected}} \right) \times 100 = \left(\frac{1}{n} \sum_{i=1}^n \varepsilon_i \right) \times 100, \quad (7.20)$$

$$\bar{E} = \left(\frac{1}{n} \sum_{i=1}^n \left| \frac{HTC_{calculated} - HTC_{expected}}{HTC_{expected}} \right| \right) \times 100 = \left(\frac{1}{n} \sum_{i=1}^n |\varepsilon_i| \right) \times 100, \quad (7.21)$$

$$\sigma = \sqrt{\frac{1}{n-1} \sum_{i=1}^n (\varepsilon_i - \bar{\varepsilon})^2} \times 100, \quad (7.22)$$

where $HTC_{expected}$ is the heat transfer coefficient [$\text{kW m}^{-2} \text{K}^{-1}$] calculated with (4.11), $HTC_{calculated}$ is the heat transfer coefficient [$\text{kW m}^{-2} \text{K}^{-1}$] calculated with the model and n is the number of experimental points taken during the test sessions.

The results of the model are reported in Figure 7.2.

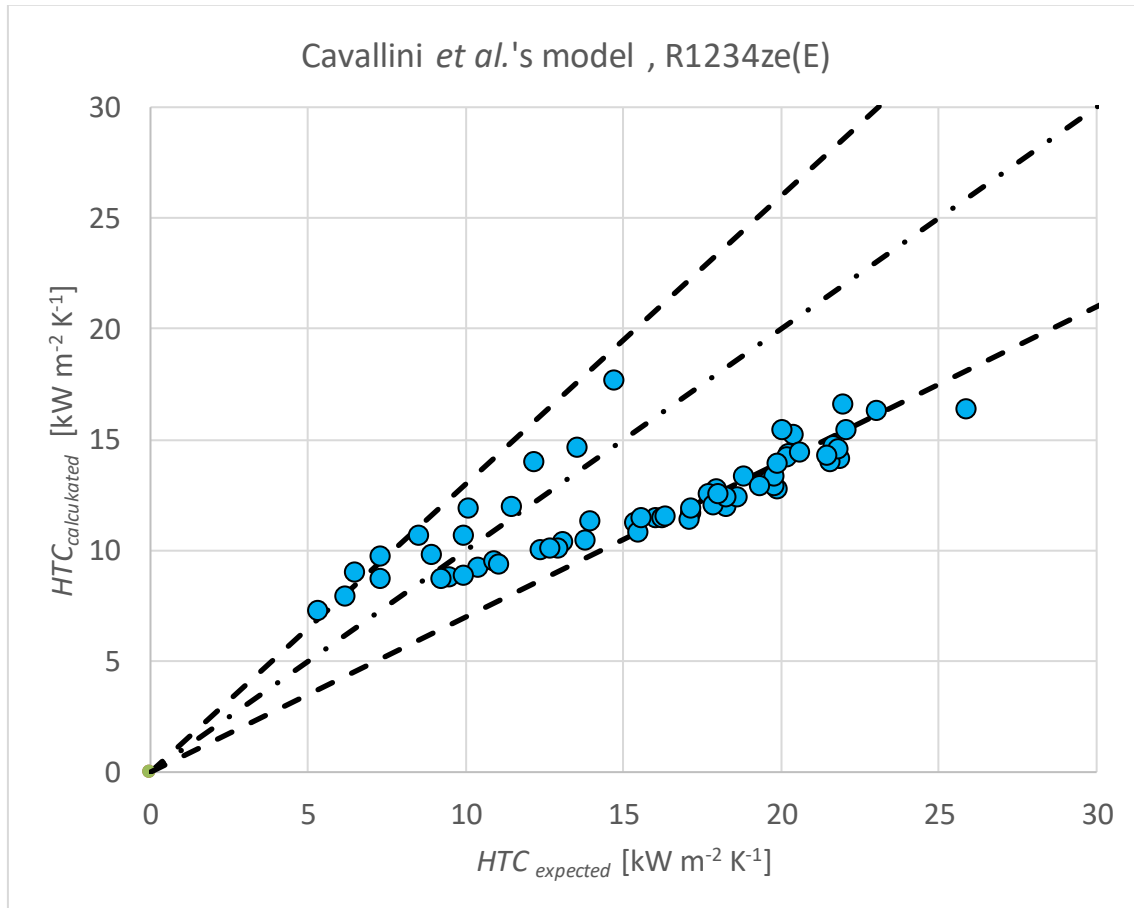


Figure 7.2. $HTC_{calculated}$ with the Cavallini et al.'s correlation vs $HTC_{expected}$.

The black lines in the figure represent a $\pm 30\%$ error compared to the expected value of heat transfer coefficient. The $\bar{\epsilon}$ is equal to -17.93% , \bar{E} is equal to 25.91% and σ is equal to 20.91% . The error for this type of correlation is still acceptable, since the correlation was not developed for this type of study. It is clearly noticeable that the correlation tends to underestimate the heat transfer coefficient when $HTC_{expected}$ exceeds $15 \text{ kW m}^{-2} \text{K}^{-1}$. As shown in Figure 7.3., when the mass velocity increases, the predictability of the model decreases.

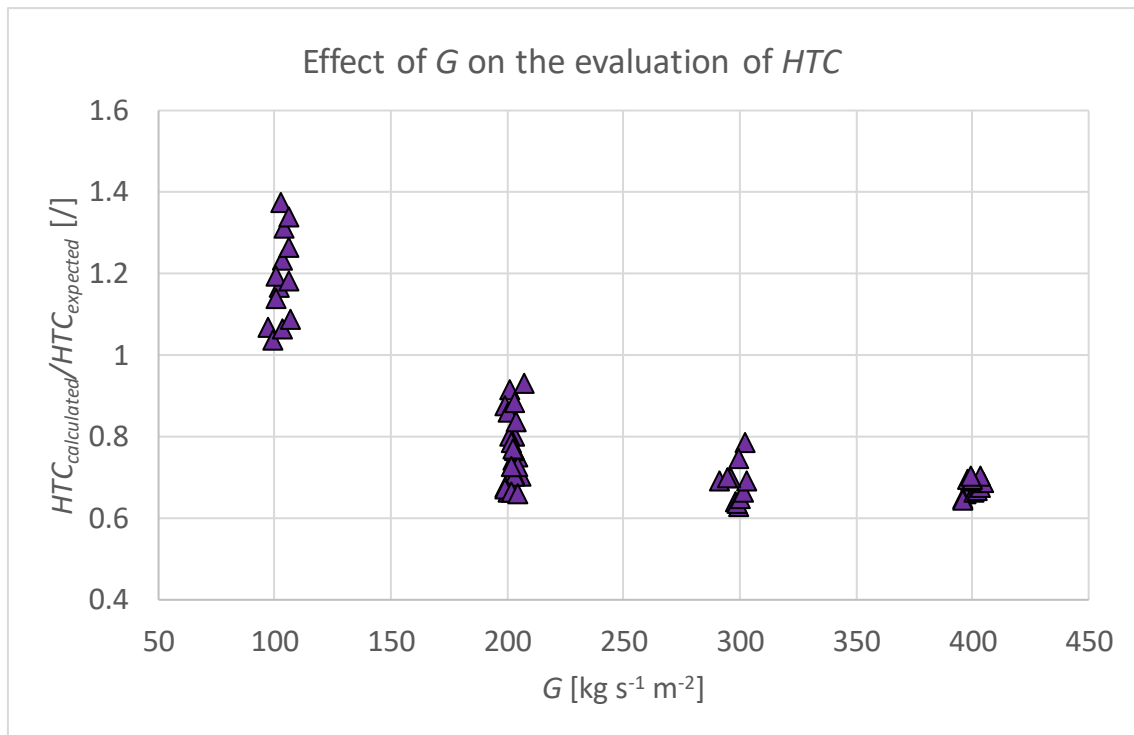


Figure 7.3. Effect of the mass velocity on the calculation of HTC.

This phenomenon is probably related to the effect of the sensible heat on the total heat transfer: when the mass velocity becomes more important, the outlet vapor quality increases since the vapor does not have enough time to proceed with the condensation. This means that the sensible mechanism becomes more relevant in the case of high mass velocities and consequently the modelling becomes less precise. A trial of correction of the error is presented in §7.5.

Nevertheless, the modelling adopted considering the heat transfer just as latent mechanism gives satisfying result. It should be considered the fact that, when a real condenser operates, the section concerning the condensation with superheated vapor is very small compared to the total length of the heat exchanger. Consequently, for design application, this correlation gives results more than satisfying, despite the simplification adopted as starting hypothesis.

7.3 The Hirose *et al.*'s model for microfin tubes

7.3.1 Description of the model

Hirose *et al.* [3] proposed a new method for the evaluation of the heat transfer coefficient in condensation both for smooth and micro fin tubes. The model is based on the Yu and Koyama [23] correlation:

$$\text{Nu} = \sqrt{\text{Nu}_F^2 + \text{Nu}_B^2}, \quad (7.23)$$

where the Nusselt number is given by the combination of two different terms: Nu_F , which is the forced convection condensation Nusselt, and Nu_B , which is the free convection condensation Nusselt, proposed by Yu and Koyama (1996) [23]:

$$\text{Nu}_B = \left(\frac{0.725}{\eta^{0.25}} \right) H(\xi) \left(\frac{\text{GaPr}_L}{\text{Ph}_L} \right)^{0.25}, \quad (7.24)$$

where η is the area magnifying ratio (R_x in Cavallini *et al.*³), Ga is the Galileo number, Pr_L is the Prandlt number in liquid phase (7.5) and Ph_L is the phase change number, defined as follow:

$$\text{Ga} = g \frac{ID_{max}^3 \rho_L^2}{\mu_L^2}, \quad (7.25)$$

$$\text{Ph}_L = \frac{c_{p,L}(T_{sat} - T_{w,i})}{h_{LV}}. \quad (7.26)$$

$H(\xi)$ is a function of the void fraction ξ :

$$H(\xi) = \xi + \{10(1 - \xi)^{0.1} - 8\} \sqrt{\xi} (1 - \sqrt{\xi}), \quad (7.27)$$

³ In this model, all the calculations are referred to the cross-sectional area at the base of the fin. This means that the diameter taken as reference is ID_{max} , not ID_{apex} .

$$\xi = 0.81\xi_{Smith} + 0.19x^{100}\left(\frac{\rho_V}{\rho_L}\right)^{0.8} \xi_{homo},^4 \quad (7.28)$$

$$\xi_{homo} = \left[1 + \left(\frac{\rho_V}{\rho_L}\right)\left(\frac{1-x}{x}\right)\right]^{-1} \quad (7.29)$$

$$\xi_{Smith} = \left[1 + \left(\frac{\rho_V}{\rho_L}\right)\left(\frac{1-x}{x}\right)\left(0.4 + 0.6\sqrt{\frac{\frac{\rho_V}{\rho_L} + 0.4\left(\frac{1-x}{x}\right)}{1 + 0.4\left(\frac{1-x}{x}\right)}}\right)\right]^{-1}. \quad (7.30)$$

The Nu_F is defined as follow:

$$Nu_F = \sqrt{0.5 f_v} Re_L \Phi_V \left(\frac{\rho_V}{\rho_L}\right)^{0.5} \left(\frac{x}{1-x}\right) \left(\frac{Pr_L}{T_i^*}\right), \quad (7.31)$$

where Re_L and Re_V are the Reynolds numbers in liquid and vapor phase, f_v is the friction factor, Φ_V is the two-phase flow pressure drop multiplier and T_i^* is the dimensionless temperature difference:

$$Re_L = \frac{G_{max}(1-x)ID_{max}}{\mu_L}, \quad (7.32)$$

$$Re_V = \frac{G_{max} x ID_{max}}{\mu_L}, \quad (7.33)$$

$$f_v = 0.26 Re_V^{-0.38} \eta^{0.95} \cos(\beta)^{-2.8}, \quad (7.34)$$

$$\Phi_V = 1 + 1.55X_{tt}^{0.4}. \quad (7.35)$$

To identify the flow regime, the Soliman Froude number Fr_{sol} is adopted:

$$Fr_{sol} = \frac{0.025Re_L^{1.59} \left\{\frac{(1 + 1.09X_{tt}^{0.039})}{X_{tt}}\right\}^{1.5}}{Ga^{0.5}} \quad \text{if } Re_L \leq 1250, \quad (7.36)$$

$$Fr_{sol} = \frac{1.26Re_L^{1.04} \left\{\frac{(1 + 1.09X_{tt}^{0.039})}{X_{tt}}\right\}^{1.5}}{Ga^{0.5}} \quad \text{if } Re_L > 1250. \quad (7.37)$$

⁴ x is even in this case the mean vapor quality between the inlet and the outlet of the test section

Interpolating their experimental points with the equations presented, Hirose *et al.* modified the equations (7.29) for wavy flow (7.36) and annular flow (7.37):

$$\text{Nu}_F = 7.85\sqrt{f_v} \left(\frac{\Phi_V}{X_{tt}}\right) \left(\frac{\rho_V}{\rho_L}\right)^{0.5} \left(\frac{\mu_L}{\mu_V}\right)^{0.1} \left(\frac{x}{1-x}\right)^{0.1} \text{Re}_L^{0.47} \text{ if } \text{Fr}_{sol} < 20, \quad (7.38)$$

$$\text{Nu}_F = 15.4\sqrt{f_v} \left(\frac{\Phi_V}{X_{tt}}\right) \left(\frac{\rho_V}{\rho_L}\right)^{0.5} \left(\frac{\mu_L}{\mu_V}\right)^{0.1} \left(\frac{x}{1-x}\right)^{0.1} \text{Re}_L^{0.43} \text{ if } \text{Fr}_{sol} > 20. \quad (7.39)$$

Hirose *et al.* modified the equation for the free convection Nusselt Nu_B adding the Bond number Bo to consider the effect of the buoyancy and surface tension:

$$\text{Nu}_B = \left(\frac{1.60}{\eta^{0.25}}\right) \text{H}(\xi) \left(\frac{\text{GaPr}_L}{\text{Ph}_L}\right)^{0.25} \text{Bo}^{-0.20}, \quad (7.40)$$

$$\text{Bo} = \frac{(\rho_L - \rho_V)gID_{max}}{\Gamma}, \quad (7.41)$$

where Γ is the surface tension [N m^{-1}].

7.3.2 Hypothesis for the application of the model

Even in this case, the model was originally developed to study condensation from saturated vapor, not from superheated state. The same hypothesis adopted for Cavallini *et al.* in §7.2.2 in order to evaluate a mean thermodynamic vapor quality is used here: the inlet condition is supposed equals to 0.9999 and the sensible heat transferred from vapor to the liquid is considered negligible and though is not modelled.

It is important to notice that in the current model, it is not specified how to calculate the parameter Rx . Consequently, the value 1.967 given by the manufacturer is assumed for the application of the model (this value is referred to the diameter at the base of the fins).

7.3.3 Implementation and results

Following the hypothesis of the previous subparagraph, the Hirose *et al.* model is implemented. The code is B.3 in the APPENDIX B. The results are shown in Figure 7.4.

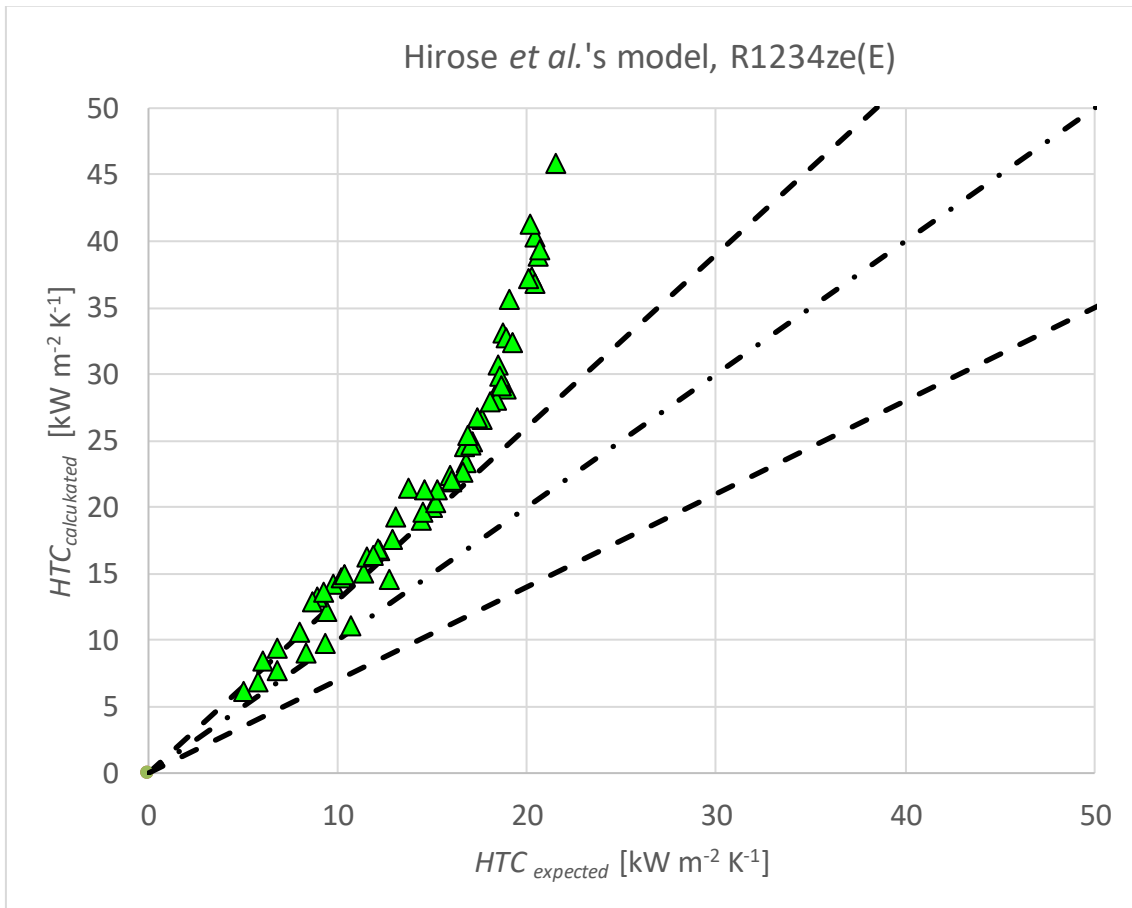


Figure 7.4. $HTC_{calculated}$ with the Hirose et al.'s model vs $HTC_{expected}$.

The black lines in the figure represent a $\pm 30\%$ error compared to the expected value of heat transfer coefficient. The $\bar{\varepsilon}$ and \bar{E} are equal to 50.78% and σ is equal to 30.37%. The correlation tends to overestimate the expected heat transfer coefficient. This identical behaviour was found by the same authors in [3] using the model for the interpolation of the experimental results by Diani and colleagues, as shown in Figure 7.5.

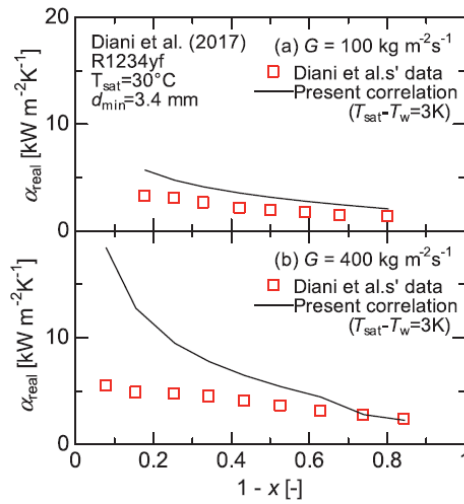


Figure 7.5. Comparison between the Diani et al. values with the Hirose et al.'s model [3].

The model tends to overestimate the *HTC* in the region where the vapor quality is higher. This can be seen in Figure 7.6.

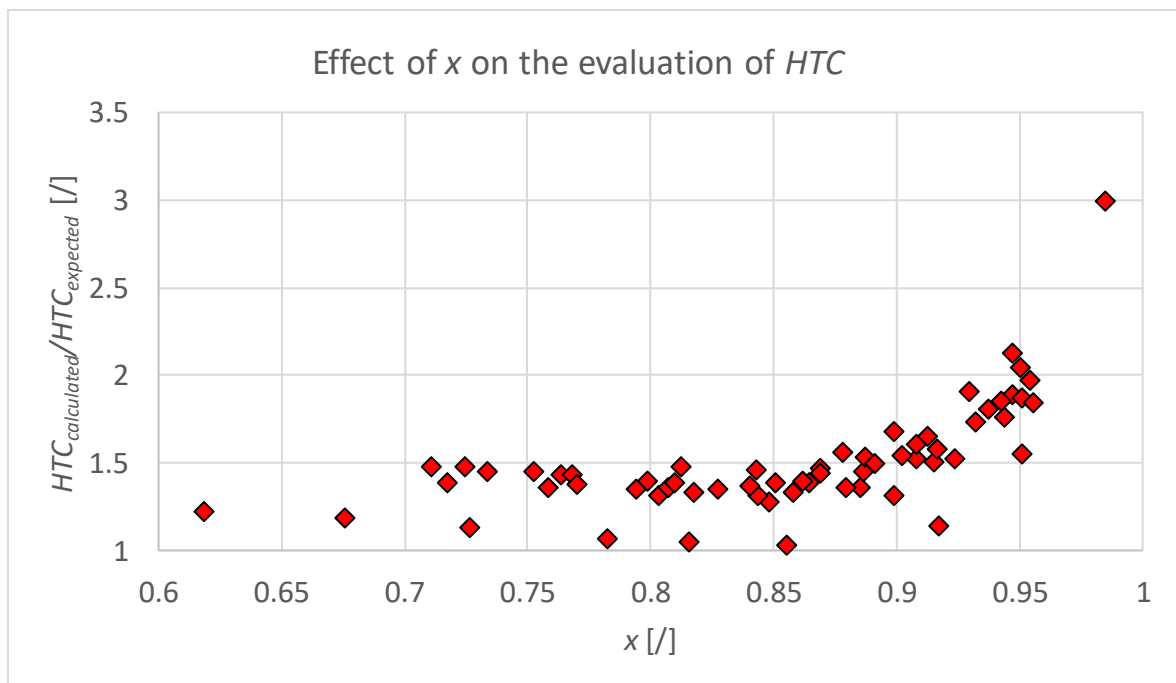


Figure 7.6. Effect of *x* on the calculation of the heat transfer coefficient.

The reason for this behaviour could be the points on which the model has been calibrated: Hirose *et al.* [3] defined the equations presented in the previous chapter

using an interpolation of their experimental data. The refrigerants used on their experiments were R32, R410A (which is a mixture which contains R32) and R152a. No hydrofluoroolefin was present in their experiment. Indeed, the exponential pattern trend in Figure 7.3 and 7.4. is presented with R1234yf and R1234ze(E), which are both HFO. Consequently, a recalibration of the model is performed in the following paragraph to adapt it to the HFO.

7.4. The Hirose *et al.*'s modified model

7.4.1 Recalibration of the equations

The procedure adopted to recalibrate the equations is the same described in [3]. Starting from equation (7.29), it is possible to write:

$$\left(\frac{Pr_L}{T_i^*}\right) = \frac{(Nu^2 - Nu_B^2)^{0.5}}{\sqrt{0.5} f_v Re_L \Phi_V \left(\frac{\rho_V}{\rho_L}\right)^{0.5} \left(\frac{x}{1-x}\right)}, \quad (7.42)$$

which can be rewritten as:

$$\left(\frac{Pr_L}{T_i^*}\right) = A Re_L^b, \quad (7.43)$$

where A and b are the two coefficients obtained by the linear logarithmic interpolation of the data. The points are distinguished between wavy stratified flow ($Fr_{sol} < 20$) and annular flow ($Fr_{sol} > 20$) and the interpolation is performed. In APPENDIX B, the code B.4 is the interpolation for wavy stratified flow points and the code B.5 is the interpolation for the annular flow points. The Nu_B is not corrected with the Bond number since no explanation on how the coefficients are obtained is given in the article. Consequently, the equation used in the modified model is (7.22). The new recalibrated equations become:

$$Nu_F = 3.90 \sqrt{f_v} \left(\frac{\Phi_V}{X_{tt}}\right) \left(\frac{\rho_V}{\rho_L}\right)^{0.5} \left(\frac{\mu_L}{\mu_V}\right)^{0.1} \left(\frac{x}{1-x}\right)^{0.1} Re_L^{0.55} \text{ if } Fr_{sol} < 20, \quad (7.44)$$

$$\text{Nu}_F = 2.67\sqrt{f_v} \left(\frac{\Phi_V}{X_{tt}}\right) \left(\frac{\rho_V}{\rho_L}\right)^{0.5} \left(\frac{\mu_L}{\mu_V}\right)^{0.1} \left(\frac{x}{1-x}\right)^{0.1} \text{Re}_L^{0.63} \text{ if } \text{Fr}_{\text{sol}} > 20. \quad (7.45)$$

7.4.2 Implementation and results

The Hirose *et al.*'s modified model is implemented with the modification presented in the previous paragraph. The code implemented is the B.6 in APPENDIX B. The results are reported in Figure 7.7 and they are compared with the ones obtained with the original model.

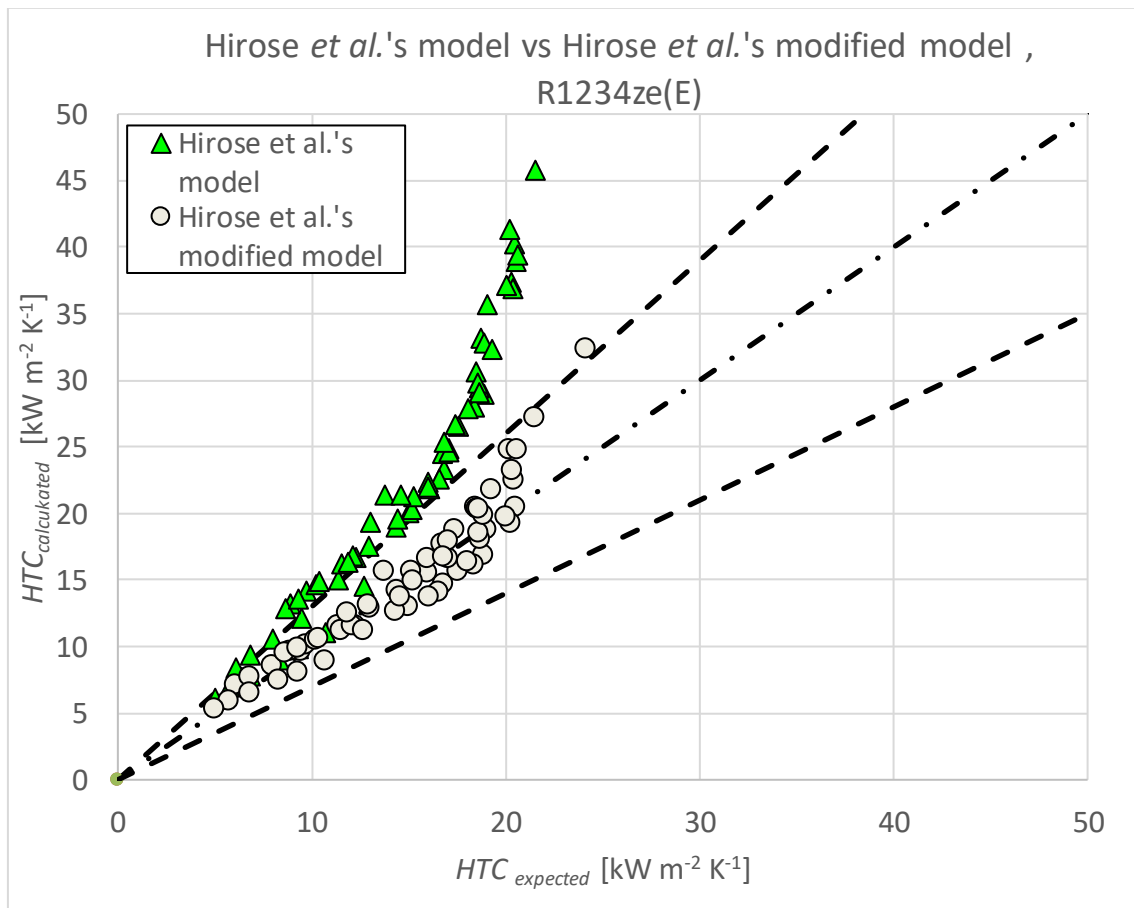


Figure 7.7. $HTC_{\text{calculated}}$ with the Hirose *et al.*'s and with Hirose *et al.*'s modified correlations vs HTC_{expected} .

The black lines in the figure represent a $\pm 30\%$ error compared to the expected value of heat transfer coefficient. The $\bar{\epsilon}$ is equal to 0.91%, \bar{E} is equal to 8.24% and σ is equals to 10.57%. The new model presents a much better precision in the evaluation of the heat

transfer coefficient for the R1234ze(E). Furthermore, no exponential trend is highlighted when the vapor quality increases, as shown in figure 7.8.

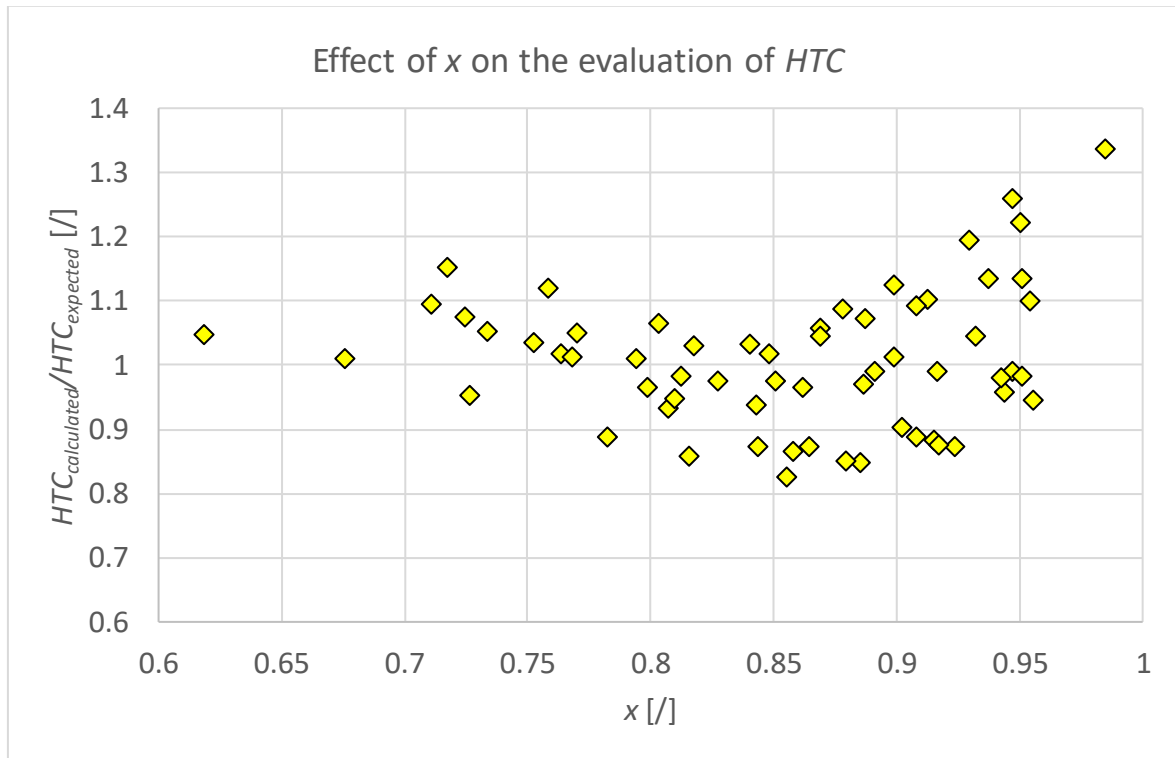


Figure 7.8. Effect of x on the calculation of the heat transfer coefficient.

The new correlation works better compared to the old one with the data acquired in the present work, since it has been calibrated to fit them as better as possible. However, to validate a new correlation, it is necessary to compare the results with other experimental data.

7.4.3 Comparison with R450A and R515B experimental data

The new model is used to evaluate the heat transfer coefficient for the data obtained by Donno [10]. The experiments were performed using two different refrigerants: R450A, which is a zeotropic mixture of 42% R134a and 58% R1234ze (E), and R515B, which is an azeotropic mixture of 91.1% R1234ze(E) and 8.9% of R277ea. Since the model was calibrated with the R1234ze(E), a greater performance is expected with R515B compared to R450A. It is important to notice these data were taken with a saturation condition at

the inlet of the test section. Consequently, the real inlet vapor quality is used as input to the model.

7.4.3.1 Comparison of the models using R450A

In Figure 7.9, the results with R450A are presented with the Hirose's model compared with the results obtained with the Hirose's modified model.

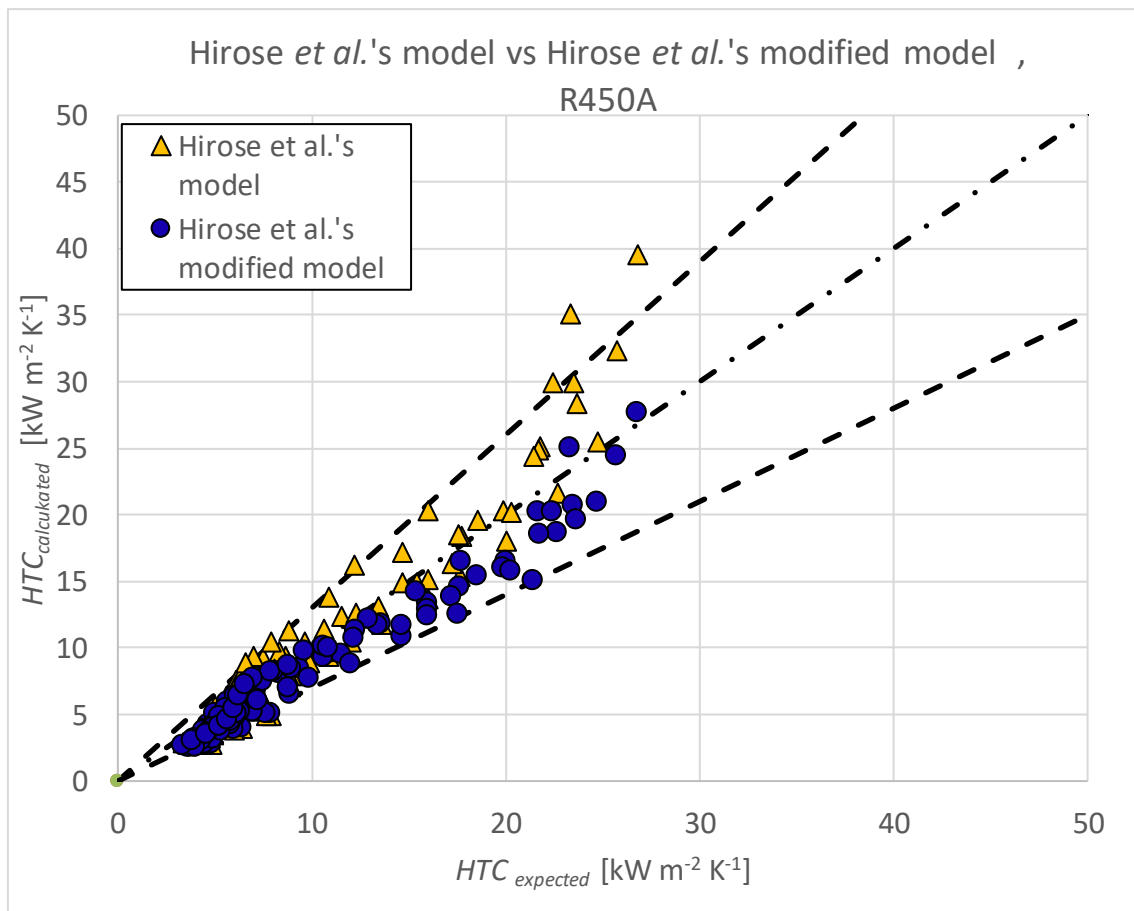


Figure 7.9. $HTC_{calculated}$ with the Hirose *et al.*'s and with Hirose *et al.*'s modified correlation vs $HTC_{expected}$ for R450A.

The black lines in the figure represent a $\pm 30\%$ error compared to the expected value of heat transfer coefficient. The $\bar{\epsilon}$ is equal to -4.18% , \bar{E} is equal to 16.71% and σ is equal to 19.71% for the Hirose's model, whereas the $\bar{\epsilon}$ is equal to -17.23% , \bar{E} is equal to 18.03% and σ is equal to 11.86% for the Hirose's modified model. The original model seems to be more precise with R450A compared to the new one in terms of relative error. Despite

this fact, the absolute error is quite similar. This could be related to the composition of the R450A, which presents a 42% of R134a. Despite the difference on $\bar{\epsilon}$, the new correlation presents a better trend since the results are less scattered compared to the old one (indeed, the standard deviation is smaller for the modified model).

7.4.3.2 Comparison of the models using R515B

In Figure 7.10, the results with R515B are presented with the Hirose's model compared with the results obtained with the Hirose's modified model.

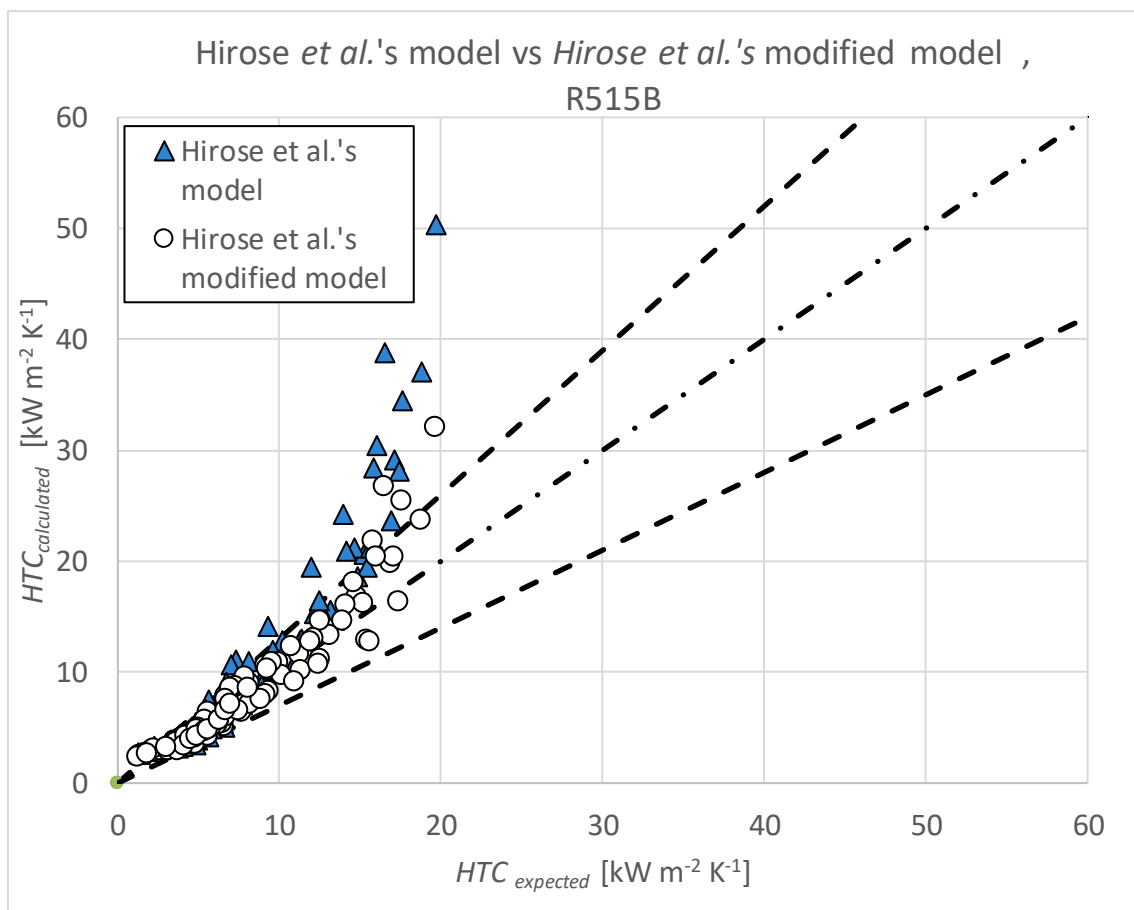


Figure 7.10. $HTC_{calculated}$ with the Hirose *et al.*'s and with Hirose *et al.*'s modified correlation vs $HTC_{expected}$ for R515B.

The black lines in the figure represent a $\pm 30\%$ error compared to the expected value of heat transfer coefficient. The $\bar{\epsilon}$ is equal to 21.27%, \bar{E} is equal to 27.11% and σ is equal to 34.35% for the Hirose *et al.*'s model, whereas the $\bar{\epsilon}$ is equal to 2.84%, \bar{E} is equal to

16.04% and σ is equals to 21.92% for the Hirose *et al.*'s modified model. As expected, since the R515B is made principally of R1234ze(E), the new correlation fits better the experimental points than the old one, presenting a lower relative and absolute percentage error and a better standard deviation.

7.4.4 Conclusions

Since the Hirose model presented a too big error for the evaluation of the heat transfer coefficient, a modification has been proposed. The new model seems to perform better than the old one, with the maximum error of underestimating the heat transfer coefficient lower than Cavallini *et al.*'s correlation. The model has been validated for different substances which present as components the R1234ze(E), on which the correlation has been calibrated. Further investigations would be necessary to understand the applicability of the modified model on different types of substances. However, in the case the fluid used presents as component the R1234ze(E), the results should be acceptable.

7.5 Webb's model

The last model is a modification of the one presented in §7.2. As stated in the hypothesis for the application of the model, a vapor quality equals to 0.9999 is supposed at the inlet of the condenser to allow the calculation of the properties at the mean vapor quality. Furthermore, the sensible heat transfer from the vapor to the saturated state is neglected. However, the mechanism of condensation from superheated vapor involves both a sensible and latent heat transfer (Paragraph §1.3). According to Webb [4], the total heat flux during condensation from superheated vapor would be expressed as:

$$\alpha(T_{sat} - T_{wall,i}) = \alpha_{TP}(T_{sat} - T_{wall,i}) + \alpha_{SH}(T_{b,r} - T_{sat}), \quad (7.46)$$

where α_{TP} and α_{SH} could be evaluated, for smooth tubes, using respectively Shah's (in Shah [24]) and Dittus and Boelter's correlations (in Dittus and Boelter [25]). As stated in §7.2, neglecting the sensible heat transfer introduces an error in the calculations, since it is a simplification of the real mechanism. In this paragraph, different equations will be

used to predict the heat transfer coefficients. In particular, the Cavallini *et al.*'s model for microfin tubes will be adopted to calculate α_{TP} (Paragraph §7.2) and the Gnielinski's model [5] will be used to evaluate α_{SH} with the attempt to simulate with more details the condensation from superheated vapor.

7.5.1 Gnielinski's model

According to Kondou and Hrnjack [8], the sensible heat transfer can be modelled using the Gnielinski's correlation. First, it is necessary to classify the type of flow inside the tube. The Reynolds number is evaluated:

$$\text{Re}_V = x_{mean} G \frac{ID_{apex}}{\mu_{bulk}}, \quad (7.47)$$

where μ_{bulk} is the dynamic viscosity [$\text{kg m}^{-1} \text{s}^{-1}$] evaluated at the refrigerant bulk temperature T_{bulk} , which is the average between the saturation and the inlet one. All the properties are evaluated using T_{bulk} and the mean pressure P_{mean} .

It is true that the region where the sensible heat transfer appears is very small compared to the tube length. However, for this model, it is supposed that the sensible heat transfer appears for all the length of the tube. Consequently, the mean pressure must be used in REFPROP 10 [12] to calculate the properties of the vapor. This assumption is verified when the outlet vapor quality is higher than 0, which is the case of the experimental points analysed.

7.5.1.1 Turbulent flow

If the Reynolds number Re_V inside the tube is higher than 4000, the flow could be considered turbulent. The friction factor f_{bulk} can be evaluated:

$$f_{bulk} = \left[1.8 \log_{10} \left(G \frac{ID_{apex}}{\mu_{bulk}} \right) - 1.5 \right]^{-2}. \quad (7.48)$$

Nusselt number Nu_{bulk} and the heat transfer coefficient are calculated:

$$Nu_{bulk} = \frac{\left[\left(\frac{f_{bulk}}{8} \right) \left(G \frac{ID_{apex}}{\mu_{bulk}} - 1000 \right) Pr_{bulk} \right]}{\left[1 + 12.7 \left(\frac{f_{bulk}}{8} \right)^{0.5} \left(Pr_{bulk}^{\frac{2}{3}} - 1 \right) \right]} \times \left[1 + \frac{ID_{apex}}{L} \right]^{\frac{2}{3}} K, \quad (7.49)$$

where K is equal to:

$$K = \left(\frac{Pr_{bulk}}{Pr_{wall}} \right)^{0.11}, \quad (7.50)$$

where Pr_{wall} is the Prandtl number evaluated at the mean wall temperature $T_{wall,i}$ and L is the heat transfer tube length. The sensible heat transfer appears just in the inlet section of the tube. However, the experimental section adopted does not allow to divide the tube in more parts. As first approximation, it is possible to consider the sensible heat transfer that appears along all the length of the tube (in the hypothesis the refrigerant core always presents an infinitesimal temperature difference compared to the saturation temperature of the liquid-vapor interface). This hypothesis can be adopted since in the performed experiments the outlet vapor quality was always greater than 0, which means vapor would be always present even at the outlet of the test section.

The heat transfer coefficient is then evaluated as:

$$\alpha_{sensible} = \frac{Nu_{bulk} \lambda_{bulk} Rx}{ID_{apex}}. \quad (7.51)$$

Since the equation was originally developed for smooth tubes, it is required to multiply the Nusselt number for the enhancement geometry factor Rx to quantify the presence of fins. The total heat transfer coefficient (combination of sensible and latent heat) α is evaluated with the equation (7.46).

7.5.1.2 Laminar flow

The laminar flow appears when $Re_V < 2300$. In this case, Nusselt number can be evaluated as follows, in the case the heat flux imposed from the external conditions is constant:

$$Nu_{bulk} = \left[Nu_{m,q,1}^3 + 0.6^3 + (Nu_{m,q,2} - 0.6)^3 + Nu_{m,q,3}^3 \right]^{\frac{1}{3}}, \quad (7.52)$$

where:

$$Nu_{m,q,1} = 4.354, \quad (7.53)$$

$$Nu_{m,q,2} = 1.953 \sqrt[3]{Re_V Pr_{bulk} \left(\frac{ID_{apex}}{L} \right)}, \quad (7.54)$$

$$Nu_{m,q,3} = 0.924 \sqrt[3]{Pr_{bulk}} \sqrt{Re_V \left(\frac{ID_{apex}}{L} \right)}. \quad (7.55)$$

Using (7.51) it is possible to calculate the sensible heat transfer coefficient. The total heat transfer coefficient (combination of sensible and latent heat) α is evaluated with the equation (7.46).

7.5.1.3 Transition region

When $2300 < Re_V < 4000$, the flow is in an intermediary region between the laminar and the turbulent one. Gnielinski in his recent work [5] developed a new correlation for this transition region:

$$Nu_{bulk} = (1 - \gamma)Nu_{2300} + \gamma Nu_{4000}, \quad (7.56)$$

where γ is defined as intermittency factor:

$$\gamma = \frac{Re - 2300}{4000 - 2300}. \quad (7.57)$$

Nu_{4000} is calculated with equation (7.49) for $Re_V=4000$ and Nu_{2300} is calculated with (7.52) for $Re_V=2300$. Using (7.51) it is possible to calculate the sensible heat transfer coefficient. The total heat transfer coefficient (combination of sensible and latent heat) α is evaluated with the equation (7.46).

7.5.2 Implementation and results

The Webb's model is implemented. The code implemented is the B.7 in APPENDIX B. The results are reported in Figure 7.11.

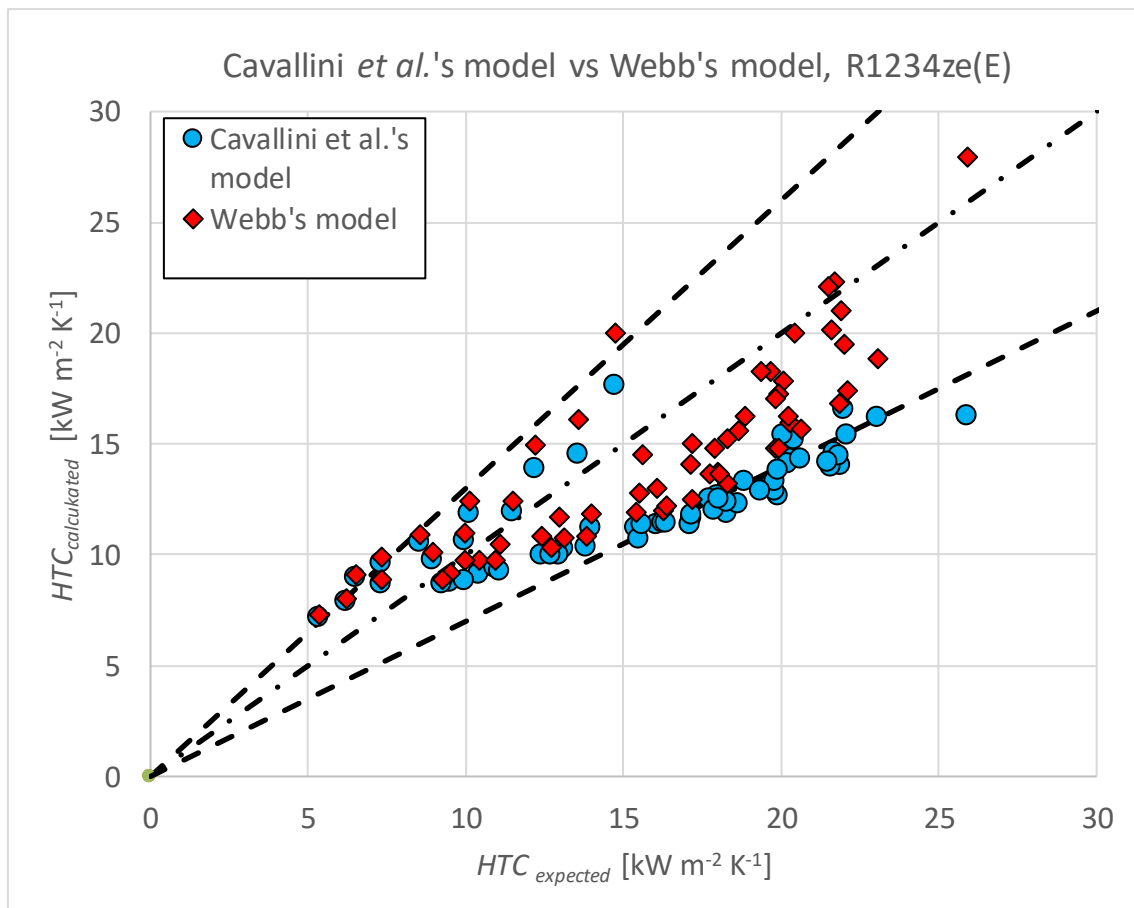


Figure 7.11. $HTC_{calculated}$ with the Cavallini *et al.*'s model and Webb's model vs $HTC_{expected}$ with R1234ze(E).

The black lines in the figure represent a $\pm 30\%$ error compared to the expected value of heat transfer coefficient. The $\bar{\epsilon}$ is equal to -6.19% , \bar{E} is equal to 16.95% and σ is equal to 18.40% . The new model presents a lower error and a lower dispersion compared to the Cavallini *et al.*'s correlation. This is due to the sensible heat transfer term: despite being a smaller part of the heat transfer mechanism (the sensible heat transfer coefficient is one order of magnitude lower than the latent one), the new model which considers both the latent and sensible heat transfer and consequently describes with more precision the overall phenomenon, especially at high mass velocities (where the sensible mechanism can play a more important role), as it is possible to see in Figure 7.12.

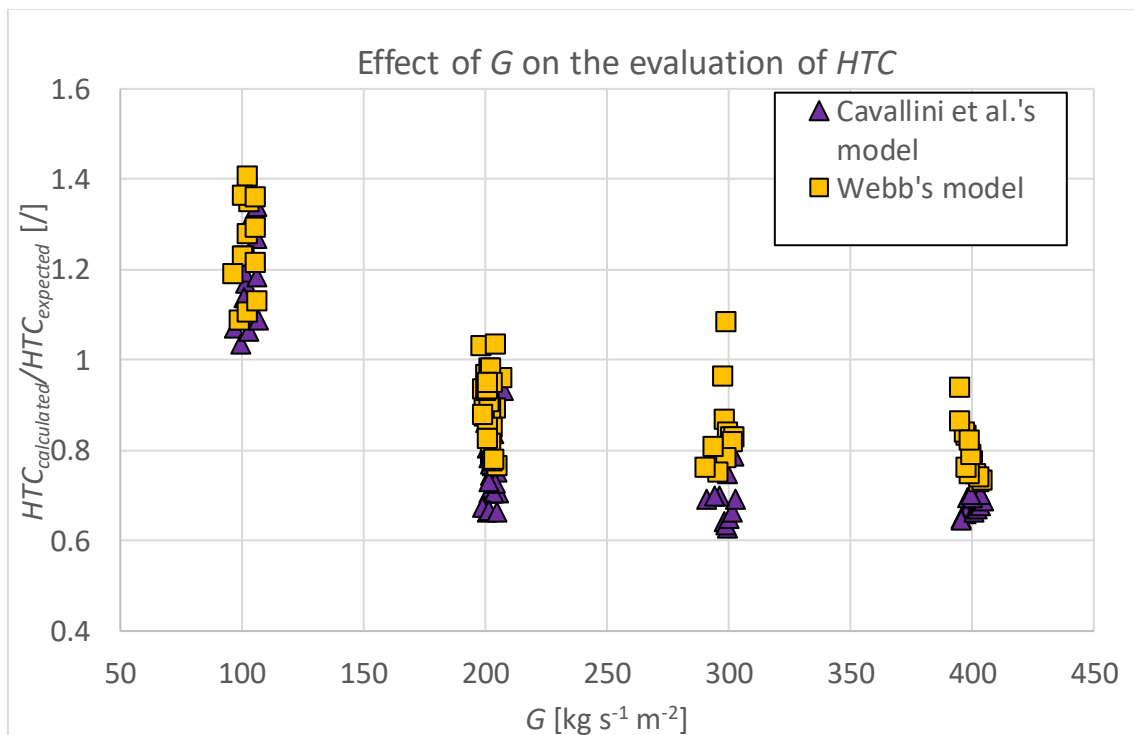


Figure 7.12. Effect of G on the calculation of the heat transfer coefficient for both the correlations.

7.5.3 Conclusions

In this paragraph, the Cavallini *et al.*'s model has been extended in order to simulate even the sensible heat transfer of the vapor phase at the interface between vapor and liquid. The Webb's model presents a lower error and a lower dispersion compared to the Cavallini *et al.*'s model. Despite this, the Cavallini *et al.*'s model gives satisfactory results.

7.6 Comparison between the models

In Table 7.1, the mean relative percentage error (MRPE or $\bar{\epsilon}$), the mean absolute percentage error (MAPE or \bar{E}) and the standard deviation (ST or σ) for all the four models are reported considering just the case with R1234ze(E), since just for this refrigerant the experimental points for condensation from superheated vapor are available.

Model	MRPE %	MAPE %	ST %
Cavallini	-17.93	25.91	20.91
Hirose	50.78	50.78	30.37
Hirose modified	0.91	8.24	10.57
Webb	-6.19	16.95	18.40

Table 7.1. Mean relative percentage error, mean absolute percentage error and standard deviation of the four models for R1234ze(E).

Among the four models, the Hirose *et al.*'s modified one seems to have the best results: this is due to the recalibration done on the experimental points. A further investigation on the applicability of the new correlation should be performed considering other refrigerants which do not contain R1234ze(E) as component. Nevertheless, in the case of R1234ze(E) or mixtures which contain R1234ze(E), the model gives very good results. The Hirose *et al.*'s original model presents the highest relative and absolute error, as well as the highest standard deviation (the trend is exponential at high vapor qualities, as shown in Figure 7.5).

The Cavallini *et al.*'s model gives MRPE and MAPE of around -18% and 26% with ST of 21%. It must be specified that this model was originally developed to study saturated condensation, not condensation from superheated vapor. Furthermore, the model was originally studied with older refrigerants compared to R1234ze(E). Considering these limitations, the model performs quite well.

The Webb's model is a combination of the Cavallini *et al.*'s and Gnielinski's correlations. It presents lower errors and lower standard deviation compared to the Cavallini *et al.*'s model. It is the most complete between the models presented, since it is the only one which includes inside the sensible heat transfer mechanism in condensation from superheated vapor, whereas in the other three models the mechanism is neglected.

Summarizing, apart for the Hirose *et al.*'s original correlation, the studied models give satisfying results in predicting the heat transfer coefficient during condensation from superheated vapor. The Cavallini *et al.*'s, the modified Hirose *et al.*'s and the Webb's models can be all adopted for the design of the condenser. The results obtained are considered satisfying and, in the future, other correlations could be developed or deeply analysed for this phenomenon, based on the research carried out with the present work.

Chapter 8:

Design of the condenser

In this Chapter, a detailed analysis of the condenser design is presented. The idea is to propose a preliminary calculation for the design of an helicoidal condenser with flowing water as coolant. The heat exchanger is equipped with a shell. The present work could be used to build an experimental test section in which the condenser can be tested in different regimes (forced or natural convection of the water inside the tank). For sake of simplicity, a water mass flow rate is imposed inside the tank. In this way, no transient problems will be taken into consideration. The code is suitable to study the applicability of the correlations used in Chapter §7. In particular, the Cavallini *et al.*'s and the Hirose *et al.*'s modified model will be adopted for the design. For sake of simplicity, the Webb's correlation is not implemented (as stated in the previous chapter, the results obtained by Webb's model do not differ dramatically from the ones obtained by Cavallini *et al.*'s correlation).

8.1 Shell and helical condenser

The idea is to design an helicoidal heat pump condenser integrated inside a water tank with a water flow rate. This type of condenser requires a much greater area compared to the plate heat exchanger to exchange a large quantity of heat. It is suitable in the case the heat flow rate is limited (at maximum 1 kW) or in the case a storage is present (like a tank for the domestic hot water generation).

Before sizing the tank, however, the overall heat transfer coefficient of the condenser must be known. This requires preliminary calculations, which is the aim of the present work. After the computational code is written, the condenser can be built and consequently tested in different conditions (forced or natural water convection in the shell side, with or without a water flow rate) to evaluate the real heat transfer coefficient, the real heat flow rate exchanged, and the energy that can be stored inside the tank.

The hypothetical future experimental section on which the prototype of the condenser could be tested is similar to the one reported in Dabas *et al.* [26] represented in Figure 8.1.

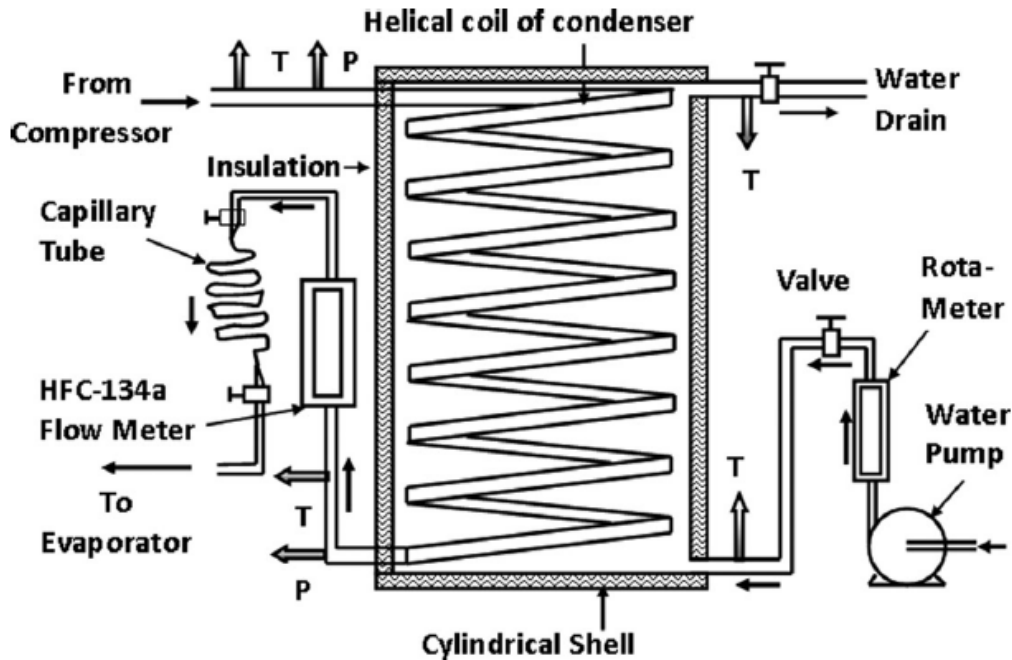


Figure 8.1. Test section for an helicoydal heat pump condenser [26].

In the case of [26], the test section was already built. The aim of the paper was to validate a model for the evaluation of the performance of the shell and helical condenser. To proceed with the calculations, it is necessary to find a suitable correlation for the heat transfer coefficient on the shell (water) side.

Note that in the picture, the test section is in counter flow configuration. On the other hand, the condenser in the present work will be designed in equi-current cross flow configuration. Indeed, the inlet conditions for both fluids will be known and consequently the ϵ -NTU method can be applied.

8.2 The heat transfer coefficient on the water side

In a real tank for domestic hot water generation (DHW), the water in the shell exchanges heat in natural convection, with an increase of the temperature in the time. The problem is in a transitory regime. The design of a heat exchanger in transitory regime is extremely complex, since the water changes temperature in the time (from when is loaded inside the tank to when it reaches the maximum desired temperature) but also in the space, because, when the fluid is heated, a natural convective motion starts in the tank.

Generally, the heat exchanger is chosen as a function of the heat flow rate required in the tank to heat up the water in the desired amount of time (De Carli [27]) and the overall heat transfer coefficient should be already known by the constructor. To simplify the problem, the water is modelled with correlations related to forced convection since a water mass flow rate is supposed to flow inside the tank (looking at the Figure 8.1., a pump for the circulation of the water is represented). In this way, the transitory problem is not considered and it could be analysed once the heat exchanger and the experimental section is built.

8.2.1 *Cross flow around a smooth cylinder*

Normally, when this type of heat exchanger is built, the overall heat transfer coefficient is empirically evaluated, and the geometry is chosen according to the experience of the manufacturer. However, no empirical information are available in the laboratory of the University since the water heat transfer coefficient inside a tank (in natural or forced convection) has never been tested before. Consequently, the correlation for the heat transfer coefficient on water side must be searched in literature.

As previously stated, the water is supposed to be pumped inside the tank in the hypothetical experimental test section. This means that the heat transfer mechanism is forced convection, despite having the fluid is moving very slowly inside the shell.

The correlation adopted for the design can be found in Incompera & Dewitt [28], in Chapter §7: External flow. In the book, a correlation for an external cross flow around an isothermal cylinder is given. The flow can be schematized as shown in Figure 8.2.

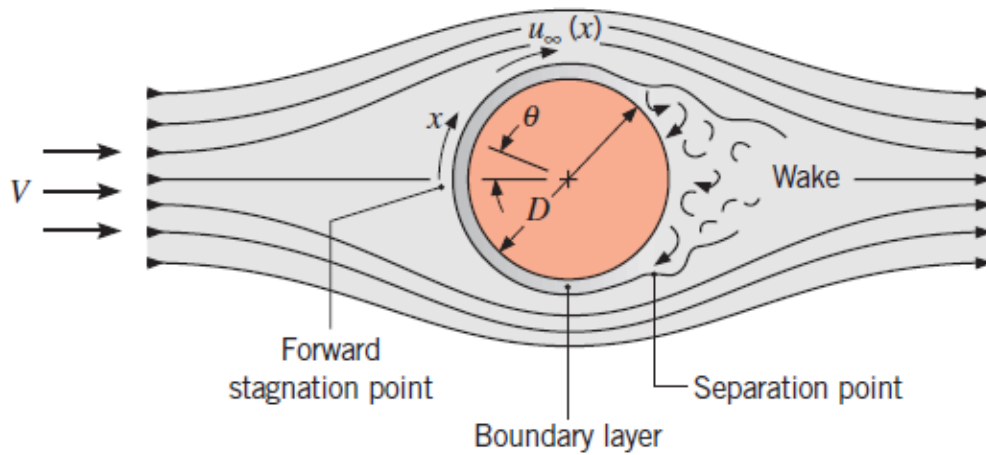


Figure 8.2. Cross water flow outside a cylinder [28].

If the water is supposed to enter from the bottom of the tank, the heat exchanger coils can be visualized as cylinders in cross flow. Three important simplifications must be adopted:

1. The tube in an helicoidal heat exchanger is not straight but it is wrapped to form a coil and this could affect the heat transfer mechanism;
2. The coils which follow the first one will encounter a disturbed flow and, consequently, the heat transfer coefficient may be different compared to the one estimated for the first one;
3. the coils will be disposed vertically. In this correlation, the effect of the gravity force is neglected, as well as the convective effect induced by the temperature difference of the fluid.

According to Incompera & Dewitt [28], it is possible to define the Reynolds number of the water as:

$$Re_{water} = \frac{v_{water} OD \rho_{water}}{\mu_{water}}, \quad (8.1)$$

where v_{water} is the water velocity [$m\ s^{-1}$], OD is the outer diameter of the tube [m], ρ_{water} is the water density [$kg\ m^{-3}$] and μ_{water} is the water viscosity [$kg\ m^{-1}\ s^{-1}$]. All the

properties of the water should be evaluated at the film temperature, calculated as the average between the mean water temperature and the temperature of the wall.

The equation used for the calculation of the Nusselt number on water side is:

$$Nu_{water} = CRe_{water}^m Pr_{water}^{\frac{1}{3}}, \quad (8.2)$$

where Pr_{water} is the Prandtl number, C and m are two constants which depend on the values of Re_{water} . The velocity of the water inside the shell is expected to be very small since the tank would have a diameter of at least 30 cm. Consequently C and m are respectfully assumed equals to 0.989 and to 0.33 [28].

This equation should be applied in case the surface is isothermal. However, since the refrigerant inside the tube is condensing, the external surface temperature is not expected to change dramatically. Though, the hypothesis is acceptable.

According to Incompera & Dewitt [28], if the Reynolds number of the water (equation (8.1)) is lower than 2, the flow can be assumed laminar and the effect of wake separation can be considered negligible. This means that the simplification 2 is acceptable if the velocity of the water is low enough. In Figure 8.3, the drag coefficient C_D is shown as function of Reynolds number. When the velocity is small (Reynolds number is lower than 2), the drag coefficient is very high: this leads to negligible separation effects and laminar flow around the tubes.

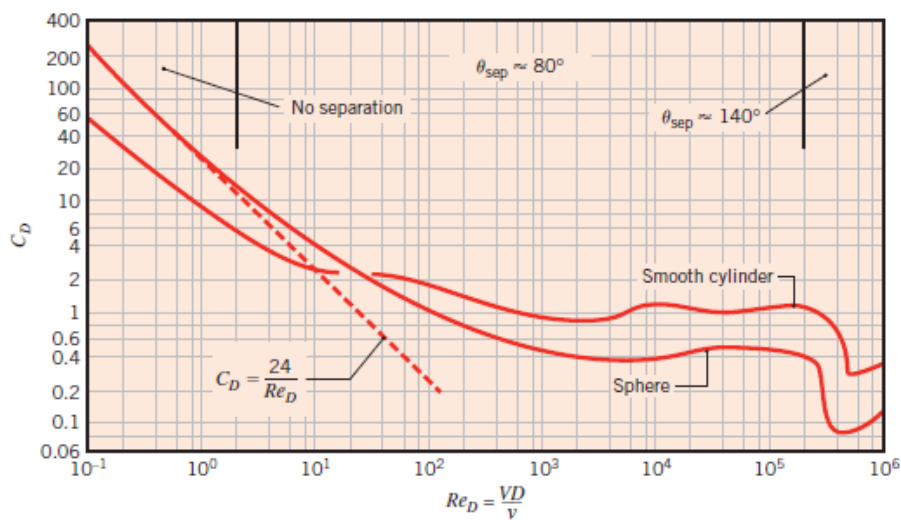


Figure 8.3. Drag coefficient C_D as a function of Re_D (Re_{water} in the previous equations) [28].

For the other two hypotheses, however, no possibility of verification is available since the experimental section has not been built yet. Consequently, the two hypotheses must be assumed as true in order to apply the correlation (8.2).

8.2.2 Other correlations for the evaluation of the heat transfer coefficient on water side

The water is supposed to flow in the experimental section thanks to a pump. However, due to the dimensions of the tank, the velocity inside the shell is expected to be very small. For sake of simplicity, the flow is still modelled as in forced convection. Note that, in the calculations that follow, the range of application of the equation (8.2) is verified and, consequently the flow can be still modelled as if it is in forced convection.

In literature, others correlation have been found for the calculation of the heat transfer coefficient on the water side. For instance, Ali [29] formulated two different empirical correlations for the evaluation of the heat transfer coefficient on water side in natural convection. However, these correlations are applicable just in specific ranges of the Rayleigh number and just for specific geometry of the heat exchanger. Since the calculations are a first attempt, it seemed to the author the best choice to select a correlation which is applicable in a wide range of conditions. The equation (8.2) presents all the required characteristics. For further investigations of the topic, other correlations could be implemented to study the difference on the geometry design, or they can be empirically tested once the experimental section is ready to operate.

8.3 Geometry of the condenser

Once the correlation for the calculation of the heat transfer coefficient on water side is chosen, it is required to select a starting geometry for the helicoidal heat exchanger. In Figure 8.4, the most important dimensions of the heat exchanger are reported.

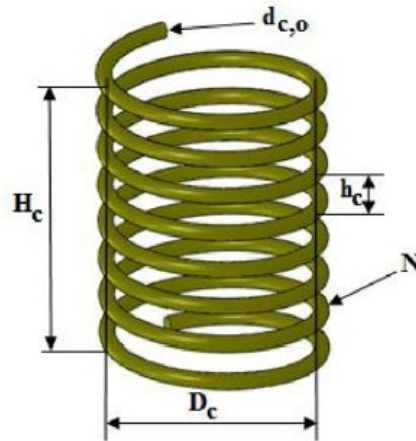


Figure 8.4. Helical coil heat exchanger dimensions [30].

Looking at the picture, the different parameters can be highlighted:

- Number of coils N ;
- Outer diameter of the tube $d_{c,o}$, which corresponds to OD [m];
- Diameter of the coil D_c [m];
- Height of the heat exchanger H_c ⁵ [m];
- Coil pitch h_c , which from now on is referred as p [m].

8.3.1 Tube selection

Two different kinds of tubes are chosen for this design. The first one is the same microfin tube used during the experiments ($OD=5$ mm) and described in Table §3.1. The second is the tube used in Diani *et al.* [9]. The geometrical characteristics of the tube are reported in Table 8.1.

⁵ the height of the heat exchanger, as well as the total length, is an output of the program

OD	ID_{apex}	ID_{base}	n	β	h	Rx
mm	mm	mm	/	°	mm	/
7	6.14	6.5	50	18	0.18	1.63

Table 8.1. Geometrical parameters of the tube. From left: Outer diameter, Inner diameter at the apex of the fin (D in Figure 2.9), Inner diameter at the base of the fins, number of fins, elix anglol, high of the fin (e in Figure 2.9), enhancement factor with respect to the base of the fins.

The tubes are made of copper, which presents a thermal conductivity of $390 \text{ W m}^{-1} \text{ K}^{-1}$. The aim of choosing two tubes is to compare the different design and performance of the two heat exchangers to evaluate which one could be the best for the experimental apparatus.

8.3.2 Geometrical parameters

The diameter of the coil D_c on the horizontal direction is chosen equal to 20 cm. The reason of this choice is to obtain a compact heat exchanger: since this condenser would be used inside an experimental test section, it would be in the best interest to have a compact design in order to occupy as less space as possible. The tank diameter is also chosen equals to 30 cm for the same reason.

The coil pitch p is chosen equals to $1.5 OD$. The length of each coil is evaluated with the following geometrical equation:

$$dL = \sqrt{D_c^2 + p^2}, \quad (8.3)$$

and results equal to 0.63 m. The inner and outer heat transfer area are calculated for each coil as:

$$A_i = \pi \cdot ID \cdot dL, \quad (8.4)$$

$$A_e = \pi \cdot OD \cdot dL, \quad (8.5)$$

where ID could be the inner diameter at the apex or at the base of the fins depending on the model used for the calculations of the heat transfer coefficient on the refrigerant side.

The geometrical characteristics of each coil are reported in Table 8.2.

<i>Tube</i>	p	D_c	D_{tank}	dL	A_e	$A_{i,apex}$	$A_{i,base}$
	m	m	m	m	m ²	m ²	m ²
<i>OD 5 mm</i>	7.50E-03	0.2	0.3	0.63	9.87E-03	8.45E-03	9.04E-03
<i>OD 7 mm</i>	1.05E-02	0.2	0.3	0.63	1.38E-02	1.21E-02	1.28E-02

Table 8.2. Geometrical parameters of the coil.

8.4 Design parameters and preliminary calculations

A maximum heat flow rate Q of 1 kW is supposed to be supplied to the water from the condenser. The condenser will provide a complete condensation of the refrigerant without subcooling. The heat exchanger is schematized according to §8.1.1, in cross flow configuration: the water enters from the lower part of the tank (see Figure 8.1), it is heated and rises up by means of the pump. At the same time, the condensing fluid enters from the bottom of the helical condenser as superheated vapor and progressively condenses. In this way, the inlet conditions for each coil are known and the calculations are expected to be simplified. The water is supposed to be heated from the aqueduct temperature (10 °C) up to 40 °C.

8.4.1 Preliminary calculations on the refrigerant side

At the exit of the compressor, the refrigerant is supposed to be superheated with a superheating degree equal to 15 K. The saturation temperature is supposed equal to 50 °C. With REPFROP 10 [11], the inlet pressure of the refrigerant $P_{ref,IN}$ is evaluated using the T_{sat} . With the software, the inlet specific enthalpy $h_{ref,IN}$ of the fluid is calculated with the $T_{ref,IN} = 65$ °C and the $P_{ref,IN}$. The outlet specific enthalpy $h_{ref,OUT}$ is computed using T_{sat} and an output vapor quality equal to 0, since no subcooling is supposed to appear inside the condenser. The refrigerant mass flow rate [kg s⁻¹] is evaluated:

$$\dot{m}_{ref} = \frac{Q}{h_{ref,IN} - h_{ref,OUT}}, \quad (8.6)$$

and the specific mass velocity can be calculated [$\text{kg s}^{-1} \text{ m}^{-2}$]:

$$G_{ref} = \frac{4 \dot{m}_{ref}}{\pi ID_{apex}^2}, \quad (8.7)$$

$$G_{ref,max} = \frac{4 \dot{m}_{ref}}{\pi ID_{base}^2}. \quad (8.8)$$

Depending on the model chosen for the calculation of the heat transfer coefficient on the refrigerant side, the specific mass flow rate can be evaluated with (8.7) or with (8.8). In particular, the first equation is adopted when the Cavallini *et al.*'s model is used, whereas the second one is adopted when the Hirose *et al.*'s modified model is implemented in the code.

8.4.2 Preliminary calculations on water side

To calculate the heat transfer coefficient on water side, the water mass flow rate is required. Assuming a constant specific heat capacity of the water, the mass flow rate is calculated:

$$\dot{m}_{H_2O} = \frac{Q}{c_{H_2O} (T_{H_2O,OUT} - T_{H_2O,IN})}. \quad (8.9)$$

8.5 Pressure drops models

Before introducing the functioning of the code, it is necessary to describe which models are implemented for the total pressures drops on the refrigerant side. To simplify the model, the pressure drops on the shell side are not computed. Indeed, the properties of the water are not heavily modified by the changing of the pressure. For these simulations, the pressure on the shell side is assumed equal to the atmospheric one.

8.5.1. Total pressure drops

The total pressure drops inside the tube are given by three different components:

$$\Delta P_{tot} = \Delta P_{friction} + \Delta P_{momentum} + \Delta P_{gravity}, \quad (8.10)$$

where:

- $\Delta P_{friction}$ are the pressure drops due to friction;
- $\Delta P_{momentum}$ are the pressure drops due the momentum variation between the inlet and the outlet of each coil;
- $\Delta P_{gravity}$ are the pressure drops due to the gravitational force (since the helicoidal heat exchanger will be disposed vertically inside the tank).

8.5.2 Frictional pressure gradients

The frictional pressure gradients $\Delta P_{friction}$ are calculated differently depending on the model on which they are applied.

8.5.2.1 The Diani *et al.*'s model

Diani *et al.* [6] investigated the flow boiling of R1234ze(E) inside a microfin tube. In the same article, they proposed a new model for the calculation of the frictional pressure gradients inside a microfin tube. The pressure drops can be calculated as:

$$\left(\frac{dp}{dz}\right)_f = \Phi_{LO}^2 2 \frac{f_{LO} G^2}{ID_{apex} \rho_L}, \quad (8.11)$$

where Φ_{LO} is the two-phase liquid only multiplier, calculated as:

$$\Phi_{LO}^2 = Z + 3.595 \cdot F \cdot H \cdot (1 - E)^W, \quad (8.12)$$

$$Z = (1 - x_{mean})^2 + x_{mean}^2 \frac{\rho_L}{\rho_V} \left(\frac{\mu_V}{\mu_L}\right)^{0.2}, \quad (8.13)$$

$$\begin{cases} 1 - E = -0.33 \ln \left[\frac{x_{mean} \mu_L G}{\rho_V \sigma} \right] - 0.0919, \\ E = 0.95 \text{ if } E > 0.95, \\ E = 0 \text{ if } E < 0, \end{cases} \quad (8.14)$$

$$W = 1.398 \cdot p_{red}, \quad (8.15)$$

$$F = x_{mean}^{0.9525} (1 - x_{mean})^{0.414}, \quad (8.16)$$

$$H = \left(\frac{\rho_L}{\rho_V} \right)^{1.132} \left(\frac{\mu_V}{\mu_L} \right)^{0.44} \left(1 - \frac{\mu_V}{\mu_L} \right)^{3.542}, \quad (8.17)$$

where x_{mean} is the mean vapor quality, σ is the surface tension [N m^{-1}], μ and ρ are the dynamic viscosity [Pa s] and the density [kg m^{-3}] of the liquid or vapor phase depending on the subscript. The reduced pressure p_{red} is calculated as:

$$p_{red} = \frac{P_{ref}}{P_{cr}}, \quad (8.18)$$

where P_{cr} is the refrigerant critical pressure. The relative roughness is calculated as proposed by Cavallini *et al.* [31]:

$$\frac{e}{D} = \frac{0.18 + \left(\frac{h}{ID_{apex}} \right)}{0.1 + \cos \beta}, \quad (8.19)$$

and the friction factor f_{LO} can be calculated from the Moody diagram using the equivalent roughness calculated in (8.19).

This model, as Cavallini *et al.*'s, was developed to predict the friction pressure losses considering a saturated condition: the inlet vapor quality must be calculated to find x_{mean} . Consequently, the same approach proposed in the subparagraph §7.2.2 is adopted: if the vapor is superheated a fictitious inlet quality of 0.99 is assumed [8]. In this way, the calculations are possible at the mean vapor quality.

8.5.2.2 The Hirose *et al.*'s model

In the Hirose *et al.*'s model presented in §7.3, the pressure drop multiplier and the friction factor are already calculated as:

$$f_{VO} = 0.26 \text{Re}_V^{-0.38} \eta^{0.95} \cos(\beta)^{-2.8}, \quad (8.20)$$

$$\Phi_{VO} = 1 + 1.55 X_{tt}^{0.4}. \quad (8.21)$$

The friction pressure drops if only vapor flows in the tube can be calculated as:

$$\left(\frac{dp}{dz}\right)_{f,VO} = 2x_{mean}^2 \frac{f_{VO} G_{max}^2}{ID_{base} \rho_V}. \quad (8.22)$$

The frictional pressure drops are then calculated:

$$\left(\frac{dp}{dz}\right)_f = \Phi_{VO}^2 \left(\frac{dp}{dz}\right)_{f,VO}. \quad (8.23)$$

8.5.3 The momentum pressure gradients

The momentum pressure drops can be considered negligible in the case of single-phase flow, where no phase change is involved. However, during condensation, the fluid is progressively decelerated since the vapor is converted into liquid. As consequence, a gain in pressure is expected.

The momentum pressure gradients are calculated as:

$$\Delta P_{momentum} = \Delta P_{momentum,OUT} - \Delta P_{momentum,IN}, \quad (8.24)$$

where $\Delta P_{momentum,OUT}$ and $\Delta P_{momentum,IN}$ are calculated at the inlet and at the outlet of each coil and they are equals to:

$$\Delta P_{momentum,OUT} = G^2 \left(\frac{x_{OUT}^2}{\xi_{OUT} \rho_V} + \frac{(1 - x_{OUT})^2}{(1 - \xi_{OUT}) \rho_L} \right) \quad (8.25)$$

$$\Delta P_{momentum,IN} = G^2 \left(\frac{x_{IN}^2}{\xi_{IN} \rho_V} + \frac{(1 - x_{IN})^2}{(1 - \xi_{IN}) \rho_L} \right) \quad (8.26)$$

where ξ is the void fraction at the inlet and at the outlet of the coil. It can be calculated with the following equations presented by Hirose *et al.* [3]:

$$\xi = 0.81 \xi_{Smith} + 0.19 x^{100} \left(\frac{\rho_V}{\rho_L} \right)^{0.8} \xi_{homo}, \quad (8.27)$$

$$\xi_{homo} = \left[1 + \left(\frac{\rho_V}{\rho_L} \right) \left(\frac{1 - x}{x} \right) \right]^{-1} \quad (8.28)$$

$$\xi_{Smith} = \left[1 + \left(\frac{\rho_V}{\rho_L} \right) \left(\frac{1 - x}{x} \right) \left(0.4 + 0.6 \frac{\sqrt{\frac{\rho_V}{\rho_L} + 0.4 \left(\frac{1 - x}{x} \right)}}{\sqrt{1 + 0.4 \left(\frac{1 - x}{x} \right)}} \right) \right]^{-1}. \quad (8.29)$$

where all the properties in the equation can be referred to the inlet or the outlet of the tube.

8.5.4. Gravity pressure gradients

Since the helical coil condenser will be disposed vertically within the tank, the gravity pressure drops must be taken into consideration. Considering the void fraction ξ calculated at the mean vapor quality x_{mean} between the inlet and the outlet of each coil (equation (8.27)), it is possible to write:

$$\Delta P_{gravity} = g [\xi \rho_V + (1 - \xi) \rho_L] dL \sin \theta = g [\xi \rho_V + (1 - \xi) \rho_L] p, \quad (8.30)$$

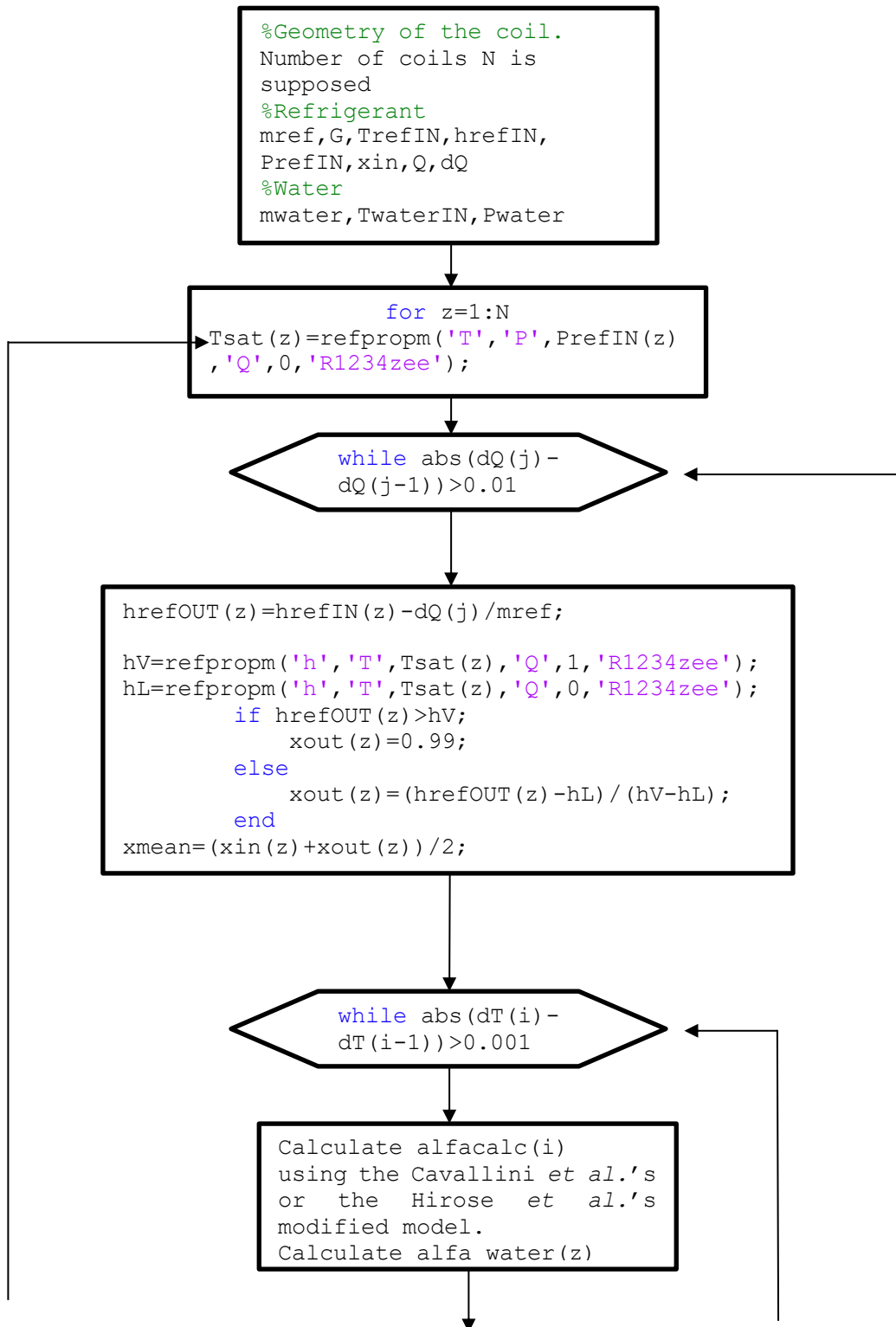
where θ is the angle of inclination of each coil compared to the horizontal direction.

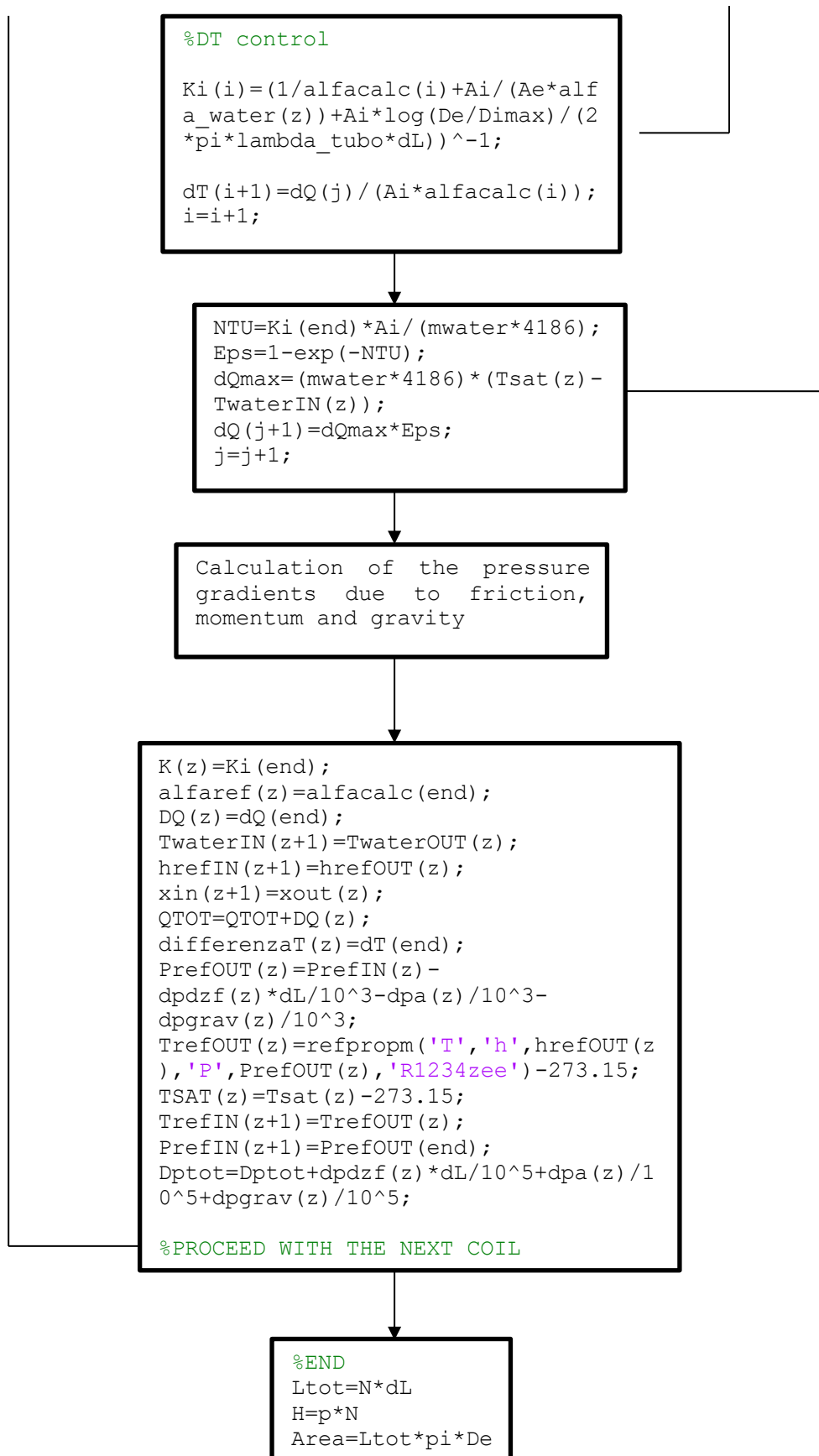
8.6 Refrigerant heat transfer coefficient

Among the four models presented in the previous paragraph, for the simulations, it is decided to study the applicability of two of them: the Cavallini *et al.*'s and the Hirose *et al.*'s modified correlations. As demonstrated in §7.3, the original Hirose *et al.*'s model does not fit well the experimental points. Consequently, the modified one is chosen for the calculations. The Webb's model is probably the more complete among the 4 presented but it is also the more complex to apply since it requires to simulate even the sensible heat transfer coefficient. To avoid overcomplicating the code, the Cavallini *et al.*'s model is chosen for the simulations instead of Webb's model, since the results showed in Table 7.1 are similar between the two correlations. The fluid used in the models is the R1234ze(E).

8.7 The program

Figure 8.5. Diagram of flux of the program.





In Figure 8.5 the diagram of flux of the program is presented. In APPENDIX B, the CODE B.8 is the condenser design with Cavallini *et al.*'s model and *OD* 7 mm. Instead, the CODE B.9 is the condenser design with Hirose *et al.*'s modified model and *OD* 7 mm. The codes with *OD* 5 mm are not reported since they are similar to the previous ones with just the geometrical parameters modified.

8.7.1 *Input of the program*

Together with the geometry of each coil, the number of coils *N* is an input of the program: depending on the values of the temperature of the water at the output, the outlet vapor quality, the pressure drops and the heat exchanged, the number of coils can be increased or decreased to obtain the desired performance. For instance, if the condenser exchanges a too low heat flow rate, *N* can be increased in the following simulation. Some preliminary calculations are required before using the code to estimate *N*. The preliminary calculations are not reported. They are performed considering an isobaric condensation process.

Before proceeding with the program, the inlet refrigerant conditions, as well as the inlet water conditions must be known (paragraph §8.3).

8.7.2 *Structure of the program*

The code is organized in three different loops:

- the first loop is a *for* cycle, which indicates the coil at which the calculations are performed;
- the second loop is a *while* condition for the calculation of the actual heat transferred in the coil
- the third and inner loop is a *while* condition for the calculation of the actual heat transfer coefficients.

8.7.2.1. Calculation coil per coil

The first cycle counts the number of coils of the heat exchanger on which the calculations are performed with a counter index z which evolves from 1 up to N . Knowing $P_{ref,IN}$, the saturation temperature T_{sat} can be calculated with REFPROP 10 [11].

8.7.2.2. Heat transferred per coil supposed

At the beginning of each outer *while* loop, the heat transferred in each coil is supposed to be equal to:

$$dQ(j) = \frac{Q}{N}, \quad (8.31)$$

where j is a second index counter which accounts the number of iterations required to evaluate the real heat transfer per coil. Known $dQ(j)[W]$, the code evaluate the outlet specific enthalpy of the refrigerant:

$$h_{ref,OUT}(z) = h_{ref,IN}(z) - \frac{dQ(j)}{\dot{m}_{ref}}. \quad (8.32)$$

Knowing $P_{ref,IN}$, the saturation specific enthalpy of the vapor h_V and of the liquid h_L can be calculated with REFPROP 10. An *if* condition is introduced:

$$\begin{cases} \text{if } h_{ref,OUT}(z) > h_V \rightarrow x_{OUT}(z) = 0.99, \\ \text{if } h_{ref,OUT}(z) \leq h_V \rightarrow x_{OUT}(z) = \frac{h_{ref,OUT}(z) - h_L}{h_V - h_L}. \end{cases} \quad (8.33)$$

This condition is necessary whenever the vapor enters superheated inside the tube. Otherwise, it would be impossible to calculate the outlet vapor quality. Consequently, if

the specific enthalpy of the vapor is lower than the refrigerant outlet one, the outlet vapor quality is supposed equals to 0.99 until saturated condensation appears⁶.

8.7.2.3. Heat transfer coefficients

To calculate the heat transfer coefficients, it is necessary to postulate that the condensation begins immediately at the inlet of the coil. It is initially supposed a temperature difference $dT(i)$ between the saturation and the inner wall temperature. The i index is the counter for the inner *while* cycle on which $dT(i)$ is calculated. Starting from this $dT(i)$, it is possible to calculate $\alpha_{ref}(i)$ depending on the model adopted in the code. The properties of the refrigerant are calculated using the $P_{ref,IN}$.

Knowing $dT(i)$, the inner wall temperature $T_{wall,IN}(z)$ and the external wall temperature $T_{wall,OUT}$ are calculated:

$$T_{wall,IN}(z) = T_{sat}(z) - dT(i), \quad (8.34)$$

$$T_{wall,OUT}(z) = T_{wall,IN}(z) - dQ(j) \frac{\ln\left(\frac{OD}{ID}\right)}{2\pi dL \lambda_{copper}}. \quad (8.35)$$

Once the external wall temperature is known, the water film temperature T_{film} is computed:

$$T_{H_2O,OUT}(z) = \frac{dQ(j)}{\dot{m}_{H_2O} 4186} + T_{H_2O,IN}(z), \quad (8.36)$$

$$T_{H_2O,mean} = \frac{T_{H_2O,OUT}(z) + T_{H_2O,IN}(z)}{2}, \quad (8.37)$$

$$T_{film} = \frac{T_{H_2O,mean} + T_{wall,OUT}(z)}{2}. \quad (8.38)$$

⁶ Note that $x_{OUT}(j) = 0.99$ and not to 0.9999. This is due to the Hirose *et al.*'s modified model, which at high vapor quality, tends to dramatically overestimate the heat transfer coefficient, even if the correlation has been recalibrated.

Using equation (8.2), the heat transfer coefficient on water side $\alpha_{water}(z)$ is calculated. A verification of the initial hypothesis is carried out: knowing $\alpha_{water}(z)$, the internal wall temperature is recalculated to verify if it is lower than the saturation temperature. The overall heat transfer coefficient is calculated as:

$$K_i(i) = \left[\frac{1}{\alpha_{ref}(i)} + \frac{A_i}{A_e \alpha_{water}(z)} + \frac{A_i \ln\left(\frac{OD}{ID}\right)}{2\pi dL \lambda_{copper}} \right]^{-1}, \quad (8.39)$$

The $dT(i+1)$ is recalculated:

$$dT(i+1) = \frac{dQ(j)}{A_i \alpha_{ref}(i)}, \quad (8.40)$$

At the end of the loop, the counter i is increased by one. The inner *while* cycle in the next iteration verifies if:

$$dT(i) - dT(i-1) > 0.001. \quad (8.41)$$

If this condition is verified, the loop continues until convergence. If the condition is not verified, the program proceeds with the calculations.

8.7.2.4. Calculation of the real heat transferred

The approach for the evaluation of the real heat transferred is called ϵ -NTU method and can be found in Bonacina *et al.* [32]. Since the loop on the $dT(i)$ converges, the global heat transfer coefficient $K_i(i)$ is known from equation (8.39), the number of transport units NTU can be calculated:

$$NTU = \frac{K_i(i)A_i}{\dot{m}_{H_2O} c_{H_2O}}. \quad (8.42)$$

The maximum heat transfer rate dQ_{max} and the efficiency of the coil ε are calculated:

$$dQ_{max} = \dot{C}_{min} [T_{sat}(z) - T_{H_2O,IN}(z)] = \dot{m}_{H_2O} c_{H_2O} [T_{sat}(z) - T_{H_2O,IN}(z)], \quad (8.43)$$

$$\varepsilon = 1 - e^{-NTU}. \quad (8.44)$$

The actual heat transferred for each coil is calculated:

$$dQ(j+1) = \varepsilon \cdot dQ_{max}. \quad (8.45)$$

At the end of the loop, the counter j is increased by one. The outer *while* cycle in the next iteration verifies if:

$$dQ(j) - dQ(j-1) > 0.01. \quad (8.46)$$

If this condition is verified, the loop continues until convergence. If the condition is not verified, the program proceeds with the calculations.

8.7.2.5 Pressure drops calculation

The pressure drops are calculated as described §8.5. The pressure at the outlet of the coil is equal to:

$$P_{ref,OUT}(z) = P_{ref,IN}(z) - \Delta P. \quad (8.47)$$

8.7.2.6 Subsequent coil

Knowing $P_{ref,OUT}(z)$ and $h_{ref,OUT}(z)$, the outlet refrigerant temperature $T_{ref,OUT}(z)$ can be calculated. Since the two internal loops reached the convergency, the code, by mean of the *for* cycle, can proceed to the following coil, imposing:

$$T_{ref,IN}(z + 1) = T_{ref,OUT}(z), \quad (8.48)$$

$$h_{ref,IN}(z + 1) = h_{ref,OUT}(z), \quad (8.49)$$

$$x_{IN}(z + 1) = x_{OUT}(z), \quad (8.50)$$

$$P_{ref,IN}(z + 1) = P_{ref,OUT}(z), \quad (8.51)$$

$$T_{H_2O,IN}(z + 1) = T_{H_2O,OUT}(z). \quad (8.52)$$

The calculations proceeds until $z = N$. If the number of coils is too big and the liquid exits subcooled, the code returns an error since is not capable to calculate the outlet vapor quality.

Once the simulation stops, the code will return the total length of the heat exchanger L_{tot} , [m], the height H [m], the external heat transfer area A_{tot} [m²]:

$$L_{tot} = N \cdot dL, \quad (8.53)$$

$$H = N \cdot p, \quad (8.54)$$

$$A_{tot} = \pi \cdot OD \cdot L_{tot}. \quad (8.55)$$

The other outputs of the codes are the actual heat transferred Q_{tot} [W] and the total pressure drop ΔP_{tot} [bar].

8.8 Results

8.8.1 Cavallini et al.'s model with OD 5 mm tube

The refrigerant temperature and the water temperature as function of the length of the heat exchanger are reported in Figure 8.6.

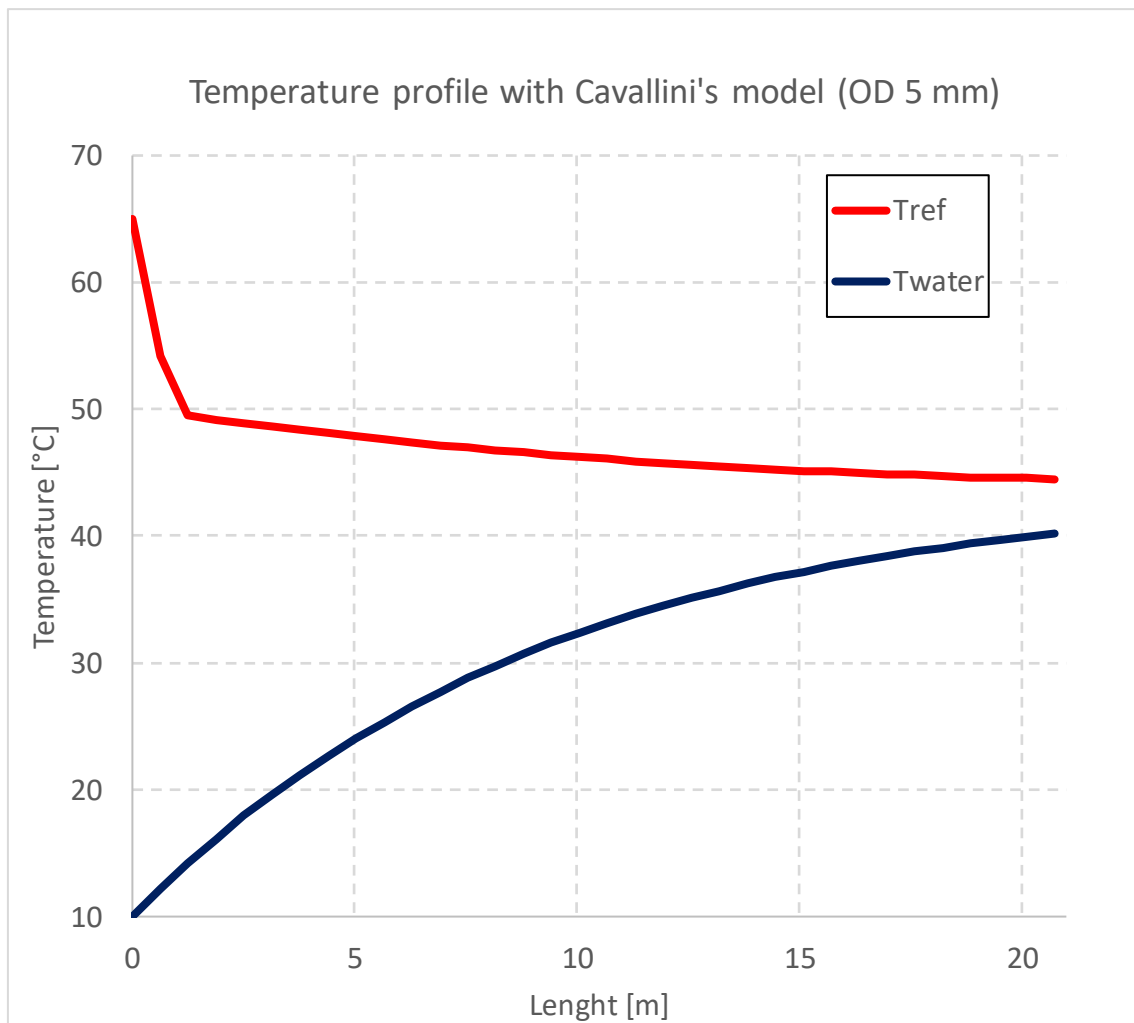


Figure 8.6. Temperature profiles with Cavallini et al.'s model and OD= 5 mm.

The heat exchanger total length is 20.74 m, with a height of 25 cm. In this configuration, 33 coils are necessary to exchange a total amount of heat of 1007 W (for the results, please refer to Table 8.3).

The pressure drops in this configuration play a decisive role. The T_{sat} is computed at the beginning of each coil as function of the $P_{ref,IN}$. If the pressure drops are large, the saturation temperature decreases because the inlet pressure on the refrigerant side

decreases. As consequence, the maximum heat which can be exchanged per coil (equation (8.43)) progressively decreases. Subsequently, a large number of coils are required in order to reach 1 kW of heat exchanged. The total ΔP_{tot} for this configuration is around 1.3 bar, which is too high for this type of condenser, leading to a temperature drop of around 5°C between the beginning and the end of the saturated condensation process. The large pressure drops are related to the tube chosen: with this tube, the mass velocity G is around $430 \text{ kg m}^{-2}\text{s}^{-1}$. The frictional pressure gradients are a function of the mass velocity. A solution for decreasing the pressure drops is choosing a tube with a larger inner diameter, in order to obtain a lower G . Indeed, the results of the simulation with the Cavallini's *et al.* model with the OD 7 mm tube are presented in §8.7.3.

8.8.2 Hirose et al.'s modified model with OD 5 mm tube

The refrigerant temperature and the water temperature as function of the length of the heat exchanger are reported in Figure 8.7.

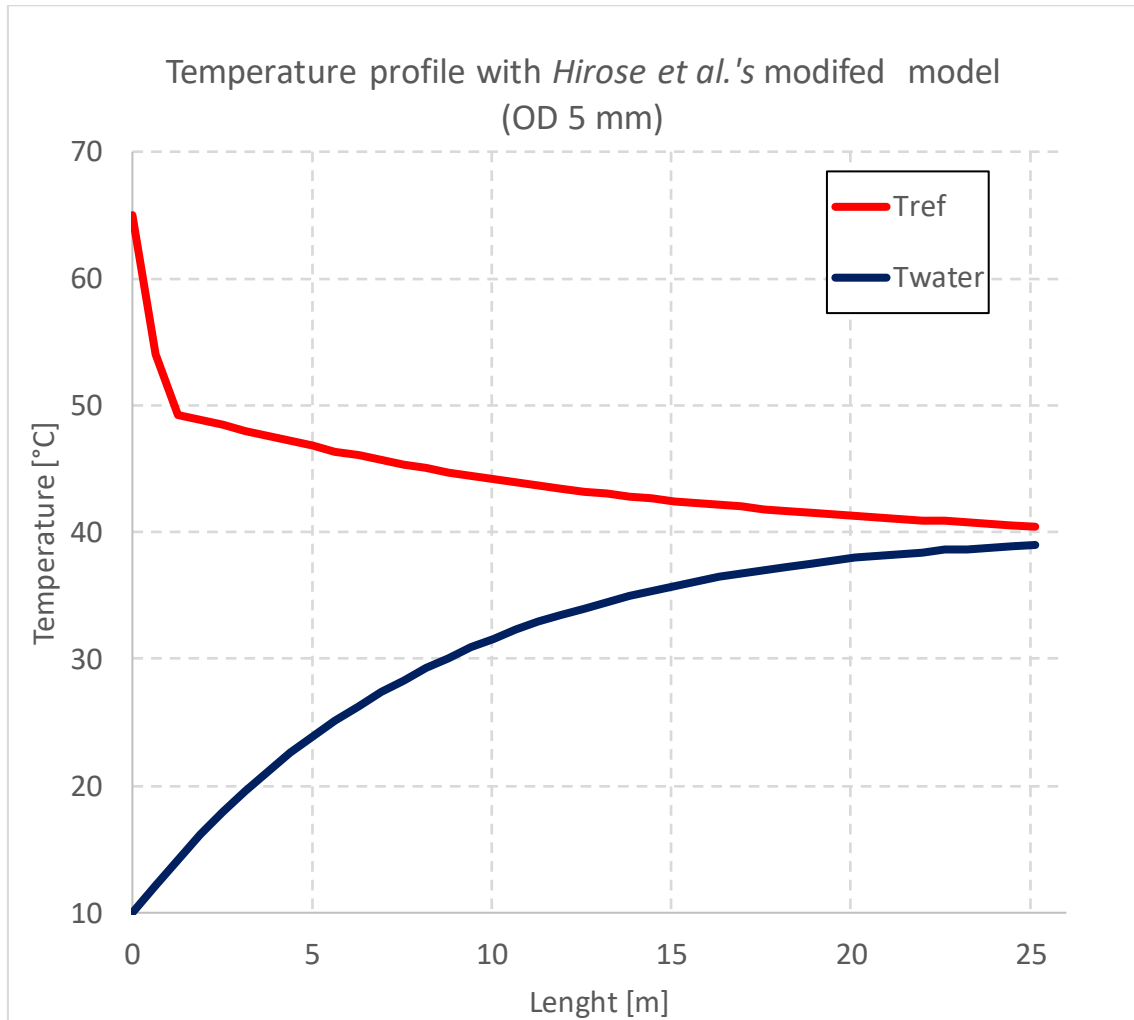


Figure 8.7. Temperature profiles with the Hirose et al.'s modified model (OD 5 mm).

The heat exchanger total length is 25.13 m, with a height of 30 cm. In this configuration, 40 coils are not sufficient to reach 1 kW. Indeed, 966 W are exchanged with the water, that exits from the tank with a temperature of 39°C (for the results please refer to Table 8.3).

The pressure drops calculated with this model are even higher than the ones predicted with the Diani et al.'s model in the previous code. The pressure gradients are so large that the saturation temperature drops of roughly 9.5 °C from the beginning of the

saturated condensation. The total pressure drops is around 2 bar, which is unacceptable. Even in this case, a substitution with the *OD* 7 mm tube is recommended. Both the models with *OD* 5 mm are simply used as demonstration of the importance of the pressure drops whenever a long tube is used for the design of a heat exchanger. If the experimental test section will be built and assembled, the *OD* 7 mm microfin tube will be probably adopted.

8.8.3 Cavallini *et al.*'s model with *OD* 7 mm tube

The refrigerant temperature and the water temperature as function of the length of the heat exchanger are reported in Figure 8.8.

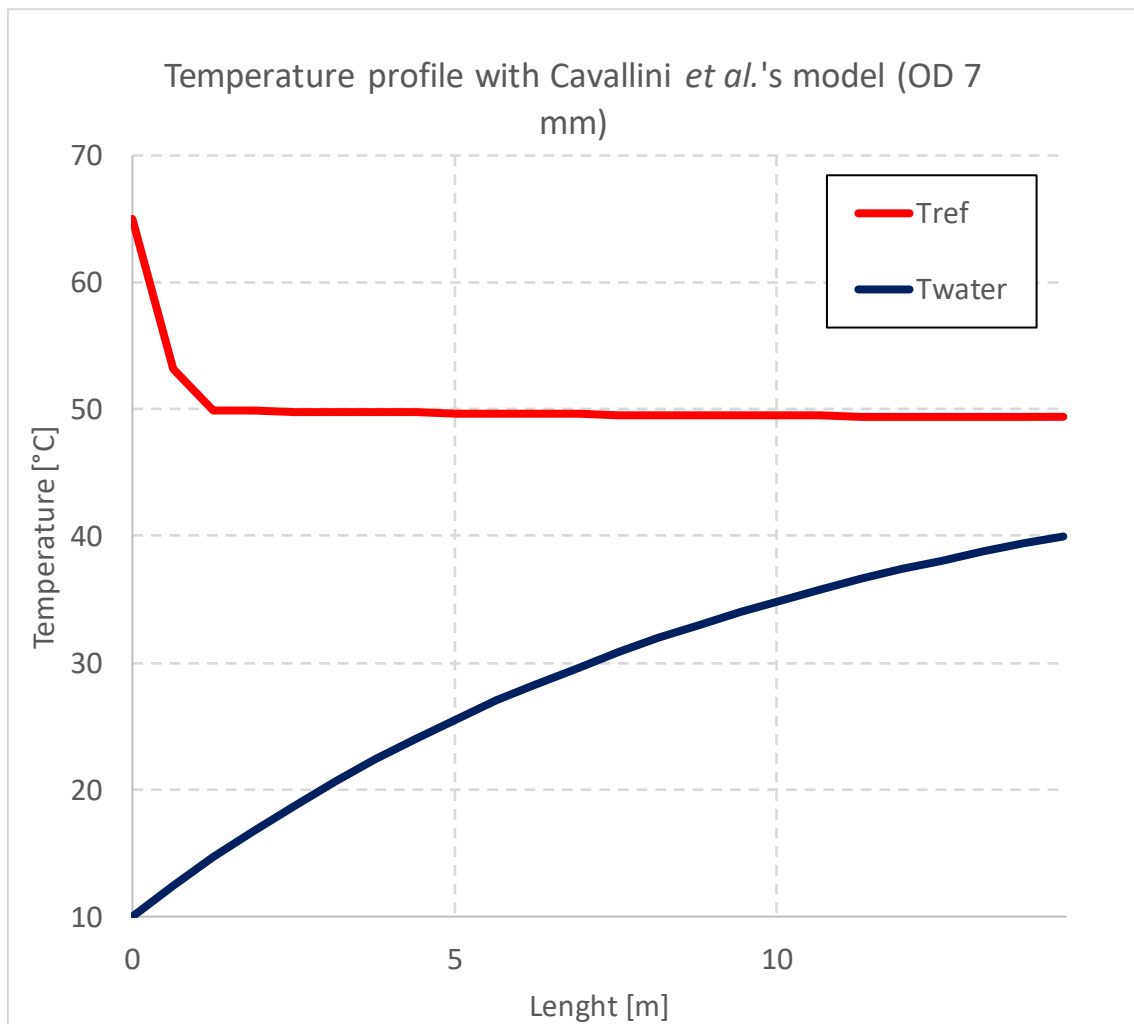


Figure 8.8. Temperature profiles with the Cavallini *et al.*'s model (*OD* 7 mm).

The heat exchanger total length is 14.45 m, with a height of 24 cm. In this configuration, 23 coils are sufficient to exchange a total amount of heat of 999 W. The effect of the pressure drops on the saturation temperature is contained. Indeed, a temperature difference of less than 1°C is present between the beginning and the end of the saturated condensation process and ΔP_{tot} is 0.15 bar (for the results, please refer to Table 8.3).

Since the tube presents a larger inner diameter compared to the previous one, the mass velocity is much lower ($208 \text{ kg m}^{-2}\text{s}^{-1}$). The pressure drops are reduced and, consequently, the saturation temperature decreases much less than the previous cases. Each coil can exchange a larger heat flow rate. As final result, a more compact heat exchanger is designed.

8.8.4 Hirose et al.'s modified model with OD 7 mm tube

The refrigerant temperature and the water temperature as function of the length of the heat exchanger are reported in Figure 8.9.

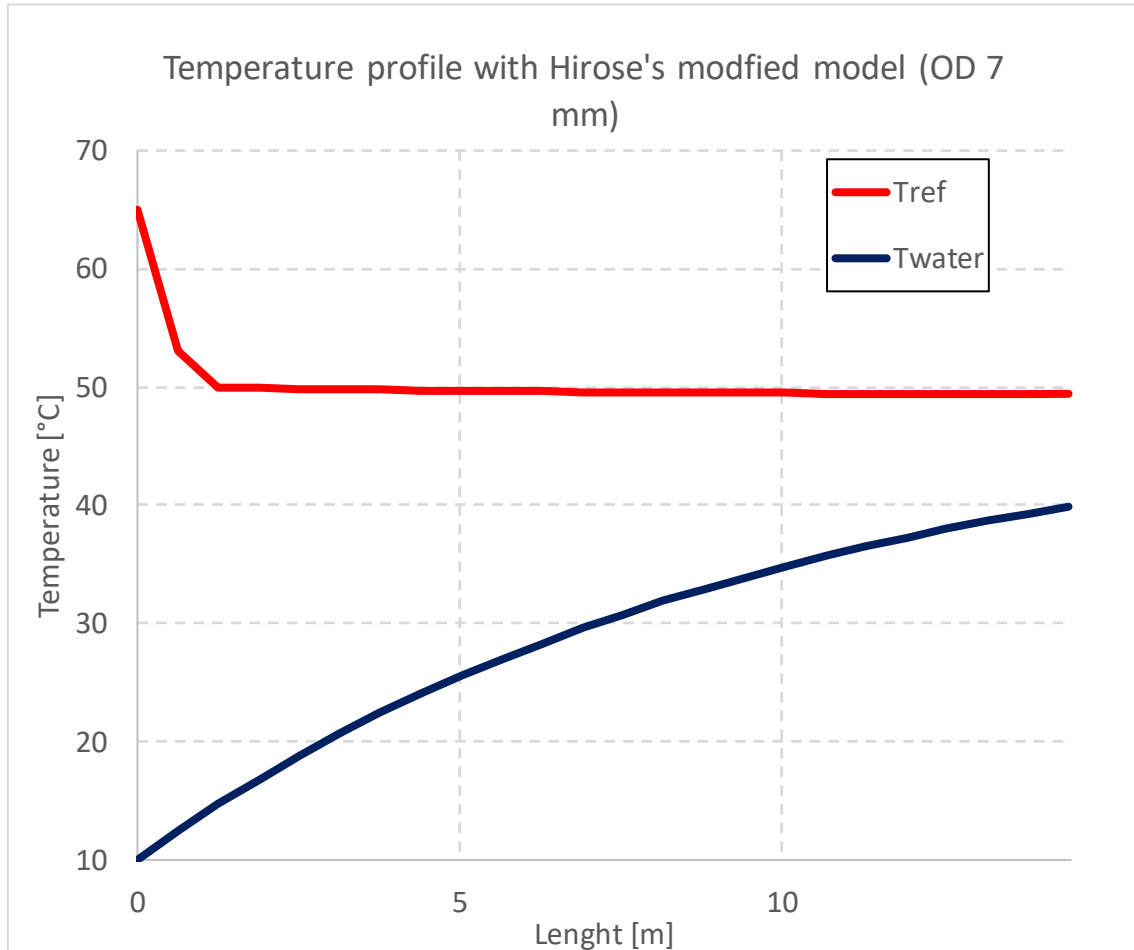


Figure 8.9. Temperature profiles with the Hirose et al.'s modified model (OD 7 mm).

The heat exchanger total length is 14.45 m, with a high of 24 cm. In this configuration, 23 coils are sufficient to exchange a total amount of heat of 996 W. The effect of the pressure drops on the saturation temperature is contained. Indeed, a temperature difference of less than 1°C is present between the beginning and the end of the saturated condensation process and ΔP_{tot} is 0.15 bar (for the results, please refer to Table 8.3).

As in §8.7.3, the heat exchanged per coil is greater compared to OD 5 mm. As consequence, a more compact and performing heat exchanger can be designed.

8.8.5 Heat transfer coefficient

The Figure 8.10 presents the different heat transfer coefficient obtained in the refrigerant side.

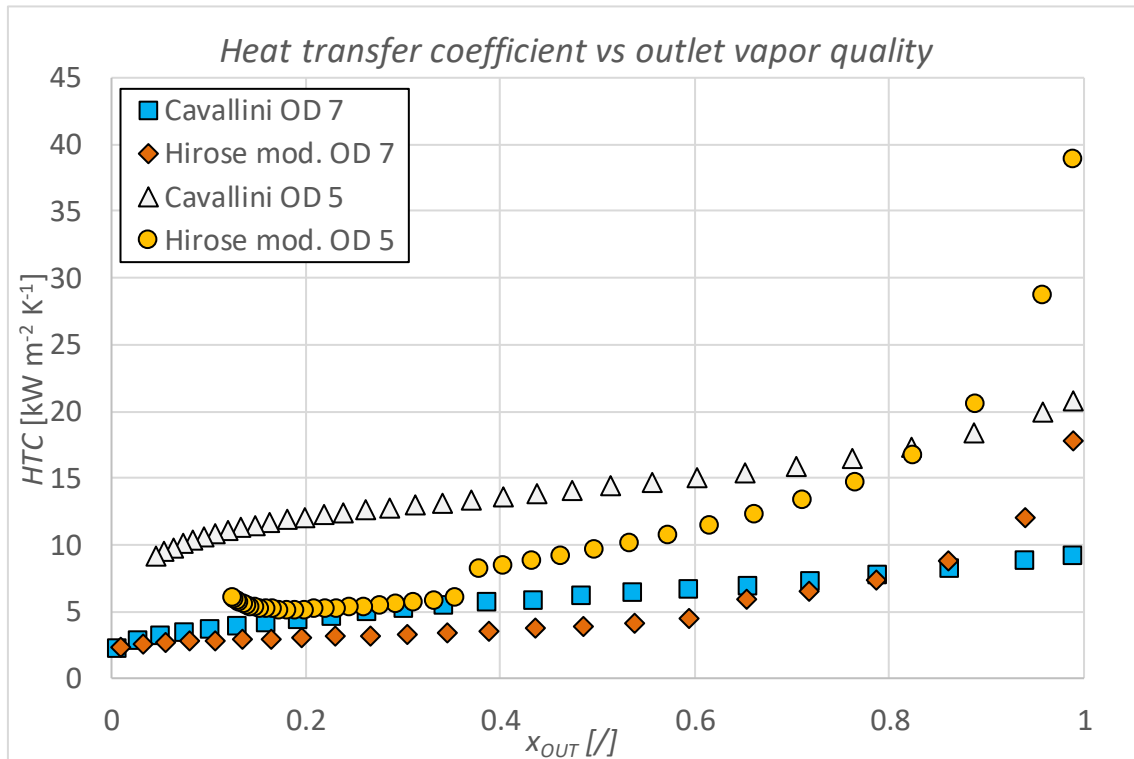


Figure 8.10. Heat transfer coefficient vs outlet vapor quality.

In both the tubes the same behaviour can be observed: the Hirose *et al.*'s modified model tends to overestimate the heat transfer coefficient at high vapor quality. This is a characteristic feature of the correlation which has been already observed in §7.3.3. When the vapor quality drops below 0.6-0.7, the heat transfer coefficient calculated by Cavallini *et al.*'s model becomes greater than the one evaluated with Hirose *et al.*'s modified correlation. The results are similar for the *OD 7* mm tube when the vapor quality is below 0.6. However, for the *OD 5* mm, the difference between the heat transfer coefficients calculated with the two models seems to increase.

An interesting fact can be observed in the model with the Hirose *et al.*'s correlation and 5 mm tube: when the outlet vapor quality drops below 0.3, the heat transfer coefficient increases. This fact found no physical explanation since, when the condensation is ending, the liquid film should be thicker: the thermal resistance should be higher, and

the heat transfer coefficient should decrease. The reason of such strange behaviour could be due to the Hirose *et al.*'s correlation itself. Indeed, another simulation with the original correlation has been performed and the same trend can be observed. Furthermore, as the number of coils increases, as lower the heat exchanged becomes. When the number of coils is high, the temperature difference between the saturation and the wall decreases. In the case of 5 mm tube, the temperature difference becomes lower than 0.2 K after 28 coils. This leads to a dramatic increase of the Nusselt number in free convection condensation Nu_B , and consequently, to an increase of the overall heat transfer coefficient. Probably, the model was not calibrated to operate with such low temperature differences.

To trigger the code, a constant heat transfer coefficient of $5100 \text{ W m}^{-2} \text{ K}^{-1}$ is imposed when temperature difference becomes lower than 0.2 K. In Figure 8.11, the new pattern of the heat transfer coefficients for the model with Hirose *et al.*'s correlation and OD 5 mm can be seen.

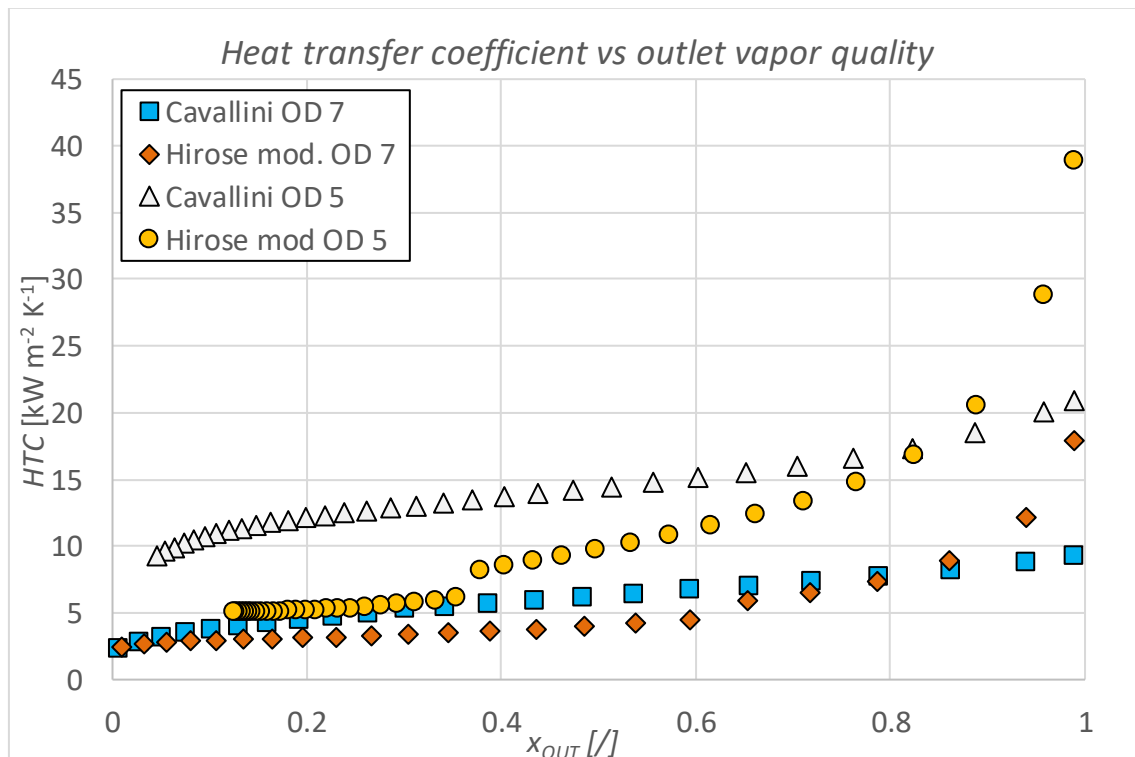


Figure 8.11. Heat transfer coefficient vs outlet vapor quality

8.9 Conclusions

In Table 8.3, the results of the four codes are reported.

Model	N	L_{tot}	H	A_{tot}	Q_{tot}	ΔP_{tot}	$\Delta P_{tot}/L$	$T_{H2O,OUT}$
	/	m	m	m ²	W	bar	bar m ⁻¹	°C
OD 5 Cavallini	33	20.74	0.25	0.33	1007	1.33	0.064	40.20
OD 5 Hirose	40	25.13	0.3	0.39	966	2.22	0.088	38.99
OD 7 Cavallini	23	14.45	0.24	0.32	999	0.15	0.011	39.97
OD 7 Hirose	23	14.45	0.24	0.32	996	0.15	0.010	39.87

Table 8.3. Results of the simulation for the four different models.

Four different models have been implemented to design an helicoidal condenser. From the simulations, the following results have been obtained:

- The heat transfer coefficients for condensation from superheated vapor calculated with Hirose *et al.*'s modified method and with Cavallini *et al.*'s correlation present a similar trend for the same outer diameter tube. Initially, the heat transfer coefficient calculated by Hirose *et al.*'s modified model gives higher heat transfer coefficients. When the vapor quality decreases, Cavallini *et al.*'s model presents a higher heat transfer coefficient;
- The pressure drops calculated with the Diani *et al.*'s model are similar compared to the ones calculated with Hirose *et al.*'s modified model with the *OD* 7 mm tube. The difference between the two calculated pressure drops seems to increase when the tube diameter is reduced from 7 to 5 mm;
- In the case of the *OD* 7 mm tube, the models present roughly the same results in terms of geometry, outlet water temperature, total heat exchanged and overall pressure drops;
- In the case of the *OD* 5 mm tube, the pressure drops calculated are larger in Hirose *et al.*'s modified model compared to Diani *et al.*'s model due to the different way in which the friction factor is calculated. In both the cases, the saturation temperature drop due to the friction gradients is so high that, in order to exchange 1 kW, a much larger condenser is required. In the case of Hirose *et al.*'s modified model with *OD* 5 mm, the condenser is not capable to reach 1 kW of heat exchanged even with 40 coils because the difference between the

saturation temperature and the outlet water temperature is practically negligible, leading to a very low driving force which allows the heat to be exchanged.

Overall, the best solution is the one with *OD* 7 mm tube, despite presenting a lower heat transfer coefficient. The lower pressure drops allows to obtain a more performing and a more compact condenser. In all the four designs, a height of 35 cm of the tank can be supposed in order to contain roughly 25 L of water.

Chapter 9:

Conclusions

In this Chapter, a summary of all the work and of all the results obtained for this master thesis are reported. Furthermore, a description of the future possible works is presented.

9.1 Results

The aim of the present work was to investigate experimentally, theoretically and finally analytically the condensation from superheated vapor inside microfin tubes. The following results have been obtained:

- Modelling the heat exchange mechanism as Webb [4] describes, no particular effect of the superheating degree has been experimentally observed in the condensation from superheated vapor. This confirms the initial hypothesis: the condensation from superheated vapor can be modelled as saturated condensation, if the driving temperature difference in the Newton's law is the one between the saturation and the inner wall temperature [1]. The heat transfer coefficient calculated is expected to be very close to the one from saturated condensation;
- Two models have been tested and modified (Cavallini *et al.* and Hirose *et al.*) in order to predict the heat exchanged during the condensation from superheated vapor, assuming to simulate the overall process considering just the latent heat transfer mechanism. The results are satisfying for a two-phase flow phenomenon. A third model (Webb) is tested in the attempt to simulate the entire heat transfer mechanism (latent + sensible heat transfer) and good results are obtained. However, for the practical point of view, the use of the Cavallini *et al.*'s and the Hirose *et al.*'s modified models are more convenient since their applicability is simpler compared to Webb's;
- A model for the design of an helicoidal condenser is proposed. Four different simulations have been performed, two with an outer diameter tube of 5 mm and

two with an outer diameter tube of 7 mm. The results are more satisfying for the 7 mm tube: despite a lower heat transfer coefficient, the pressure drops are much more contained, allowing to exchange a greater amount of heat per coil, since the saturation temperature drop is much less relevant.

9.2 Future developments

From the present study, different works can start:

1. All the correlations studied in Chapter §7 are based on the Webb's theory. More complex theories, such as Kondou and Hrnjack [8] have been introduced and discussed in Chapter §1, but not experimentally validated. With the modification of the existing experimental apparatus for the calculation of local heat transfer coefficients, even the theories proposed by other researchers can be tested and experimentally validated;
2. The modification on the number of optimal fins in the Cavallini *et al.*'s model requires a deeper study to understand on which refrigerants and on which geometries this modification can be applied;
3. The Hirose *et al.*'s modified model presents good results with the R1234ze(E) and mixtures which have as principal component the R1234ze(E). However, a deeper study must be performed to understand the applicability of this correlation even to other types of refrigerants, such as HFC;
4. With the models presented for the design of the helicoidal condenser, a new experimental test section can be built. The new experimental setup will allow to verify the predictability and the eventual improving of the code. The heat transfer coefficient on water side can be experimentally tested and a computational fluid dynamics model can be written to study the performance of the heat exchanger in transient regime (without a water mass flow rate). Even an integration with the phase change material is possible to increase the heat storing capability. The properties of the PCM are investigated in APPENDIX A.

Appendix A:

T-history

In this appendix, the calculations of the thermal properties of the phase change materials by means of the T-history method are reported, presented for the first time by Zhang *et al.* [33] and then adjusted and corrected by Hong *et al.* [34].

A.1 Introduction

In the world of tomorrow, renewables energy technologies will become the dominant way to produce electricity. However, they present an important issue: these sources are intermittent in time. As consequence, the necessity of storing the energy when there is a surplus of production to utilize it when there is a lack of availability is becoming a priority research field all over the world.

Phase change materials (PCMs) are gaining more and more importance today thanks to their capability of storing large quantity of energy through a phase change process. Indeed, when the material melts, the energy released by the source remains trapped in form of latent heat inside the PCM for a long time and it can be released later for different purposes through the solidification process. This peculiarity makes the PCMs a very good solution to store heat in domestic applications (for instance, to produce hot water in a tank coupled with a thermal solar system) and non-domestic ones.

The measurement of the thermal properties of the PCMs, such as the specific heat capacity and the latent heat, are of primary importance to understand the applicability of these materials in the energy sector for the proxime future. Unfortunately, the traditional methodologies like differential thermal analysis (DTA) and differential scanning calorimetry (DSC) require very expensive equipment. Furthermore, the samples tested in these methodologies are generally very small (1-10 mg) and their behaviour is generally different compared to the bulk materials (for instance, the supercooling degree in salt hydrates is heavily affected by the mass of the specimen analysed).

In 1998, Zhang *et al.* [33] proposed an alternative method for the calculation of the thermal properties of PCM: it is called Temperature history (T-history) and it can be used to calculate with a discrete level of precision the heat capacity, the heat of fusion and solidification and finally the temperature range of phase change of the material with a relative cheap experimental apparatus.

In 2003, Hong *et al.* [34] proposed an improvement of the experimental method. Indeed, the original approach was able to calculate the properties of the materials which presented an important degree of supercooling or a phase change which appears mostly at constant temperature. However, a particular family of PCMs, called paraffins, does not present supercooling and neither a constant temperature during the solidification or the fusion. Subsequently, the original T-history cannot be used for the paraffines. Hong *et al.* modified the method to apply it even to this type of PCMs. Since the experimental tests are carried out with 3 different types of paraffins, the present work takes as principal reference the article by Hong *et al.* [34].

A.2 Thermocouples calibration

Before entering in the details of the T-history method, a calibration of the thermocouples that will be used in the experiment is required.

A.2.1 Types of thermocouples

The thermocouples used in the experiments are essentially constituted by a constantan-copper junction. The sensor is protected by a stainless-steel rod. This type of protection assures more mechanical resistance to the sensitive element. However, the precision of the sensor is obviously lower compared to the thermocouples without protective rods (the constructor declared a precision of ± 0.5 °C on the measurements).

Two types of thermocouples were tested for the calibration, one shorter than the other one. Due to the size of the test tubes used (§A.4.2.1) in the experiments just the short ones will be adopted.

A.2.2. Experimental setup

Calibration of thermocouples is carried out by means of a thermostatic bath and a reference sensor, which is a Pt100 resistance. The Pt100 is put together with other 4 thermocouples (2 short and 2 long) inside the thermostatic bath. The temperature of the bath is settled, the system is left to stabilize for at least an hour. Subsequently, the output signals [mV] of the four tested thermocouples are registered with the acquisition system and the average value for each channel is taken as reference value. The test is repeated 6 times, starting from 10°C up to 70°C with a temperature increase of 10°C per test. In Figure A.1, the experimental setup can be seen.

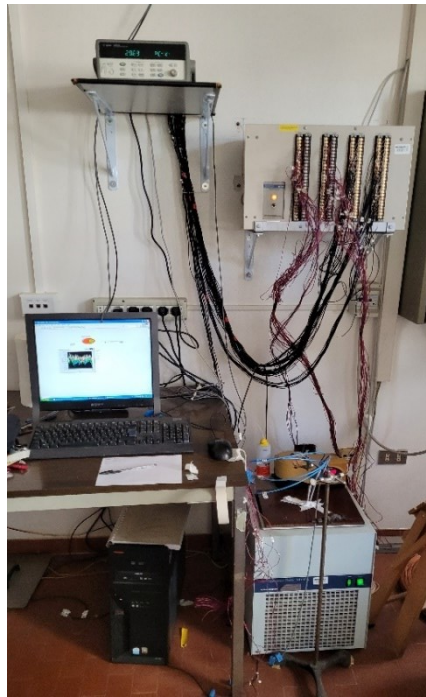


Figure A.1. *Experimental setup for the thermocouples calibration. On the right, the thermostatic bath and the thermocouples. On top, the acquisition system.*

A.2.3 Calibration

Once the averaged value of the voltage for each test has been calculated, a mathematical interpolation is carried out to find the new polynomial coefficients. The code is the B.10. in Appendix B. The averaged values of the voltage V are interpolated with the temperature values registered by the Pt100 with a 4 degree polynomial. Figure A.2 shows the difference between the old polynomial used before the calibration and the new one.

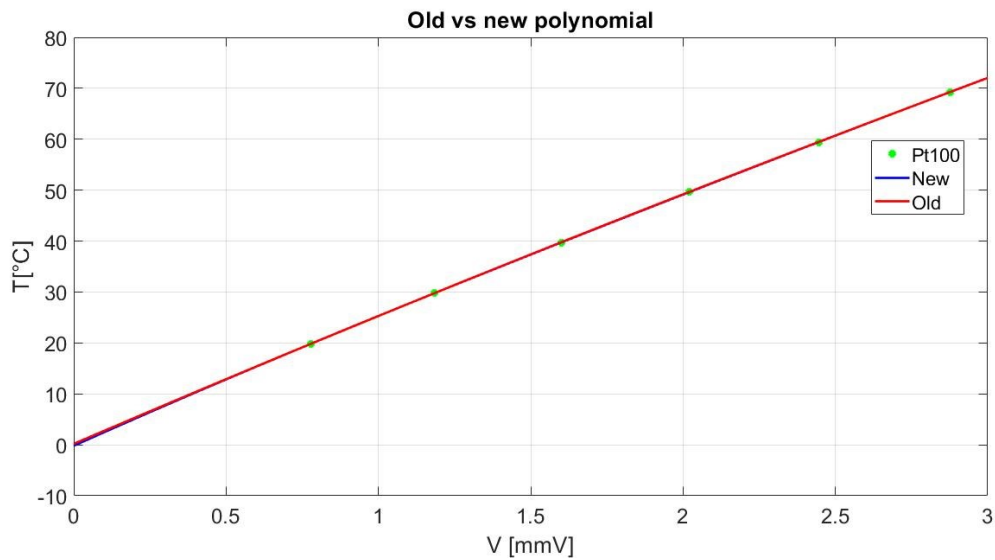


Figure A.2. Polynomial interpolation of the experimental values. In green, the experimental points, in blue the new polynomial and in red the old one.

Table A.1 shows the different coefficients of the two 4 degrees polynomials. The structure is the one reported in the equation (A. 1), where T is the temperature [°C] and V is the voltage [mV]:

$$T = AV^4 + BV^3 + CV^2 + DV + E . \quad (\text{A. 1})$$

Coefficients	Old	New
E	1.17E-02	-4.18E-02
D	-4.25E-02	3.68E-01
C	-5.57E-01	-1.63E+00
B	2.57E+01	2.68E+01
A	1.86E-01	-1.88E-01

Table A.1. Polynomial coefficients of the new and the old polynomial.

A.2.4. Results

In Table A.2, the error for the test at 20°C is reported, both for the new and the old polynomial and for all the 4 thermocouples. It is possible to notice the error is well below the limit of ± 0.5 °C given by the constructor (the errors obtained from the other tests are similar). Subsequently, since the difference between the two interpolations is negligible, the old polynomial was the one chosen for the experimental tests of the T-history.

Channels	V [mmV]	T_{old} [°C]	Pt100 [°C]	Err	Type	T_{new} [°C]	Err
301	0.778	19.83	19.82	6.71E-03	LONG	19.83	1.04E-02
302	0.778	19.82	19.82	1.50E-03	LONG	19.82	2.12E-03
303	0.778	19.81	19.82	8.04E-03	SHORT	19.82	4.44E-03
304	0.777	19.81	19.82	1.42E-02	SHORT	19.81	1.06E-02

Table A.2. Temperature obtained for the 4 thermocouples with the 2 polynomials and the correspondent error. It is possible to notice that the errors are similar. Consequently, the old polynomial is considered reliable for the experimental tests.

A.3 T-history: mathematical model

The T-history method was originally proposed by Zhang *et al.* [33] and then modified and improved by Hong *et al.* [34].

A.3.1. Principles of the original method

Consider having a tube which contains inside a certain known quantity of PCM at a temperature $T_0 > T_m$, where T_m is the melting temperature. Suppose to expose the sample to an atmosphere at a temperature $T_{\infty,a}$ (the temperature can be time dependent). The curve that is obtained is like the one reported in Figure 1.3., depending on if the PCM presents or not a supercooling phase (ΔT_m in the Figure 1.3 (a)).

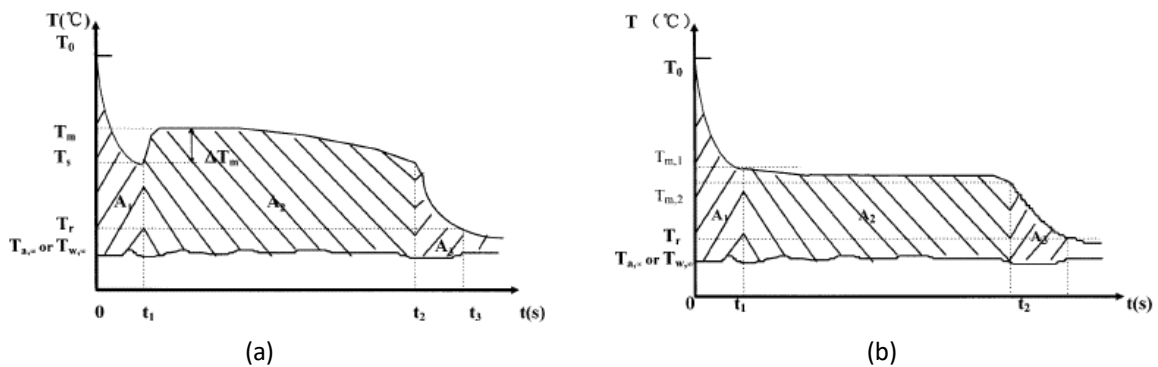


Figure A.3. Time-temperature curve of a general PCM with supercooling (a) and time-temperature curve of a general PCM with no supercooling (b) [33].

The most important condition for the application of the method is:

$$Bi = \frac{hR}{2k} < 0.1, \quad (A.2)$$

where Bi is the Biot number, R [m] is the radius of the tube, h is the heat transfer coefficient of the air outside the tube [$W m^{-2} K^{-1}$] and k [$W m^{-1} K^{-1}$] is the thermal conductivity of the PCM. If this condition is verified, the temperature distribution can be considered uniform in the sample and consequently the lumped-capacitance method can be applied (the following equations take as reference the Figure A.3(a)):

$$(m_{t,pcm}c_{p,t} + m_{pcm}c_{p,l})(T_0 - T_s) = hA_c \int_0^{t_1} (T - T_{\infty,a})dt , \quad (\text{A. 3})$$

where $m_{t,pcm}$ [kg] is the mass of the tube containing PCM, $c_{p,t}$ [$\text{kJ kg}^{-1} \text{K}^{-1}$] is the specific heat capacity of the tube, m_{pcm} [kg] is the mass of PCM in the tube, $c_{p,l}$ [$\text{kJ kg}^{-1} \text{K}^{-1}$] is the specific heat capacity of PCM in liquid phase, T_0 [$^{\circ}\text{C}$] is the initial temperature, T_s [$^{\circ}\text{C}$] is the subcooling temperature, h is the heat transfer coefficient of the air [$\text{W m}^{-2} \text{K}^{-1}$], A_c is the heat transfer area of the tube [m^2] and the integral corresponds to the area A_1 in the Figure A.3 (a).

During the phase transition, the energy balance becomes:

$$m_{pcm}H_m = hA_c \int_{t_1}^{t_2} (T - T_{\infty,a})dt , \quad (\text{A. 4})$$

where H_m [kJ kg^{-1}] is the latent heat of solidification and the integral corresponding to the area A_2 in the Figure A.3 (a). Finally, for the solid state, it is possible to write:

$$(m_{t,pcm}c_{p,t} + m_{pcm}c_{p,s})(T_s - T_r) = hA_c \int_{t_2}^{t_3} (T - T_{\infty,a})dt , \quad (\text{A. 5})$$

where $m_{t,pcm}$ [kg] is the mass of the tube containing PCM, $c_{p,t}$ [$\text{kJ kg}^{-1} \text{K}^{-1}$] is the specific heat capacity of the tube, m_{pcm} [kg] is the mass of PCM in the tube, $c_{p,s}$ [$\text{kJ kg}^{-1} \text{K}^{-1}$] is the specific heat capacity of PCM in solid phase, T_s [$^{\circ}\text{C}$] is the subcooling temperature, T_r [$^{\circ}\text{C}$] is the reference temperature (arbitrarily chosen 5°C greater than the air temperature $T_{\infty,a}$), h is the heat transfer coefficient of the air [$\text{W m}^{-2} \text{K}^{-1}$], A_c is the heat transfer area [m^2] of the tube and the integral corresponding to the area A_3 in the Figure A.3 (a).

To calculate the thermal properties of the material, a reference sample of pure water is required. If the water is suddenly exposed to the same atmosphere, supposing to have the same initial temperature T_0 of the PCM, the temperature-time curve obtained will be like the one in Figure A.4.

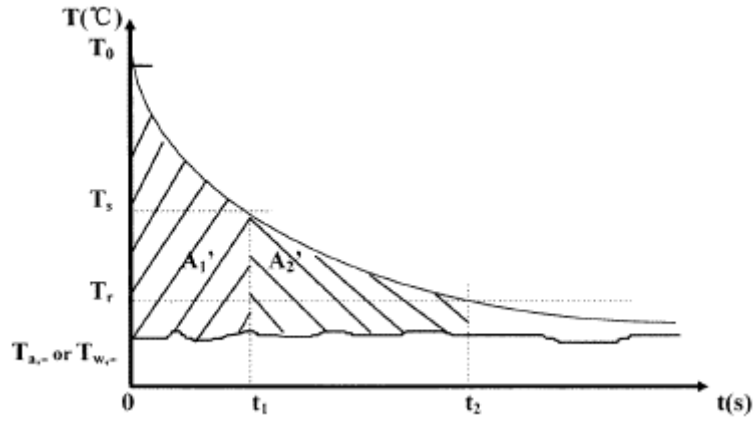


Figure A.4. Temperature-time curve for the water as reference substance⁷ [33].

The interval of time t'_1 and t'_2 can be obtained intercepting the curve of the water with the temperatures evaluated in the PCM curve. It is possible to write:

$$(m_{t,w}c_{p,t} + m_w c_w)(T_0 - T_s) = hA_c \int_0^{t'_1} (T - T_{\infty,a}) dt, \quad (\text{A. 6})$$

$$(m_{t,w}c_{p,t} + m_w c_w)(T_s - T_r) = hA_c \int_{t'_1}^{t'_2} (T - T_{\infty,a}) dt. \quad (\text{A. 7})$$

where $m_{t,w}$ [kg] is the mass of the tube containing water, $c_{p,t}$ [kJ kg⁻¹ K⁻¹] is the specific heat capacity of the tube (assuming the two tubes are made by the same material and present the same heat transfer area A_c), m_w [kg] is the mass of water in the tube, $c_{p,w}$ [kJ kg⁻¹ K⁻¹] is the specific heat capacity of the water, the integral in the equation (A. 6) corresponds to the area A'_1 in the Figure A.4 and the integral in the equation (A. 7) corresponds to the area A'_2 in the Figure A.4.

Solving the system composed by the last 5 equations, it is possible to obtain:

$$c_{p,s} = \frac{(m_{t,w}c_{p,t} + m_w c_w)}{m_{pcm}} \times \frac{A_3}{A'_2} - \frac{m_{t,pcm}}{m_{pcm}} c_{p,t}, \quad (\text{A. 8})$$

$$c_{p,l} = \frac{(m_{t,w}c_{p,t} + m_w c_w)}{m_{pcm}} \times \frac{A_1}{A'_1} - \frac{m_{t,pcm}}{m_{pcm}} c_{p,t}, \quad (\text{A. 9})$$

⁷ The values t_1 and t_2 in the picture correspond to t'_1 and t'_2 in the following equations.

$$H_m = \frac{(m_{t,w}c_{p,t} + m_w c_w)}{m_{pcm}} \times \frac{A_2}{A_1'} (T_0 - T_s). \quad (\text{A. 10})$$

In the case the material does not present supercooling and the phase transition appears at almost constant temperature (Figure A.3 (b)), the equations (A. 8) and (A. 9) remain unchanged. Instead, a modification of the equation (A. 10) is introduced to consider even the sensible heat exchanged during the phase transition:

$$H_m = \frac{(m_{t,w}c_{p,t} + m_w c_w)}{m_{pcm}} \times \frac{A_2}{A_1'} (T_0 - T_{m,1}) - \frac{m_{t,pcm}}{m_{pcm}} c_{p,t} (T_{m,1} - T_{m,2}), \quad (\text{A. 11})$$

where $T_{m,1}$ and $T_{m,2}$ [°C] are respectively the temperatures when the phase transition starts and when it ends.

Despite the good mathematical explanation of the article, there is no specification on how to find the initial and the final points of the solidification process in the case of Figure A.3(b). Furthermore, there is no explanation of the method in case the phase change process is appearing at a temperature which is not constant (like in the case of the paraffines). Indeed, Hong *et al.* [34] proposed a modification of the original method, which is deeply described in the following subparagraph.

A.3.2. Hong *et al.*'s modified method

In their work, Hong *et al.* specify a way to identify the boundaries of the phase change process:

1. The inflection point (or the minimum of the first derivative of the curve) is considered as the end of the solidification process;
2. The point where the derivative abruptly changes is considered as starting of the solidification process (solidification point, Figure A.5).

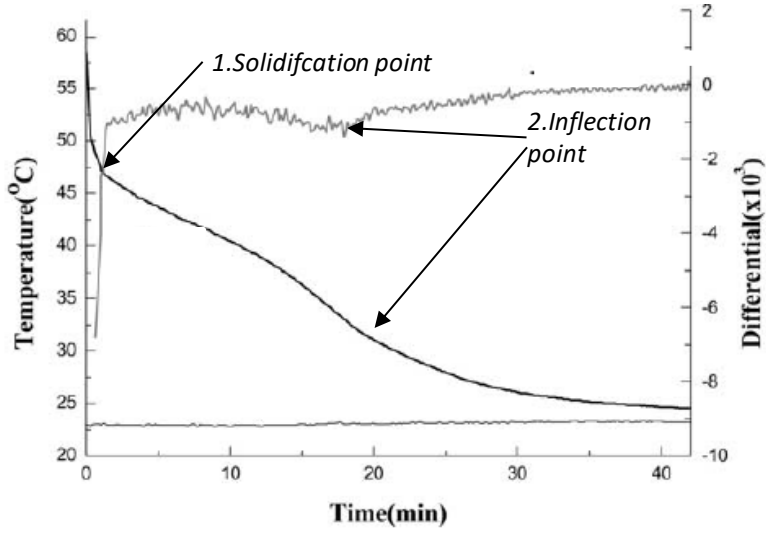


Figure A.5. *T*-history curve of the paraffin and the first derivative of the curve. It is possible to notice the points where the derivate abruptly changes and the minimum of the differential [34].

In order to consider the specific heat capacity of the PCM during the phase change process, the equations are modified as follow:

$$(m_{t,pcm}c_{p,t} + m_{pcm}c_{p,l})(T_0 - T_s) = hA_c \int_0^{t_1} (T - T_{\infty,a})dt, \quad (\text{A. 12})$$

$$m_{pcm}H_m + (m_{t,pcm}c_{p,t} + m_{pcm}\frac{c_{p,s} + c_{p,l}}{2})(T_s - T_i) = hA_c \int_{t_1}^{t_2} (T - T_{\infty,a})dt, \quad (\text{A. 13})$$

$$(m_{t,pcm}c_{p,t} + m_{pcm}c_{p,s})(T_i - T_{end}) = hA_c \int_{t_2}^{t_3} (T - T_{\infty,a})dt, \quad (\text{A. 14})$$

where T_s [°C] is the solidification temperature (corresponding to the point 1 in Figure A.5), T_i [°C] is the inflection point (corresponding to the point 2 in Figure A.5 in the temperature-time curve) and T_{end} [°C] is the reference temperature (in the experiments, it will be taken 5°C greater than the temperature settled in the thermostatic chamber).

The equations of the water are modified too:

$$(m_{t,w}c_{p,t} + m_w c_w)(T_0 - T_s) = hA_c \int_0^{t'_1} (T - T_{\infty,a})dt, \quad (\text{A. 15})$$

$$(m_{t,w}c_{p,t} + m_w c_w)(T_s - T_i) = hA_c \int_{t'_1}^{t'_2} (T - T_{\infty,a}) dt , \quad (\text{A.16})$$

$$(m_{t,w}c_{p,t} + m_w c_w)(T_i - T_{end}) = hA_c \int_{t'_2}^{t'_3} (T - T_{\infty,a}) dt , \quad (\text{A.17})$$

where the integral in the equation (A.17) is defined as A'_3 (this area was not present in the original method since the temperature difference in the phase change process was almost constant).

Solving the system, the final equations can be found:

$$c_{p,s} = \frac{(m_{t,w}c_{p,t} + m_w c_w)}{m_{pcm}} \times \frac{A_3}{A'_3} - \frac{m_{t,pcm}}{m_{pcm}} c_{p,t} , \quad (\text{A.18})$$

$$c_{p,l} = \frac{(m_{t,w}c_{p,t} + m_w c_w)}{m_{pcm}} \times \frac{A_1}{A'_1} - \frac{m_{t,pcm}}{m_{pcm}} c_{p,t} , \quad (\text{A.19})$$

$$H_m = \frac{(m_{t,w}c_{p,t} + m_w c_w)}{m_{pcm}} \times \frac{A_2}{A'_2} (T_s - T_i) - \left(\frac{m_{t,pcm}}{m_{pcm}} c_{p,t} + \frac{c_{p,s} + c_{p,l}}{2} \right) (T_s - T_i). \quad (\text{A.20})$$

With this approach, it is possible to calculate with discrete good precision the heat of solidification and the specific heat capacity of materials which present a phase change process with a marked temperature difference.

The temperature range during which the solidification appears could be determined with a greater precision using the tangent lines. However, as in the following paragraphs (§A.5.1) will be described, a greater precision in the selection of the temperature phase change leads to a greater error in the evaluation of the specific heat capacity and, as consequence, of the heat of solidification.

A.4: Experiment

In this paragraph, a deep explanation of the experiment and of the models used in laboratory is presented. The results and the conclusions are discussed in the paragraph §A.5.

A.4.1 Paraffins data

The three PCMs investigated in this work are three different paraffines produced all by Rubitherm [35, 36, 37]. They are named according to the temperature at which the phase change occurs: RT42 [35], RT55 [36] and RT64HC [37] (HC means high capacity. Indeed, this paraffin presents a heat storage capacity significantly higher than the others two). The properties given by the constructor are listed in Table A.3.

Paraffin	Congeaing area [°C]	Soldification temperature [°C]	Heat storage capacity [kJ kg ⁻¹]	Specific heat capacity [kJ kg ⁻¹ K ⁻¹]	Thermal conductivity [W m ⁻¹ K ⁻¹]
RT42	43-37	42	165 ⁸	2	0.2
RT55	57-56	55	170 ⁹	2	0.2
RT64HC	64-61	64	250 ¹⁰	2	0.2

Table A.3. Properties of parffins. For other information, consult the blibliographic references [35, 36, 37].

The diagram related to the partial enthalpy distribution is reported in Figure A.6, Figure A.7 and Figure A.8 for each paraffine. The diagrams are obtained using a 3-layer calorimeter.

⁸ The heat storage capacity is calculated as combination of latent and sensible heat in a range between 35°C to 50 °C for RT42. Indeed, an uncertainty of $\pm 7.5^\circ\text{C}$ must be considered in the values of the table.

⁹ The heat storage capacity is calculated as combination of latent and sensible heat in a range between 48°C to 63°C for RT55. Indeed, an uncertainty of $\pm 7.5^\circ\text{C}$ must be considered in the values of the table.

¹⁰ The heat storage capacity is calculated as combination of latent and sensible heat in a range between 57°C to 72°C for RT64HC. Indeed, an uncertainty of $\pm 7.5^\circ\text{C}$ must be considered in the values of the table.

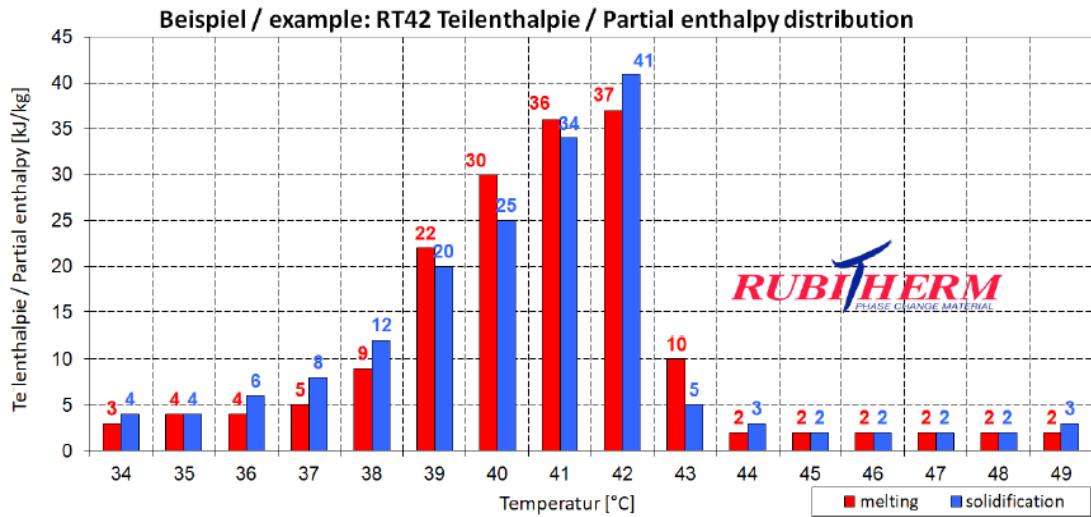


Figure A.6. Partial enthalpy distribution of the RT42 [35].

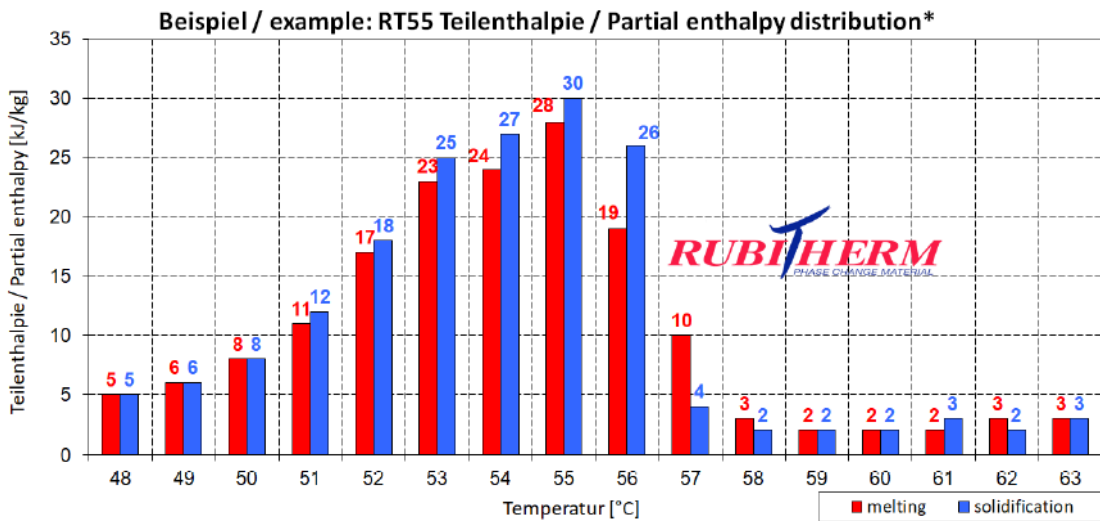


Figure A.7. Partial enthalpy distribution of the RT55 [36]

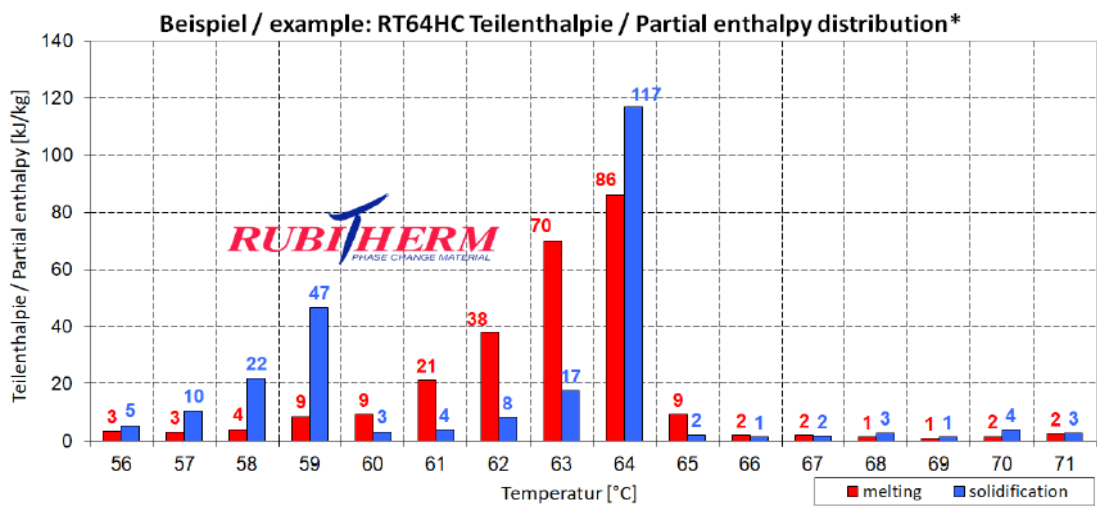


Figure A.8. Partial enthalpy distribution of the RT64HC [37].

A.4.2 Experimental system

A.4.2.1 Tubes

As stated in the subparagraph §A.3.1 (equation (A. 2)), the Biot number must be lower than 0.1 to guarantee the uniformity of the temperature inside the sample (this assumption will be verified in the subparagraph §A.4.6). Consequently, even the size of the test tubes should be chosen carefully (Hong *et al.* specified that with an external diameter of 10 mm of the sample for inorganic hydrates, the condition of $Bi < 0.1$ is satisfied [34]). In fact, a too large diameter tube could lead to a too high value of Biot, leading to an inapplicability of the method. The dimensions of the tubes and their volumes are listed in Table A.4.

D_i	D_e	s	H	V	A_c
mm	mm	mm	mm	mm ³	mm ²
9.7	10.1	0.2	125	9237	3966

Table A.4. Tubes dimensions. From the left: internal diameter D_i , external diameter D_e , thickness s , height H , volume V and heat transfer area A_c .

The tests tubes were created in laboratory. Despite presenting the same geometry, the weight of some of them was slightly different. The proper weight is reported in the Table A.5.

In the same table, the masses of the PCM and the mass of the water for each test are reported. The weight of the PCM is calculated as difference between the mass of the tube with the paraffine inside and the mass of the empty tube (both values are weighted). The mass of water is instead estimated using the volume of the tube and the density of the water (assumed equals at 1000 kg m^{-3}).

Paraffin	$m_{t,pcm}$	m_{t,H_2O}	m_{pcm}	m_{H_2O}
	g	g	g	g
RT42	7.98	7.76	7.18	9.24
RT55	7.98	7.76	7.09	9.24
RT64HC	7.12	7.76	7.27	9.24

Table A.5. Masses of the tubes which contains PCM $m_{t,pcm}$, mass of the tubes which contains water m_{t,H_2O} , masses of PCM m_{pcm} and masses of water estimated m_{H_2O} .

The tubes are made of steel 304 with specific heat capacity c_t of $0.5 \text{ kJ kg}^{-1} \text{ K}^{-1}$. In Figure A.9, the test tubes can be seen: the left one is prepared with the aluminium foil to screen it from radiation and ready to be inserted in the thermostatic chamber.



Figure A.9. Tests tubes. The left one is prepared for the experiment, the right one is empty.

A.4.2.2. Thermostatic chamber

The original method uses a thermostatic bath to uniform the temperature of the samples of the water and of the PCM. After a sufficient amount of time, both the samples are consequently exposed to the atmosphere where the registration of the temperature values can start.

However, in order to have a much strict control of the temperature of the environment, a thermostatic chamber was adopted (Figure A.10). The machine is produced by F.Ili Galli and the name of the product is Genviro. For this type of machine, the stability of the temperature is within $\pm 1 \text{ }^\circ\text{C}$. Indeed, as specified in the following paragraph, two thermocouples are used for the measurement of the air temperature inside the machine. For the calculations, the average value is taken as reference.



(a)



(b)

Figure A.10. Thermostatic chamber Genviro open (a) and closed (b) during the operation.

The machine operates by means of a fan which is capable to keep the temperature almost constant inside. However, to apply the T-history, the fan must be screened: in this way, the natural convection of air should be assured and Biot could remain well below the critical value of 0.1.

A.4.2.3. Thermocouples

The total number of thermocouples adopted in the experiment is 4:

- 2 thermocouples without protection for the sensor are displaced inside the thermostatic chamber to measure the temperature of the air;
- 2 thermocouples with the sensor protected with stainless-steel rod are used inside the samples to measure the temperature of PCM and the temperature of the water (these are of the same type described in paragraph §A.2).

For other information concerning the thermocouples, it is possible to consult the paragraph §A.2.

A.4.3 Experimental procedure

The tubes which are going to be used in the experiment are all weighted empty (both the ones for the water and the ones for the PCM). The paraffines are melt and inserted inside the sample in liquid phase. After the solidification process is terminated, the sample is weighted again and the weight of the PCM is calculated (§A.4.2.1). The results are reported in Table A.5.

The samples are inserted in the thermostatic chamber surrounded by an aluminium foil to screen the heat exchange through radiation. Figure A.11 presents the system before starting the operation of the thermostatic chamber.

Once the thermocouples are inserted inside the samples, the thermostatic chamber is closed, the new temperature is settled. The initial temperature is around 10-15 °C greater than the phase change temperature of the tested paraffine. The samples are left inside the machine until all the thermocouples present almost the same temperature (this process takes roughly about 30 min). After the stabilization is achieved, the machine is settled to a new final temperature, which is around 20-25 °C lower than the phase change temperature (each range is reported in Table A.6). The experimental points are acquired for around one hour (for the calculations, the specific heat capacity of water is assumed equals to $4.2 \text{ kJ kg}^{-1} \text{ K}^{-1}$).

Paraffin	T_0 [°C]	T_{final} [°C]
RT42	55	25
RT55	70	35
RT64HC	80	40

Table A.6. *Temperature range for each paraffine.*

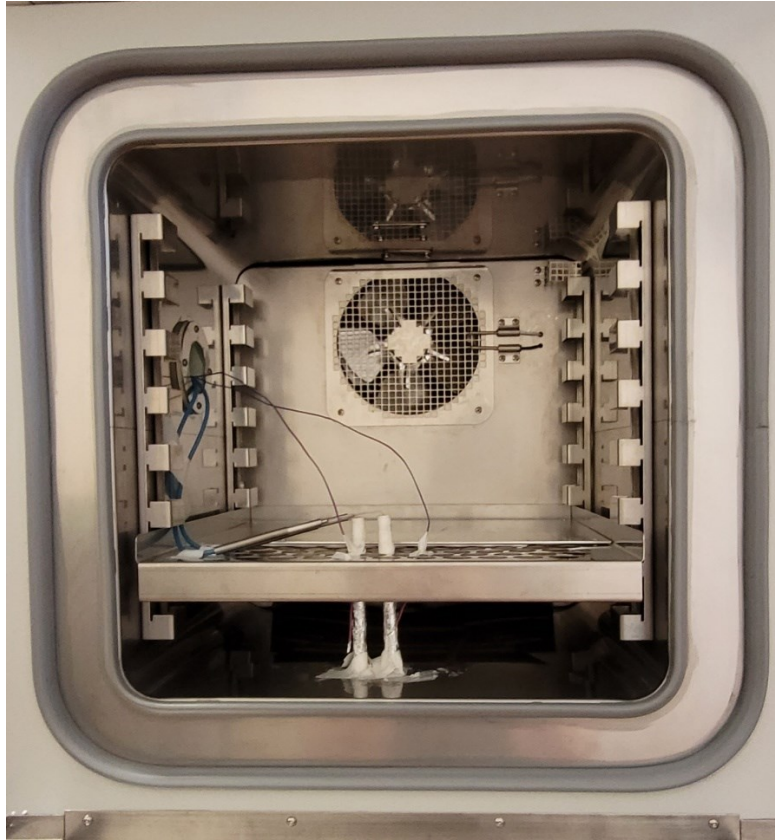
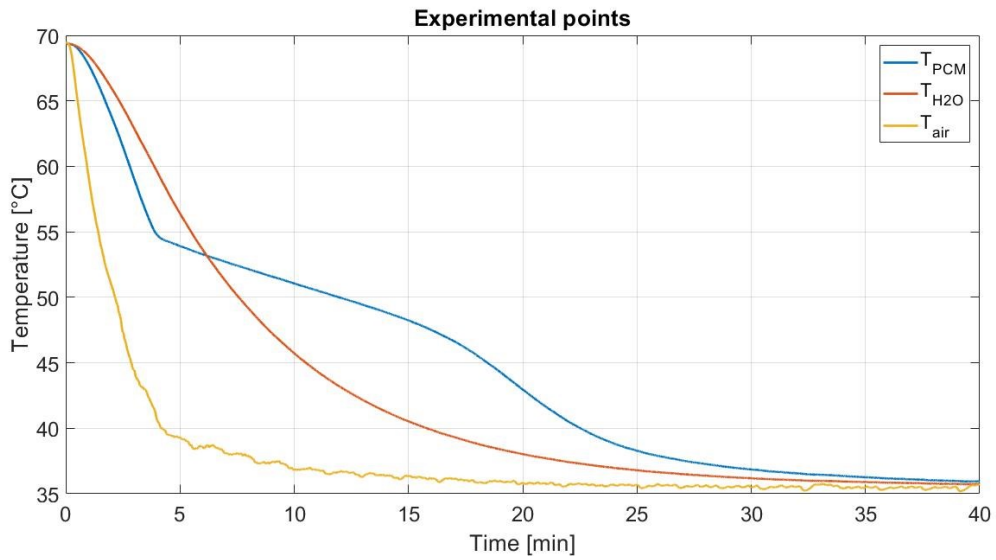


Figure A.11. *Experimental system. In the centre of the chamber it is possible to see the two samples, one containing PCM and the other containing water. Behind the samples, the plate used for screening the fan can be seen, as well as the 4 thermocouples.*

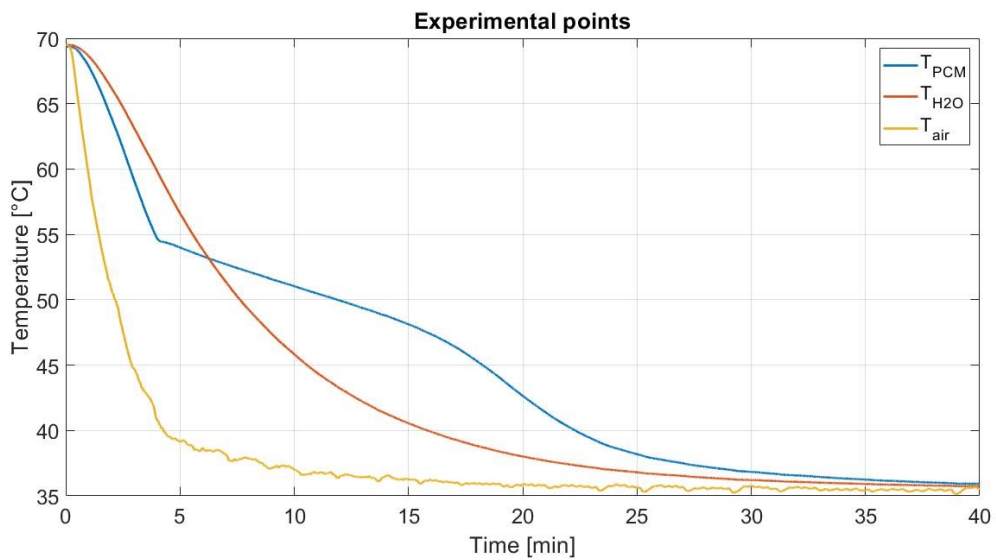
In literature, no data are available for the RT42 and for the RT64HC. Instead, the papers by Martinez *et al.* [38] and by Rolka *et al.* [39] present some results related to the RT55 thermal properties calculated with the T-history method. Since the RT55 is the only paraffine where in literature some information are available, the test for the RT55 is repeated 3 times in the exact same conditions to verify the repeatability of the method. For the other two paraffines, once the repeatability is verified with the RT55, the test is done just one time. For a more detailed information regarding the RT42 and the RT64HC, further studies should be conducted in future.

A.4.4. Experimental points

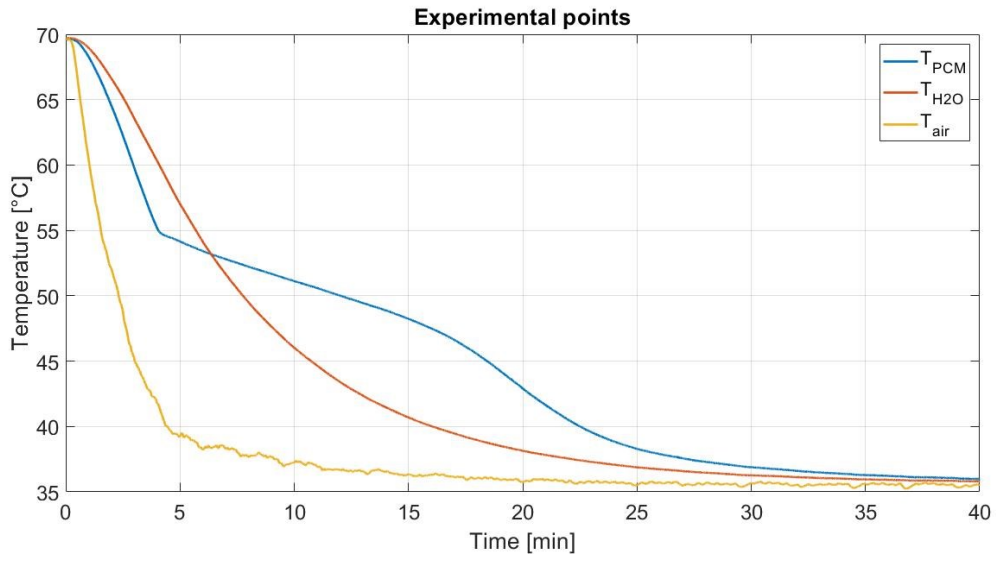
The experimental points of the three different tests conducted with the RT55 are reported in Figure A.12. In Figure A.13 and in Figure A.14, the experimental points related to the RT42 and to the RT64HC can be seen.



(a)



(b)



(c)

Figure A.12. Experimental points of the three tests for the RT55.

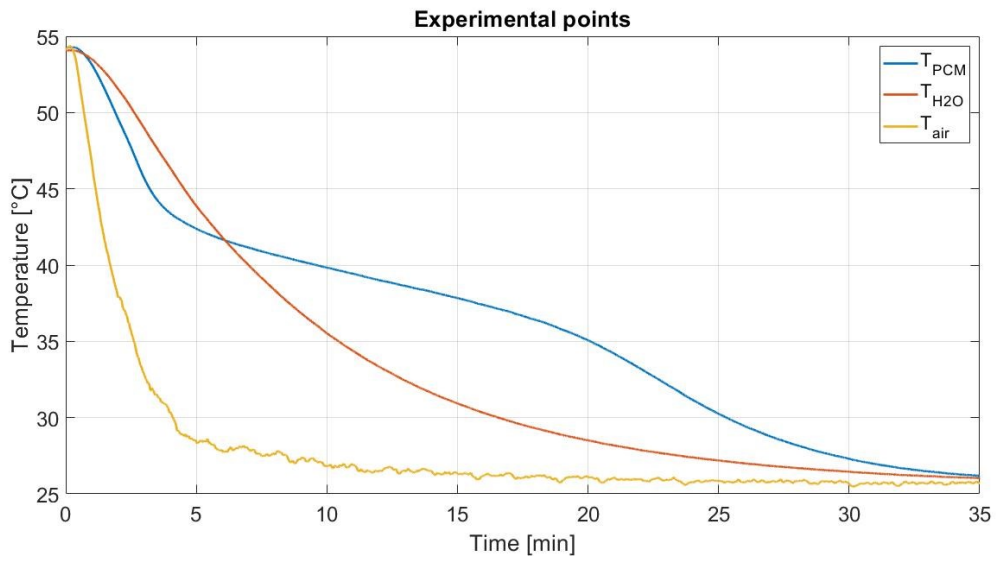


Figure A.13. Experimental points of the RT42.

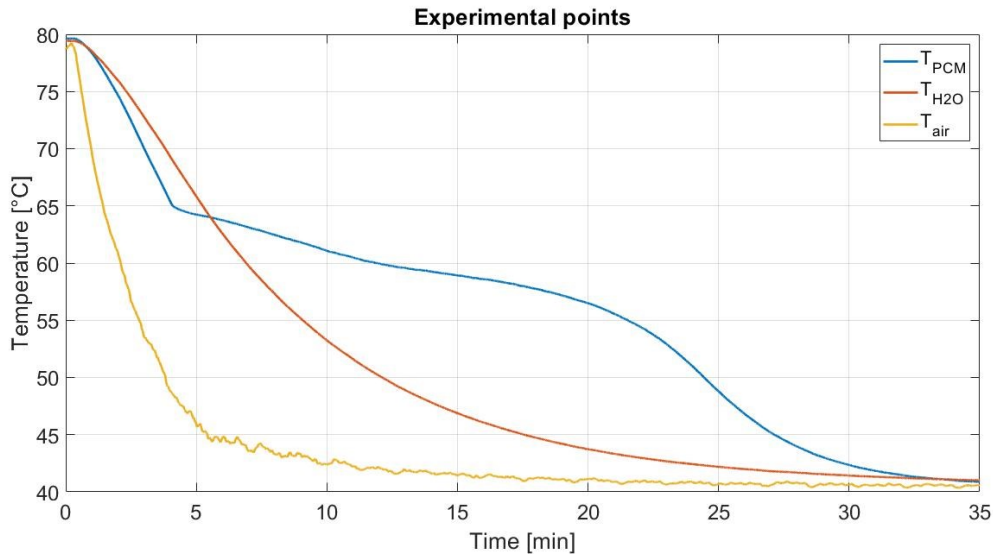


Figure A.14. *Experimental points of the RT64HC.*

Looking at Figure A.12 and A.14, a net change of the curvature of the solidification curve can be seen (for the RT55, at a temperature around 55°C, for the RT64HC, at a temperature around 65 °C). However, this net change in the slope of the curve cannot be seen in Figure A.13: this fact will make more difficult the choice of the starting point of the solidification process for the RT42.

In Figure A.14, a change of the slope of the curve can be seen at a temperature around 60°C. This is according with the partial enthalpy distribution diagram in Figure 1.8, where a small peak of the specific enthalpy can be noticed at 59°C.

A.4.5. Mathematical models

For the calculations, two different approaches are tested: a first approach uses the polynomial interpolation of the experimental points, the second approach uses the spline interpolation (which is a series of polynomials) to perfectly reflect the experimental behaviour of the curves. The results are going to be analysed in the next subparagraphs.

A.4.5.1 Polynomial interpolation

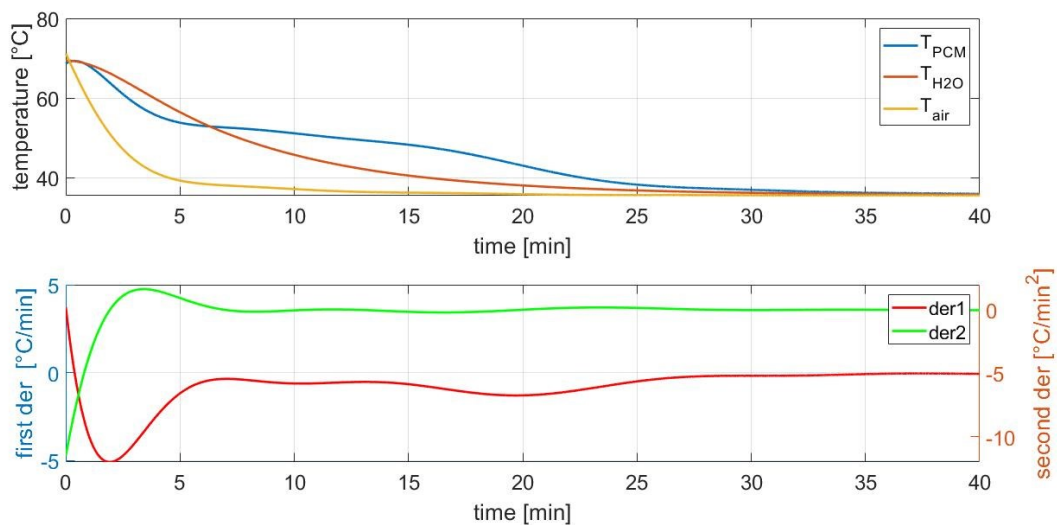
In this first approach, the polynomial interpolation is used for making the calculations. The polynomials used present a degree of 20 in order to obtain a good behaviour of the derivative (the coefficient of determination is calculated for all the curves and it approaches 1 in all the cases. This means that the polynomial interpolations fit well the experimental points).

In this approach, the points where the phase change appears are chosen as follow:

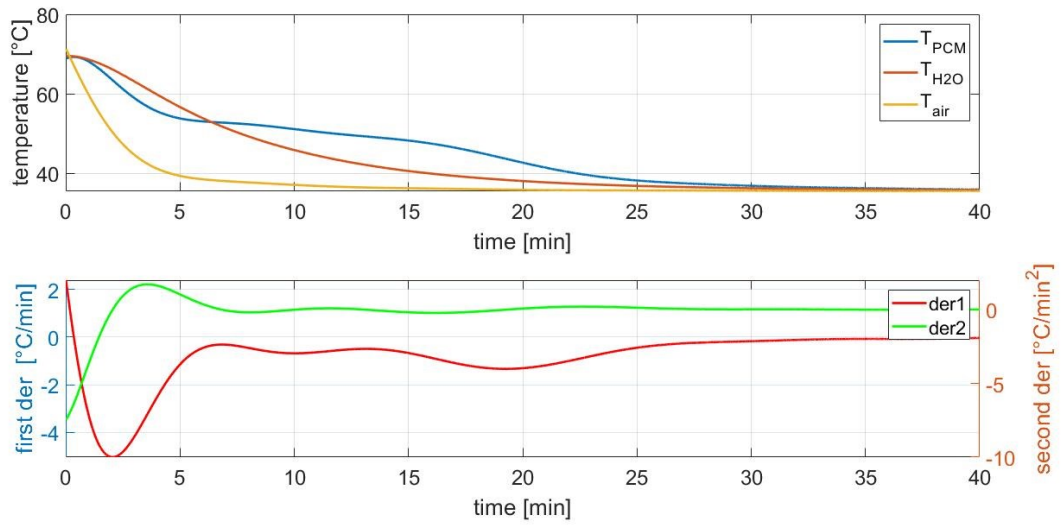
1. The starting point is the maximum point of the second derivative (where the first derivative changes more rapidly);
2. The inflection point (or the end of the solidification process) is the minimum of the first derivative;
3. The reference temperature is chosen 5°C greater than the final temperature of the thermostatic chamber.

The code is B.11 in Appendix B. The code is the same for all the others test with different input data.

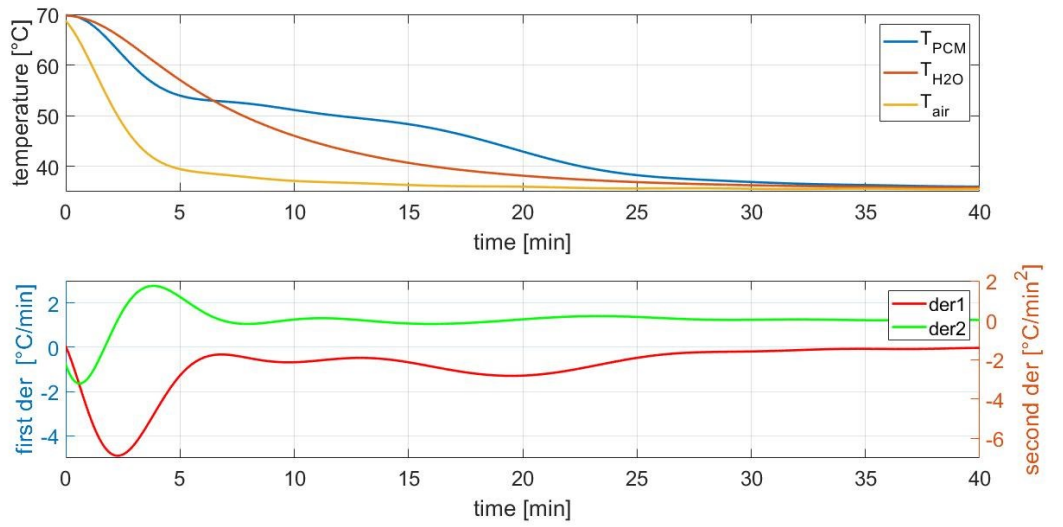
The graph resulted from the interpolation are reported in Figure A.15 for the RT55, Figure A.16 for the RT42 and Figure A.17 for the RT64HC.



(a)



(b)



(c)

Figure A.15. Interpolation of the experimental points of the RT55, first and second derivative.

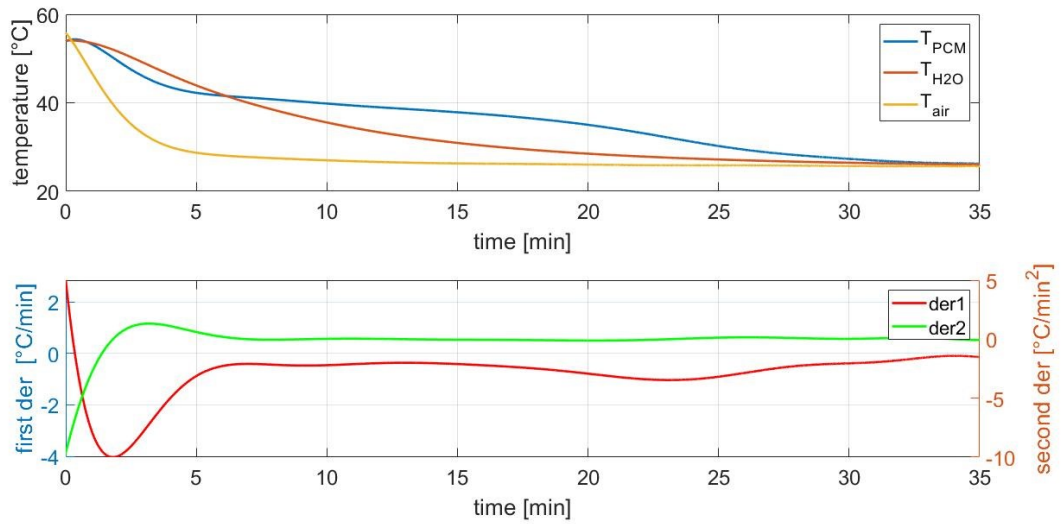


Figure A.16. Interpolation of the experimental points of the RT42, first and second derivative.

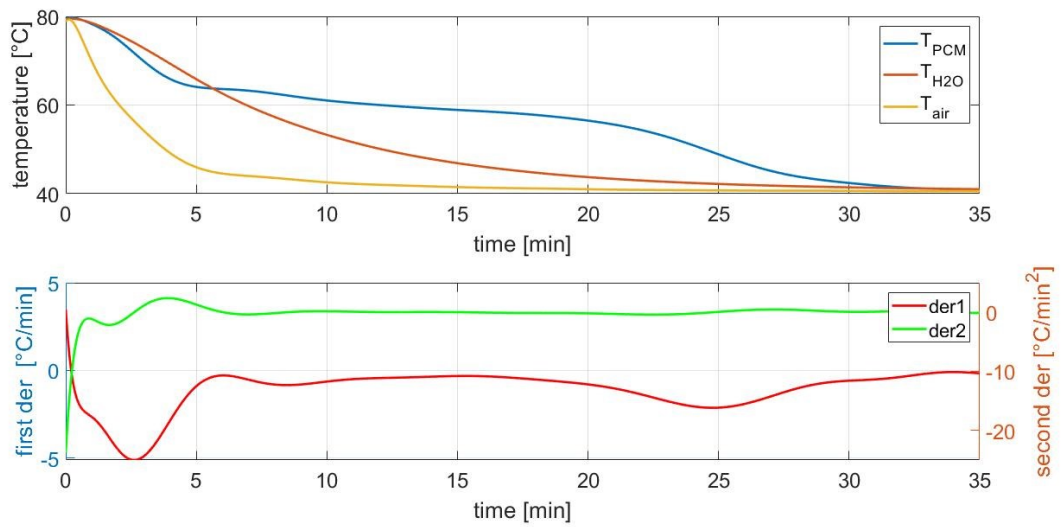


Figure A.17. Interpolation of the experimental points of the RT64HC, first and second derivative.

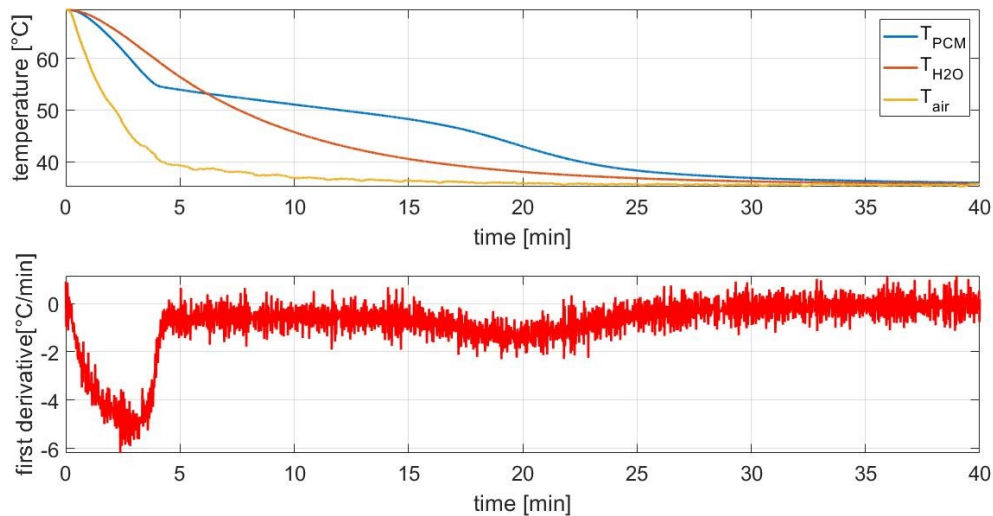
The results are reported in the paragraph §A.5, where they will be compared and discussed with the other mathematical approach used for the experiment.

A.4.5.2 Spline method

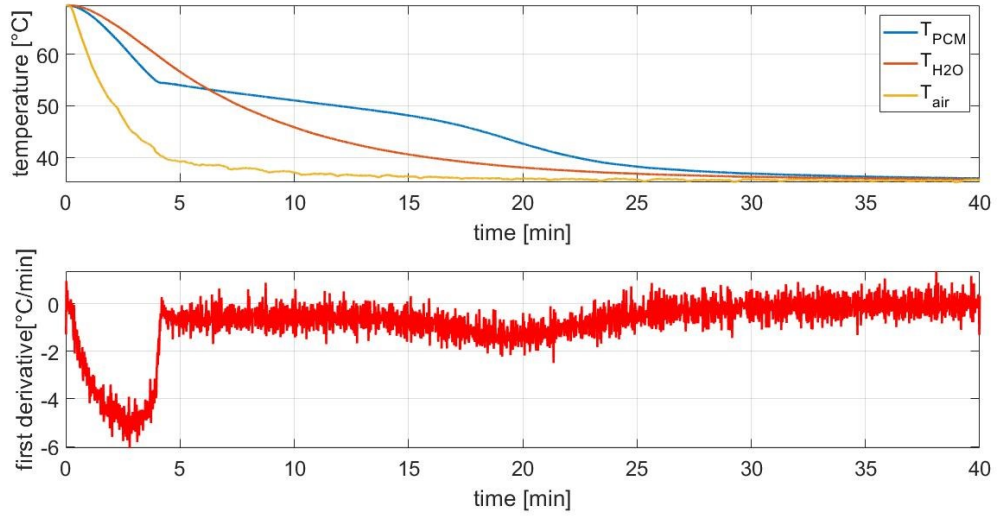
The second mathematical approach is the spline one. A spline is a function built by a set of polynomials which must interpolate a series of data in order to have a continuous first derivative. With this approach, the coefficient of determination results one for each curve: this means the spline perfectly fits the experimental points. The phase change boundaries are chosen as follow:

1. The solidification temperature is the point where the derivative abruptly changes [34]. This point is clearly visible in the RT55 and in the RT64HC, (as stated in subparagraph §A.4.4). However, for the RT42, a greater uncertainty is present due to the smoother change in the slope of the curve;
2. The inflection point is the minimum of the first derivative. In this case, it is quite hard to identify a precise point of inflection. The value is chosen graphically according to the results obtained in the first simulation;
3. The reference temperature is chosen 5°C greater than the final temperature of the thermostatic chamber.

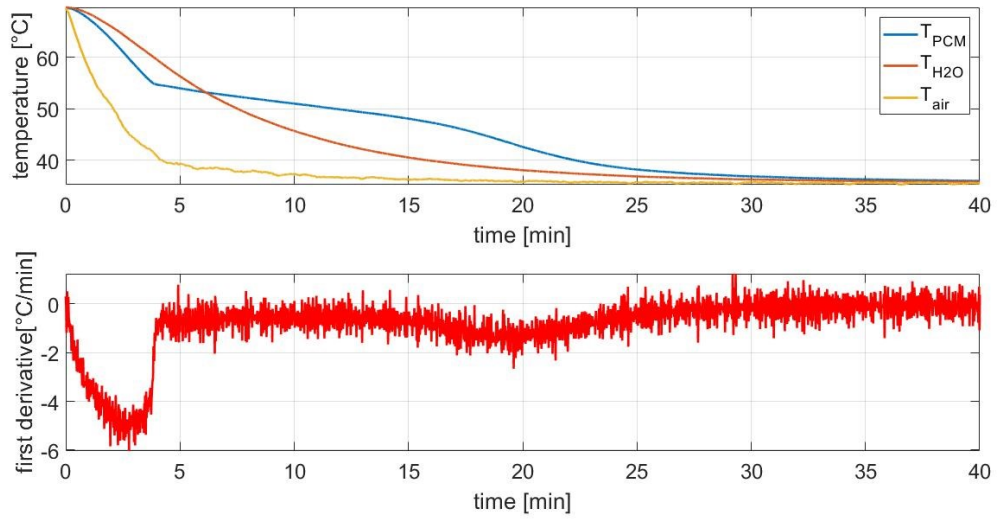
The code is B.12 in the Appendix B. The code is the same for all the others test with different input data. The graph resulted from the interpolations are reported in Figure A.18 for the RT55, Figure A.19 for the RT42 and Figure A.20 for the RT64HC.



(a)



(b)



(c)

Figure A.18. Interpolation of experimental points with spline of RT55 and first derivative.

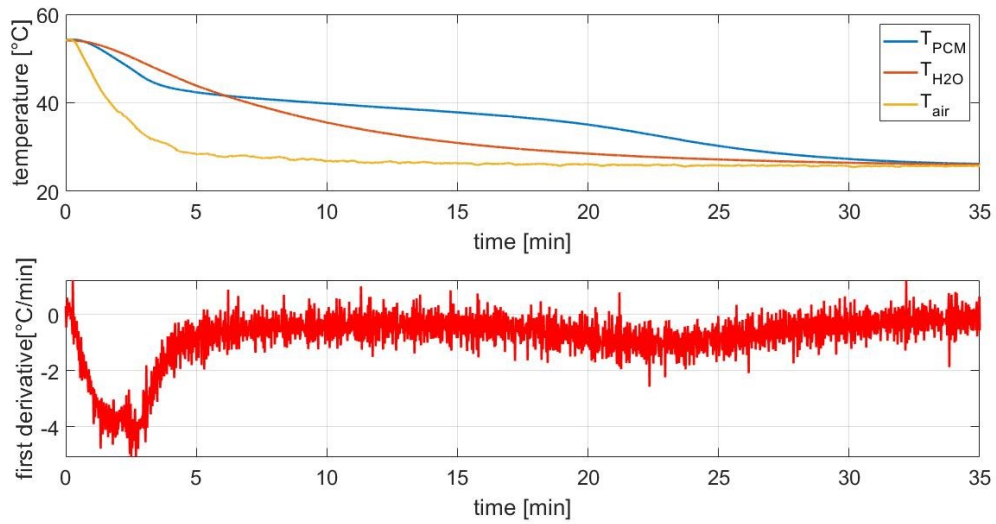


Figure A.19. Interpolation of experimental points with spline of RT42 and first derivative.

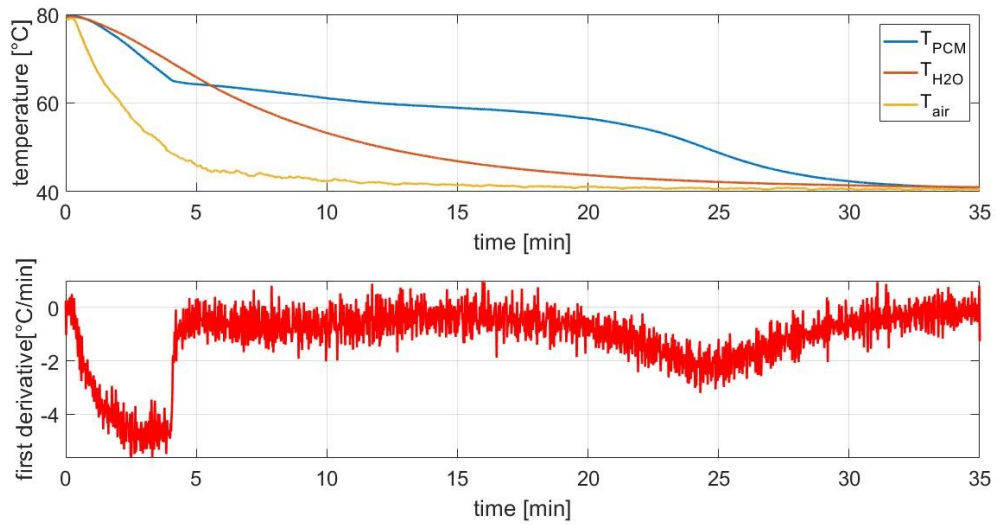


Figure A.20. Interpolation of experimental points with spline of RT64HC and first derivative.

The results are reported in the paragraph §A.5, where they will be compared and discussed with the other mathematical approaches used for the experiment.

A.4.6 Investigation on Biot number

Before presenting the results, it is necessary to verify the initial hypothesis ($Bi < 0.1$). Two different approaches are used for the verification. Results are reported in Table A.8. at the end of the subparagraph.

A.4.6.1 Method 1

The first approach presented is intrinsic in the T-history method. The equation (A. 16) can be rewritten as follow:

$$h = \frac{(m_{t,w}c_{p,t} + m_w c_w)(T_s - T_i)}{A_c A'_2} \quad (\text{A. 21})$$

where $m_{t,w}$ [kg] is the mass of the tube containing water, $c_{p,t}$ [$\text{kJ kg}^{-1} \text{K}^{-1}$] is the specific heat capacity of the tube, m_w [kg] is the mass of water in the tube, c_w [$\text{kJ kg}^{-1} \text{K}^{-1}$] is the specific heat capacity of water, T_s [$^{\circ}\text{C}$] is the solidification temperature, T_i [$^{\circ}\text{C}$] is the inflection point temperature, A_c area [m^2] of the tube and the integral is A'_2 .

Once the heat transfer coefficient has been determined, the Biot number can be calculated with equation (A.2). The calculation is done both for the method of the polynomial interpolation and for the spline method.

A.4.6.2 Method 2

The second approach follows the equations reported in Bonacina *et al* (1985) [32] for the natural convection of a fluid which is in contact with a vertical cylindrical surface¹¹

Once, for each time step, the temperature of the PCM T_{PCM} [$^{\circ}\text{C}$] and the temperature of the air T_{air} [$^{\circ}\text{C}$] have been determined, the film temperature T_f [$^{\circ}\text{C}$] can be calculated as follow:

¹¹ The temperature of the surface is assumed constant in space and, since the thickness of the tube is negligible, equals to the temperature of the paraffine.

$$T_f = \frac{T_{PCM} + T_{air}}{2}, \quad (\text{A. 22})$$

At this temperature and at a pressure of 1 atm, the thermal conductivity λ [$\text{W m}^{-1} \text{K}^{-1}$], the Prandtl number Pr , the kinematic viscosity ν [$\text{m}^2 \text{s}^{-1}$] and the thermal dilatation coefficient β [K^{-1}] are calculated with Refprop for each timestep.

The Grashof number is then calculated:

$$\text{Gr} = \frac{gL^3\beta(T_{PCM} - T_{air})}{\nu^2}, \quad (\text{A. 23})$$

where g is the gravity acceleration (9.81 m s^{-2}) and L is the characteristic dimension of the tube (which, in case of vertical surface, corresponds to the height h).

Rayleigh (Ra) and then Nusselt (Nu) numbers are then calculated:

$$\text{Ra} = \text{Gr} \times \text{Pr}, \quad (\text{A. 24})$$

$$\text{Nu} = 0.59 \text{Ra}^{\frac{1}{4}} \text{ if } 10^4 < \text{Ra} < 10^9,^{12} \quad (\text{A. 25})$$

$$h = \frac{\text{Nu} \lambda}{L}. \quad (\text{A. 26})$$

Once the heat transfer coefficient has been determined, the Biot number can be calculated with equation (A. 2). The maximum value between all the ones calculated in all the timestep is considered as the most critical.

¹² Equation (8.13) in [32]

A.4.6.3 Results

In Table A.7 the Biot values calculated with the two different approaches are both presented.

Paraffine	Bi Method 1 interpolation	Bi Method 1 spline	Bi Method 2
RT55 (1)	0.0230	0.0229	0.0623
RT55 (2)	0.0229	0.0229	0.0623
RT55 (3)	0.0231	0.0231	0.0626
RT42	0.0195	0.0193	0.0618
RT64HC	0.0225	0.0225	0.0660

Table A.7. Biot calculation with the two methods.

In all cases the Biot number is well below the critical values of 0.1. This justifies the initial hypothesis of uniform temperature distribution in the sample [33] and verifies the applicability of the lumped capacitance method, which is the core of the T-history approach.

A.5 Results and conclusions

A.5.1 Results

In Table A.8 the results of the polynomial interpolation method (§A.4.5.1) are presented and in Table A.9 the results of the spline interpolation are reported (§A.4.5.2).

Paraffine	T_s [°C]	T_i [°C]	Cp_s [kJ kg ⁻¹ K ⁻¹]	Cp_l [kJ kg ⁻¹ K ⁻¹]	$Cp_{averaged}$ [kJ kg ⁻¹ K ⁻¹]	H [kJ kg ⁻¹]	Err Cp %	Err H %
RT55 (1)	57.24	43.40	4.40	2.63	3.51	157.66	75.64	7.48
RT55 (2)	56.79	43.64	4.37	2.60	3.49	153.90	74.34	9.76
RT55 (3)	56.44	43.56	4.44	2.70	3.57	153.10	78.60	10.24
RT42	45.33	32.10	3.78	2.55	3.17	146.92	58.26	10.96
RT64HC	66.16	49.36	2.58	3.24	2.91	283.27	45.50	13.31

Table A.8. Experimental results of the polynomial interpolation method.

Paraffine	T_s [°C]	T_i [°C]	Cp_s [kJ kg ⁻¹ K ⁻¹]	Cp_l [kJ kg ⁻¹ K ⁻¹]	$Cp_{averaged}$ [kJ kg ⁻¹ K ⁻¹]	H [kJ kg ⁻¹]	Err Cp %	Err H %
RT55 (1)	54.73	43.32	4.29	2.69	3.49	158.78	74.54	6.60
RT55 (2)	54.49	43.38	4.26	2.64	3.45	156.00	72.42	8.24
RT55 (3)	54.92	43.15	4.22	2.59	3.40	158.29	70.17	6.89
RT42	43.60	32.09	4.04	2.82	3.43	140.96	71.67	14.57
RT64HC	65.00	50.32	2.94	3.18	3.06	280.47	52.98	12.19

Table A.9. Experimental results of the spline method.

It is possible to notice the three experiments conducted with the RT55 presents very similar results. This means that, in the same operative conditions, the method is replicable with high accuracy of the results presented. To validate the thesis, more tests should be conducted for the RT42 and for the RT64HC.

Both the methods present a solidification temperature very close to the one declared by the constructor in all the three paraffines. However, the spline interpolation is more precise in the definition of the solidification temperature. This is due to the nature of the spline itself: since it perfectly reflects the experimental points, the change in the slope of the curves is clearly visible (Figure A.16, A.17, A.18) and this allows to find with good precision the first point.

Looking at the two tables, it is possible to notice an important error on the calculation of the specific heat capacity. This is due to the lack of information given by the manufacturer. According to Table A.3, all the paraffines should present the same specific heat, which is 2 kJ kg⁻¹ K⁻¹. However, it is unknown if the values reported are related to the solid or the liquid phase. Furthermore, it is unknown even the temperature at which the specific heat capacity is evaluated. Despite this fact, looking at the tests for the RT55, the results are very similar to the ones in the articles by Martinez *et al.* [38] and by Rolka *et al.* [39]. A possible hypothesis of such differences from the constructor data is the proximity to the phase transition. During the experiments, different approaches were tested for the definition of the starting and ending points of the solidification and an important fact was noticed: the more precise the definition of the phase change interval, the higher is the error on the evaluation of the specific heat capacity. This is due to the thermodynamic definition of the specific heat capacity:

$$c_p = \frac{dh}{dT}, \quad (\text{A.27})$$

where dh is the enthalpy variation [kJ kg^{-1}] and dT is the temperature variation [K]. During the phase change process, the temperature variation is very small: as consequence, the c_p becomes huge (Figure A.21).

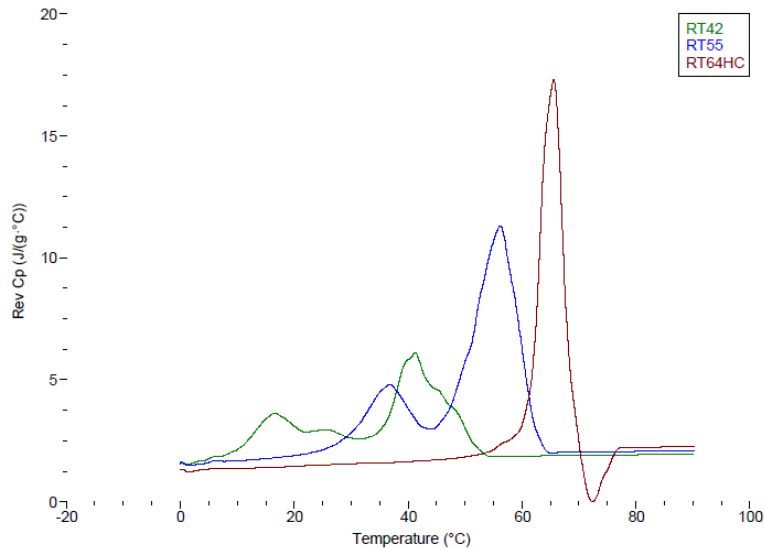


Figure A.21. Specific heat capacity of paraffines calculated with DSC method.

This is a big limitation of the T-history method: the extremes of the phase change intervals must be chosen very carefully. If the two points are selected in the area where the phase change occurs, despite being more precise in the definition of the phase change interval, the values of the specific heat (and consequently the values of the heat of solidification) are completely incorrect. It is probable that the manufacturer calculated the specific heat capacity very far away from the phase change interval. This could explain such differences between the results presented and the values obtained by the constructor.

Regarding the latent heat, the values are all presented with an error at maximum of 15% compared to the values of the constructor. The spline approach seems more precise in the calculation of the latent heat. This is probably due to the choice of the starting point, which is indeed more precise compared to the polynomial one. Furthermore, the values from the constructor are affected by an uncertainty of $\pm 7.5\%$.

Some experiments even for the fusion process have been tried. However, the fusion presents a crucial problem: the values of the specific heat of the solidus is completely wrong, much bigger than the water one. This could be due to two facts:

1. The starting point of the melting process is not as defined as it is in the case of the solidification. Since the method is extremely sensible to the phase change intervals, the error can be dramatically high;
2. After the loading of the PCM inside the tubes, a hole of air is formed inside the test tubes during the solidification. The air trapped inside the PCM could alter the measurement, leading to an important error in the evaluation of the specific heat capacity of the solidus.

For these two reasons, no results are presented for the fusion. A deeper investigation should be required to verify the hypothesis listed above.

A.5.2 Conclusions

The conclusions of the experience are here summarized:

1. Despite being a very simple and cheap method, the T-history is a very delicate approach. In particular, the choice of the intervals where the phase change process occurs is crucial for a proper determination of the specific heat capacity. A more precise choice of the temperature interval leads to a bigger error on the calculations. It is better to enlarge the phase change intervals to have a greater safety in the definition of the specific heat capacity (a greater interval does not affect importantly the values of latent heat calculated);
2. If the specific heat capacity is well defined, the latent heat calculations are reliable;
3. Despite the difference from the constructor data, the specific heats of the RT55 are similar to the ones found in literature [38, 39] and the results in the three different tests are close. This verifies the repeatability of the method;
4. For the RT42 and the RT65HC, no data have been found in literature as source of comparison apart from the ones presented by the manufacturer. To have a greater validation of the results of the present work, the tests should be repeated. Despite this, the values of the latent heat found are comparable with the manufacturer data

Appendix B:

MATLAB Codes

In this appendix, all the codes used in the present work are reported with the proper reference name. All the codes have been implemented in MATLAB [40], which is an environment for the numerical calculations written in C.

CODE B.1: Matrix extraction

```
clc
clear all
close all
load 20221007
z=[6000,7600,10150,14100,15900,17200,18500,19700,21000,22500];
A=A{:,:};
for i=1:10;
    B=A(z(i):z(i)+99,:);
    M(i,:)=mean(B);
    STD(i,:)=std(B);
end
M=array2table(M);
STD=array2table(STD);
```

CODE B.2: Cavallini *et al.*'s model for microfin tubes

```
lc
clear all
load ('Data_R1234zeE.mat');
num_righe=size(G,1);

%leggo file .txt
for i=1:num_righe
    pout(i)=pin(i)-Dptot(i); %bar
    pmean(i)=(pin(i)+pout(i))/2;%bar
    xin(i)=0.9999;
    xmean(i)=(xin(i)+xout(i))/2;
    deltax(i)=xin(i)-xout(i);
end

%caratteristiche microfin
h=0.15*10^-3; %altezza aletta
ng=54; %numero di alette
beta=30; %angolo d'elica
gamma=12; %angolo all'apice dell'aletta
Di=4.28*10^-3; %diametro all'apice dell'aletta
L=0.5; %lunghezza tubo totale
LHT=0.217;

%calcolo HTC
for i=1:num_righe
    HTC(i)=qtot(i)/DT(i)/(Di*pi*LHT);
end

% calcolo temperature medie
for i=1:num_righe
    Tsat(i)=refpropm('T','p',(pmean(i)*100),'Q',0,'R1234zee');
    Tsatwall(i)=(Tsat(i)+twmean(i)+273.15)/2;
end

%calcolo proprietà refrigerante
for i=1:num_righe

    rho_L(i)=(refpropm('D','T',Tsat(i),'Q',0,'R1234zee')+refpropm('D',
    'T',twmean(i)+273.15,'Q',0,'R1234zee'))/2;
    rho_V(i)=refpropm('D','T',Tsat(i),'Q',1,'R1234zee');

    lambda_L(i)=(refpropm('L','T',Tsat(i),'Q',0,'R1234zee')+refpropm('
    L','T',twmean(i)+273.15,'Q',0,'R1234zee'))/2;
    hLV(i)=(refpropm('H','T',Tsat(i),'Q',1,'R1234zee')-
    refpropm('H','T',Tsat(i),'Q',0,'R1234zee'));

    mu_L(i)=(3*refpropm('V','T',twmean(i)+273.15,'Q',0,'R1234zee')+ref
    propm('V','T',Tsat(i),'Q',0,'R1234zee'))/4;
    mu_V(i)=refpropm('V','T',Tsat(i),'Q',1,'R1234zee');

    cp_L(i)=(refpropm('C','T',Tsat(i),'Q',0,'R1234zee')+refpropm('C','
    T',twmean(i)+273.15,'Q',0,'R1234zee'))/2;
end

%modello Cavallini IJR2009
for i=1:num_righe
    JG(i)=xmean(i)*G(i)/(9.81*Di*rho_V(i)*(rho_L(i)-rho_V(i))^0.5;
    ReLO(i)=G(i)*Di/mu_L(i);
```

```

Pr_L(i)=cp_L(i)*mu_L(i)/lambda_L(i);
Xtt(i)=(mu_L(i)/mu_V(i))^0.1*(rho_V(i)/rho_L(i))^0.5*((1-
xmean(i))/xmean(i))^0.9;
alfaLO(i)=0.023*ReLO(i)^0.8*Pr_L(i)^0.4*lambda_L(i)/Di;
JGstar(i)=0.6*((7.5/(4.3*Xtt(i)^1.111+1))^-3+2.5^-3)^-0.3333;
if JG(i)<JGstar(i)
    C1(i)=JG(i)/JGstar(i);
else
    C1(i)=1;
end
alfaDS(i)=0.725/(1+0.741*((1-
xmean(i))/xmean(i))^0.3321)*(lambda_L(i)^3*rho_L(i)*(rho_L(i)-
rho_V(i))...
*9.81*hLV(i)/(mu_L(i)*Di*DT(i)))^0.25;
Rx=(2*h*ng*(1-sind(gamma/2))/(pi*Di*cosd(gamma/2))+1)/cosd(beta);
nopt=4064.4*Di+23.257;
%if nopt/ng<0.8
    %C=(nopt/ng)^1.904;
%else
    %C=1;
%end
C=1;

alfaD(i)=C*(2.4*xmean(i)^0.1206*(Rx-
1)^1.466*C1(i)^0.6875+1)*alfaDS(i)+C*(1-
xmean(i)^0.087)*Rx*alfaLO(i);
Fr(i)=G(i)^2/(9.81*Di*(rho_L(i)-rho_V(i))^2);
A(i)=1+1.19*Fr(i)^-0.3821*(Rx-1)^0.3586;

alfaAS(i)=alfaLO(i)*(1+1.128*xmean(i)^0.817*(rho_L(i)/rho_V(i))^0.3
685*(mu_L(i)/mu_V(i))^0.2363*...
(1-mu_V(i)/mu_L(i))^2.144*Pr_L(i)^-0.1);
alfaA(i)=alfaAS(i)*A(i)*C;
alfacalc(i)=(alfaA(i)^3+alfaD(i)^3)^0.333;

dev(i)=(alfacalc(i)-HTC(i))/HTC(i);
ratio(i)=alfacalc(i)/HTC(i);
dT(i)=Tb(i)+273.15-Tsat(i);
end
x1=[0 100000];
x2=[0 130000];
x3=[0 70000];
figure(1)
plot(HTC,alfacalc,'b*',x1,x1,'k',x1,x2,'k',x1,x3,'k','LineWidth',3)
axis([0 30000 0 30000])
set(gca,'FontSize',20)
xlabel('HTC_e_x_p_e_c_t_e_d [W m^-2 K^-1]')
ylabel('HTC_c_a_l_c_u_l_a_t_e_d [W m^-2 K^-1]')
title('Cavallini correlation, R1234ze(E)')

figure(2)
plot(G,ratio,'m+', 'LineWidth',3)
xlabel('G [kg s^-1 m^-2]')
set(gca,'FontSize',20)
ylabel('HTC_c_a_l_c_u_l_a_t_e_d /HTC_e_x_p_e_c_t_e_d ')
title('Effect of G on the evaluation of HTC')

rad=1/num_righe*sum(dev)*100
rad_abs=mean(abs(dev))*100
sigma=std(dev)*100

```

CODE B.3: Hirose *et al.*'s model for microfin tubes

```
clc
clear all
close all
load ('Data_R1234zeE.mat');
num_righe=size(G,1);

%leggo file .txt
for i=1:num_righe
    pout(i)=pin(i)-Dptot(i); %bar
    pmean(i)=(pin(i)+pout(i))/2;%bar
    xin(i)=0.9999;
    xmean(i)=(xin(i)+xout(i))/2;
    deltax(i)=xin(i)-xout(i);
end

%caratteristiche microfin
h=0.15*10^-3; %altezza aletta
ng=54; %numero di alette
beta=30; %angolo d'elica
gamma=12; %angolo all'apice dell'aletta
Di=4.28*10^-3; %diametro all'apice dell'aletta
Dmax=4.58*10^-3; %diametro alla base dell'aletta
L=0.5; %lunghezza tubo totale
Rx_base=1.967;
LHT=0.217;

%calcolo HTC
for i=1:num_righe
    HTC(i)=qtot(i)/DT(i)/(Dmax*pi*LHT);
end

% calcolo temperature medie
for i=1:num_righe
    Tsat(i)=refpropm('T','p',(pmean(i)*100),'Q',0,'R1234zee');
    Tsatwall(i)=(Tsat(i)+twmean(i)+273.15)/2;
end

%calcolo proprietà refrigerante
for i=1:num_righe

    rho_L(i)=(refpropm('D','T',Tsat(i),'Q',0,'R1234zee')+refpropm('D',
    'T',twmean(i)+273.15,'Q',0,'R1234zee'))/2;
    rho_V(i)=refpropm('D','T',Tsat(i),'Q',1,'R1234zee');

    lambda_L(i)=(refpropm('L','T',Tsat(i),'Q',0,'R1234zee')+refpropm('
    L','T',twmean(i)+273.15,'Q',0,'R1234zee'))/2;
    hLV(i)=(refpropm('H','T',Tsat(i),'Q',1,'R1234zee')-
    refpropm('H','T',Tsat(i),'Q',0,'R1234zee'));

    mu_L(i)=(3*refpropm('V','T',twmean(i)+273.15,'Q',0,'R1234zee')+ref
    propm('V','T',Tsat(i),'Q',0,'R1234zee'))/4;
    mu_V(i)=refpropm('V','T',Tsat(i),'Q',1,'R1234zee');

    cp_L(i)=(refpropm('C','T',Tsat(i),'Q',0,'R1234zee')+refpropm('C','
    T',twmean(i)+273.15,'Q',0,'R1234zee'))/2;

    sigma(i)=(refpropm('I','T',Tsat(i),'Q',0,'R1234zee')+refpropm('I',
    'T',twmean(i)+273.15,'Q',0,'R1234zee'))/2;
```

```

end

%modello Hirose
for i=1:num_righe
    eps_homo(i)=(1+rho_V(i)/rho_L(i)*((1-xmean(i))/xmean(i)))^-1;
    eps_smith(i)=(1+rho_V(i)/rho_L(i)*((1-xmean(i))/xmean(i))*0.4+0.6*sqrt(rho_V(i)/rho_L(i)+0.4*(1-xmean(i))/xmean(i)))/...
    sqrt(1+0.4*(1-xmean(i))/xmean(i)))^-1;

    eps(i)=0.81*eps_smith(i)+0.19*xmean(i)^(100*(rho_V(i)/rho_L(i))^0.8)*eps_homo(i);
    H(i)=eps(i)+(10*(1-eps(i))^0.1-8)*sqrt(eps(i))*(1-sqrt(eps(i)));
    Re_L(i)=Gmax(i)*(1-xmean(i))*Dmax/mu_L(i);
    Re_V(i)=Gmax(i)*xmean(i)*Dmax/mu_V(i);
    Xtt(i)=(mu_L(i)/mu_V(i))^0.1*(rho_V(i)/rho_L(i))^0.5*((1-xmean(i))/xmean(i))^0.9;
    Ga(i)=9.81*Dmax^3*rho_L(i)^2/mu_L(i)^2;
    fv(i)=0.26*Re_V(i)^-(0.38)*Rx_base^0.95*(cosd(beta))^-2.8;
    phi_V(i)=1+1.55*Xtt(i)^0.4;
    Pr_L(i)=cp_L(i)*mu_L(i)/lambda_L(i);
    Ph_L(i)=cp_L(i)*DT(i)/hLV(i);
    Bo(i)=(rho_L(i)-rho_V(i))*9.81*Dmax^2/sigma(i);

    if Re_L(i)<= 1250

        Fr_sol(i)=0.025*Re_L(i)^1.59*(((1+1.09*Xtt(i))^0.039)/Xtt(i))^1.5)/Ga(i)^0.5;
    else

        Fr_sol(i)=1.26*Re_L(i)^1.04*(((1+1.09*Xtt(i))^0.039)/Xtt(i))^1.5)/Ga(i)^0.5;
    end

    if Fr_sol(i)<20

        NuF(i)=7.85*sqrt(fv(i))*(phi_V(i)/Xtt(i))*(mu_L(i)/mu_V(i))^0.1*(xmean(i)/(1-xmean(i)))^0.1*Re_L(i)^0.47;
    else

        NuF(i)=15.4*sqrt(fv(i))*(phi_V(i)/Xtt(i))*(mu_L(i)/mu_V(i))^0.1*(xmean(i)/(1-xmean(i)))^0.1*Re_L(i)^0.43;
    end

    NuB(i)=1.60*Rx_base^-0.25*Bo(i)^-0.2*H(i)*(Ga(i)*Pr_L(i)/Ph_L(i))^0.25;
    Nu(i)=sqrt(NuF(i)^2+NuB(i)^2);
    alfacalc(i)= lambda_L(i)* Nu(i)/Dmax;

    dev(i)=(alfacalc(i)-HTC(i))/HTC(i);
    ratio(i)=alfacalc(i)/HTC(i);
end

x1=[0 100000];
x2=[0 130000];
x3=[0 70000];
figure(1)
plot(HTC,alfacalc,'b*',x1,x1,'k',x1,x2,'k',x1,x3,'k','LineWidth',3)
set(gca,'FontSize',20)
axis([0 40000 0 40000])

```

```

set(gca, 'FontSize', 18)
xlabel('HTC_e_x_p_e_c_t_e_d [W m^-^2 K^-^1]')
ylabel('HTC_c_a_l_c_u_l_a_t_e_d [W m^-^2 K^-^1]')
title('Hirose correlation, R1234ze(E)')

figure(2)
plot(xmean, ratio, 'r*')
set(gca, 'FontSize', 20)
ylabel('HTC_c_a_l_c_u_l_a_t_e_d /HTC_e_x_p_e_c_t_e_d [-]')
xlabel('x_m_e_a_n [-]')
title('Effect of x on the evaluation of HTC,
R1234ze(E)', 'LineWidth', 3)

rad=1/num_righe*sum(dev)*100
rad_abs=mean(abs(dev))*100
sigma=std(dev)*100

```

CODE B.4: Interpolation for wavy flow points

```
clc
clear all
close all
load ('Data_R1234zeE.mat');
num_righe=size(G,1);

%leggo file .txt
for i=1:num_righe
    pout(i)=pin(i)-Dptot(i); %bar
    pmean(i)=(pin(i)+pout(i))/2;%bar
    xin(i)=0.9999;
    xmean(i)=(xin(i)+xout(i))/2;
    deltax(i)=xin(i)-xout(i);
end

%caratteristiche microfin
h=0.15*10^-3; %altezza aletta
ng=54; %numero di alette
beta=30; %angolo d'elica
gamma=12; %angolo all'apice dell'aletta
Di=4.28*10^-3; %diametro all'apice dell'aletta
Dmax=4.58*10^-3; %diametro alla base dell'aletta
L=0.5; %lunghezza tubo totale
LHT=0.217;
Rx_base=1.97;
%calcolo HTC
for i=1:num_righe
    HTC(i)=qtot(i)/DT(i)/(Dmax*pi*LHT);
end

% calcolo temperature medie
for i=1:num_righe
    Tsat(i)=refpropm('T','p',(pmean(i)*100),'Q',0,'R1234zee');
    Tsatwall(i)=(Tsat(i)+twmean(i)+273.15)/2;
end

%calcolo proprietà refrigerante
for i=1:num_righe

    rho_L(i)=(refpropm('D','T',Tsat(i),'Q',0,'R1234zee')+refpropm('D',
    'T',twmean(i)+273.15,'Q',0,'R1234zee'))/2;
    rho_V(i)=refpropm('D','T',Tsat(i),'Q',1,'R1234zee');

    lambda_L(i)=(refpropm('L','T',Tsat(i),'Q',0,'R1234zee')+refpropm('
    L','T',twmean(i)+273.15,'Q',0,'R1234zee'))/2;
    hLV(i)=(refpropm('H','T',Tsat(i),'Q',1,'R1234zee')-
    refpropm('H','T',Tsat(i),'Q',0,'R1234zee'));

    mu_L(i)=(3*refpropm('V','T',twmean(i)+273.15,'Q',0,'R1234zee')+ref
    propm('V','T',Tsat(i),'Q',0,'R1234zee'))/4;
    mu_V(i)=refpropm('V','T',Tsat(i),'Q',1,'R1234zee');

    cp_L(i)=(refpropm('C','T',Tsat(i),'Q',0,'R1234zee')+refpropm('C','
    T',twmean(i)+273.15,'Q',0,'R1234zee'))/2;

    sigma(i)=(refpropm('I','T',Tsat(i),'Q',0,'R1234zee')+refpropm('I',
    'T',twmean(i)+273.15,'Q',0,'R1234zee'))/2;
end
```

```

%modello Hirose
for i=1:num_righe
    eps_hom0(i)=(1+rho_V(i)/rho_L(i)*((1-xmean(i))/xmean(i)))^-1;
    eps_smith(i)=(1+rho_V(i)/rho_L(i)*((1-xmean(i))/xmean(i))* (0.4+0.6*sqrt(rho_V(i)/rho_L(i)+0.4*(1-xmean(i))/xmean(i)))/...
    sqrt(1+0.4*(1-xmean(i))/xmean(i))))^-1;

    eps(i)=0.81*eps_smith(i)+0.19*xmean(i)^(100*(rho_V(i)/rho_L(i))^0.8)*eps_homo(i);
    H(i)=eps(i)+(10*(1-eps(i))^0.1-8)*sqrt(eps(i))*(1-sqrt(eps(i)));
    Re_L(i)=Gmax(i)*(1-xmean(i))*Dmax/mu_L(i);
    Re_V(i)=Gmax(i)*xmean(i)*Dmax/mu_V(i);
    Xtt(i)=(mu_L(i)/mu_V(i))^0.1*(rho_V(i)/rho_L(i))^0.5*((1-xmean(i))/xmean(i))^0.9;
    Ga(i)=9.81*Dmax^3*rho_L(i)^2/mu_L(i)^2;
    fv(i)=0.26*Re_V(i)^-0.38*Rx_base^0.95*(cosd(beta))^-2.8;
    phi_V(i)=1+1.55*Xtt(i)^0.4;
    Pr_L(i)=cp_L(i)*mu_L(i)/lambda_L(i);
    Ph_L(i)=cp_L(i)*DT(i)/hLV(i);
    Bo(i)=(rho_L(i)-rho_V(i))*9.81*Dmax^2/sigma(i);
    if Re_L(i)<= 1250

        Fr_sol(i)=0.025*Re_L(i)^1.59*(((1+1.09*Xtt(i)^0.039)/Xtt(i))^1.5)/Ga(i)^0.5;
    else

        Fr_sol(i)=1.26*Re_L(i)^1.04*(((1+1.09*Xtt(i)^0.039)/Xtt(i))^1.5)/Ga(i)^0.5;
    end
    if Fr_sol(i)<20
        NuB(i)=0.725*Rx_base^-0.25*H(i)*(Ga(i)*Pr_L(i)/Ph_L(i))^0.25;
        Nu(i)=HTC(i)*Dmax/lambda_L(i);
        Ratio(i)=(Nu(i)^2-NuB(i)^2)^0.5/(sqrt((0.5)*fv(i))*Re_L(i)*phi_V(i)*(rho_L(i)/rho_V(i))^0.5*((xmean(i)/(1-xmean(i)))));
    else
        NuB(i)=0;
        Nu(i)=0;
        Ratio(i)=0;
        Re_L(i)=0;
    end
end
end
Ratio=nonzeros(Ratio);
Re_L=nonzeros(Re_L);
p=polyfit(log10(Re_L),log10(Ratio),1);
b=p(1);
a=10^p(2);
yy=a*Re_L.^b;
figure(1)
plot(log(Re_L),log(Ratio),'b*')
hold on
plot(log(Re_L),log(yy))

```

CODE B.5: Interpolation for annular flow points

```
clc
clear all
close all
load ('Data_R1234zeE.mat');
num_righe=size(G,1);

%leggo file .txt
for i=1:num_righe
    pout(i)=pin(i)-Dptot(i); %bar
    pmean(i)=(pin(i)+pout(i))/2;%bar
    xin(i)=0.9999;
    xmean(i)=(xin(i)+xout(i))/2;
    deltax(i)=xin(i)-xout(i);
end

%caratteristiche microfin
h=0.15*10^-3; %altezza aletta
ng=54; %numero di alette
beta=30; %angolo d'elica
gamma=12; %angolo all'apice dell'aletta
Di=4.28*10^-3; %diametro all'apice dell'aletta
Dmax=4.58*10^-3; %diametro alla base dell'aletta
L=0.5; %lunghezza tubo totale
Rx_base=1.97; %incremento area considerando base aletta
LHT=0.217;
%calcolo HTC
for i=1:num_righe
    HTC(i)=qtot(i)/DT(i)/(Dmax*pi*LHT);
end

% calcolo temperature medie
for i=1:num_righe
    Tsat(i)=refpropm('T','p',(pmean(i)*100),'Q',0,'R1234zee');
    Tsatwall(i)=(Tsat(i)+twmean(i)+273.15)/2;
end

%calcolo proprietà refrigerante
for i=1:num_righe

    rho_L(i)=(refpropm('D','T',Tsat(i),'Q',0,'R1234zee')+refpropm('D',
    'T',twmean(i)+273.15,'Q',0,'R1234zee'))/2;
    rho_V(i)=refpropm('D','T',Tsat(i),'Q',1,'R1234zee');

    lambda_L(i)=(refpropm('L','T',Tsat(i),'Q',0,'R1234zee')+refpropm('
    L','T',twmean(i)+273.15,'Q',0,'R1234zee'))/2;
    hLV(i)=(refpropm('H','T',Tsat(i),'Q',1,'R1234zee')-
    refpropm('H','T',Tsat(i),'Q',0,'R1234zee'));

    mu_L(i)=(3*refpropm('V','T',twmean(i)+273.15,'Q',0,'R1234zee')+ref
    propm('V','T',Tsat(i),'Q',0,'R1234zee'))/4;
    mu_V(i)=refpropm('V','T',Tsat(i),'Q',1,'R1234zee');

    cp_L(i)=(refpropm('C','T',Tsat(i),'Q',0,'R1234zee')+refpropm('C',
    'T',twmean(i)+273.15,'Q',0,'R1234zee'))/2;

    sigma(i)=(refpropm('I','T',Tsat(i),'Q',0,'R1234zee')+refpropm('I',
    'T',twmean(i)+273.15,'Q',0,'R1234zee'))/2;
end
```

```

%modello Hirose
for i=1:num_righe
    eps_homo(i)=(1+rho_V(i)/rho_L(i)*((1-xmean(i))/xmean(i)))^-1;
    eps_smith(i)=(1+rho_V(i)/rho_L(i)*((1-xmean(i))/xmean(i))*(0.4+0.6*sqrt(rho_V(i)/rho_L(i)+0.4*(1-xmean(i))/xmean(i)))/...
    sqrt(1+0.4*(1-xmean(i))/xmean(i))))^-1;

    eps(i)=0.81*eps_smith(i)+0.19*xmean(i)^(100*(rho_V(i)/rho_L(i))^0.8)*eps_homo(i);
    H(i)=eps(i)+(10*(1-eps(i))^0.1-8)*sqrt(eps(i))*(1-sqrt(eps(i)));
    Re_L(i)=Gmax(i)*(1-xmean(i))*Dmax/mu_L(i);
    Re_V(i)=Gmax(i)*xmean(i)*Dmax/mu_V(i);
    Xtt(i)=(mu_L(i)/mu_V(i))^0.1*(rho_V(i)/rho_L(i))^0.5*((1-xmean(i))/xmean(i))^0.9;
    Ga(i)=9.81*Dmax^3*rho_L(i)^2/mu_L(i)^2;
    fv(i)=0.26*Re_V(i)^-0.38*Rx_base^0.95*(cosd(beta))^-2.8;
    phi_V(i)=1+1.55*Xtt(i)^0.4;
    Pr_L(i)=cp_L(i)*mu_L(i)/lambda_L(i);
    Ph_L(i)=cp_L(i)*DT(i)/hLV(i);
    Bo(i)=(rho_L(i)-rho_V(i))*9.81*Dmax^2/sigma(i);
    if Re_L(i)<= 1250

        Fr_sol(i)=0.025*Re_L(i)^1.59*(((1+1.09*Xtt(i)^0.039)/Xtt(i))^1.5)/Ga(i)^0.5;
    else

        Fr_sol(i)=1.26*Re_L(i)^1.04*(((1+1.09*Xtt(i)^0.039)/Xtt(i))^1.5)/Ga(i)^0.5;
    end
    if Fr_sol(i)>20
        NuB(i)=0.725*Rx_base^-0.25*H(i)*(Ga(i)*Pr_L(i)/Ph_L(i))^0.25;
        Nu(i)=HTC(i)*Dmax/lambda_L(i);
        Ratio(i)=(Nu(i)^2-NuB(i)^2)^0.5/(sqrt((0.5)*fv(i))*Re_L(i)*phi_V(i)*(rho_L(i)/rho_V(i))^0.5*((xmean(i)/(1-xmean(i)))));
    else
        NuB(i)=0;
        Nu(i)=0;
        Ratio(i)=0;
        Re_L(i)=0;
    end
end
Ratio=nonzeros(Ratio);
Re_L=nonzeros(Re_L);
p=polyfit(log10(Re_L),log10(Ratio),1);
b=p(1);
a=10^p(2);
yy=a*Re_L.^b;
figure(1)
plot(log(Re_L),log(Ratio),'b*')
hold on
plot(log(Re_L),log(yy))

```

CODE B.6: Hirose *et al.*'s modified model

```
clc
clear all
close all
load ('Data_R1234zeE.mat');
num_righe=size(G,1);

%leggo file .txt
for i=1:num_righe
    pout(i)=pin(i)-Dptot(i); %bar
    pmean(i)=(pin(i)+pout(i))/2;%bar
    xin(i)=0.9999;
    xmean(i)=(xin(i)+xout(i))/2;
    deltax(i)=xin(i)-xout(i);
end

%caratteristiche microfin
h=0.15*10^-3; %altezza aletta
ng=54; %numero di alette
beta=30; %angolo d'elica
gamma=12; %angolo all'apice dell'aletta
Di=4.28*10^-3; %diametro all'apice dell'aletta
Dmax=4.58*10^-3; %diametro alla base dell'aletta
L=0.5; %lunghezza tubo totale
Rx_base=1.967;
LHT=0.217;

%calcolo HTC
for i=1:num_righe
    HTC(i)=qtot(i)/DT(i)/(Dmax*pi*LHT);
end

% calcolo temperature medie
for i=1:num_righe
    Tsat(i)=refpropm('T','p',(pmean(i)*100),'Q',0,'R1234zee');
    Tsatwall(i)=(Tsat(i)+twmean(i)+273.15)/2;
end

%calcolo proprietà refrigerante
for i=1:num_righe

    rho_L(i)=(refpropm('D','T',Tsat(i),'Q',0,'R1234zee')+refpropm('D',
    'T',twmean(i)+273.15,'Q',0,'R1234zee'))/2;
    rho_V(i)=refpropm('D','T',Tsat(i),'Q',1,'R1234zee');

    lambda_L(i)=(refpropm('L','T',Tsat(i),'Q',0,'R1234zee')+refpropm('
    L','T',twmean(i)+273.15,'Q',0,'R1234zee'))/2;
    hLV(i)=(refpropm('H','T',Tsat(i),'Q',1,'R1234zee')-
    refpropm('H','T',Tsat(i),'Q',0,'R1234zee'));

    mu_L(i)=(3*refpropm('V','T',twmean(i)+273.15,'Q',0,'R1234zee')+ref
    propm('V','T',Tsat(i),'Q',0,'R1234zee'))/4;
    mu_V(i)=refpropm('V','T',Tsat(i),'Q',1,'R1234zee');

    cp_L(i)=(refpropm('C','T',Tsat(i),'Q',0,'R1234zee')+refpropm('C','
    T',twmean(i)+273.15,'Q',0,'R1234zee'))/2;
```

```

sigma(i)=(refpropm('I','T',Tsat(i),'Q',0,'R1234zee')+refpropm('I',
'T',twmean(i)+273.15,'Q',0,'R1234zee'))/2;
end

%modello Hirose
for i=1:num_righe
eps_homo(i)=(1+rho_V(i)/rho_L(i)*((1-xmean(i))/xmean(i)))^-1;
eps_smith(i)=(1+rho_V(i)/rho_L(i)*((1-
xmean(i))/xmean(i))*(0.4+0.6*sqrt(rho_V(i)/rho_L(i)+0.4*(1-
xmean(i))/xmean(i)))/...
sqrt(1+0.4*(1-xmean(i))/xmean(i)))^-1;

eps(i)=0.81*eps_smith(i)+0.19*xmean(i)^(100*(rho_V(i)/rho_L(i))^0.
8)*eps_homo(i);
H(i)=eps(i)+(10*(1-eps(i))^0.1-8)*sqrt(eps(i))*(1-sqrt(eps(i)));
Re_L(i)=Gmax(i)*(1-xmean(i))*Dmax/mu_L(i);
Re_V(i)=Gmax(i)*xmean(i)*Dmax/mu_V(i);
Xtt(i)=(mu_L(i)/mu_V(i))^0.1*(rho_V(i)/rho_L(i))^0.5*((1-
xmean(i))/xmean(i))^0.9;
Ga(i)=9.81*Dmax^3*rho_L(i)^2/mu_L(i)^2;
fv(i)=0.26*Re_V(i)^-0.38*Rx_base^0.95*(cosd(beta))^-2.8;
phi_V(i)=1+1.55*Xtt(i)^0.4;
Pr_L(i)=cp_L(i)*mu_L(i)/lambda_L(i);
Ph_L(i)=cp_L(i)*DT(i)/hLV(i);
Bo(i)=(rho_L(i)-rho_V(i))*9.81*Dmax^2/sigma(i);

if Re_L(i)<= 1250

    Fr_sol(i)=0.025*Re_L(i)^1.59*(((1+1.09*Xtt(i))^0.039)/Xtt(i))^1
    .5)/Ga(i)^0.5;
else

    Fr_sol(i)=1.26*Re_L(i)^1.04*(((1+1.09*Xtt(i))^0.039)/Xtt(i))^1.
    5)/Ga(i)^0.5;
end

if Fr_sol(i)<20

    NuF(i)=3.90*sqrt(fv(i))*(phi_V(i)/Xtt(i))*(mu_L(i)/mu_V(i))^0.
    1*(xmean(i)/(1-xmean(i)))^0.1*Re_L(i)^0.55;
else

    NuF(i)=2.67*sqrt(fv(i))*(phi_V(i)/Xtt(i))*(mu_L(i)/mu_V(i))^0.
    1*(xmean(i)/(1-xmean(i)))^0.1*Re_L(i)^0.63;
end

NuB(i)=0.725*Rx_base^-0.25*H(i)*(Ga(i)*Pr_L(i)/Ph_L(i))^0.25;
Nu(i)=sqrt(NuF(i)^2+NuB(i)^2);
alfacalc(i)= lambda_L(i)* Nu(i)/Dmax;

dev(i)=(alfacalc(i)-HTC(i))/HTC(i);
ratio(i)=alfacalc(i)/HTC(i);
end

x1=[0 100000];
x2=[0 130000];
x3=[0 70000];
figure(1)
plot(HTC,alfacalc,'b*',x1,x1,'k',x1,x2,'k',x1,x3,'k','LineWidth',3)

```

```

axis([0 30000 0 30000])
set(gca,'FontSize',20)
xlabel('HTC_e_x_p_e_c_t_e_d [W m^-^2 K^-^1]')
ylabel('HTC_c_a_l_c_u_l_a_t_e_d [W m^-^2 K^-^1]')
title('Hirose modified correlation, R1234ze(E)')
figure(2)
plot(xmean, ratio, 'r*')
set(gca,'FontSize',20)
ylabel('HTC_c_a_l_c_u_l_a_t_e_d /HTC_e_x_p_e_c_t_e_d [-]')
xlabel('x_m_e_a_n [-]')
title('Effect of x on the evaluation of HTC,
R1234ze(E)', 'LineWidth',3)

rad=1/num_righe*sum(dev)*100
rad_abs=mean(abs(dev))*100
sigma=std(dev)*100

```

CODE B.7: Webb's model

```
clc
clear all
load ('Data_R1234zeE.mat');
num_righe=size(G,1);

%% Cavallini
%leggo file .txt
for i=1:num_righe
    pout(i)=pin(i)-Dptot(i); %bar
    pmean(i)=(pin(i)+pout(i))/2;%bar
    xin(i)=0.9999;
    xmean(i)=(xin(i)+xout(i))/2;
    deltax(i)=xin(i)-xout(i);
end

%caratteristiche microfin
h=0.15*10^-3; %altezza aletta
ng=54; %numero di alette
beta=30; %angolo d'elica
gamma=12; %angolo all'apice dell'aletta
Di=4.28*10^-3; %diametro all'apice dell'aletta
L=0.5; %lunghezza tubo totale
LHT=0.217;

%calcolo HTC
for i=1:num_righe
    HTC(i)=qtot(i)/DT(i)/(Di*pi*LHT);
end

% calcolo temperature medie
for i=1:num_righe
    Tsat(i)=refpropm('T','p',(pmean(i)*100),'Q',0,'R1234zee');
    Tsatwall(i)=(Tsat(i)+twmean(i)+273.15)/2;
end

%calcolo proprietà refrigerante
for i=1:num_righe

    rho_L(i)=(refpropm('D','T',Tsat(i),'Q',0,'R1234zee')+refpropm('D',
    'T',twmean(i)+273.15,'Q',0,'R1234zee'))/2;
    rho_V(i)=refpropm('D','T',Tsat(i),'Q',1,'R1234zee');

    lambda_L(i)=(refpropm('L','T',Tsat(i),'Q',0,'R1234zee')+refpropm('
    L','T',twmean(i)+273.15,'Q',0,'R1234zee'))/2;
    hLV(i)=(refpropm('H','T',Tsat(i),'Q',1,'R1234zee')-
    refpropm('H','T',Tsat(i),'Q',0,'R1234zee'));

    mu_L(i)=(3*refpropm('V','T',twmean(i)+273.15,'Q',0,'R1234zee')+r
    efprom('V','T',Tsat(i),'Q',0,'R1234zee'))/4;
    mu_V(i)=refpropm('V','T',Tsat(i),'Q',1,'R1234zee');

    cp_L(i)=(refpropm('C','T',Tsat(i),'Q',0,'R1234zee')+refpropm('C','
    T',twmean(i)+273.15,'Q',0,'R1234zee'))/2;
end

%modello Cavallini IJR2009
for i=1:num_righe
    JG(i)=xmean(i)*G(i)/(9.81*Di*rho_V(i)*(rho_L(i)-rho_V(i))^0.5;
    ReLO(i)=G(i)*Di/mu_L(i);
```

```

Pr_L(i)=cp_L(i)*mu_L(i)/lambda_L(i);
Xtt(i)=(mu_L(i)/mu_V(i))^0.1*(rho_V(i)/rho_L(i))^0.5*((1-
xmean(i))/xmean(i))^0.9;
alfaLO(i)=0.023*ReLO(i)^0.8*Pr_L(i)^0.4*lambda_L(i)/Di;
JGstar(i)=0.6*((7.5/(4.3*Xtt(i)^1.111+1))^-3+2.5^-3)^-0.3333;
if JG(i)<JGstar(i)
    C1(i)=JG(i)/JGstar(i);
else
    C1(i)=1;
end
alfaDS(i)=0.725/(1+0.741*((1-
xmean(i))/xmean(i))^0.3321)*(lambda_L(i)^3*rho_L(i)*(rho_L(i)-
rho_V(i))...
*9.81*hLV(i)/(mu_L(i)*Di*DT(i))^0.25;
Rx=(2*h*ng*(1-sind(gamma/2))/(pi*Di*cosd(gamma/2))+1)/cosd(beta);
nopt=4064.4*Di+23.257;
%if nopt/ng<0.8
    %C=(nopt/ng)^1.904;
%else
    %C=1;
%end
C=1;

alfaD(i)=C*(2.4*xmean(i)^0.1206*(Rx-
1)^1.466*C1(i)^0.6875+1)*alfaDS(i)+C*(1-
xmean(i)^0.087)*Rx*alfaLO(i);
Fr(i)=G(i)^2/(9.81*Di*(rho_L(i)-rho_V(i))^2);
A(i)=1+1.19*Fr(i)^-0.3821*(Rx-1)^0.3586;

alfaAS(i)=alfaLO(i)*(1+1.128*xmean(i)^0.817*(rho_L(i)/rho_V(i))^0.3
685*(mu_L(i)/mu_V(i))^0.2363*...
(1-mu_V(i)/mu_L(i))^2.144*Pr_L(i)^-0.1);
alfaA(i)=alfaAS(i)*A(i)*C;
alfacalc(i)=(alfaA(i)^3+alfaD(i)^3)^0.333;
end

%% Gnieliski
%calcolo proprietà refrigerante
for i=1:num_righe;
    mu_V(i)=refpropm('V','T',Tb(i)+273.15,'P',pmean(i),'R1234zee');
    Prb(i)=refpropm('^','T',Tb(i)+273.15,'P',pmean(i),'R1234zee');
    Prb_w(i)=refpropm('^','T',twmean(i)+273.15,'P',pmean(i),'R1234zee'
);
    lambda_V(i)=refpropm('L','T',Tb(i)+273.15,'P',pmean(i),'R1234zee')
;
    Re_V(i)=G(i)*xmean(i)*Di/mu_V(i);
end

%Gnieliski
for i=1:num_righe
    if Re_V(i)<2300
        Numq1=4.354;
        Numq2=1.953*(Re_V(i)*Prb(i)*Di/LHT)^(1/3);
        Numq3=0.924*(Re_V(i)*Di/LHT)^0.5*(Prb(i))^(1/3);
        Nuo(i)=(Numq1^3+0.6^3+(Numq2-0.6)^3+Numq3^3)^(1/3);
    elseif Re_V(i)>4000
        fb(i)=[1.8*log10(Re_V(i))-1.5]^(-2);
        Nuo(i)=[(fb(i)/8)*(Re_V(i)-
1000)*Prb(i)]/[1+12.7*(fb(i)/8)^(1/2)*(Prb(i)^(2/3)-1)]*...
(1+(Di/LHT)^(2/3))*Prb(i)/Prb_w(i)^0.11;
    else

```

```

    Numq1=4.354;
    Numq2_2300=1.953*(2300*Prb(i)*Di/LHT)^(1/3);
    Numq3=0.924*(2300*Di/LHT)^0.5*(Prb(i))^(1/3);
    Nu2300(i)=(Numq1^3+0.6^3+(Numq2-0.6)^3+Numq3^3)^(1/3);
    fb(i)=[1.8*log10(4000)-1.5]^(-2);
    Nu4000(i)=[(fb(i)/8)*(4000-1000)*Prb(i)]/[1+12.7*(fb(i)/8)^(1/2)*(Prb(i)^(2/3)-1)]*...
    (1+(Di/LHT)^(2/3))*(Prb(i)/Prb_w(i))^0.11;
    gamma(i)=(Re_V(i)-2300)/(4000-2300);
    Nuo(i)=(1-gamma(i))*Nu2300(i)+gamma(i)*Nu4000(i);
end
    alfa_sensible(i)=Nuo(i)*Rx*lambda_V(i)/Di;
end

%% alfa totale
for i=1:num_righe
    alfa(i)=alfa_sensible(i)*(Tb(i)+273.15-Tsat(i))/DT(i)+alfacalc(i);
    dev(i)=(alfa(i)-HTC(i))/HTC(i);
    ratio1(i)=alfa(i)/HTC(i);
    ratio(i)=alfacalc(i)/HTC(i);
end

x1=[0 100000];
x2=[0 130000];
x3=[0 70000];
figure(1)
plot(HTC,alfa,'r*',HTC,alfacalc,'b*',x1,x1,'k',x1,x2,'k',x1,x3,'k','LineWidth',3)
hold on
axis([0 30000 0 30000])
set(gca,'FontSize',20)
legend('Gnielinski+Cavallini','Cavallini')
xlabel('HTC_expected [W m^-2 K^-1]')
ylabel('HTC_calculated [W m^-2 K^-1]')
title('Webb correlation vs Cavallini correlation , R1234ze(E)')

figure(2)
plot(G,ratio1,'g+', 'LineWidth',3)
hold on
plot(G,ratio,'m+', 'LineWidth',3)
legend('Gnielinski+Cavallini','Cavallini')
xlabel('G [kg s^-1 m^-2]')
set(gca,'FontSize',20)
ylabel('HTC_calculated /HTC_expected ')
title('Effect of G on the evaluation of HTC')

rad=1/num_righe*sum(dev)*100
rad_abs=mean(abs(dev))*100
sigma=std(dev)*100

```

CODE B.8: Condenser design with Cavallini *et al.*'s model and OD 7mm

```

clc
clear all
close all

%% Geometria
De=7*10^-3; %[m]
Di=6.14*10^-3; %[m]
Dimax=6.5*10^-3; %[m]
%Rx_base=1.967;
e=0.18*10^-3; %altezza aletta
ng=50; %numero di alette
beta=18; %angolo d'elica
gamma=43; %angolo all'apice dell'aletta
lambda_tubo=390;
Rx=(2*e*ng*(1-sind(gamma/2))/(pi*Di*cosd(gamma/2))+1)/cosd(beta);
p=1.5*De; %[m] pitch
Rcoil=0.1; %[m]
Dcoil=2*Rcoil; %[m]
Dtank=0.3; %[m]
dL=sqrt((Dcoil*pi)^2+p^2); %[m] lunghezza spira
Ai=dL*pi*Di; %[m^2] area spira interna rispetto a Di
Ae=dL*pi*De; %[m^2] area spira esterna rispetto a De
N=23; %numero di mezze spire supposte

%% Refrigerante
Tsat=50; %[C]
SH=15;
TrefIN=Tsats+SH;
PrefIN=refpropm('p','T',Tsats+273.15,'Q',1,'R1234zee'); %[kPa]
hrefIN=refpropm('h','T',TrefIN+273.15,'p',PrefIN,'R1234zee'); %[J/kg]
hrefOUT=refpropm('h','T',Tsats+273.15,'Q',0,'R1234zee'); %[J/kg]
hV=refpropm('h','T',Tsats+273.15,'Q',1,'R1234zee'); %[J/kg]
hL=refpropm('h','T',Tsats+273.15,'Q',0,'R1234zee'); %[J/kg]
Q=1000; %[W]
mref=Q/(hrefIN-hrefOUT);
G=4*mref/(pi*Di^2);
Gmax=4*mref/(pi*Dimax^2);

%% Acqua
TwaterIN=283.15;
TwaterOUT=313.15;
Pwater=101.325; %[kPa]
mwater=Q/(4186*(TwaterOUT-TwaterIN));

%% Calcoli spira per spira
n=0;
TwaterOUT=ones(1,N);
TwaterIN=ones(1,N);
TwaterIN(1)=283.15; %K
hrefIN=ones(1,N);
hrefIN(1)=refpropm('h','T',TrefIN+273.15,'p',PrefIN,'R1234zee');
hrefOUT=ones(1,N);
xin=ones(1,N);
xin(1)=0.99;
xout=ones(1,N);
TrefIN=ones(1,N);
TrefIN(1)=65; %°C

```

```

TrefOUT=ones(1,N);
QTOT=0;
K=ones(1,N);
alfaref=ones(1,N);
TwallEX=ones(1,N);
TwallIN=ones(1,N);
differenzaT=ones(1,N);
PrefIN=ones(1,N);
PrefIN(1)=refpropm('p','T',Tsat+273.15,'Q',1,'R1234zee'); %[kPa]
Tsat=ones(1,N);
twmean=ones(1,N);
Dptot=0;

for z=1:N
    j=2;
    Tsat(z)=refpropm('T','P',PrefIN(z),'Q',0,'R1234zee');
    dQ=[1;Q/N]; %[W] calore supposto scambiato per ogni spira

    while abs(dQ(j)-dQ(j-1))>0.01
        hrefOUT(z)=hrefIN(z)-dQ(j)/mref;
        hV=refpropm('h','T',Tsat(z),'Q',1,'R1234zee'); %[J/kg]
        hL=refpropm('h','T',Tsat(z),'Q',0,'R1234zee');

        if hrefOUT(z)>hV;
            xout(z)=0.99;
        else
            xout(z)=(hrefOUT(z)-hL)/(hV-hL);
        end

        xmean=(xin(z)+xout(z))/2;
        dT=[1,5]; %differenza temperatura saturazione e parete
        i=2; %contatore secondo ciclo
        alfacalc=[0,0];

        while abs(dT(i)-dT(i-1))>0.001

            %Cavallini
            twmean(z)=Tsat(z)-dT(i);

            rho_L=(refpropm('D','T',Tsat(z),'Q',0,'R1234zee')+refpropm(
                'D','T',twmean(z),'Q',0,'R1234zee'))/2;
            rho_V=refpropm('D','T',Tsat(z),'Q',1,'R1234zee');

            lambda_L=(refpropm('L','T',Tsat(z),'Q',0,'R1234zee')+refpro
                pm('L','T',twmean(z),'Q',0,'R1234zee'))/2;
            hLV=(refpropm('H','T',Tsat(z),'Q',1,'R1234zee')-
                refpropm('H','T',Tsat(z),'Q',0,'R1234zee'));

            mu_L=(3*refpropm('V','T',twmean(z),'Q',0,'R1234zee')+refpro
                pm('V','T',Tsat(z),'Q',0,'R1234zee'))/4;
            mu_V=refpropm('V','T',Tsat(z),'Q',1,'R1234zee');

            cp_L=(refpropm('C','T',Tsat(z),'Q',0,'R1234zee')+refpropm('
                C','T',twmean(z),'Q',0,'R1234zee'))/2;
            sigma=refpropm('I','T',Tsat(z),'Q',0,'R1234zee');
            JG=xmean*G/(9.81*Di*rho_V*(rho_L-rho_V)^0.5;
            ReLO=G*Di/mu_L;
            Pr_L=cp_L*mu_L/lambda_L;
            Xtt=(mu_L/mu_V)^0.1*(rho_V/rho_L)^0.5*((1-
                xmean)/xmean)^0.9;
            alfaLO=0.023*ReLO^0.8*Pr_L^0.4*lambda_L/Di;

```

```

JGstar=0.6*((7.5/(4.3*Xtt^1.111+1))^-3+2.5^-3)^-0.3333;
if JG<JGstar
    C1=JG/JGstar;
else
    C1=1;
end
alfaDS=0.725/(1+0.741*((1-xmean)/xmean)^0.3321)*(lambda_L^3*rho_L*(rho_L-rho_V)...
    *9.81*hLV/(mu_L*Di*dT(i)))^0.25;

nopt=4064.4*Di+23.257;

C=1;

alfaD=C*(2.4*xmean^0.1206*(Rx-1)^1.466*C1^0.6875+1)*alfaDS+C*(1-xmean^0.087)*Rx*alfaLO;
Fr=G^2/(9.81*Di*(rho_L-rho_V)^2);
A=1+1.19*Fr^-0.3821*(Rx-1)^0.3586;

alfaAS=alfaLO*(1+1.128*xmean^0.817*(rho_L/rho_V)^0.3685*(mu_L/mu_V)^0.2363*...
    (1-mu_V/mu_L)^2.144*Pr_L^-0.1);
alfaA=alfaAS*A*C;
alfacalc(i)=(alfaA^3+alfaD^3)^0.333;

%alfa lato acqua
TwallIN(z)=twmean(z);
TwallEX(z)=TwallIN(z)-
dQ(j)*log(De/Di)/(2*pi*lambda_tubo*dL);
TwaterOUT(z)=dQ(j)/(mwater*4186)+TwaterIN(z);
TwaterMEAN(z)=(TwaterIN(z)+TwaterOUT(z))/2;
Tfilm(z)=(TwaterMEAN(z)+TwallEX(z))/2;

Pr_water=refpropm('^','T',Tfilm(z),'P',Pwater,'water');
lambda_water=refpropm('L','T',Tfilm(z),'P',Pwater,'water'); %[W m^-1 K^-1]
mu_water=refpropm('V','T',Tfilm(z),'P',Pwater,'water');
rho_water=refpropm('D','T',Tfilm(z),'P',Pwater,'water');
v_water=4*mwater/(rho_water*pi*(Dtank)^2);
Re_water(z)=v_water*De*rho_water/mu_water;

alfa_water(z)=0.989*Re_water(z)^0.330*Pr_water^(1/3)*(lambda_water/De);

%controllo temperatura di parete
Twallout(z)=dQ(j)/(Ae*alfa_water(z))+TwaterMEAN(z);

Twallinside(z)=Twallout(z)+dQ(j)*log(De/Di)/(2*pi*lambda_tubo*dL);

%Verifica del DT
Ki(z)=(1/alfacalc(i)+Ai/(Ae*alfa_water(z))+Ai*log(De/Dimax))/(2*pi*lambda_tubo*dL)^-1;
dT(i+1)=dQ(j)/(Ai*alfacalc(i));
i=i+1;
n=n+1;

```

```

end

%calcolo dQ effettivo scambiato
NTU=Ki(z)*Ai/(mwater*4186);
Eps=1-exp(-NTU);
dQmax=(mwater*4186)*(Tsat(z)-TwaterIN(z));
dQ(j+1)=dQmax*Eps;
j=j+1;

end

%perdite di carico per quantità di moto
eps_homoIN=(1+rho_V/rho_L*((1-xin(z))/xin(z)))^-1;
eps_smithIN=(1+rho_V/rho_L*((1-xin(z))/xin(z))*(0.4+0.6*sqrt(rho_V/rho_L+0.4*(1-xin(z))/xin(z)))/...
sqrt(1+0.4*(1-xin(z))/xin(z))))^-1;

epsIN=0.81*eps_smithIN+0.19*xin(z)^(100*(rho_V/rho_L)^0.8)*eps_homoIN;
dpain(z)=((xin(z)^2)/(epsIN*rho_V)+((1-xin(z))^2)/((1-epsIN)*rho_L));

eps_homoOUT=(1+rho_V/rho_L*((1-xout(z))/xout(z)))^-1;
eps_smithOUT=(1+rho_V/rho_L*((1-xout(z))/xout(z))*(0.4+0.6*sqrt(rho_V/rho_L+0.4*(1-xout(z))/xout(z)))/...
sqrt(1+0.4*(1-xout(z))/xout(z))))^-1;

epsOUT=0.81*eps_smithOUT+0.19*xout(z)^(100*(rho_V/rho_L)^0.8)*eps_homoOUT;
dpaout(z)=((xout(z)^2)/(epsOUT*rho_V)+((1-xout(z))^2)/((1-epsOUT)*rho_L));
dpa(z)=G^2*(dpaout(z)-dpain(z));

%Perdite di carico per frizione
pcr=refpropm('p','C',0,'',0,'R1234ZEE');
pr=PrefIN(z)/pcr;
H=(rho_L/rho_V)^1.132*(mu_V/mu_L)^0.44*(1-mu_V/mu_L)^3.542;
F=xmean^0.9525*(1-xmean)^0.414;
Z=(1-xmean)^2+xmean^2*rho_L/rho_V*(mu_V/mu_L)^0.2;
unomenoE=-0.331*log(mu_L*G*xmean/rho_V/sigma)-0.0919;
if unomenoE>1
    unomenoE=1;
end
W=1.398*pr;
philo=Z+3.595*F*H*unomenoE^W;
%flot=0.00875;
fold=0.3164*(G*Di/mu_L)^-0.25;
esud=0.18*e/Di/(0.1+cosd(beta));
AA=2*esud+18.7/10000000/fold;
flot=(1.74-2*log10(AA))^-2;
dpdzf(z)=philo*2*flot*G^2/Di/rho_L/4;

%Perdite di carico per gravità
eps_homo=(1+rho_V/rho_L*((1-xmean)/xmean))^-1;
eps_smith=(1+rho_V/rho_L*((1-xmean)/xmean)*(0.4+0.6*sqrt(rho_V/rho_L+0.4*(1-xmean)/xmean)))/...
sqrt(1+0.4*(1-xmean)/xmean))^-1;
eps=0.81*eps_smith+0.19*xmean^(100*(rho_V/rho_L)^0.8)*eps_homo;
rho_mean=eps*rho_V+(1-eps)*rho_L;

```

```

dpgrav(z)=9.81*rho_mean*p;
K(z)=Ki(end);
alfaref(z)=alfacalc(end);
DQ(z)=dQ(end);
TwaterIN(z+1)=TwaterOUT(z);
hrefIN(z+1)=hrefOUT(z);
xin(z+1)=xout(z);
QTOT=QTOT+DQ(z);
differenzaT(z)=dT(end);
PrefOUT(z)=PrefIN(z)-dpdzf(z)*dL/10^3-dpa(z)/10^3-dpgrav(z)/10^3;
TrefOUT(z)=refpropm('T','h',hrefOUT(z),'P',PrefOUT(z),'R1234zee')-
273.15;
TSAT(z)=Tsat(z)-273.15;
TrefIN(z+1)=TrefOUT(z);
PrefIN(z+1)=PrefOUT(end);
Dptot=Dptot+dpdzf(z)*dL/10^5+dpa(z)/10^5+dpgrav(z)/10^5;
dP(z)=dpdzf(z)*dL/10^5+dpa(z)/10^5+dpgrav(z)/10^5;
end

Ltot=N*dL
H=p*N
Area=Ltot*pi*De

```

CODE B.9: Condenser design with Hirose *et al.*'s modified model and OD 7mm

```

clc
clear all
close all

%% Geometria
De=7*10^-3; %[m]
Di=6.14*10^-3; %[m]
Dimax=6.5*10^-3; %[m]
e=0.18*10^-3; %altezza aletta
ng=50; %numero di alette
beta=18; %angolo d'elica
gamma=43; %angolo all'apice dell'aletta
lambda_tubo=390;
Rx_base=1.63;
p=1.5*De; %[m] pitch
Rcoil=0.1; %[m]
Dcoil=2*Rcoil; %[m]
Dtank=0.3; %[m]
dL=sqrt((Dcoil*pi)^2+p^2); %[m] lunghezza spira
Ai=dL*pi*Dimax; %[m^2] area spira interna rispetto a Dmax
Ae=dL*pi*De; %[m^2] area spira esterna rispetto a De
N=23; %numero alette supposte

%% Refrigerante
Tsat=323.15; %[K]
SH=15;
TrefIN=Tsats+SH;
PrefIN=refpropm('p','T',Tsats,'Q',0,'R1234zee'); %[kPa]
hrefIN=refpropm('h','T',TrefIN,'p',PrefIN,'R1234zee'); %[J/kg]
hrefOUT=refpropm('h','T',Tsats,'Q',0,'R1234zee'); %[J/kg]

Q=1000; %[W]
mref=Q/(hrefIN-hrefOUT);
G=4*mref/(pi*Di^2);
Gmax=4*mref/(pi*Dimax^2);

%% Acqua
TwaterIN=10;
TwaterOUT=40;
Pwater=101.325; %[kPa]
mwater=Q/(4186*(TwaterOUT-TwaterIN));

%% Calcoli spira per spira
n=0;
TwaterOUT=ones(1,N);
TwaterIN=ones(1,N);
TwaterIN(1)=283.15;
hrefIN=ones(1,N);
hrefIN(1)=refpropm('h','T',TrefIN,'p',PrefIN,'R1234zee');
hrefOUT=ones(1,N);
xin=ones(1,N);
xin(1)=0.99;
xout=ones(1,N);
TrefIN=ones(1,N);
TrefIN(1)=65;
TrefOUT=ones(1,N);

```

```

QTOT=0;
K=ones(1,N);
alfaref=ones(1,N);
TwallEX=ones(1,N);
TwallIN=ones(1,N);
differenzaT=ones(1,N);
alfa_water=ones(1,N);
PrefIN=ones(1,N);
PrefIN(1)=refpropm('p','T',Tsat,'Q',0,'R1234zee'); %[kPa]
dp=ones(1,N);
Dptot=0;

for z=1:N
    j=2;
    Tsat(z)=refpropm('T','p',PrefIN(z),'Q',0,'R1234zee');
    dQ=[1;Q/N];

    while abs(dQ(j)-dQ(j-1))>0.01
        hrefOUT(z)=hrefIN(z)-dQ(j)/mref;
        hV=refpropm('h','T',Tsat(z),'Q',1,'R1234zee'); %[J/kg]
        hL=refpropm('h','T',Tsat(z),'Q',0,'R1234zee'); %[J/kg]
        if hrefOUT(z)>hV;
            xout(z)=0.99;
        else
            xout(z)=(hrefOUT(z)-hL)/(hV-hL);
        end

        xmean=(xin(z)+xout(z))/2;
        dT=[1,5]; %differenza temperatura saturazione e parete
        i=2; %contatore secondo ciclo
        alfacalc=[0,0];

        while abs(dT(i)-dT(i-1))>0.001

            %Hirose
            twmean(z)=Tsat(z)-dT(i);

            rho_L=(refpropm('D','T',Tsat(z),'Q',0,'R1234zee')+refpropm(
                'D','T',twmean(z),'Q',0,'R1234zee'))/2;
            rho_V=refpropm('D','T',Tsat(z),'Q',1,'R1234zee');
            hLV=(refpropm('H','T',Tsat(z),'Q',1,'R1234zee')-
                refpropm('H','T',Tsat(z),'Q',0,'R1234zee'));

            lambda_L=(refpropm('L','T',Tsat(z),'Q',0,'R1234zee')+refpro
                pm('L','T',twmean(z),'Q',0,'R1234zee'))/2;

            hLV=(refpropm('H','T',Tsat(z),'Q',1,'R1234zee')-
                refpropm('H','T',Tsat(z),'Q',0,'R1234zee'));

            mu_L=(3*refpropm('V','T',twmean(z),'Q',0,'R1234zee')+refpro
                pm('V','T',Tsat(z),'Q',0,'R1234zee'))/4;
            mu_V=refpropm('V','T',Tsat(z),'Q',1,'R1234zee');

            cp_L=(refpropm('C','T',Tsat(z),'Q',0,'R1234zee')+refpropm('
                C','T',twmean(z),'Q',0,'R1234zee'))/2;
            sigma=refpropm('I','T',Tsat(z),'Q',0,'R1234zee');
            eps_homo=(1+rho_V/rho_L*((1-xmean)/xmean))^-1;
            eps_smith=(1+rho_V/rho_L*((1-
                xmean)/xmean))*(0.4+0.6*sqrt(rho_V/rho_L+0.4*(1-
                xmean)/xmean))/...

```

```

sqrt(1+0.4*(1-xmean)/xmean))^-1;

eps=0.81*eps_smith+0.19*xmean^(100*(rho_V/rho_L)^0.8)*eps_h
omo;
H=eps+(10*(1-eps)^0.1-8)*sqrt(eps)*(1-sqrt(eps));
Re_L=Gmax*(1-xmean)*Dimax/mu_L;
Re_V=Gmax*xmean*Dimax/mu_V;
Xtt=((mu_L/mu_V)^0.1)*((rho_V/rho_L)^0.5)*((1-
xmean)/xmean)^0.9;
Ga=9.81*Dimax^3*rho_L^2/mu_L^2;
fv=0.26*Re_V^-0.38*Rx_base^0.95*(cosd(beta))^-2.8;
phi_V=1+1.55*Xtt^0.4;
Pr_L=cp_L*mu_L/lambda_L;
Ph_L=cp_L*dT(i)/hLV;
Bo=(rho_L-rho_V)*9.81*Dimax^2/sigma;

if Re_L<= 1250

    Fr_sol=0.025*Re_L^1.59*(((1+1.09*Xtt^0.039)/Xtt)^1.5)/Ga
    ^0.5;
else

    Fr_sol=1.26*Re_L^1.04*(((1+1.09*Xtt^0.039)/Xtt)^1.5)/Ga^
    0.5;
end

if Fr_sol<20

    NuF=3.90*sqrt(fv)*(phi_V/Xtt)*(mu_L/mu_V)^0.1*(xmean/(1
xmean))^0.1*Re_L^0.55;
else

    NuF=2.67*sqrt(fv)*(phi_V/Xtt)*(mu_L/mu_V)^0.1*(xmean/(
1-xmean))^0.1*Re_L^0.63;
end

NuB=0.725*Rx_base^-0.25*H*(Ga*Pr_L/Ph_L)^0.25;
Nu=sqrt(NuF^2+NuB^2);
alfacalc(i)=lambda_L* Nu/Dimax;

%alfa lato acqua
TwallIN(z)=twmean(z);
TwallEX(z)=TwallIN(z)-
dQ(j)*log(De/Di)/(2*pi*lambda_tubo*dL);
TwaterOUT(z)=dQ(j)/(mwater*4186)+TwaterIN(z);
TwaterMEAN(z)=(TwaterIN(z)+TwaterOUT(z))/2;
Tfilm(z)=(TwaterMEAN(z)+TwallEX(z))/2;

Pr_water=refpropm('^','T',Tfilm(z),'P',Pwater,'water');
lambda_water=refpropm('L','T',Tfilm(z),'P',
Pwater,'water'); %[W m^-1 K^-1]
mu_water=refpropm('V','T',Tfilm(z),'P',Pwater,'water');
rho_water=refpropm('D','T',Tfilm(z),'P',Pwater,'water');
v_water=4*mwater/(rho_water*pi*(Dtank)^2);
Re_water(z)=v_water*De*rho_water/mu_water;

alfa_water(z)=0.989*Re_water(z)^0.330*Pr_water^(1/3)*(lambd
a_water/De);

%controllo temperatura di parete
Twallout(z)=dQ(j)/(Ae*alfa_water(z))+TwaterMEAN(z);

```

```

Twallinside(z)=Twallout(z)+dQ(j)*log(De/Di)/(2*pi*lambda_tu
bo*dL);

%Verifica del DT

Ki(z)=(1/alfacalc(i)+Ai/(Ae*alfa_water(z))+Ai*log(De/Dima
x)/(2*pi*lambda_tubo*dL))^-1;
dT(i+1)=dQ(j)/(Ai*alfacalc(i));
i=i+1;
n=n+1;
end

NTU=Ki(z)*Ai/(mwater*4186);
Eps=1-exp(-NTU);
dQmax=(mwater*4186)*(Tsat(z)-TwaterIN(z));
dQ(j+1)=dQmax*Eps;
j=j+1;
end

%perdite carico frizione
dpvap=2*fv*Gmax^2*xmean^2/(rho_V*Dimax);
dpfcalc(z)=phi_V^2*dpvap;

%perdite di carico per accelerazione
eps_homoIN=(1+rho_V/rho_L*((1-xin(z))/xin(z)))^-1;
eps_smithIN=(1+rho_V/rho_L*((1-
xin(z))/xin(z))*(0.4+0.6*sqrt(rho_V/rho_L+0.4*(1-
xin(z))/xin(z)))/...
sqrt(1+0.4*(1-xin(z))/xin(z))))^-1;

epsIN=0.81*eps_smithIN+0.19*xin(z)^(100*(rho_V/rho_L)^0.8)*eps_homo
IN;
dpain(z)=((xin(z)^2)/(epsIN*rho_V)+((1-xin(z))^2)/((1-
epsIN)*rho_L));

eps_homoOUT=(1+rho_V/rho_L*((1-xout(z))/xout(z)))^-1;
eps_smithOUT=(1+rho_V/rho_L*((1-
xout(z))/xout(z))*(0.4+0.6*sqrt(rho_V/rho_L+0.4*(1-
xout(z))/xout(z)))/...
sqrt(1+0.4*(1-xout(z))/xout(z))))^-1;

epsOUT=0.81*eps_smithOUT+0.19*xout(z)^(100*(rho_V/rho_L)^0.8)*eps_h
omoOUT;
dpaout(z)=((xout(z)^2)/(epsOUT*rho_V)+((1-xout(z))^2)/((1-
epsOUT)*rho_L));
dpa(z)=Gmax^2*(dpaout(z)-dpain(z));

%Perdite di carico per gravità
eps_homo=(1+rho_V/rho_L*((1-xmean)/xmean))^-1;
eps_smith=(1+rho_V/rho_L*((1-
xmean)/xmean)*(0.4+0.6*sqrt(rho_V/rho_L+0.4*(1-xmean)/xmean)/...
sqrt(1+0.4*(1-xmean)/xmean))))^-1;
eps=0.81*eps_smith+0.19*xmean^(100*(rho_V/rho_L)^0.8)*eps_homo;
rho_mean=eps*rho_V+(1-eps)*rho_L;
dpgrav(z)=9.81*rho_mean*p;

K(z)=Ki(end);
alfaref(z)=alfacalc(end);

```

```

DQ(z)=dQ(end);
TwaterIN(z+1)=TwaterOUT(z);
hrefIN(z+1)=hrefOUT(z);
xin(z+1)=xout(z);
PrefOUT(z)=PrefIN(z)-dpfcalc(z)*dL/10^3-dpa(z)/10^3-
dpgrav(z)/10^3;
TrefOUT(z)=refpropm('T','h',hrefOUT(z),'P',PrefOUT(z),'R1234zee')-
273.15;
TrefIN(z+1)=TrefOUT(z);
TSAT(z)=Tsat(z)-273.15;
PrefIN(z+1)=PrefOUT(end);
QTOT=QTOT+DQ(z);
Dptot=Dptot+dpfcalc(z)*dL/10^5+dpa(z)/10^5+dpgrav(z)/10^5;
differenzaT(z)=dT(end);
dP(z)=dpfcalc(z)*dL/10^5+dpa(z)/10^5+dpgrav(z)/10^5;
end

Ltot=N*dL
H=p*N
Area=Ltot*pi*De

```

CODE B.10. Thermocouples calibration

```
%THERMOCOUPLES CALIBRATION
clc
clear all
close all
T_PT100=[19.82 29.79 39.74 49.63 59.44 69.26];
V=[0.777803642 1.184884803 1.600102125 2.021257873 2.444672801
2.876038363];

a=polyfit(V,T_PT100,4)
x=0:0.1:3;
y=polyval(a,x);

old=[0.0116683 -0.0425488 -0.556815 25.6901 0.186496];
y1=polyval(old,x);

plot(V,T_PT100,'*g','LineWidth',4);
xlabel('V [mV]');
ylabel('T[°C]');
hold on
plot(x,y,'b','LineWidth',2);
plot(x,y1,'r-','LineWidth',2);
grid on
title('Old vs new polynomial')
legend('Pt100','New','Old')
set(gca,'FontSize',18)
```

CODE B.11. T-history: polynomial interpolation

```
%% START
clc
clear all
close all
load DATA_SOLIDIFICATION

%% POLYNOMIAL INTERPOLATION
t=tempoTrascorso/60;
p=polyfit(t,TPCM,20);
y=polyval(p,t);

p2=polyfit(t,TAcqua,20);
y2=polyval(p2,t);

t_media_aria=(TCamera1+TCamera2)/2;
p3=polyfit(t,t_media_aria,20);
y3=polyval(p3,t);

t0=3068/60;

%% DERIVATE
pd1=polyder(p);
der1=polyval(pd1,t);

pd2=polyder(pd1);
der2=polyval(pd2,t);

pd3=polyder(pd2);
der3=polyval(pd3,t);

%% PLOT
figure
plot(t-t0,TPCM,'LineWidth',2)
hold on
plot(t-t0,TAcqua,'LineWidth',2)
plot(t-t0,t_media_aria,'LineWidth',2)
legend('T_P_C_M','T_H_2_O','T_a_i_r')
title('Experimental points')
xlabel('Time [min]')
ylabel('Temperature [°C]')
grid on
set(gca,'FontSize',18)
xlim([0 40])

figure
subplot(2,1,1)
plot(t-t0,y,'LineWidth',2)
grid on
hold on
plot(t-t0,y2,'LineWidth',2)
plot(t-t0,y3,'LineWidth',2)
xlabel('time [min]')
ylabel('temperature [°C]')
set(gca,'FontSize',18)
legend('T_P_C_M','T_H_2_O','T_a_i_r')
xlim([0 40])
```

```

subplot(2,1,2)
yyaxis left
plot(t-t0,der1,'r','LineWidth',2)
grid on
xlabel('time [min]')
ylabel('first der [°C/min]')
set(gca,'FontSize',18)
xlim([0 40])

hold on
yyaxis right
plot(t-t0,der2,'g','LineWidth',2)
grid on
xlabel('time [min]')
ylabel('second der [°C/min^2]')
set(gca,'FontSize',18)
legend('der1','der2')
xlim([0 40])

%% PHASE CHANGE POINTS
r=roots(pd2);
r=r(imag(r)==0);
r1=roots(pd3);
r1=r1(imag(r1)==0);

ts=54.55;
ti=70.83;

Ts=polyval(p,ts);
Ti=polyval(p,ti);

%% INTEGRATION
pintPCM=polyint(p);
pintH2O=polyint(p2);
pintAIR=polyint(p3);

%% AREA A1
intAIR(1)=-polyval(pintAIR,t0)+polyval(pintAIR,ts);
intPCM(1)=-polyval(pintPCM,t0)+polyval(pintPCM,ts);
A1=-intAIR(1)+intPCM(1);

n=length(t);
u=ones(1,n);
line1=Ts*u;
[t_1_H2O,y_1_H2O] = polyxpoly(t,y2,t,line1);

intH2O(1)=-polyval(pintH2O,t0)+polyval(pintH2O,t_1_H2O);
intAIR_H2O(1)=-polyval(pintAIR,t0)+polyval(pintAIR,t_1_H2O);
A1_H2O=-intAIR_H2O(1)+intH2O(1);

%% AREA A2
intAIR(2)=polyval(pintAIR,ti)-polyval(pintAIR,ts);
intPCM(2)=polyval(pintPCM,ti)-polyval(pintPCM,ts);
A2=intPCM(2)-intAIR(2);

line2=Ti*u;
[t_2_H2O,y_2_H2O] = polyxpoly(t,y2,t,line2);

intH2O(2)=polyval(pintH2O,t_2_H2O)-polyval(pintH2O,t_1_H2O);
intAIR_H2O(2)=polyval(pintAIR,t_2_H2O)-polyval(pintAIR,t_1_H2O);

```

```

A2_H2O=intH2O(2)-intAIR_H2O(2);

%% AREA A3
Tend=40;
line3=Tend*u;
[t_end,y_end] = polyxpoly(t,y,t,line3);

intAIR(3)=-polyval(pintAIR,ti)+polyval(pintAIR,t_end);
intPCM(3)=-polyval(pintPCM,ti)+polyval(pintPCM,t_end);
A3=intPCM(3)-intAIR(3);

[t_end_H2O,y_end_H2O] = polyxpoly(t,y2,t,line3);
intH2O(3)=polyval(pintH2O,t_end_H2O)-polyval(pintH2O,t_2_H2O);
intAIR_H2O(3)=polyval(pintAIR,t_end_H2O)-polyval(pintAIR,t_2_H2O);
A3_H2O=intH2O(3)-intAIR_H2O(3);

%% DATA
m_t_pcm=0.00798;
c_t=0.5;
m_t_w=0.00776;
m_w=0.00924;
c_w=4.2;
m_pcm=0.00709;

%% CALCULATION
% Cp
Cp_s=(m_t_w*c_t+m_w*c_w)/m_pcm*(A3/A3_H2O)-(m_t_pcm/m_pcm)*c_t;
Cp_l=(m_t_w*c_t+m_w*c_w)/m_pcm*(A1/A1_H2O)-(m_t_pcm/m_pcm)*c_t;
Cp=(Cp_s+Cp_l)/2;
% Error Cp
Cp_real=2;
Error_cp=(Cp-Cp_real)/Cp_real*100;

% Latent Heat
H=(m_w*c_w+m_t_w*c_t)/m_pcm*A2/A2_H2O*(Ts-Ti)-
(m_t_pcm*c_t/m_pcm+Cp)*(Ts-Ti)
% Error latent heat
H_real=170;
Error_H=abs(H-H_real)/H_real*100;

%% RESULTS
T=table(Ts,Ti)
CP=table(Cp_s,Cp_l,Cp,Cp_real,Error_cp)
H=table(H,H_real,Error_H)
h=(m_w*c_w+m_t_w*c_t)*(Ts-Ti)/(A2_H2O*0.003966);
Bi=(h*0.005/(2*0.2))

```

CODE B.12. T-history: spline interpolation

```
%% START
clc
clear all
close all
load DATA_SOLIDIFICATION_B

%% POLYNOMIAL INTERPOLATION
t=tempoTrascorso/60;
p=spline(t,TPCM);
y=fnval(p,t);

p2=spline(t,TAcqua);
y2=fnval(p2,t);

t_media_aria=(TCamera1+TCamera2)/2;
p3=spline(t,t_media_aria);
y3=fnval(p3,t);

t0=3068/60;

%% DERIVATE
pd1=fnder(p);
der1=fnval(pd1,t);

%% PLOT
figure
subplot(2,1,1)
plot(t-t0,y,'LineWidth',2)
grid on
hold on
plot(t-t0,y2,'LineWidth',2)
plot(t-t0,y3,'LineWidth',2)
legend('PCM','Water','Air')
xlabel('time [min]')
ylabel('temperature [°C]')
legend('T_P_C_M','T_H_2_O','T_a_i_r')
hold off
set(gca,'FontSize',18)
xlim([0 40])

subplot(2,1,2)
plot(t-t0,der1,'r','LineWidth',2)
grid on
xlabel('time [min]')
ylabel('first derivative[°C/min]')
set(gca,'FontSize',18)
xlim([0 40])

%% POINTS
ts=55.15;
ti=70.87;

Ts=fnval(p,ts);
Ti=fnval(p,ti);

%% AREA A1
pintPCM=fnint(p);
```

```

pintH2O=fnint(p2);
pintAIR=fnint(p3);

intAIR(1)=-fnval(pintAIR,t0)+fnval(pintAIR,ts);
intPCM(1)=-fnval(pintPCM,t0)+fnval(pintPCM,ts);
A1=-intAIR(1)+intPCM(1);

n=length(t);
u=ones(1,n);
line1=Ts*u;
[t_1_H2O,y_1_H2O] = polyxpoly(t,y2,t,line1);

intH2O(1)=-fnval(pintH2O,t0)+fnval(pintH2O,t_1_H2O);
intAIR_H2O(1)=-fnval(pintAIR,t0)+fnval(pintAIR,t_1_H2O);
A1_H2O=-intAIR_H2O(1)+intH2O(1);

%% AREA A2
intAIR(2)=fnval(pintAIR,ti)-fnval(pintAIR,ts);
intPCM(2)=fnval(pintPCM,ti)-fnval(pintPCM,ts);
A2=intPCM(2)-intAIR(2);

line2=Ti*u;
[t_2_H2O,y_2_H2O] = polyxpoly(t,y2,t,line2);

intH2O(2)=fnval(pintH2O,t_2_H2O)-fnval(pintH2O,t_1_H2O);
intAIR_H2O(2)=fnval(pintAIR,t_2_H2O)-fnval(pintAIR,t_1_H2O);
A2_H2O=intH2O(2)-intAIR_H2O(2);

%% AREA A3
Tend=40;
line3=Tend*u;
[t_end,y_end] = polyxpoly(t,y,t,line3);
intAIR(3)=-fnval(pintAIR,ti)+fnval(pintAIR,t_end);
intPCM(3)=-fnval(pintPCM,ti)+fnval(pintPCM,t_end);
A3=intPCM(3)-intAIR(3);

[t_end_H2O,y_end_H2O] = polyxpoly(t,y2,t,line3);
intH2O(3)=fnval(pintH2O,t_end_H2O)-fnval(pintH2O,t_2_H2O);
intAIR_H2O(3)=fnval(pintAIR,t_end_H2O)-fnval(pintAIR,t_2_H2O);
A3_H2O=intH2O(3)-intAIR_H2O(3);

%% DATA
m_t_pcm=0.00798;
c_t=0.5;
m_t_w=0.00776;
m_w=0.00924;
c_w=4.2;
m_pcm=0.00709;

%% CALCULATION
% Cp
Cp_s=(m_t_w*c_t+m_w*c_w)/m_pcm*(A3/A3_H2O)-(m_t_pcm/m_pcm)*c_t;
Cp_l=(m_t_w*c_t+m_w*c_w)/m_pcm*(A1/A1_H2O)-(m_t_pcm/m_pcm)*c_t;
Cp=(Cp_s+Cp_l)/2;
%Error Cp
Cp_real=2;
Error_cp=(Cp-Cp_real)/Cp_real*100;

```

```

%Latent heat
H=((m_w*c_w+m_t_w*c_t)/m_pcm)*A2/A2_H2O*(Ts-Ti)-
(m_t_pcm*c_t/m_pcm+Cp)*(Ts-Ti);
%Error H
H_real=170;
Error_H=abs(H-H_real)/H_real*100;

%% RESULTS
T=table(Ts, Ti)
CP=table(Cp_s, Cp_l, Cp, Cp_real, Error_cp)
H=table(H, H_real, Error_H)
h=(m_w*c_w+m_t_w*c_t)*(Ts-Ti)/(A2_H2O*0.003966);
Bi=(h*0.005/(2*0.2))

```


Bibliografy

- [1] L. Rossetto, "Capitolo 9: Condensazione," in *Dispense di trasmissione del calore*, Padova, 2020.
- [2] A. Cavallini, D. Del Col, S. Mancin and L. Rossetto, "Condensation of pure and near-azeotropic refrigerants in microfin tubes: a new computational procedure," *International Journal of Refrigeration*, no. 32, pp. 162-174, 2008.
- [3] M. Hirose, J. Ichinose and N. Inoue, "Development of the general correlation for condensation heat transfer and pressure drop inside horizontal 4 mm small-diameter smooth and microfin tubes," *International Journal of Refrigeration*, vol. 90, pp. 238-248, 2018.
- [4] R. L. Webb, "Convective condensation of superheated vapor," *Journal of heat transfer*, vol. 120, no. 2, pp. 418-421, 1998.
- [5] V. Gnielinski, "On the heat transfer in tubes," *International Journal of Heat and Mass Transfer*, vol. 63, pp. 134-140, 2013.
- [6] A. Diani, S. Mancin and L. Rossetto, "R1234ze(E) flow boiling inside a 3.4 mm ID microfin tube," *International Journal of Refrigeration*, vol. 47, pp. 105-119, 2014.
- [7] E. Granryd, I. Ekroth, P. Lundqvist, A. Melinder, B. Palm and P. Rohlin, *Refrigerating engineering*, Stockholm, 2011.
- [8] C. Kondou and P. Hrnjak, "Condensation from superheated vapor flow of R744 and R410A at subcritical pressures in horizontal smooth tube," *International Journal of Heat and Mass Transfer*, vol. 55, pp. 2779-2791, 2012.
- [9] A. Diani, Y. Liu, J. Wen and L. Rossetto, "Experimental investigation on the flow condensation of R450A, R515B and R1234ze(E) in a 7.0 mm OD micro-fin tube," *International Journal of Heat and Mass Transfer*, vol. 196, pp. 1-13, 2022.
- [10] E. Donno, "CONDENSAZIONE DI R515B E R450A IN UN TUBO MICROALETTATO DI DIAMETRO ESTERNO 5 mm: ANALISI SPERIMENTALE E TEORICA," Padova, 2022.
- [11] E. W. Lemmon, I. H. Bell, M. L. Huber and M. O. McLinden, *NIST Standard Reference Database 23: Reference Fluid Thermodynamic and Transport Properties-REFPROP, Version 10.0*, National Institute of Standards and Technology, Standard Reference Data Program, Gaithersburg, 2018.
- [12] E. W. Lemmon, M. O. McLinden and M. Thol, "Thermodynamic Properties of trans-1,3,3,3-tetrafluoropropene [R1234ze(E)]: Measurements of Density and Vapor Pressure and a Comprehensive Equation of State," in *International Refrigeration and Air Conditioning Conference*, Purdue, 2010.

- [13] A. Mota-Babiloni, J. Navarro-Esbrí, Á. B. Cervera, F. Molés and B. Peris, "Drop-in energy performance evaluation of R1234yf and R1234ze(E) in a vapor compression system as R134a replacements," *Applied Thermal Engineering*, vol. 71, no. 1, pp. 259-265, 2014.
- [14] L. Pietro, M. Colombo, A. Lucchini and L. Molinaroli, "Experimental analysis of the use of R1234yf and R1234ze(E) as," *International Journal of Refrigeration*, vol. 115, pp. 18-27, 2020.
- [15] S. Fukuda, C. Kondou, N. Takata and S. Koyama, "Low GWP refrigerants R1234ze(E) and R1234ze(Z)," *International Journal of Refrigeration*, vol. 40, pp. 161-173, 2014.
- [16] D. Del Col, M. Bortolato, M. Azzolin and S. Bortolin, "Condensation heat transfer and two-phase," *International Journal of Refrigeration*, vol. 50, pp. 87-103, 2015.
- [17] A. G. Longo, S. Mancin, G. Righetti and C. Zilio, "Saturated vapour condensation of R134a inside a 4 mm ID horizontal," *International Journal of Heat and Mass Transfer*, vol. 133, pp. 461-473, 2019.
- [18] A. Diani, M. Campanale and L. Rossetto, "Experimental study on heat transfer condensation of R1234ze(E) and R134a inside a 4.0 mm OD horizontal microfin tube," *International Journal of Heat and Mass Transfer*, vol. 126, no. B, pp. 1316-1325, 2018.
- [19] R. Bitter, T. Mohiuddin and M. Nawrocki, *LabVIEW: Advanced programming techniques*, Crc Press, 2006.
- [20] UNI-CEI-ENV-13005:Guide to the Expression of Uncertainty in Measurement, 2000.
- [21] S. J. Kline and F. McClintock, "Describing uncertainties in a single-sample experiments," *Mechanical Engineering*, vol. 75, pp. 3-8, 1953.
- [22] A. Cavallini, D. Del Col, L. Doretti, M. Matkovic, L. Rossetto, C. Zilio and G. Censi, "Condensation in horizontal smooth tubes: a new heat transfer model for heat exchanger design," *Heat transfer engineering*, vol. 27, no. 8, pp. 31-38, 2006.
- [23] J. Yu and S. Koyama, "Condensation of Pure Refrigerants in Microfin Tubes – A Correlation for Local Heat Transfer Coefficient.," *The Reports of IAMS*, Vols. 10-2, p. 145–150, 1996.
- [24] M. M. Shah, "A general correlation for the heat transfer during film condensation inside pipes," *International Journal of Heat and Mass Transfer*, vol. 22, no. 4, pp. 547-556, 1979.
- [25] F. W. Dittus and L. M. K. Boelter, "Heat transfer in automobile radiators of the tubular type," *International Communications in Heat and Mass Transfer*, vol. 12, no. 1, pp. 3-22, 1985.

- [26] J. K. Dabas, S. Kumar, A. K. Dodeja and K. S. Kasana, "Modeling of a Cylindrical Shell and Helical Tube Condenser," *Heat Transfer—Asian Research*, vol. 3, no. 45, p. 209–227, 2016.
- [27] M. De Carli, *Dispense di HVAC systems*, Padova, 2022.
- [28] F. P. Incropera, D. P. Dewitt, T. L. Bergman and A. S. Lavine, *Heat and Mass transfer (seventh edition)*, Jefferson City: JOHN WILEY & SONS, 2011.
- [29] M. E.-S. Ali, "Experimental investigation of natural convection from vertical coiled tubes," *International Journal of Heat and Mass Transfer*, vol. 37, no. 4, pp. 665-671, 1994.
- [30] S. Missaoui, Z. Driss, R. B. Slama e B. Chaouachi, «Effects of pipe turns on vertical helically coiled tube heat exchangers for water heating in a household refrigerator,» *International Journal of Air-Conditioning and Refrigeration*, vol. 30, n. 6, pp. 1-13, 2022.
- [31] A. Cavallini, D. Del Col, M. Matkovic and L. Rossetto, "Pressure drop during two-phase flow of R134a and R32 in a single minichannel," *Journal of Heat Transfer*, vol. 131, pp. 033107-1-033107-8, 2009b.
- [32] C. Bonacina, A. Cavallini and L. Mattrolo, *Trasmissione del calore*, Padova: CLEUP, 1985.
- [33] Y. Zhang and Y. Jiang, "A simple method, the T-history method, of determining the heat of fusion, specific heat and thermal conductivity of phase change materials," *Measurement Science and Technology*, vol. 10, pp. 201-205, 1999.
- [34] H. Hong, S. K. Kim and Y.-S. Kim, "Accuracy improvement of T-history method for measuring heat of fusion of various materials," *International Journal of Refrigeration*, vol. 27, pp. 360-366, 2004.
- [35] Rubitherm, *RT42 Datasheet*, 2020.
- [36] Rubitherm, *RT55 Datasheet*, 2020.
- [37] Rubitherm, *RT64HC Datasheet*, 2020.
- [38] A. Martínez, M. Carmona, C. Cortés and I. Arauzo, "Characterization of thermal properties of phase change materials using unconventional experimental technologies," *Energies*, vol. 13, pp. 4687-4710, 2020.
- [39] P. Rolka, R. Kwidzinski, T. Przybylinski and A. Tomaszewski, "Thermal characterization of medium-temperature phase change materials (PCMs) for thermal energy storage using the T-history method," *Materials*, vol. 14, pp. 7371-7392, 2021.
- [40] The Math Work Inc., *MATLAB 2020b*, Natick, Massachusetts, USA, 2020.

